# ANALYSIS, DESIGN AND CHARACTERIZATION OF SMALL-GAP PHOTOCONDUCTIVE DIPOLE ANTENNA FOR TERAHERTZ IMAGING APPLICATIONS

by

**ISHA MALHOTRA**

*Thesis submitted in fulfillment for the requirement of the degree of*

**Doctor of Philosophy**

**In**

**Electronics and Communication Engineering**

DEPARTMENT OF ELECTRONICS AND COMMUNICATION ENGINEERING

JAYPEE UNIVERSITY OF INFORMATION TECHNOLOGY

WAKNAGHAT, SOLAN, HIMACHAL PRADESH, INDIA.

DECEMBER, 2017

# ANALYSIS, DESIGN AND CHARACTERIZATION OF SMALL-GAP PHOTOCONDUCTIVE DIPOLE ANTENNA FOR TERAHERTZ IMAGING APPLICATIONS

by

**ISHA MALHOTRA**

*Thesis submitted in fulfilment for the requirement of the degree of*

**Doctor of Philosophy**

**In**

**Electronics and Communication Engineering**

DEPARTMENT OF ELECTRONICS AND COMMUNICATION ENGINEERING

JAYPEE UNIVERSITY OF INFORMATION TECHNOLOGY

WAKNAGHAT, SOLAN, HIMACHAL PRADESH, INDIA.

DECEMBER, 2017

@ Copyright JAYPEE UNIVERSITY OF INFORMATION TECHNOLOGY,

WAKNAGHAT

DECEMBER, 2017

ALL RIGHTS RESERVED

# TABLE OF CONTENTS

Date:

# CANDIDATE’S DECLARATION

I declare that the written submission signifies my ideas in my own work and where others ideas have been included. I have adequately cited and referenced the original sources. I have followed all the principles of academic honesty and integrity. I understand that any violation of the above will be the cause of disciplinary action by the Institute and can also induce penal action from the sources which have thus not been correctly cited or from whom proper permission has not been taken when required.

**Isha Malhotra**

(Enrolment No. 126002)

Date: / /

Date:

# CERTIFICATE

This is to certify that the work presented in the thesis entitled ***"Analysis, Design and Characterization of Small-Gap Photoconductive Dipole Antenna for Terahertz Imaging Applications "***, which is being submitted by **Isha Malhotra** in fulfillment of the requirement for the award of the degree of **Doctor of Philosophy** (Electronics and Communication Engineering) in the Department of Electronics and Communication Engineering of Jaypee University of Information Technology, Waknaghat, Distt. Solan, Himachal Pradesh, India is an authentic record of candidate's own work, carried out by her under my supervision.

The matter presented in this thesis has not been submitted by her for the award of any other degree in this Institute or any other Institute/University.

**Prof. (Dr.) Ghanshyam Singh**
Professor,
Department of Electronics and Communication Engineering,
Jaypee University of Information Technology, Waknaghat, Distt. Solan, Himachal Pradesh, India.

Research is to see what everybody else has seen,

And to think what nobody else has thought.

# DEDICATION

**I am here because of the blessings and good wishes of my father Er. K. L. Verma, my mother Mrs. Anita Verma and support of my loving brother Er. Kushal Verma.**

# ACKNOWLEDGEMENT

*"Dreams don't work unless you do"*

First of all, I express my sincere gratitude to my supervisor, Prof. (Dr.) Ghanshyam Singh, Department of Electronics and Communication Engineering (ECE), Jaypee University of Information Technology (JUIT) Waknaghat, Solan, Himachal Pradesh, India, for his guidance and encouragement. His experienced mentoring, insightful conversations during the development of the ideas in this thesis and comments proved to be immense helpful to me, and also his profound view-points and extraordinary motivation enlightened me in many ways. I am highly indebted for his guidance, support and cooperation. I shall always remain grateful to him. I am grateful to Dr. Kumud Ranjan Jha, for his valuable guidance that helps me improving my work.

My sincere thanks are to Vice-Chancellor, Director and Dean (Academic and Research) and Head, Department of Electronics and Communication Engineering (ECE), Jaypee University of Information Technology, Waknaghat, Solan, Himachal Pradesh, India, for providing me all the needed support to complete the research work. I am sincerely thankful to my committee members, Dr. Rajiv Kumar (ECE), Dr. Meenakshi Sood (ECE) and Dr. Hemraj Saini (CSE) for their constructive feedback and comments that have helped me in my research work. I also sincerely thank every member of the ECE Department and Administration of the Jaypee University of Information Technology, Waknaghat, Solan, Himachal Pradesh, India, for their kind support. I would like to take this opportunity to thank all my teachers and professors throughout my student life who have inspired and motivated me to realize this dream.

I give my greatest gratitude to my parents, who have been offering all around support during the period of my studies and research. It is the tremendous blessings and endless sacrifice of my parents. They have shown immense patience and supported me in every possible way. Words alone can never express my gratitude to them. I owe everything to them. I am pleased to thank my father Er. K. L. Verma and mother Mrs. Anita Verma for always listening to me and finding time to have fun with the instances of stress throughout these years. I express the deepest gratitude to my brother Er. Kushal Verma for his unconditional love, encouragement, appreciation and support during my studies as well as research and lifting me uphill during this phase of life. I would like to extend warm thanks to my niece Tejal Verma and son Modit Malhotra, their innocent smiles and chats always bring a smile on my face and bring cheerfulness even in the odd time. I express my profound thanks to my husband Er. Deepak Malhotra for his concerns and support during the final stages of my research work.

I am thankful to my friend Dr. Shweta Pandit for her valuable support, suggestions, motivation and prolific editing in my thesis. I consider myself fortunate to meet her. The writing of this thesis could not be possible without her kind assistance, suggestions and corrections. I also thank my friends and lab-mates including (but not limited to), Dr. Garima Bharti, Dr. Keerti Tiwari, Jhonny Dhiman, Prabhat Thakur, Ashutosh Sharma, Kanishka Katoch and Jyotsana Dogra for their encouragement and maintaining research atmosphere in the lab. They always showed concern and discussed the things whenever required. I would like to thank all those people from the core of my heart who made this thesis possible. To those individuals I neglect to mention here by name, I still offer my deepest thanks.

In the last but not least, I thank the ultimate source of energy of every particle in the universe, the Almighty, for giving me enough energy and strength to complete the work. All praise and gratitude belongs to Him.

**(Isha Malhotra)**

# ABSTRACT

The terahertz (THz) regime of the electromagnetic spectrum is rich because of its unique properties with the emerging possibilities in various applications such as wireless communications, imaging, non-destructive testing, security scanning and process control. The unique features of THz waves are non-ionizing radiation, better resolution than the microwave, unique spectral absorption, and an ability to propagate through dielectric materials. The spectroscopy with high spectral resolution at frequencies in THz range is an influential analytical tool for investigating the structure as well as the energy levels of molecules and atoms. Using THz spectroscopy, it is potentially possible to detect explosive and illicit drugs even though they are obscured because THz radiations can rapidly transmit through materials such as plastics, paper products, luggage, clothing and other non-conductive materials. Moreover, on comparing the measured reflectivity of the THz spectra with known calibration spectra, it is easier to identify the presence of these agents and distinguish them from benign objects.

For the imaging applications, the continuous wave (narrowband) or pulsed wave (broadband) THz systems for the generation of THz radiation is used and this classification is based on the laser source used to generate photocurrent. Moreover, the applications such as homeland security, defence as well as safety of aviation industry have placed huge demands on the growth of advanced imaging systems. However, the visible and the infrared imagery is providing high image quality, but they are mired by atmospheric obscurants such as cloud cover, dust storms, sand, smoke, fog and rain. Therefore, the THz imaging provides an attractive means to diminish or eliminate the impact of low visibility conditions due to such atmospheric conditions. Further, in close-range sensing and imaging applications, the pulsed THz sources are more favourable for acquiring depth information. The advantages of pulsed THz time-domain spectroscopy are that broad spectral information from 0.1-3 THz can be obtained using a single picoseconds THz pulse and the depth information can be achieved from the difference in arrival times of THz short pulses.

The potential challenges in the present THz pulsed imaging system includes size, cost, output power, signal-to-noise ratio (SNR), bandwidth, spatial resolution, depth penetration, water sensitivity and speed of data acquisition. Various THz applications would be benefited from the compact integration of THz devices and other types of functional devices. Moreover, for the THz imaging application there is a potential requirement of planar and compact THz

antenna sources with on-chip fabrication in addition to high directivity so as to attain large depth-of-field (DoF) for enhanced image resolution. Therefore, all the relevant literature on the current state-of-the-art pulsed THz imaging applications and potential challenges of THz antenna technology for imaging applications has been reviewed. The THz antennas which rely on photoconduction technique are the most common devices in THz systems. Among them, a photoconductive dipole antenna being simple in fabrication is the extensively utilized THz source for pulsed broadband system used in THz imaging and spectroscopy systems. A well-designed sub-wavelength (micrometer) scale photoconductive dipole antenna structure has the potential for high output power generation and broadband THz pulse emission which are useful for THz imaging system. However, the low values of gain, directivity and the low optical-to-THz conversion efficiency are the important limitations of basic photoconductive dipole antenna. Therefore, the inspiration of this research work is to theoretically ascertain the key modalities of improving photoconductive dipole antenna's performance for imaging applications. We have presented several methods/ techniques to enhance the directivity of the photoconductive dipole antenna analytically and validate the proposed models by using CST Microwave Studio simulation software.

Initially, a simple synthesis technique to find out the physical parameters of small-gap photoconductive dipole antenna is exploited. To enhance the antenna radiation efficiency which also contributes to the total efficiency of photoconductive dipole antenna, a thin superstrate below the dipole antenna is employed which also enables the antenna to withstand high biased voltage. Moreover, to have a diffraction limited imaging, there is a requirement to design an antenna of shorter wavelength. Consequently, the proposed antenna design is compact in size. Further the use of silicon lens with the designed antenna configuration helps in focusing the beam in the desired direction. In addition, the proposed photoconductive dipole antenna with silicon lens improves the antenna performance which is potentially helpful for THz sensing and imaging applications such as the detection of hidden explosives and some commonly used explosive related compounds whose spectral absorption peaks lies in 1-2THz range. By using proposed simple photoconductive dipole antenna along with thin superstrate and silicon lens, we have attained the directivity 10.7dBi and radiation efficiency of 91.59% in both E-plane and H-plane.

Further, there are certain modalities for improving the photoconductive dipole antenna performance which must be identified to achieve high THz average radiated power with improved total efficiency. Therefore, a thorough systematic framework to assess the physical phenomenon occurring across the small-gap photoconductive dipole antenna is determined using an analytical procedure utilizing explicit mathematical expression. A pragmatic description of the small-gap photoconductive dipole antenna which gives a relationship between the parameters of equivalent circuit model and dimensions of antenna electrodes is presented. The effects of biased lines on the photoconductive dipole antenna performance parameters are examined with the help of proposed equivalent circuit model. Moreover, the performance of antenna is also examined with variation in the photoconductive gap size for the time-dependent physical phenomenon's like time-dependent source capacitance, source conductance, and radiated voltage across the antenna electrodes and THz radiated power and the total antenna efficiency of the photoconductive dipole antenna. The insight of distributed components for half-wavelength planar biased-lines helps to get better impedance matching efficiency of the antenna which results into an increase in the total antenna efficiency. The optimization of size of photoconductive gap to improve the total antenna efficiency is examined and its effect on radiated power is determined.

To enhance the directivity of small-gap photoconductive dipole antenna, the frequency selective surface (FSS) as bandpass spatial filter is employed with the antenna. Further, to preserve the purity of incoming THz wave on the receiving antenna side where the electromagnetic interference (EMI) is the major hindrance, the use of FSS structure with antenna geometry in THz region is beneficial to enhance the antenna performance parameters. The physical parameters of proposed bandpass FSS with photoconductive dipole antenna are obtained using simple synthesis technique of a single square loop bandpass FSS. Further, the effect of unit-cell periodicity and slot-size of FSS on the resonance condition, gain, directivity as well as the front-to-back lobe ratio of photoconductive dipole antenna structure is investigated.

In addition to this, the photoconductive dipole antenna array is also formed on a single photoconductive substrate to make it compact and suitable for THz imaging applications. The photoconductive dipole array antenna improves the gain and directivity and therefore, is useful to enhance the imaging capabilities to address the considerations such as limited depth-of-field (DoF) i.e. the distance over which an object is judged in focus and size-weight-and-power (SWaP) of THz source for imaging applications. These are important considerations for applications like stand-off imaging and surveillance of moving targets where the high

angular resolution as well as extended depth-of-field is the key parameters for successful detection of hidden explosives and illicit drugs. The designed antenna array configuration provides a radiation efficiency upto 72% for $(1 \times 2)$ and 84% for $(2 \times 2)$ PCA array, respectively. A directivity enhancement technique of using FSS with photoconductive dipole antenna array is also proposed without using a lens-system to limit the fabrication complexity in array configuration of the THz radiating structure to yield high image resolution. Using the FSS superstrate with array configuration, the directivity is increased by 4.55dBi in E-plane and 4.66dBi in H-plane for (1×2) array assembly and 6.95dBi in E-plane and 6.96dBi in H-plane for (2×2) array assembly at the resonance frequency 1.95THz. The proposed antenna array with FSS results into planar configuration of highly directive radiating THz source for the imaging applications. Moreover, by using this technique, radiation energy become confined to the desired frequency band rather than spreading over a wide spectrum range. The complete antenna array assembly with FSS is made useful to outline an image by scanning a single beam in both the principle planes. Further, the functioning of beam-steering phenomenon in planar array of photoconductive dipole antenna using progressive phase-shift for sensing and imaging application is a challenging issue. A highly directive $(2 \times 2)$ small-gap photoconductive dipole phased array antenna has been realized and the beam steering characteristics of the small antenna array configuration at 1.95 THz operating frequency is presented. With progressive phase shift of $10^\circ$ for the scanning range $0^\circ \leq \theta \leq 40^\circ$ with $\varphi = 0^\circ$ along x-axis as well as y-axis antenna elements of the array, the simulation results show the occurrence of beam steering by $3^\circ$ in E-Plane and $1^\circ$ in H-Plane, respectively

However, for the proposed small-gap photoconductive dipole antenna, there are certain design techniques which can be integrated such as using the dielectric structure with periodic LT-GaAs strips inside the gap area and use of anti-reflection coating materials on the surface of photoconductive substrate for future work. These techniques will help to improve the laser-to-electrical conversion efficiency of the antenna which contributes into the total efficiency of the antenna. A graphene based artificial magnetic conductor for directivity enhancement of photoconductive dipole antenna can be investigated for tunable antenna applications in THz pulsed imaging system.

# LIST OF PUBLICATIONS

[1] I. Malhotra, K. R. Jha, and G. Singh, "Analysis of highly directive photoconductive dipole antenna at terahertz frequency for sensing and imaging applications," *Optics Communication*, vol. 397, pp. 129-139, 2017.

http: //doi.org/10.1016/j.optcom.2017.04.008

[2] I. Malhotra, P. Thakur, S. Pandit, K. R. Jha, and G. Singh, "Analytical framework of small-gap photoconductive dipole antenna using equivalent circuit model," *Optical and Quantum Electronics*, vol. 49, no. 10, pp. 334/1-23, 2017.

http://doi.org/10.1007/s11082-017-1175-4

[3] I. Malhotra, K. R. Jha, and G. Singh, "Terahertz antenna technology for imaging applications- a technical review," *International Journal of Microwave and Wireless Technologies*, vol. 10, no. 3, pp. 271-290, 2018.

https://doi.org/10.1017/S175907871800003X

[4] I. Malhotra, K. R. Jha, and G. Singh, "Design of highly directive terahertz photoconductive dipole antenna using frequency selective surface for sensing and imaging application," *Journal of Computational Electronics*, vol. 17, pp. 1-20, 2018.

https://doi.org/10.1007/s10825-018-1217-6.

[5] I. Malhotra, K. R. Jha, and G. Singh, "Design of highly directive lens-less photoconductive dipole antenna array with frequency selective surface for terahertz imaging applications," *Optik: International Journal for Light and Electron Optics*, vol. 173, pp. 206-219, 2018.

https://doi.org/10.1016/j.ijleo.2018.08.010

[6] I. Malhotra, K. R. Jha, and G. Singh, "Beam steering characteristics of highly directive photoconductive dipole phased array antenna for terahertz imaging application", *Optical and Quantum Electronics*, (Under Revision), September, 2018.

# LIST OF ACRONYMS / ABBREVATIONS

| | |
|---|---|
| AMC | Artificial Magnetic Conductor |
| BS | Beam Splitter |
| CCD | Charged Coupled Device |
| CT | Computed Tomography |
| CW | Continuous Wave |
| DAR | Distributed Active Radiator |
| DAST | 4-Dimethylamino-Afmethyl-4-Stilbazolium-Tosylate |
| DFG | Difference Frequency Generation |
| DoF | Depth of Field |
| EBG | Electromagnetic Band Gap |
| EMI | Electromagnetic Interference |
| EO | Electro-Optic |
| ERCs | Explosive Related Compounds |
| FEL | Free-Electron Laser |
| FFT | Fast Fourier Transform |
| FPC | Fabry-Perot Cavity |
| FSS | Frequency Selective Surface |
| GHz | Gegahertz |
| GaAs | Gallium Arsenide |
| HMX | High Melting Explosive |
| InAlAs | Indium Aluminium Arsenide |
| InGaAs | Indium Gallium Arsenide |
| LHM | Left-Handed Metamaterial |
| LT-GaAs | Low-Temperature Gallium Arsenide |
| MRI | Magnetic Resonance Imaging |
| MSM | Metal-Semiconductor-Metal |
| NDT | Non-Destructive Testing |
| NEP | Noise Equivalent Power |
| NETD | Noise-Equivalent Temperature Difference |
| NFFT | Numerical Fast Fourier Transform |
| NIR | Near Infrared |
| NLTL | Non-Linear Transmission Line |
| OR | Optical Rectification |
| PCA | Photoconductive Antenna |
| PET | Positron Emission Tomography |
| PETN | Pentaerythritol Tetranitrate |
| PM | Parabolic Mirror |
| PRS | Partially Reflecting Surface |
| QCL | Quantum Cascade Laser |
| RDX | Research Department Explosive |
| SI-GaAs | Semi-Insulating Gallium Arsenide |
| SNR | Signal to Noise Ratio |
| SWaP | Size-Weight-and-Power |
| TDS | Time-Domain Spectroscopy |

| | |
|---|---|
| THz | Terahertz |
| TMI | THz Molecular Imaging |
| TMICs | THz Monolithic and array compatible Integrated Circuits |
| TPI | THz Pulsed Imaging |
| TPS | Thermal Protection Systems |
| UWB | Ultra Wide Band |
| VCD | Vibrational Circular Dichroism |
| VNA | Vector Network Analyzer |
| WP | Watson Prism |
| 1-D | 1- Dimensional |
| 2-D | 2- Dimensional |

# LIST OF SYMBOLS

| | |
|---|---|
| $\varepsilon$ | permittivity of thin − layer superstrate |
| $\varepsilon_0$ | permittivity of free space |
| $\varepsilon_r$ | relative permittivity of photoconductive substrate |
| $\mu_0$ | permeability of free space |
| $\sigma_c$ | conductivity of metal |
| $h$ | Planck′s constant |
| $c$ | speed of light in free space |
| $e$ | electron charge |
| $\mu_e$ | electron mobility in thin − layer superstrate |
| $\tau_l$ | laser pulse duration |
| $f_l$ | light frequency |
| $f_{rep}$ | optical pulse repetition frequency |
| $\alpha$ | optical absorption coefficient |
| $R$ | power reflection coefficient |
| $w_0$ | beam waist |
| $\tau_c$ | carrier lifetime |
| $\tau_r$ | recombination lifetime |
| $\xi$ | geometrical factor of the substrate which denotes the screening factor |
| $E_{bias}$ | biased voltage |
| $W$ | width of antenna electrodes |
| $G$ | photoconductive gap |
| $S$ | photoconductive gap area |
| $L_2$ | width of biased line |
| $L$ | separation between biased lines |
| $Z_a$ | antenna impedance |
| $n$ | refractive index of air |
| $\eta_t$ | optical − to − THz conversion effeciency |
| $t$ | varying time |
| $D$ | diameter of the laser beam falling on the lens |
| $f$ | operating frequency of antenna |
| $\delta$ | skin depth or depth of penetration |
| $T_{LT-GaAs}$ | laser skin depth at the excitation region |
| $G_{con}$ | line conductance |
| $L_{ext}$ | line inductance |
| $A(t)$ | temporal amplitude of Gaussian pulse laser |
| $P_{av}$ | average optical power |
| $I(t)$ | temporal intensity function |
| $n(t)$ | time-varying carrier density |
| $G_S(t)$ | time − varying source conductance |
| $C(t)$ | time-varying capacitance |
| $\beta(t)$ | reverse voltage coefficient |
| $V_C(t)$ | voltage at the antenna gap |
| $V_{rad}(t)$ | voltage across the antenna gap or votage across the time − varying capacitor |
| $P_{opt-peak}$ | peak laser power |

# LIST OF FIGURES

**Figure No.** **Title of the Figure** **Page No.**

# LIST OF TABLES

# CHAPTER 1

# INTRODUCTION

## 1.1 INTRODUCTION TO TERAHERTZ (THz) RADIATIONS

A portion of the electromagnetic spectrum which lies in-between the optical and microwave regime is known as terahertz (THz) gap [1]. It is named so, because earlier, in comparison to a well-developed technology at microwave regime and the optical domain of the electromagnetic spectrum, the basic research, advanced technology developments, and new initiatives in the THz band have been very limited and stayed relatively unexplored. As shown in Figure 1.1, the electronics (millimetre waves) and photonics (infrared waves) sandwich the THz band where the semiconductor electronics and the optical technologies find their applications. The unavailability of reliable, compact, temperature insensitive, and efficient power sources and detectors were the key obstacles in the popularity of THz band of the electromagnetic spectrum. However, in the last two decades, with a significant progress in the technology, the development of solid-state mode-locked and quantum cascade lasers, laser based THz time-domain spectroscopy and microelectronic fabrication of planar antennas have paved a way in the imaging technology at the THz frequency band.

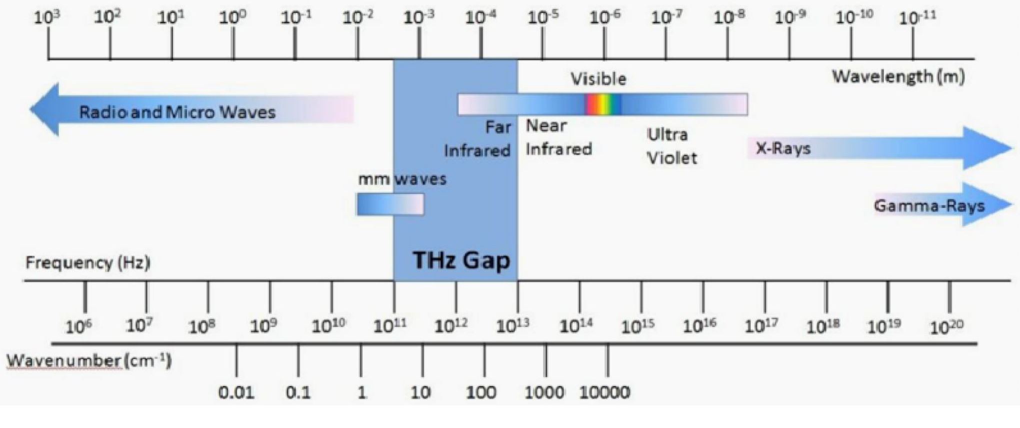

**Figure 1.1: The position of terahertz (THz) region in the electromagnetic spectrum [1].**

Moreover, the advent of $Er^{+}$-doped femto-second fiber lasers has replaced the costly systems made of titanium: sapphire lasers for THz systems [2]. With many more such technological come through in the field of semiconductor physics and technology, many researchers [3] are now exploring the utilization of the license-free THz band of the electromagnetic spectrum for several potential applications. Recently, for THz electromagnetic spectrum, various emerging applications have been introduced in the biological imaging [4], non-destructive testing [5], security scanning [6, 7] and process control [8] upto the next-generation wireless communication systems [9]. Within THz regime of the electromagnetic spectrum, there is a capability of multiple interaction of the electromagnetic wave with the matter which results into several biological, chemical, molecular as well as physical structures to show the unique spectral fingerprints in addition to the rotational modes at specific frequencies of THz band. Moreover, the high absorption of THz radiation by oxygen molecules with polar liquids such as water are the main limitation for the wave to travel over a long distance in the atmosphere [10]. Further, the THz radiation penetrates the fabric, foam, and plastic [11], even as they are almost totally reflected by metals and the photon energy levels of THz rays derive an extra characteristic. Categorically, Figure 1.2 shows that applications of THz radiations fall within either of the material characterization, sensing and imaging, and the communication fields. However, the THz band characteristics itself interlink these application which is widening gradually.

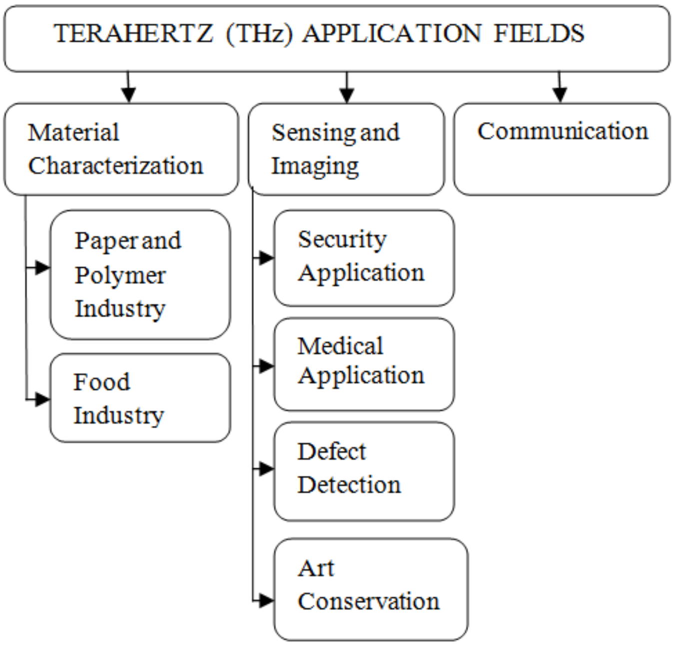

**Figure 1.2: The potential THz application areas.**

The use of THz waves in numerous application areas become possible due to several advantages and salient features of THz waves relating to microwave and infrared region, as mentioned below:

- In comparison to the microwave, the THz band comprises of wider bandwidth. Moreover, the microwave band is already being utilized for different services and applications. On the other hand, the terahertz frequency range is unregulated (license-free) by regulatory authorities and a 250 GHz is the maximum allocated frequency of this range, therefore, THz band can be used for several applications.

- The THz wave is a non-ionizing radiation which has an advantage over the ionized imaging systems such as Positron emission tomography (PET), Magnetic resonance imaging (MRI), planar X-rays, and X-ray with computed tomography (CT) scans being presently used. Therefore, the THz wave is useful for biological imaging applications. Moreover, with the frequency sensitivity feature of THz absorption, the THz waves can be used to identify differences in biological tissues without providing any harm.
- The THz wave scatters less in comparison to the infrared frequencies and light wave because scattering depends on the wavelength of the wave. Moreover, due to the longer wavelength of THz wave, the alignment of the wave is high and this feature helps in non-destructive testing of the materials.
- The radiating beam of THz band of electromagnetic spectrum is highly directional which is advantageous for the applications such as security scanning. This is because of the low diffraction of the THz beam in contrast to the microwave range.
- Under certain atmospheric conditions such as presence of fog, smoke, and dust, the attenuation of the THz wave is less in contrast to the infrared wave and therefore helps to utilize this license-free THz band of frequency of the electromagnetic spectrum useful for reliable sensing techniques.
- With an increase in the frequency of THz band, better resolution can be achieved which is useful for the imaging applications. The THz band offers enhanced far-field spatial resolution of about 300μm and reduced Rayleigh scattering (because the Rayleigh scattering intensity, $I \propto \lambda^{-4}$ ) in comparison to the millimetre-waves and infrared rays, respectively.
- For the spread spectrum communication, the THz regime of the electromagnetic spectrum provides large channel bandwidth. Moreover, the scintillation effect is more in infrared communication system and the use of THz communication system can minimize this effect.

### 1.1.1 Material characterization

Due to the unique signature ability, the THz band finds number of industrial applications in the material characterization. In one of the interesting application in the paper manufacturing industries [12], the production of the finished goods is being ingeniously controlled using the THz systems where it monitors the thickness as well as the moisture content of the paper during the production process. Mousavi et al. [13] have demonstrated the experimental set-up to differentiate two different paper samples using THz wave. In addition, the THz systems also find its utility in the polymer manufacturing industry such as the 1) on-line regulation of polymeric processes such as real-time paint meter [14], 2) quality control check of the plastic weld joints [15], 3) conductive possessions of polyaniline films [16], 4) estimation of moisture level [17], 5) fiber orientation [18], and 6) glass-transition temperature of polymers [19]. Similarly, in the industry of manufacturing food items, it is desirous to detect the unwanted and harmful objects in food before its final packaging. The THz systems detect the possibility of both the metallic and non-metallic contamination [20] in the food item. Moreover, the food items having low water content such as chocolates are transparent to the THz waves. This enabled to differentiate metallic and non-metallic contamination in the chocolate bars [21]. Furthermore, for the brewery industry, the detection of corked substance is important.  Therefore, the significant scattering of THz radiations due to the presence of defects or voids, in addition to the variation in the cork-cell structure results into emergence of the contrasts images of the crocked substances with imperfections [22].

### 1.1.2 Sensing and imaging

Among the security applications of THz imaging, the luggage and postal mail inspection [23] at airports is a major concern. The molecular crystals of the matter present specific features when gets interacted with the THz wave, therefore, the explosives [24-26] or illicit drugs [27] are well localized and explicitly recognized inside an envelope, or a parcel, or a suitcase [28]. The packages made up of metallic sheet are opaque to the THz waves and thus, the spectrometers designed in the THz band are not probably an alternative to X-ray scanners. Though, THz waves offer additional information about the sample under test, generally for the low density materials and the chemical separation. For highly responsive facilities and public places like airports, railway platforms, compound areas of governmental offices, or open grounds during the festival celebrations, there is a requirement of full-body scanners for the security purposes. Initially, the security screening is either based on using metal-detectors, X-Ray backscatter, or millimetre wave passive and/or active imaging systems. However, the deployment of security systems based on THz radiation in such areas is comparatively much safe than X-rays because of the smaller photon energy of THz waves which does not create any harm to the human tissues all the way through ionization [29]. Therefore, THz radiation shows potential for its usage in the airport non-invasive full-body security scanners [30, 31]. The THz system also finds its application in the liquid explosives detection. This is due to the reason that numerous liquids exhibit very different dielectric response in THz band distinguishable from the other alcoholic substances [32].

The medical and biomedical imaging is also a promising field where the THz imaging technique finds several applications [33]. Due to the high degree of aligning property of the THz beam with respect to the microwave waves and the lesser Rayleigh scattering with respect to the infrared and visible beams, it finds a unique place in the biomedical imaging. An exposure to the THz wave with intensities of sub-hundred milli-watt per square centimetre or even greater, does not show any significant variation at a cellular and molecular level of the living substance [34]. Thus, it facilitates a safer medical imaging for the human beings [35]. The THz imaging has found its potential application in analyzing breast-tumours [36], skin hydration and skin cancer [37, 38], and liver cancer [39]. Oh et al. [40] have demonstrated the diagnostic images of cancerous tumours which are acquired by using THz molecular imaging technique (TMI). In this technique, when the near infrared (NIR) beam is allowed to irradiate the surface of nano-particles then a change in the THz response due to the surface plasmon resonance is measured which helps in the detection of tumours. The authors [40] further have extended the differential measurement technique wherein the NIR beam is directly modulated and helps to eliminate the background noise which results into an improvement in the SNR values. Moreover, a high sensitivity has been achieved with this technique which arises due to the sensitive interaction of the THz waves in the water. However, it also makes possible the target-specific sensing of tumours as well as helps to recognize the miniscule differences at a cellular level. Similarly, to show the benefits of THz radiation in the dental imaging and monitoring the tooth-decay, Berry et al.[41] developed a detailed list of optical properties of the tissues which are exposed to THz pulsed radiation, experimentally. The pharmaceutical industries are also using THz radiations in the analysis of tablets and chemicals for the purpose of quality check during their production process [42, 43]. The crystalline structures of different isomers shows altering spectral fingerprints in the THz range, therefore using the THz imaging technique the polymorphic forms of the tablet coatings [44] can be detected in quality control applications. This also helps to control the discharge of the active pharmaceutical ingredients [45]. Like microwave radiations, the THz radiation has the potential to penetrate a variety of non-conducting materials such as clothing, plastic, ceramics, wood, paper, and cardboard. However, the infiltration depth of THz waves is usually not more than that of the microwave radiation, therefore, THz waves finds its applications to non-destructive quality control with inspection of hidden defects, surfaces with non-uniformity and cracks [46]. Such salient feature of THz wave is beneficial to evade any catastrophic failures similar to the NASA Space Shuttle Columbia in future. As the THz beams are capable to detect the damage in the polymer foam tiles due to the induced heat and using the condition based monitoring of the thermal protection systems (TPS) a secure operation of the space shuttle can be monitored. Zhong et al. [47, 48] have established the THz time-of-flight tomographic imaging in the non-destructive recognition of foam insulation on space shuttle fuel tanks having pre-fabricated defects. The authors have determined the insulation foam defects with the help of a Gunn diode oscillator and a pyroelectric camera as a source of THz wave and detector, respectively. Rahani et al. [49] have investigated the potential of THz waves to detect heat induced damages that occurs in porous materials. The authors have analyzed the emergence of defects which are generated during the manufacturing process or in-service processes such as formation of voids, de-lamination or damage due to impact/ burn in the porous materials by analyzing the THz absorption information from the transmission-type characteristics of the image. Likewise, as the THz waves can infiltrate through all composite material so THz transmission images of composite material [50] can be obtained for security applications. Amenabar et al. [5] have reviewed the most significant feature of the THz technology as a tool for non-destructive testing (NDT) inspection of composite materials. The reflection of the THz wave (in conductive materials) and absorption of the THz wave (in polar liquids) show the way to a clear examination in the composite inspection field. However, there are certain limitations to the detection of composite matter using THz waves such as carbon fibres which is not penetrated by THz radiation and water content in air or else in the composite itself may compromise on the correctness of the inspection system.

Our work has explored the pulsed THz imaging system with respect to the performance parameters of photoconductive dipole antenna for security applications and these are discussed in detail in Section 1.3 and Section 1.4, respectively.

### 1.1.3 Next generation communication

To cater the requirement of high data rate communication, there is a prerequisite to use higher operating frequency in the THz range of the electromagnetic spectrum [51]. However, the deployment of higher operating frequency of THz band in setting up a communication link, several design issues are required to be addressed. In wireless communication system, an antenna plays a vital role and at THz frequencies the design characteristics of an antenna needs significant consideration. Moreover, to increase the overall length of any wireless communication link, the antenna performance parameters such as gain and directivity represents the decisive factors. Jha and Singh [52] have reviewed the technical issues of THz antennas with the particular consideration to the planar technologies that can contribute to the compact, low profile, and inexpensive future THz wireless communication system design. As, the signal attenuation and the power levels are high and low, respectively in THz regime of the electromagnetic spectrum, therefore wireless communication links with a highly directive system provides point-to-point communication within some short ranges. This enables the establishment of secure short-range links to exchange the confidential information with high speed. Likewise, an active research in the field of THz communication systems [53, 54] is going on, specifically in indoor systems which are operating at point-to-point over several meters [55, 56], and are largely depending on integrated circuits so as to enable these point-to-point links for portable consumer devices [57, 58]. The THz communication systems share the characteristic of short-range communication and are primarily restricted by the strong atmospheric attenuation and scattering by building materials [59]. In case of the long-range outdoor point-to-point links a millimetre-wave band below 300 GHz is being reported. Recently, a wireless link operating at a centre frequency of 240 GHz realize a data rate of 64 Gbit/s over a transmission distance of 850 meter by means of QPSK and 8PSK modulation in a single-channel approach without the use of spatial diversity concept [60] and a 120 GHz link achieving 10 Gbit/s at 5.8 km [61] have been established, respectively. However, it is a myth that the millimetre-wave and the THz bands (0.1–3 THz) are unfeasible for all but short-range links due to rigorous attenuation caused by the atmospheric water vapour. Further, this myth has been contradicted with the development and usage of large-aperture telescopes by the researchers in the area of sub-millimetre radio astronomy for the dry high-altitude locations. Suen [62] has reviewed the expertise and science essential to build up a terabit-per-second THz satellite link. The author has emphasized on benefits of developing a Satellite-link with ubiquitous THz communications. Moreover, several technical characteristics of a Satellite-link which includes atmospheric attenuation, transceiver technology, aperture, and earth station properties for the terabit-per-second Satellite-link are discussed in his work.

## 1.2 OVERVIEW OF CONTINUOUS AND PULSED TERAHERTZ (THz) IMAGING SYSTEMS

The THz radiations provide higher spatial resolution in comparison to the microwave radiations because of the shorter wavelength. Moreover, the THz radiations do not cause any recognized harm to the living organisms which makes THz imaging a powerful and most likely safe imaging technology. Furthermore, the applications such as homeland security, defence and safety in aviation industry have put a huge demand on the expansion of advanced imaging systems. The types of THz sources used in imaging system is briefly discussed to have an idea about the availability of types of THz sources for THz continuous and pulsed wave imaging system.

### 1.2.1 THz sources for imaging systems

Generally, the electronic solid-state sources have limited operating bandwidth due to the transit time of carriers through semiconductor specimen which causes high frequency roll-off. This makes a limitation in the use of solid-state devices for THz frequencies. Recently, the development of a variety of THz sources is gradually filling the THz gap, providing complementary characteristics in terms of various parameters such as operating frequency, an average and peak power. The classification of THz sources used in THz imaging system is shown in Figure 1.3. Numerous systems have been developed to generate the THz radiations with each system offering different output powers, sensitivities and bandwidths. On the basis of spectroscopic techniques used in sensing and imaging applications, the THz sources have been broadly classified in three categories such as:

1) Incoherent thermal THz sources,
2) Continuous-Wave (CW) THz sources (also known as Narrowband THz source), and
3) Pulsed THz sources (also known as Broadband THz source).

The narrowband continuous wave sources are further, classified as photonic sources, non-linear optical sources, photomixing in biased semiconductors, and electronic sources. Similarly, the broadband pulsed sources are classified as photoconductive antenna, optical rectification, and the pulsed photomixing. The incoherent thermal sources generate THz radiations through mercury arc lamp or SiC rod (Globar) in an optical interferometer. In the interferometer, the characteristic interference pattern of the sample is considered through scanning the arm length. Using fast Fourier transform (FFT) and the numerical FFT (NFFT), the interferometer responds to the sample spectrum with zero-padding and aliasing [63]. Among the models for THz imaging, numerous non-coherent techniques like micro-bolometer arrays are presented by researchers whereas to increase the measurement speeds such approaches provide only limited information due to lack of information about the phase. However, due to the rapid development of coherent THz sources, the trend shows the advancement in THz imaging systems and it presents an opportunity for high-resolution, potentially non-invasive imaging suitable for security or quality-control applications [64, 65].

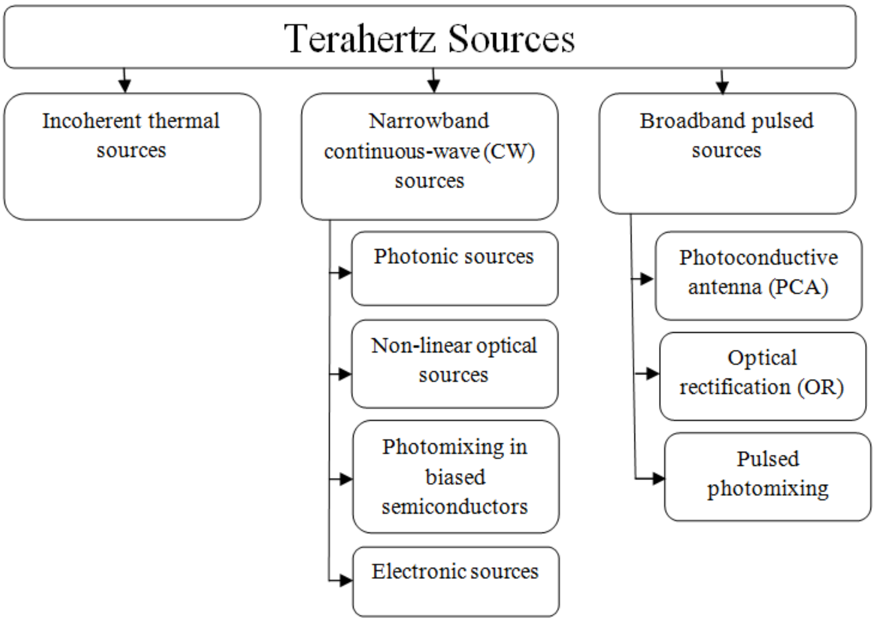

**Figure 1.3: Classification of THz sources**

The photonic CW THz source operation depends on the type of the laser used. Generally, the main hindrance in developing a THz laser is to find an inexpensive and suitable gain medium which can pump more resourcefully with high gain in addition to high output power. The nonlinear optical materials of susceptibility $\chi^{(2)}$ with non-linear optical coefficient act as a medium for the generation of THz radiation at the beat frequency of two pump sources. In case of pump sources which are having wavelengths offset by THz frequencies, the non-linear optical material can act as a source of THz radiation. In this technique, a material with second-order optical non-linearity such as 4-dimethylamino-Afmethyl-4-stilbazolium-tosylate (DAST), two continuous-wave lasers of offset resonance frequencies are combined resulting into difference frequency generation (DFG). With photomixing in biased semiconductors generation technique for CW THz radiation, the mutual interference of two laser frequencies with semiconductor material results into output oscillations which occur at the sum as well as the difference of the laser frequencies. The systems are fabricated in such a way that the difference term of laser frequencies lies in the THz range. For the low-power CW operation, the high-speed electronic devices can be used such as in case of non-contact system developed using complex impedance bridges to precisely characterize the dielectric constant of thin films between the range 30 GHz to 1 THz.

The advancement in the generation of pulsed THz radiation with the help of ultra fast optical lasers offers a new way for accessing the THz frequency range. However, there are several mechanisms to produce pulsed THz radiation which includes the techniques such as 1) photocarriers acceleration in photoconducting antennas, 2) second-order non-linear effects in electro-optic crystals, 3) plasma oscillations, and 4) electronic non-linear transmission lines. Initially, the pulsed THz techniques were originally developed for the waveguide and circuit characterization. In Table 1.1, the generation techniques of both continuous wave THz radiations and pulsed wave THz radiations are summarized for quick and easy comparison of each technique.

**Table 1.1: Summary of generation techniques of THz radiation.**

| **S.No.** | **Continuous Wave THz Radiation** | | **Pulsed THz Radiation** | |
|---|---|---|---|---|
| | **Generation Technique** | **Generated Material/ Medium** | **Generation Technique** | **Generated Material/ Medium** |
| 1 | Photomixing [66] | PC Switch | Transient photo-conductive Switching [67] | Photo-conductive antenna (PCA) |
| 2 | Difference frequency generation using parametric oscillation [68] | Non-linear crystal | Optical rectification [69] | Dielectrics, Semiconductors, Organic Materials |
| 3 | Rotational transitions [70] | Far infrared gas lasers | Emission from periodically undulated electron beam [71] | Electron accelerators |
| 4 | Streaming motion and population inversion [72] | Semiconductor laser | Surge current (super depletion field) [73] | Semiconductor surface |
| 5 | Frequency multiplication of microwaves [74] | Schottky barrier diode | Tunneling of electron wave packet [75] | Quantum semiconductor structures |
| 6 | Transitions in superlattice [76] | Quantum cascade lasers (QCL) | Coherent longitudinal optical phonons [77] | Semiconductors, Semimetals, Superconductors |
| 7 | Electron interactive with a travelling electromagnetic Wave [78] | Backward wave oscillator (BWO) | Optically short-circuiting the switch [79] | High temperature superconductor bridge |
| 8 | Relativistic electron interaction with transverse magnetic field [80] | Free electron lasers (FEL) | Non-linear transmission line (NLTL) [81] | Electronic circuits consisting NLTL |

The photoconductive approach to generate pulsed THz radiation uses the formation of the transient current due to high speed photoconductors across the radiating antenna. The optical rectification is another method for the generation of pulsed THz radiation, which is an opposite process of the electro-optic effect. The optical rectification (OR) is a second-order consequence which occurs in materials with a non-zero $\chi^{(2)}$ coefficient and is also known as the Pockel's effect. The pulsed photomixing is a technique used to generate THz signals in the photoconductive antenna, CW photomixing and CW non-linear DFG.

### 1.2.2 Performance comparison between continuous (narrowband) and pulsed (broadband) THz imaging system

The narrowband/ CW THz sources have a variety of applications in high-resolution spectroscopy, telecommunications, and high bandwidth inter-satellite links. Figure 1.4 shows the CW imaging system wherein the THz continuous wave generation is achieved using Gunn diode assembly. Initially, a Gunn diode oscillator generates a beam of 0.2THz with 12mW power. With the help of a parabolic mirror the beam is allowed to focus on to a 4mm spot and is then modulated with the help of a chopper at 1.2 kHz. A polyethylene Fresnel lens placed at a distance of 408mm from the parabolic mirror focused the modulated beam with a focal length of 204mm. The modulated beam is allowed to pass through the sample which is positioned at this focus. Later than passing through the sample, the beam once again gets focussed through a small polyethylene spherical lens and recollects at the horn of the detector which is an unbiased GaAs Schottky barrier diode. Then the signal received by the detector is read using a lock-in amplifier.

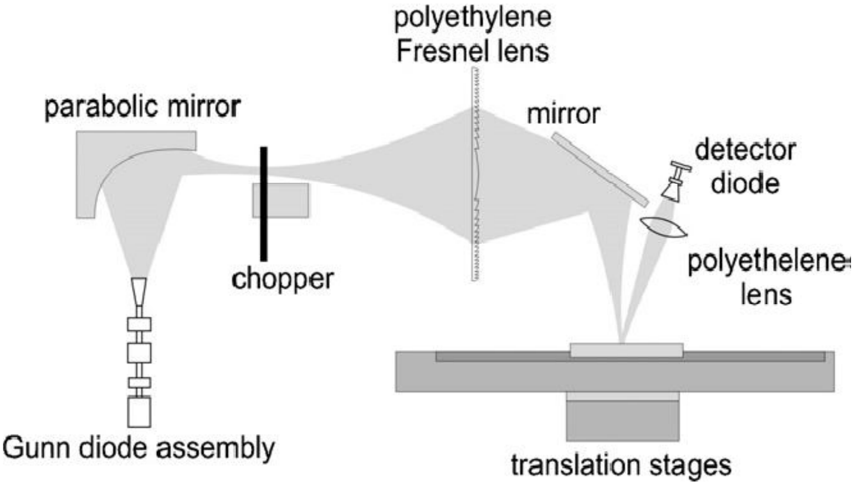

Figure 1.4: Schematic illustration of a CW THz system [84].

However, the CW imaging system presented in the Figure 1.4 only provides intensity data and does not give any depth as well as the frequency-domain or the time-domain information of the subject while a fixed-frequency source along with a single detector are used. For many imaging applications [82], only the plots of transmitted energy are adequate to detect the sample under test. Moreover, the CW imaging system provides a compact, simple, fast and comparatively low-cost system at the cost of loss of depth information of the sample under test and frequency-domain or time-domain information of the subject. The simplicity of the optics involved in the CW imaging system is due to the absence of a pump-probe system [83]. Therefore, there is no requirement of a time delay scan as is needed in pulsed imaging system and hence the image formation takes place more quickly in CW imaging system. In the pulsed terahertz imaging system a photoconductive antenna [85] is illuminated with the help of a femtosecond laser pulse acting as a source and the generated THz electromagnetic pulse is detected by non-linear crystal made up of ZnTe by means of electro-optic sampling technique based on optical pump-probe set-up [86]. Figure 1.5 shows the pulsed imaging system wherein the THz pulsed wave generation is achieved using a photoconductive antenna.

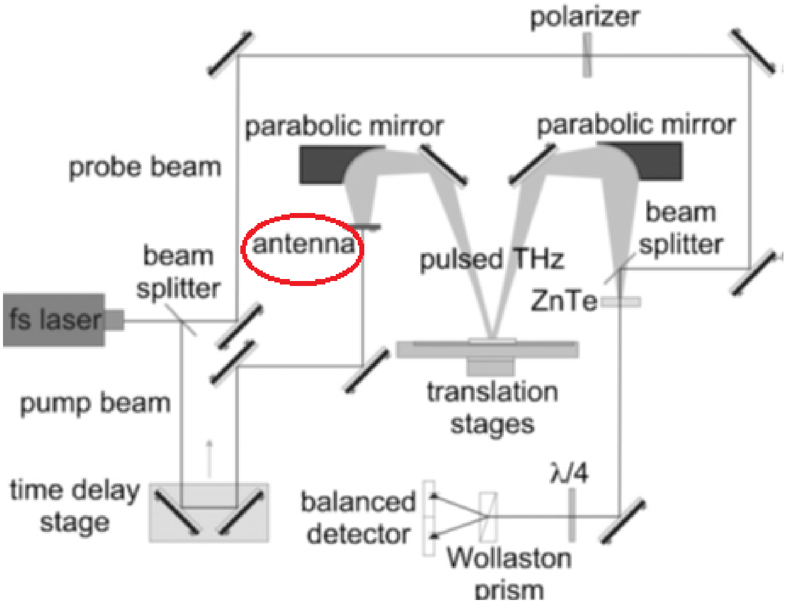

**Figure 1.5: Schematic illustration of a pulsed THz imaging system [84].**

The Coherent RegA laser used in the set-up has the characteristic features as 1) a repetition rate of 250 kHz, 2) pulse duration of 200 fs, and 3) an average power of 400 mW. Initially, the THz pulses are generated using a large aperture photoconductive antenna with a peak frequency 0.4 THz. Then, the generated THz beam resolute onto the target using a parabolic mirror which gets reflected through the sample layers as well as the aluminium substrate. The reflected beam is collected using another parabolic mirror which is then sends to a ZnTe crystal acting as THz detector where it overlies with the probe beam. Inside the ZnTe crystal, the probe beam gets modulated by the THz field. Such imaging technique records the waveform of the reflected THz pulses and therefore preserves the phase and amplitude information.

With the detailed working principle of both the CW imaging system and the pulsed imaging system as discussed above, the strengths and limitations of both imaging systems with respect to each other are now summarized in Table 1.2 for the quick and easy reference. Using more complicated arrangement for CW imaging system additional information can be extracted. Likewise, the overall weight issue of the pulsed imaging system can be abridged appreciably with the utilization of more compact laser such as a fiber laser for the pump-probe set-up.

**Table 1.2: Comparison of CW and pulsed THz imaging systems [84]**

| S.no. | Parameter | CW imaging system | Pulsed imaging system |
|---|---|---|---|
| 1. | Approximate total system cost | \$50 000–\$150 000 | \$300 000–\$1 000 000 |
| 2. | System complexity | Low | High |
| 3. | Approximate weight of imaging components | Approx. 2Kg | Approx. 300Kg |
| 4. | Information provided | Transmitted energy | 1) Magnitude of electric field,<br>2) Total transmission time (optical path length),<br>3) Absorption spectrum,<br>4) Depth of scattering centres,<br>5) Information about the phase,<br>6) Shape of pulse. |
| 5. | Scanning speed | 0.005 s per point 1 mm step size (which is limited by translation stage maximum speed of 0.2 m s−1) | 20–0.05 s per waveform |
| 6. | Data complexity | Low | High |

## 1.3 TERAHERTZ (THz) PULSED IMAGING SYSTEMS FOR DETECTION OF HIDDEN EXPLOSIVES

In the imaging application, with visible light, only a photograph can be created and with X-rays, a view within the human body through penetration at a time is performed, however it is beneficial to use THz waves as it can create the image as well as transmit the information about the spectral response of material. Moreover, in THz imaging at low values of THz frequency, the dielectric response of several organic and inorganic materials is responsible for their spectral response and at high frequencies the spectral response is subjugated by specific intra-molecular or inter-molecular vibrations as well as the rotations which are similar to those that occur with infrared radiation in case of infrared spectroscopy. The salient features of THz radiation which makes it a potentially influential technique in THz pulsed imaging for security applications [87] in detection of hidden explosives are as follows:

- **Penetration:** THz radiation has the ability to pass through the non-metallic and low-absorption materials like clothing and packaging materials. Moreover, these radiations can partially reflect from the interfaces between materials having different refractive index which enables to detect the plastic and ceramic objects containing powdered explosives hidden beneath the clothes.

- **High-resolution 3-D imaging:** The wavelengths which are used in pulsed imaging provide images with sub-millimetre resolution. Like a radar system, the use of extremely short pulses in pulsed THz techniques helps to take 3-D imaging. Moreover, in pulsed imaging system the range gating technique increase the contrast and the discrimination ability of the imaging system.
- **Spectroscopy:** Many explosives and explosive related compounds (ERCs) show spectral features in the broad frequency range of 0.1- 4 THz and thus provide unique spectroscopic information which helps in their detection using THz radiations even when they are sealed inside an object [6].
- **Safety:** The THz radiation is non-ionizing in nature and uses very low power levels in the nano-watt range because of the availability of highly sensitive coherent detection schemes.
- **Low Scattering:** The longer wavelength of the signal from the pulsed THz imaging system allows for much lower scattering from the object under detection.
- **Intensity:** In comparison to radio waves, the THz signals are much easier to focus and collimate which further helps to realize high Depth-of-field (DOF) for pulsed imaging system.

In THz pulsed imaging system, there is a use of THz electromagnetic waves to spectroscopically detect and identify concealed explosives such as research department explosive RDX (having chemical name 1,3,5-Trinitroperhydro-1,3,5-triazine) and high melting explosive HMX (having chemical name octahydro-1,3,5,7-tetranitro-1,3,5,7-tetrazocine) through their characteristic transmission or reflectivity spectra which lies in the THz range [28]. Moreover, in THz regime of the electromagnetic spectrum, spectroscopy with high spectral resolution is an effective analytical tool to determine the structure as well as the energy levels of the molecules and atoms. The THz pulsed spectrometers are essentially broadband systems because of the use of ultrafast optical pulses to create the THz radiation. Furthermore, the THz spectroscopy has the ability to determine the far-infrared optical properties of the material as a function of frequency which provides the insight into material characteristics for a broad range of security applications.

Related to the security threats to contemporary society, there is a requirement of scanning systems for screening of persons so as to identify the concealed perilous objects. However, on the other side, the use of full body scanning techniques based on X-rays hoist problems about the human health issues therefore limiting their acceptance by the public. Another significant security need such as recognizing a suicide bomber from a safe distance is not convened at all by the existing scanning technologies. However, the most constructive property of imagers which are operating in THz range has an ability to detect the small variation in temperature on the object's surface and has the ability to see even through clothing. Besides the background of the radiating human body the reflecting and the absorbing objects become noticeable with THz radiations. Therefore, the objects such as metals (which are generally highly reflective), ceramic materials and explosives which show characteristic absorption spectra in the submillimeter range [88] and even if they are concealed beneath the clothing can be detected easily using THz radiations. Therefore, due to the potential features of THz radiations in imaging applications, the THz pulsed imaging systems on the basis of type of imagers used in the THz pulsed imaging system are classified as:

- Passive imaging, and
- Active imaging.

The THz pulsed imagers offers salient features such as low signal-to-noise ratio, low spatial resolution and limited distance of imaging. However, the performance of THz pulsed imagers in terms of noise-equivalent temperature difference (NETD) value is lower and is in the range of $0.5 - 5°K$ (degree Kelvin) [89]. The passive THz imagers record the contrast in radiometric temperature within an object under scene and active THz imagers record the contrast in the scattered radiance within an object when it is illuminated with THz source. In active imaging, the imager makes the active image of the object wherein all the radiations are confined with all of its illumination to a single mode and the receiver observes the same mode on the other side of the object. However, the passive THz imaging systems which are inherently multimode has a small dynamic range in comparison to active THz imaging system [90].

With the advances in THz monolithic and array compatible integrated circuits (TMICs) [91, 92] operating at room temperature, a fully passive approach which is implemented with the use of heterodyne receivers. However, the active imaging system offers an advantage of reducing the sensitivity requirement on the THz receivers and in such case the receiver can improves the acquisition speed and number of image pixels (format). Friederich et al.[93] has presented active imaging systems to determine the pulsed imaging system potential in real-time imaging which includes a) active electronic imaging system, b) optoelectronic THz imaging system, and c) THz focal plane arrays.

### 1.3.1 Potential challenges of THz pulsed imaging system

The THz pulsed imaging is an emerging technology which finds diverse applications as discussed in preceding sections. Despite being influential technique based on salient features of THz radiations, there are many obstacles which stand in the way of large-scale industrial induction of THz pulsed imaging system. However, there are some key research areas which invite the researchers to work. Current efforts in the hardware are vital to transform the THz imaging systems from laboratory to the industry. The progresses in imaging architectures as well as algorithms are equally important for the exact and quick data processing. The THz imaging era has begun after Hu and Nuss developed the first scanning system in 1995 wherein the sample under test is scanned in x-y translation [94]. They have demonstrated a practical THz imaging system wherein the THz transients are focused on to the diffraction-limited spot localized on the sample. The transmitted THz waveforms are then acquired as well as processed in real time at each point of the sample. The authors have used THz pulses to stare through the packaging of a semiconductor chip, and also to find the water content of tree leaves. In case of conventional THz imaging system, a sample is scanned to take an image which poses a severe limitation on the available acquisition speed. However, a two-dimensional (2D) electro-optic sampling is used with a charge coupled device (CCD) camera to enhance the imaging speed. Moreover, with the necessity of accelerating the image acquisition speed and high absorption of many materials, there is a requirement of significant advancement in terms of compactness of size, cost-effective and portability of THz systems to make better feasibility of real-time imaging. Along with this, other major issues and challenges such as 1) output power, 2) signal-to-noise ratio (SNR), 3) water sensitivity, 4) depth of penetration, 5) bandwidth, 6) spatial resolution, and 7) lack of a THz frequency knowledge base, need to be considered for pulsed THz imaging systems. The spatial resolution in THz pulsed imaging is principally limited by the diffraction limit that is the function of wavelength and numerical aperture of the optical system.

Various applications in THz imaging rely on either single plano-convex lens of a spherical shape or off-axial parabolic mirrors but with increase of numerical aperture for former is inefficient leading to a significant rise of aberrations however later have good aberrational correction and high resolution although suffer from the overlapping of incident and focused beams [95]. The THz near-field microscopy is an alternative approach to overcome the diffraction limit. However, numerous disadvantages such as:

1) Detection of light scattered on very small diaphragms or confined at a tip apex placed at the object plane requires powerful emitters and highly sensitive detectors,
2) A near-field imaging requires very short object distance, thus, the scanning probe may interact with the sample and even perturb its structure, and
3) Requires a long scanning time,

are inherent to this approach and strongly limit its reliability [96]. The signal-to-noise ratio (SNR) improvement is another challenge being faced by pulsed THz imaging systems. This is inherently tied to the average power of the THz emitter. In THz time domain spectroscopy systems, a high SNR can be achieved. In imaging applications, there are certain factors that results into the reduction of SNR to a level where it becomes a matter of concern. However, the use of a THz source with high power can improve the SNR as well as the dynamic range of sensing and imaging systems by increasing the penetration depth in the scattering or absorbing materials. The polar molecules interact strongly with pulsed THz wave and due to this property the water molecules absorb the THz waves and therefore, the depth of penetration of the THz wave is limited in moist substances. Moreover, in the THz imaging applications to yield enhanced depth-of-field (DoF) for imaging purpose radiating source with highly directive antenna is required.

Several state-of-the-art THz spectroscopy systems rely on the ultrafast laser based systems which are bulky and therefore non-portable. In addition, such spectroscopy systems are complicated because of the essential mechanical parts such as a raster scan with single detector to obtain a two-dimensional image, and are therefore somewhat expensive to develop as well as to operate. Moreover, the scan process generally takes tens of minutes to produce a high-resolution THz picture of a scene. Thus, all the electronic based THz systems are required towards reducing the space, weight and power, and thus facilitate future sensing and imaging applications. Furthermore, the THz imaging technology faces some inherent problems which arise from the 1) specular reflections, 2) unwanted clothing reflections (clutter), 3) interference effects (speckles), and 4) angular orientation effects, that result into the degradation in the image quality and resolution. Moreover, in case of active imaging techniques there are certain threat scenarios also such as the presence of non-reflecting objects carried directly on the human skin. However, in case of active imaging the degradation in THz images due to speckle can be minimized by adding angular diversity or multimode mixing to the illumination THz source [97]. As the noise equivalent power (NEP) of an imaging array depends on the antenna efficiency, therefore, it is essential that the high-efficiency on-chip antennas are needed for a low system NEP. Figure 1.6 shows a broadband focal plane array camera with intrinsic cut-off frequency 2.5THz with antimonide based hetero-structure backward diodes which are monolithically integrated by means of planar THz antennas for each sensor pixel [98] for the real-time THz imaging application.

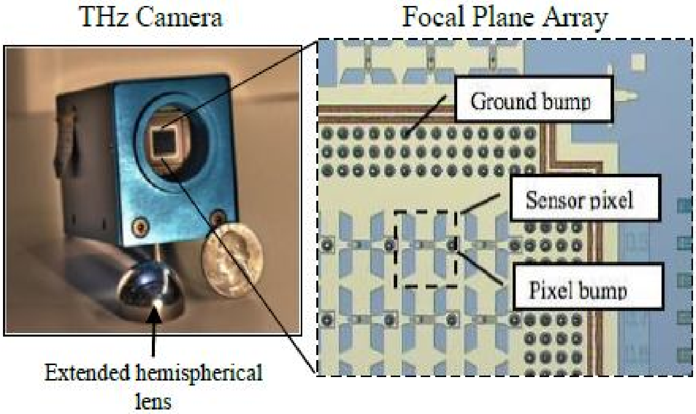

**Figure 1.6: The THz camera comprising of focal plane array pixels consisting of broadband slot–type photoconductive antenna with integrated sensors [98].**

Therefore, considering the potential challenges of pulsed THz imaging system for security applications, the advancements in the area of THz antenna technology for imaging application will open a new avenue in the biomedical and security applications in the THz regime of the electromagnetic spectrum. Moreover, both wavelength-scaled feed systems that integrate directly with electronic components and large scale beam forming systems are required. Several groups of researchers are pursuing the concept of small THz antenna which is especially targeted for shorter wavelengths to be useful for imagers, interferometers and broad-bandwidth spectrometers in THz imaging systems. As at shorter wavelengths, there is a difficulty in coupling together the multi-function elements which are fabricated individually such as diodes, transistors or passive transmission lines therefore more emphasis is being laid down on realizing these antennas with matching fabrication process as of the sensing and power converting devices which are used at the antenna terminals. Such technique result into reduction in the losses associated with excessive mode, beam mismatch and absorption. However, still there are some other challenges such as recognizing specific impedance matching, tuning or phase scanning, high gain, broad bandwidth, which needs to be considered simultaneously. Moreover, to realize a diffraction limited image using focal plane arrays, novel compact antenna designs with areas of one half wavelengths squared or less need to be designed. In Table 1.3, the performance evaluation of the characteristic parameters related to the THz imaging system for the feasibility of real-time imaging system is briefed.

To make realisable pulsed THz imaging system, the techniques which can be deployed in THz antennas to satisfy the demand of imaging system are mentioned with the respective potential challenges to work upon.

**Table 1.3: The performance evaluation of various characteristic parameters associated with the feasibility of real-time imaging system.**

| Characteristic Parameter | Performance Evaluation | Technique to Achieve | Limitation |
|---|---|---|---|
| Acquisition speed | High | Line-detection using micro-lens array | High system volume with portability challenge |
| Spatial resolution | High | Focal plane arrays | Diffraction limit and rise in aberrations |
| Signal-to-noise ratio (SNR) | High | High-power THz source | Unavailability of highly efficient single unit of THz source |
| Dynamic range | Large | Beam-steering technique and frequency scanning system | Propagation losses and non-specular reflection on the object under test |
| Depth-of-field | High | Highly directive THz source | High atmospheric attenuation |
| Noise equivalent power | Low | PCA which has low optical and thermal noise in comparison to electro-optic rectification method | Low antenna efficiency |
| Size-weight-and-power (SWaP) | Small | High-efficiency on-chip antennas | Critical fabrication issue |

## 1.4 RELATED WORK

A well-designed sub-wavelength (micrometre/nanometre) radiating structure shows the potential for high output power generation and broadband THz pulse emission which is useful for THz imaging system. An antenna is a vital component in THz imaging system as it plays a significant role of both impedance matching in addition to a power radiating source. Researchers have designed several types of THz antennas having different structures. Some of them are 1) THz dipole antenna [99], 2) Yagi-Uda antenna [100], 3) spiral type antenna [101], and 4) butterfly shaped antenna [102] with lens. Moreover, the diffraction limit in imaging system can also be overcome by the use of metamaterial biochips and nanotechnology based contrast agents. The THz antennas are broadly disturbed into two distinct areas:

- One is the use of THz antenna as wavelength scale beam forming or feed elements. In this form the THz antenna couples the energy acquired from the free-space into or out of sub-wavelength generators/receivers such as diodes, bolometers, transistors, or photoconductive elements.

- Second is the use of much larger aperture THz antenna to accumulate the signals and to focus the beam. This form is being used in variety of applications such as high resolution imaging or scanning and the light gathering power which is required by large radio telescopes.

For the emission or detection of THz waves using an optical and electrical methods a THz photoconductive antenna (PCA) is used. However, the THz PCA lacks in harnessing the modern technological advancement for the high-power THz emission. Moreover, for the advanced imaging and sensing applications, there is a rising attention in developing high power THz sources and sensitive detectors. The accessibility of high power, tunable wavelength, as well as compact optical sources by means of pulsed and continuous-wave operation becomes the major driving force of the photoconductive THz sources/detector applications. However, the inherent trade-off amid high quantum efficiency and ultrafast operation is the main obstacle in developing high power source and sensitive detectors using conventional photoconductors. This trade-off is because of the restricted carrier transport velocities inside the semiconductor substrates that are bounded with the carrier scattering occurring within the semiconductor lattice. Moreover, for the efficient generation/ detection of THz radiation in photoconductive device there is a requirement of small carrier lifetime of the photo-generated carriers to move towards the contact electrodes of the antenna. To achieve this, many researchers have used the nano-plasmonic light concentrators as well as the photoconductive sources/ detectors designed from optical nano-antennas. Jarrahi [103] has shown and discussed in detail the impact of using optical nano-antennas in active area of photoconductive THz sources. Likewise, Berry et al. [104] have reported the performance comparison between a plasmonic photoconductive emitter and a photoconductive emitter having non-plasmonic contact electrodes. In their research work they have claimed for 50 times higher THz radiated power from a plasmonic photoconductive emitter. Similarly, photoconductive detector with plasmonic effect offers, 30 times higher THz detection sensitivities in comparison to a similar photoconductive detector with non-plasmonic contact electrodes. They have also shared the future prospects of their prototype device that can be further improved with the deployment of the resonant cavities and antennas having higher radiation resistance and bandwidth. A considerable enhancement in THz radiation power and the detection sensitivity can be achieved by using plasmonic contact electrodes with high aspect ratio. Such electrodes are embedded within photo-absorbing semiconductor material which results into the generation of large number of carriers in the close-proximity to the photoconductor contact electrodes. Therefore, the nano- and micro-fabrication can open a way to numerous opportunities for enhancing the emission power of THz photoconductive antennas.

Park et at. [105] have demonstrated an increase in the THz emission power using the optical nano-antennas by tuning plasmon resonance with antenna geometry. They have designed an antenna for the high-power THz emission using large-area excitation with multiple inter-digitized microelectrodes underneath the restricted optical power. Moreover, the plasmon resonance gets precisely controlled through variation in the width of nano-antenna. The designed antenna configuration features nano-rod arrays placed in-between two microelectrodes on the photoconductive substrate [105]. The optical nano-antennas enhance the light concentration near the nano-rod arrays by the side of localized surface plasmon resonance. Moreover, the light confinement within the photoconductive region also results into generation of more photocarriers which further contributes to THz emission power enhancement. The authors of [105] have integrated the optical nano-antennas within the interstitial micro-gap of a bowtie-type photoconductive antenna on SI-GaAs photoconductive substrate by integrating multiple techniques such as the conventional photolithography, electron-beam lithography, and metal lift-off technology. Zhu et al. [106] have discussed three linearly polarized photoconductive THz antenna designed for the THz imaging system. A bow-tie antenna with a finite ground plane and DC biasing lines has been used as the reference design. In [106], the authors compare the performance of three linearly polarized photoconductive THz antennas designed using artificial magnetic conductors (AMC). The use of AMC enhances the gain of the antennas. Nguyen et al. [107] have designed a full-wavelength THz dipole antenna hold up by means of a GaAs membrane structure with high input impedance. The radiation efficiency also gets improved which further improves the overall efficiency of a THz photomixer. Further, the authors have also shown the effects of membrane thickness as well as the diameter of a hole inside the ground plane in a back-excitation configuration of THz dipole antenna. Through the optimization process, they have observed two interesting properties. One is that a relatively thin cavity is appropriate for the antenna designs which demands high input impedance as in THz photomixer antennas. Another is the use of bulk GaAs substrates which results into enhancement in the antenna performance and also possesses high input impedance along with high radiation efficiency.

Maraghechi et al. [108] have developed a correlation between the lengths of bow-tie antenna (type of photoconductive antenna) with its THz spectral emission response. Moreover, the capability to fine tune the centre frequency of THz photoconductive switch improves the accuracy of detectors/ emitters of the spectroscopy, imaging and sensing systems. In [108], for computing the effective antenna length, three approximation methods have been used such as 1) quasi-static, 2) high-frequency, and 3) Brown and Woodward. Accordingly, a number of bow-tie antennas with different lengths have been fabricated and are analyzed [109, 110]. The authors have also concluded that simple quasi-static approach to approximate the effective permittivity of the substrate can be applicable for frequencies up to 1.5 THz.

Beck et al. [111] have reported an impulsive THz radiator with characteristics such as 1) 36 kV/cm vacuum electric field, 2) 250 kHz repetition rate, 3) 1.5 mW average thermal powers, and 4) $2\times10^{-3}$ NIR-to-THz conversion efficiency. This has been obtained using photo-excitation of biased large-area photoconductive emitter with near-infrared (NIR) femto-second pulses having µJ energy. They investigated the THz emission due to the acceleration of photo-induced carriers within GaAs photoconductive substrate at high excitation densities. However, to achieve this specific metal-semiconductor-metal (MSM) structure photoconductive antenna is utilized. With the use of a specific MSM structure along with a large active photoconductive area of approximately $1\times1$ mm$^2$, the saturation effects including bias screening has been successfully reduced. Moreover, this also allows ensuring a suitable scattering strength to keep up the eigenmodes with the desired field distribution. Furthermore, a peculiar scattering response can be achieved by making use of the excitation of the resonant eigenmodes in an aptly shaped metallic antenna. Tani et al. [112] have reported two different forms of photoconductive antennas: a) Schottky photoconductive antenna, and b) multi-contacts photoconductive antenna, respectively. The Schottky photoconductive antenna has the ability to sense THz radiation intensity without the time-delay scans therefore it is helpful for applications wherein spectroscopic information is not significant like THz intensity imaging. Moreover, the multi-contacts photoconductive antenna finds application for the polarization sensitive THz spectroscopy like the THz ellipsometry. The authors have studied the characteristic features of these photoconductive antennas with the help of a THz time-domain spectroscopy system. By means of a cautious design of the contacts such as a point contact with a metal tip on n-type GaAs, the Schottky barrier diode has the ability to detect THz radiation. However, an ordinary Schottky diode is not appropriate for the detection of pulsed THz radiation (~ 1ps) generated by the excitation of a photoconductive antenna or some other THz emitting devices with femto-second laser since the authors have also detected the continuous thermal background radiation whose power is comparable or even higher than the average power of the pulsed THz waves. However, if the Schottky barrier diodes are also photo-activated using the same laser pulses which are used to pump the emitter then the problem can be solved. In other words, if a photoconductive antenna is activated using the laser pulses which can set right the THz signal within a limited time-window while rejecting the majority of the thermal radiation then they can detect the pulsed THz radiation intensity without time-delay scans. In multi-contact photoconductive antenna design [112], the authors have placed a cross-shaped photoconductive antenna on LT-GaAs photoconductive substrate using a standard photolithography and the method of chemical etching. On applying a bias voltage to the two adjacent electrodes while the other two electrodes grounded, then the bias electric field in the photoconductive gap is focussed to ±45˚ from the horizontal axis. When a short pulse light is irradiated to the biased photoconductive gap it results into the generation of linearly polarized THz radiation from the transient photocurrent directed towards the bias field. By providing a phase shift of 90˚ to the input source, the antenna's electric field polarizes in the orthogonal direction. This kind of polarization modulator is helpful for polarization sensitive THz spectroscopy like the THz ellipsometry and THz-vibrational circular dichroism (VCD) spectroscopy.

Hara et al. [113] have demonstrates an enhanced THz detection using photoconductive antennas based on self-assembled ErAs:GaAs nano-island superlattices. The authors have compared three detectors each fabricated on low-temperature grown GaAs (LT-GaAs), radiation-damaged silicon-on-sapphire (SI-GaAs) and an ErAs:GaAs superlattice, respectively. The ErAs:GaAs based detector shows a strong enhancement in the THz detection efficiency with respect to the incident optical power. Moreover, the results show improved THz bandwidth and signal-to-noise ratios. To reduce the image acquisition time, an array arrangement supported by electronic beam steering is useful in imaging application. The photoconductive antenna is fairly stable against optical and thermal noises in comparison to the electro-optic rectification. However, the total antenna efficiency which depends on the multiplication of optical-laser to THz conversion efficiency, impedance matching efficiency and radiation efficiency is low. To increase the impedance matching efficiency as well as the radiation efficiency it is required to consider the physical phenomena’s contributing to the enhancement of efficiency in photoconductive antenna. In [114], the study of equivalent circuit model of photoconductive dipole antenna and its use for photomixer are described in detail. The equivalent circuit is determined on the basis of source conductance developed in the photoconductive dipole antenna with laser excitation on the photoconductive gap. The authors have emphasized over modified expression for source conductance which occurs as a physical phenomenon across a photoconductive gap in photoconductive dipole antenna. The outcomes of variation of antenna parameters on the conductance are observed which facilitates to optimize the antenna impedance matching efficiency. Three designs of small gap photoconductive antennas as emitter's are analyzed in [115] to increase the directivity and radiation efficiency of small gap photoconductive dipole antenna which has major limitation of showing low directivity values. A simple synthesis technique is presented to resolve the antenna parameters corresponding to 1.5 THz to detect the powdered hidden explosives such as RDX, HMX and PETN. The simulation results shown in the paper recommend the use of thin layer superstrate with silicon lens for diffraction limited imaging using THz radiation in the low THz frequency region. The choice of specific photoconductive materials with essential electro-optic characteristics is a major factor which enables the photoconductive antenna for its effective performance in terms of its radiation parameters. Burford et al. [116] have reviewed the use of different photoconductive materials for antenna fabrication. Even though, LT-GaAs remains the standard for photoconductive antenna, however the potential for all fiber-based spectroscopy systems motivates to develop other photoconductive material systems. In imaging system there is a requirement of high acquisition speed which can be achieved using array configuration of THz antenna and is discussed by Pradarutti et al.[117] wherein a THz line detection with sixteen channels using micro-lens array coupled photoconductive antenna (PCA) array is implemented to improve the acquisition speed.

Moreover, the THz antennas based upon the photoconduction method have numerous advantages that they offer in comparison to the other THz sources. These antennas work in the room-temperature environment, compact in size and can operate both at the emission and detection side. Therefore, from the detailed explanation about the THz antennas for imaging applications, it is apparent that there are many avenues to improve the performance of THz photoconductive antenna technology for imaging application. Moreover, the key challenge is to design an optimized photoconductive antenna in terms of the radiation pattern, bandwidth and radiation efficiency so as to counter the problem of low radiated THz power for the pulsed THz imaging application. In Table 1.4, the recently developed THz photoconductive antenna design with respect to the imaging applications are summarized for quick reference.

**Table 1.4: Recent developments in THz photoconductive dipole antenna design with respect to the imaging applications.**

| Type of THz Antenna | Main Characteristic | Application Area | Reference |
|---|---|---|---|
| Photoconductive nano-antennas with Plasmonic contact electrode gratings | Effective in enhancing the radiation power and detection sensitivity of photoconductive THz sources and detectors. | Time-domain and Frequency-domain THz imaging and spectroscopy systems. | Jarrahi [103] |
| Photoconductive antenna with plasmonic contact electrodes | Enhances the optical-to- THz conversion efficiency of photoconductive THz emitters and the detection sensitivity of photoconductive THz detectors. | Material characterization, biological sensing andmedical imaging | Berry et al. [104] |
| Nanoplasmonic photoconductive antenna (NP-PCA) | Enhanced THz emission power by tunning the plasmon resonance | Emitters for spectroscopy, imaging and sensing systems. | Park et al. [105] |
| Bowtie-shaped photoconductive dipole antenna : a) With silicon-based lens and artificial magnetic conductor (AMC), b) Capacitively loaded dipole, c) Grid antenna | Enhanced directivity and front-to-back ratio of photoconductive antenna | High resolution THz spectral imaging system. | Zhu et al. [106] |
| Dipole antenna with GaAs membrane structure | Thin cavity provides high input resistance and use of bulk GaAs substrates provides high radiation efficiency. | Supports applications that demand large coverage, easy alignment, and high scanning speed rather than high resolution. | Nguyen et al. [107] |
| Bow-tie THz photoconductive antenna | Possesses the optimum radiation bandwidth | Emitters for spectroscopy, imaging and sensing systems. | Maraghechi et al. [108] |
| Amplifier driven large-area photoconductive antenna | Impulsive the THz radiation with high electric fields | Material Characterisation | Beck et al. [111] |
| Schottky photoconductive antenna | Detection of THz radiation intensity without the time-delay scan required for the ordinary PC antenna. | THz sensing applications | Tani et al. [112] |
| Four contact photoconductive antenna | To generate orthogonally polarized THz radiation | Polarization sensitive THz spectroscopy | |
| Photoconductive antennas based on self-assembled ErAs:GaAs nano-island superlattices | Enhanced THz detection | THz sensing and imaging | Hara et al. [113] |
| THz Photoconductive dipole antenna | Develop an equivalent circuit model based on source conductance occurring as a physical phenomenon across a photoconductive gap which is analyzed to optimize the antenna in terms of output power, impedance matching efficiency and SNR. | Emitters for spectroscopy, imaging and sensing systems. | Khiabani et al.[114] |
| Photoconductive dipole antenna using LT-GaAs superstrate and silicon lens for the detection of hidden powdered explosives such as RDX, HMX and PETN. | For directivity enhancement antenna structure parameters are computed using synthesis technique. Use of thin superstrate over the substrate of dipole antenna for increasing the radiation efficiency. For diffraction limited imaging, a shorter wavelength antenna with silicon lens is proposed. | Sensing and Imaging applications | Malhotra et al.[115] |

## 1.5 PROBLEM FORMULATION

The photoconductive antennas (PCAs) form the basis of many THz imaging and spectroscopy systems and find promising applications in various scientific fields. On the basis of the architecture of photoconductive antennas for THz pulsed systems, they are classified as an aperture antennas (large and small compared to wavelength), spiral antennas, bowtie antennas and dipole antennas. One advantage of using the photoconductive antenna in pulsed imaging system is that the photoconductive antenna can be used on both transmitter and receiver side. Only the difference lies in the use of biased voltage. On the transmitter side, the photoconductive antenna is biased with a fixed external voltage and the optical source, however, on the receiver side no biased voltage is required. For the imaging applications there is a requirement of planar and compact THz antenna sources amid on-chip fabrication along with high directivity in order to achieve large depth-of-field (DoF) for better image resolution. A small gap photoconductive dipole antenna being simple in fabrication and planar in design shows its easy deployment as THz source for pulsed broadband system utilized in THz imaging and spectroscopy systems. Moreover, a femtosecond oscillator based THz photoconductive dipole antenna systems can generate high signal-to-noise ratio (SNR) broadband THz waves and detect them with high sensitivity. However, one of the major restrictive factors of THz photoconductive dipole antenna technology is saturation at high optical pump powers. To overcome the saturation limits of PCAs, two different approaches can be used.

- Implementation of large device apertures.
- Implementation of interdigitated electrodes.

Moreover, to increase the optical-to-THz conversion efficiency, the use of large area THz photoconductive antenna emitters is proposed by the researchers. However, large area emitters have complex fabrication as well as packaging considerations. Similarly, a plasmonic nanostructure THz photoconductive dipole antenna also offers high device quantum efficiency and the antenna design comprises of nano-structured electrodes with large area emitters. However, because of the lack of maturity in nano-scale lithography technology, the fabrication of such ordered metallic nanostructures remains more difficult. Further, to increase the THz photoconductive antenna bandwidth the use of broadband antennas is required. Therefore, the use of log spiral and log periodic antenna patterns to simple face-to-face dipole THz photoconductive antenna can yield broadband response. To enhance the radiation efficiency of THz photoconductive antenna, a log spiral antenna with nano-structured electrodes can be used. However, the issues such as varying polarization and resonant / non-resonant regions across the desired operating band need to be considered while implementing these complex antenna geometries into practice.

The performance limitation of conventional small gap THz photoconductive dipole antenna in terms of low gain and low directivity values with small optical-to-THz conversion efficiency are also the major concerns in its use in security application of THz pulsed imaging systems for the detection of hidden explosives and illicit drugs. This indicates that the directivity enhancement mechanism of THz photoconducting dipole antenna needs the fair dealing. The radiation efficiency is also an important concern due to the reduced conductivity of the metal at the THz frequencies. Therefore, the key modalities of improving small gap photoconductive dipole antennas performance are identified for imaging applications and ways to improve the directivity of the photoconductive dipole antenna are discussed. Considering the need for an effective measure to combat the problem of low radiated THz power, a detailed synthesis technique to obtain the physical parameters of the small gap photoconductive dipole antenna is presented. The analysis also includes the key challenges such as how to design an optimized small gap photoconductive dipole antenna in terms of radiation pattern, bandwidth and radiation efficiency. The simulation results show the potential for further improvement of THz-TDS systems used in security applications of imaging systems.

Various researchers have reported different directivity and gain enhancement techniques such as use of fabry-perot cavity resonator, electromagnetic band gap, left-handed metamaterial with antenna. Moreover, these materials have attracted significant research interest because of their special electromagnetic properties, which are applicable to a wide range of electromagnetic devices. Therefore, a novel idea based on using bandpass frequency selective surface (FSS) as a superstrate with photoconductive dipole antenna for the prospective improvement of gain and directivity of the THz antenna is investigated. The proposed antenna configuration having planar and compact assembly is ideal for its use as an efficient THz source for the detection of powdered hidden explosives in security applications of pulsed THz imaging system. In one such application, when an individual carrying hidden explosives is moving through a corridor towards an imaging system then their hidden explosives will be visible only for the brief moment while they are in the DoF then in such situation with the use of highly directive THz antenna with short-range imaging system having a narrow depth-of-field (DoF) can detect the explosive easily. However, such scanning over an extended volume could provide security such as in a public marketplace where the security is important but a visible display is not so much important. Therefore for such application of imaging, a compact array structure of THz antenna with pulsed optical beam from femto-second laser pulse is proposed with highly directive ability of the radiating THz source. A technique of using FSS with photoconductive array antenna is also presented to further enhance the directivity from the radiating structure to yield high image resolution. Moreover, by using this technique, radiation energy will be confined to the desired frequency band rather than spreading over a wide spectrum range. We believe that the proposed advancements in the area of THz antenna technology for imaging application will open a new avenue in the biomedical and security applications in the THz regime of the spectrum.

## 1.6 THESIS ORGANIZATION

The remainder of the thesis is organized as follows. In Chapter 2, a simple synthesis technique is presented to determine the physical parameters of photoconductive dipole antenna which shows its application for THz sensing and imaging to detect the presence of hidden explosives such as RDX, HMX and PETN having spectral fingerprints in the range 1-3 THz. To increase the antenna radiation efficiency which also contributes to the total efficiency of photoconductive dipole antenna, a thin superstrate over the substrate of the dipole antenna is used to enable antenna to withstand high biased voltage. The proposed antenna design is compact in size which further helps to achieve the diffraction limited imaging. Moreover, the use of silicon lens with the photoconductive dipole antenna helps to focus the beam in the desired direction with increased directivity. In Chapter 3, an analytical procedure making use of explicit mathematical expressions leading to the physical behaviour of small-gap photoconductive dipole antenna is developed and for this, a comprehensive systematic framework to determine the physical phenomenon occurring across the small-gap photoconductive dipole antenna is presented. Moreover, an optimization of size of photoconductive gap to improve the total antenna efficiency is discussed and its consequence on radiated power is determined. As the THz antenna is one of the most important components in a THz sensing and imaging system and there is a need to have such a transmitting THz source with high directivity and optimum radiation efficiency. Therefore, to achieve this objective to enhance the directivity of photoconductive dipole antenna, in Chapter 4, a numerical calculation and design of frequency selective surface (FSS) which acts as a bandpass spatial filter is presented and is deployed with photoconductive dipole antenna. The bandpass FSS structure parameters have been computed using simple synthesis technique. The effect of slot size of FSS to improve the scattering parameter at resonating frequency of the small-gap photoconductive dipole antenna is also presented.

The most basic coherent imaging can be achieved by raster scanning a sample through the THz wave focus and generating complete spectroscopic information at each pixel corresponding to the antenna structure. Therefore, to speed up the measurements, there is a necessity of making a THz system for parallel or accelerated measurements. A potential approach to parallelization is the implementation of multi-antenna setup which enables a linear downscaling of the measurement time with the deployment of number of THz emitter and detector pairs. However, the compact size and planar arrays have to be used to counter the increase of system cost. Looking into such necessity, in Chapter 5, we have designed an array of small-gap photoconductive dipole antenna at THz frequency by using a frequency selective surface which not only provides a planar profile for THz radiating source but also offers enhanced gain and directivity for imaging application to detect the hidden explosives. Moreover, to control the transmission characteristics in a particular THz frequency band with the placement of array of FSS across the array of photoconductive dipole antenna is also discussed. The complete antenna array assembly with FSS is made useful to form an image by scanning a single beam in both principle planes. In Chapter 6, the beam steering characteristics of the small-gap photoconductive dipole phased array antenna is presented. With uniform distribution of optical source excitation and progressive phase shift in x-axis and y-axis of the antenna configuration, the beam steering phenomenon has been determined. Finally, Chapter 7 concludes the thesis and has presented the future directions in terms of certain design techniques which can be incorporated in the basic structure of our proposed small-gap photoconductive dipole antenna to further improve its performance parameters for its use in THz imaging applications.

# CHAPTER 2

## ANALYSIS AND DESIGN OF SMALL-GAP PHOTOCONDUCTIVE DIPOLE ANTENNA

### 2.1 INTRODUCTION

Various proposed applications exploit the unique capabilities of THz radiation to penetrate the packaging materials and therefore provide their spectroscopic information. However, there are certain emerging issues related to THz for imaging and sensing applications such as the water content present inside the human body eludes transmission-type imaging [118]. Moreover, in comparison with optical light the THz radiations offer lesser spatial resolution of images. In the real-world scenario, there are nine low-attenuation windows in the range of 0.1-3 THz of the spectrum, 1) 0.1-0.55 THz, 2) 0.56-0.75 THz, 3) 0.76-0.98 THz, 4) 0.99-1.09 THz, 5) 1.21-1.41 THz, 6) 1.42-1.59 THz, 7) 1.92-2.04 THz, 8) 2.05-2.15 THz, and 9) 2.47-2.62THz, respectively [119] which can be considered for effective transmission-type THz imaging. These frequency ranges are determined by considering the measurements at 23˚C temperature and 26% of relative humidity. These transmission bands are important to consider because several commonly used solid-state explosives and related compounds (ERCs) have spectral fingerprints in 0.1-2.8 THz range. Such fingerprints occur from the intra-molecular and inter-molecular vibrational modes or phonon modes of these explosive materials [120]. Therefore, the THz sensing and imaging in transmission /low attenuation windows is necessary for the detection of the hidden explosives. In THz imaging system, the electromagnetic waves are used to spectroscopically detect the presence of concealed explosives such as research department explosive (RDX) and high melting explosive (HMX) from the characteristic transmission or reflectivity spectra shown by these explosives in the THz range [28]. A detection technique to RDX pellet using THz frequency is as shown in Figure 2.1[121]. In this setup, a femto-second pulsed laser (Ti:Sapphire laser) is used for the generation of signal. The optical beam from the laser is splitted into two beams with the help of a beam splitter (BS). One beam is utilized for exciting photoconductive antenna which works as emitter and the other beam is used for measuring the THz signal at ZnTe crystal detector for modulation. Various beam splitters are used for the beam deflection. The parabolic optical mirror combination is used for the optical beam to strike the photoconductive material of the emitter to generate the THz beam which is focused on sample point. The sample (RDX pellet) is positioned at the focus point of THz wave and is perpendicular to the incident beam. The transmitted THz beam after passing through the sample is then collected and focused with the help of other pair of off-axis parabolic mirrors (PM) onto the ZnTe crystal where the probe beam from the laser detect the THz field using electro-optic sampling. When such radiations are allowed to pass through the sample, they get absorbed at their respective features and the absorption coefficients provide the information related to detection of hidden explosives at detector side.

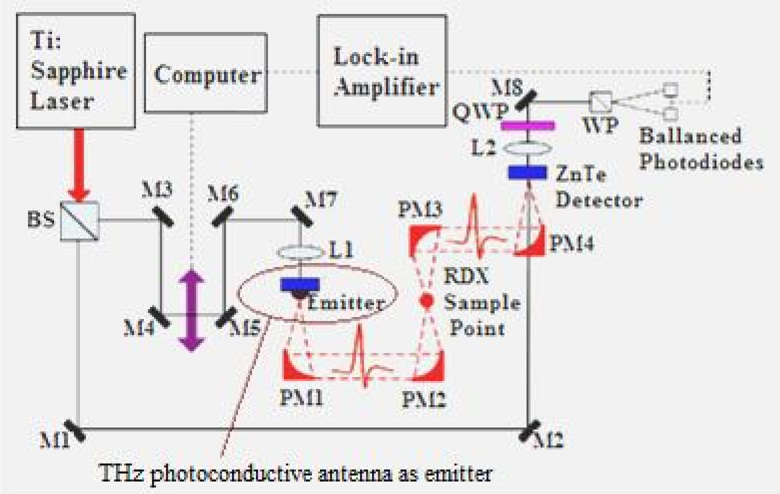

**Figure 2.1: The THz frequency system based on the principle of photoconductivity wherein LT-GaAs emitter is used as a THz photoconductive antenna [121].**

From above Figure 2.1, it is clear that the photoconductive antenna is one of the most important components in a THz sensing and imaging system as it plays significant role for both impedance matching and power source. In [121], a terahertz time-domain spectroscopy system has been deployed in 0.2 - 3.4 THz range of frequency. The bandwidth of a photoconductive antenna is generally considered as the range of frequencies over which the signal strength of the measured frequency domain exceeds the noise level of the system. However, an enlarged bandwidth is significant for the applications that make use of distinct spectral characteristics in materials such as in THz sensing and imaging applications for the detection of hidden powdered explosives and this necessitates the capability to detect narrow absorption peaks in the THz band. Accordingly, increasing the bandwidth of a THz photoconductive antenna based THz imaging system will set aside additional vibrational modes to be quantified [122]. Several companies such as TeraView Ltd., Picometrix LLC, Advantest and Menlo Systems provide absolute THz imaging and spectroscopy systems which employ photoconductive antennas as emitters and detectors. Some commercially available photoconductive antenna based THz spectroscopy systems by TeraView company with model numbers TPS Spectra 3000 and TeraPulse 4000 have a bandwidth (maximum frequency) of 4 THz and 6 THz, respectively. Similarly, Picometrix and Advantest have developed the spectroscopy systems T-Ray 5000 and TAS each having a bandwidth of 4 THz. The company Mento Systems have developed TERA K8 and TERA K15 spectroscopy systems which are photoconductive antenna based system with a bandwidth of 3.5 THz and 4 THz, respectively.

For the imaging purpose, it is required to have a highly directive low-profile photoconductive antenna which generates the desired THz radiation at operating frequency with high directivity and optimum radiation efficiency with broad bandwidth. However, one of the key issues of the various reported photoconductive dipole antennas is that the antenna efficiency is very small, which makes the difficulty for the THz imaging system to achieve high power THz waves. The photoconductive dipole antenna is unable to transfer the laser source power to the THz power efficiently because the highest power conversion efficiency as reported in literature is much less than 0.1% for THz pulsed systems[123]. Therefore, the researchers generally increase the illumination power as well as the applied bias to yield higher output power. However in such situations, the phenomena such as saturation of charges, velocity overshoot, field and thermal breakdown occur in the THz pulsed systems. The thermal and field breakdowns are required to be avoided under every condition. Furthermore, three main causes for low efficiency of the photoconductive dipole antennas are [124]:

- Space-charge also known as coulomb screening effect and screening effects due to radiation field,
- Spatial non-uniformities, and
- Inadequate field strength due to the insufficient acceleration of the charges.

Due to the space-charge field generated by the photo-excited electron-hole pairs there is an occurrence of coulomb screening effect. The movement of free charge carrier’s under the influence of the applied bias field create a static field which is responsible for moderately screening of the applied bias field. However, the occurrence of radiation screening effect is because of the THz near field radiation which is also responsible for screening of the applied bias field. With the use of THz photoconductive dipole antenna in continuous wave operation mode for high peak optical pulse intensity the effect of radiation screening gets negligible [124]. Further, the spatial non-uniformities occur in photoconductive dipole antenna since the thickness of the substrate is generally larger than the wavelength of the THz waves, which results into the generation of surface/substrate modes. The antenna performance is sensitive to the substrate thickness. If the thickness of substrate is increased, the dipole antenna couples the power to higher order substrate modes. Moreover, in several cases even more than 90% of power gets trapped within the substrate [125]. Moreover, when a photoconductive dipole antenna is fabricated on a thick substrate it results into the excitation of a surface wave mode which depends on several characteristics such as frequency, thickness of the substrate and the relative dielectric constant of the substrate. It is clear that the total power radiated from the photoconductive dipole structure does not get directly transferred into the medium, however, a fraction of the radiated power get trapped within the substrate and therefore create an effect on the radiation pattern.

## 2.2. RELATED WORK AND PROBLEM FORMULATION

With the development of ultra-short pulse femtosecond lasers like Ti-Sapphire laser and quantum cascade lasers, it is possible to generate THz signals. The electro-optic (EO) rectification which is based on different frequency mixing technique is also used to generate THz radiation but it has certain limitations. This method cannot produce THz frequency signals of broad frequency range and is also very sensitive to optical and thermal noises. Moreover, for the application of sensing and imaging there is a requirement of a broadband short-pulse THz source for spectroscopic techniques such as Time Domain Spectroscopy (TDS) or THz Pulsed Imaging (TPI). Therefore, the photoconductive antenna is one of the simple and stable devices for THz photonics used for sensing and imaging applications at THz frequency. The photoconductive antenna is relatively stable against optical and thermal noises in comparison to the electro-optic rectification [112]. However, the total antenna efficiency which includes optical-laser to THz conversion efficiency, impedance matching efficiency and radiation efficiency is small. Various photoconductive dipole antenna structures are projected and are used for the THz frequency range [126]. On the basis of the architecture of photoconductive antennas for THz pulsed systems, they are classified as an aperture antennas, spiral antennas, bowtie antennas and dipole antennas. In the large aperture photoconductive antenna, the distance between the electrodes is much larger than the centre wavelength of THz wave with it is range of few hundred micrometers. However, in the small gap photoconductive dipole antenna, the antenna gap distance is only few micrometers. Moreover, in the photoconductive dipole antenna, to increase the conversion efficiency, the electrodes with sharp tip ends can be used and the efficiency can further be improved by putting them in a laterally offset format [106]. In this case, the THz emission can be improved with less optical power because of better overlap among the laser spot and high electric field point and also stronger fringing field effects between the electrodes. For small gap photoconductive antennas, the fabrication of such tiny sharp tips is not easy. Moreover, an appropriate configuration of the electrodes may double the efficiency of the antennas, with a consequence in the bandwidth of the radiated pulse. However, the first photoconductive antenna was accounted by Mourou et al. [127] which operate in the GHz range, then the design is extended into the THz region by Auston et al. [128, 129]. Grischkowsky et al. [130, 131] have reported the application of optical technique for the generation of diffraction limited THz beams with a relatively large size of the source. This technique was further developed at Bell Labs and the IBM Watson Research Centre, which is now commercially available as a product by Picometrix Inc, MI [132]. Moreover, it is important to determine the antenna's spatial response as it is related with the power collected by the antenna. Therefore, the measurements of spatial response of infrared dipole and bow-tie lithographic antennas are discussed by Fumeauxet et al. [133]. A dipole antenna placed in a pyramidal horn cavity which is impressed in silicon operated at 0.8THz is reported in [134]. A stripline dipole antenna for a broad frequency range upto 5 THz on semi-infinite and lens substrates is discussed in terms of input impedance as well as radiation characteristics in [135].

Further, the emission efficiency of photoconductive dipole antenna is discussed by Tani et al. [136] wherein the authors have considered the saturation effect that occurs due to the field screening effect caused by the photo-generated carriers. The key features about the near-field patterns on the photoconductive antenna are discussed by Hughes et al. [137]. They introduced a finite-difference time-domain method for the pulsed laser excited vector THz fields from photoconductive antenna. Berry and Jarrahi [138] have evaluated the criteria to optimize the impedance matching in photoconductive antenna. Moreno et al. [139] presented the mobility model to describe the carrier dynamics for the analysis of radiating semiconductor photoconductive devices in the THz regime. The biased electric field analysis of photoconductive antenna for THz generation is reported by Yang et al. [140]. In their simulation results, it is illustrated that the strip-line photoconductive antenna and photoconductive dipole antenna cannot withstand high biased voltage because of the small value of breakdown electric field of the substrate material. Another exciting new technology for THz antennas is the idea of active surface correction for improving the beam efficiency [141]. However, the high directivity with high front-to-back ratio, optimum radiation efficiency, broad bandwidth and tuning/phase scanning are the significant challenges related to the design issues of photoconductive dipole antenna.

## 2.3 PARAMETRIC ESTIMATION OF PHOTOCONDUCTIVE DIPOLE ANTENNA

In this section, using a simple synthesis technique the physical parameters of THz small gap photoconductive dipole antenna are determined corresponding to 1.5 THz resonance frequency. We are interested to design a THz photoconductive dipole antenna for sensing and imaging to detect the hidden explosives (like RDX and HMX) which shows their spectral fingerprints with absorption peak position in THz regime in the range of 1THz to 2THz as reported in [119-121]. Therefore, a THz photoconductive antenna is designed at 1.5THz to detect such explosives easily. Further, the main obstacle in THz free-space sensing and imaging is the atmospheric attenuation which is dominated by the absorption of THz wave due to the presence of the water vapour, however the choice of using 1.5 THz operating frequency is also supported by the transmission windows mentioned in Section 2.1. In addition to this, to analyze the performance of designed THz photoconductive dipole antenna, the frequency range 1THz to 2THz is chosen because many home-made ammonium nitrate bombs as well as some other improvised explosive devices have featureless THz spectra below 3THz which are also posing potential challenges to THz security applications. Therefore, this proposed simple antenna design can also be used for the detection of such explosives having THz spectra lower than 3THz. The basic structure of THz photoconductive dipole antenna is shown in Figure 2.2, which consists of a dipole antenna structure, a photoconductive substrate and a ground plane placed under the substrate.

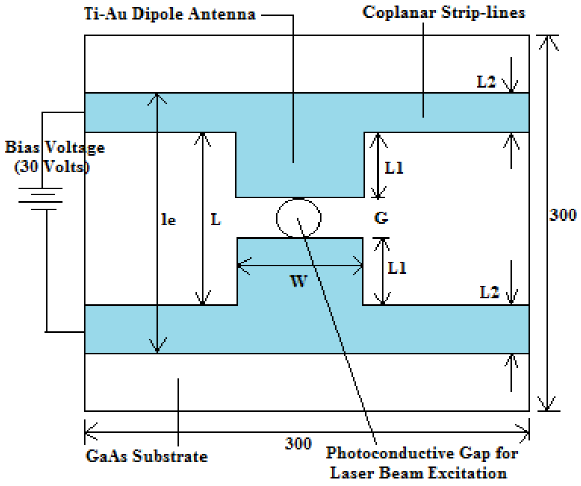

**Figure 2.2: The basic structure of THz photoconductive dipole antenna.**

At the centre of the dipole antenna of effective length ($l_e$), there is a photoconductive gap (G) biased by a voltage source (30 volts) which is illuminated at the centre with a femtosecond laser pulse.

### 2.3.1 Working phenomenon of small-gap photoconductive dipole antenna

By illuminating the photo-conductive layer of the antenna using femto-second laser pulse the electron-hole pairs are generated within the photoconductive gap of the antenna. This happens because of the higher photon energy of laser pulse in comparison with the band-gap energy of the photoconductive material. When a biased electric field ($E_{bias}$) is applied across the antenna electrodes through transmission lines then the photo-excited carriers get accelerated. A macroscopic electron-hole field ($E_{e-h}$) gets created in the reverse direction because of the physical separation of charges. As more of electron-hole pairs are generated there is also an increase in the electron-hole field and after sometime the total electric field at the location of carriers near the dipole electrodes (defined as $E_{field} = E_{bias} - E_{e-h}$) is screened. This results into the reduction of the effective electric-field across the photoconductive gap of the antenna. Due to the sudden change in the total electric field $E_{field}$ , there is a creation of the transient current which is responsible for the THz radiations from the photoconductive antenna [142]. The generated transient current decays with time constant which is determined from the carrier lifetime in the photoconductive substrate used for the antenna. The radiation efficiency of a photoconductive dipole antenna is proportional to the carrier mobility of photoconductive substrate as presented in [118], but doesn't directly depend on the carrier lifetime. Though, a short carrier lifetime is preferred to reduce the noise generated at the detector side of the THz system due to the thermal motion of the carrier. Likewise, the antenna efficiency is also proportional to the substrate resistivity because it increases linearly with the applied biasing voltage. Moreover, in addition to a low carrier lifetime along with high resistivity of photoconductive material, there is a requirement for the 1) continuance of relatively high carrier mobility, 2) suitable band gap, and 3) high breakdown voltage with suppression of zero bias photocurrent. All these factors play an important role as they influence the antenna's 1) output power, 2) maximum optical pump power, 3) maximum bias voltage, 4) bandwidth, and 5) SNR values [143-145]. Owing to these properties, gallium arsenide (GaAs), low-temperature- grown GaAs, bulk indium gallium arsenide (In GaAs), indium aluminium arsenide (InAlAs), radiation damaged silicon on sapphire, alternating nanoscale-multilayers of InGaAs, and amorphous silicon are the most promising substrate materials for THz photoconductive antennas [146]. The proposed antenna in this work usages GaAs substrate which has a photo-carrier lifetime $\tau_c$= 0.25ps, a high mobility 200 cm$^2$/Vs, a high breakdown field $4 \times 10^5$V/cm and has a room temperature bandgap of 1.424eV (871nm) [147], and makes the antenna well-matched to Titanium-doped Sapphire (Ti: Sapphire) femtosecond pulsed laser source generally used to excite photoconductive antennas. If, the thickness of substrate is kept 1µm then nearly 30 % of the light gets absorbed into the substrate therefore to reduce the absorption (i.e. below 5 %) in substrate at least 3 µm thickness of the substrate is essential. Therefore, the thickness of the substrate is taken as 10 µm in this design and its dimension is 300µm ×300µm×10µm. A lossy-metal Ti-Au is used as the material for the dipole antenna structure placed on the GaAs substrate. Due to the good Ohmic contact between Ti-Au and GaAs, they are used as the antenna and substrate material, respectively. Graphene is also a promising material for the miniaturized resonant THz antennas design [148, 149]. However, only few initial works considered the use of graphene in THz antennas. Firstly, graphene was considered as a parasitic layer below a dipole antenna made of gold (Au) and radiated at millimetre wave frequency of 120 GHz [150]. The scattering of an incident wave impinging on graphene rectangular patches was studied in [151] wherein, it has been concluded that the graphene patches support surface plasmonic resonances in the THz range. In [152], graphene has been used as an actual antenna radiator where radiation is attained by placing a THz continuous-wave (CW) photomixer as source in the middle of the graphene patch. The photomixer excites the graphene patches which are DC biased and thus enables its surface to radiate.

### 2.3.2 Antenna physical parameter estimation technique

The first physical parameter in the design of photoconductive dipole antenna is the photoconductive gap size (G) where the femto-second laser pulse strikes to generate the photo carriers.

$$E_{THz}^{peak} = e\mu T_{int} \frac{(1-R)}{h\vartheta} \frac{P_{in}}{G} \frac{E_{bias}}{G} \quad (2.1)$$

where, $e$ , $\mu$, $T_{int}$ R, $h\vartheta$, $P_{in}$, G, and $E_{bias}$ are electron charge, carrier mobility, pulse interval, reflection from the photoconductive substrate, photon energy, average pump laser power , photoconductive gap size and bias voltage, respectively. From (2.1), this is clear that the emission efficiency is inversely proportional to gap size of the photoconductive dipole antenna while the bias field $(E_{bias})$ as well as the pump-power $(P_{in})$ are kept constant. Consequently, it is important to keep the photoconductive gap as small as possible and thereby focusing the laser beam (optical excitation) very closely to the small-gap. Moreover, when the pump laser power is small then the efficiency saturates at higher pump intensities. Therefore, in such condition the antenna gap needs to adjust such as to minimize the screening effect (the cancellation of a portion of the bias field by the transient current at the surface when the near field is generated) and as a consequence improve the efficiency in THz photoconductive dipole antenna which persuades the initial spatial distribution of photo-excited carriers on photoconductive substrate. The photoconductive gap is taken as 5µm for small gap photoconductive dipole antenna in all three antenna designed configurations and its value is optimized using the simulation software (CST Microwave Studio). The length of coplanar strip-line is generally lay-down to be long enough to evade the reflection at the line end. Therefore, the length of coplanar strip-line taken is $300\mu m$, width 10µm and thickness $0.35\mu m$. The length of the dipole is determined using the relation of resonant frequency as $f_r = c/2nL$, where $c$, $L$, and $n$ are the speed of light in vacuum, separation between two coplanar strip-lines and refractive index of the material, respectively. For resonance, $L = m\times\lambda n/2$, where $m$=1,2,3…. , and the wavelength $\lambda_n$ in the material depends on the refractive index $n$ which is given by $\lambda_n = \lambda/n$ . If we take $m = 1$, then $L = \lambda/2n$. The refractive index of the semiconductor antenna material for GaAs at THz frequencies is 3.4 and for $f = 1.5$ THz, the value of $L$ (length of dipole) is: $L = C/(2n\,fr)$ = 30µm. The other equally important physical parameter of the photoconductive dipole antenna is the width ($W$) of dipole because of two reasons: 1) the directivity and 2) radiation efficiency of the photoconductive dipole antenna which depends on the relative dimensions of the dipole as both enhances appreciably by increasing the aspect ratio ($\eta \equiv L/W$). The emission efficiency also get increased with increasing the aspect ratio (L/W) of THz photoconductive dipole antenna as reported in [153]. However, an optimum value of aspect ratio for photoconductive dipole antenna can be determined by considering the following factors:

- With the decrease in the dipole length (L), the emission intensity gets decreased significantly.
- The peak frequency of emission spectra shifts to lower frequency values when the dipole length (L) is increased.
- With an increase in the dipole length (L), the bandwidth of antenna happens to be narrower.
- The peak intensity of the antenna decreases considerably with an increase in the dipole width (W), which reveals that the emission efficiency of dipole antenna is proportional to the aspect ratio.

From the aforementioned points, it is concluded that for the better performance of THz photoconductive dipole antenna, the length of dipole must be greater than the width of dipole. In the proposed antenna, we have also checked the performance of the antenna with different values of the aspect ratio by keeping the length of dipole constant to 30 µm and varying the width of the dipole to set the aspect ratios as ($L/W$) 0.5, 1, 1.5, 2, with the values of width of dipole ($W$) as 60, 30, 20, 15 (all in µm), respectively. It is observed from the simulated results discussed in section V, that by keeping aspect ratio 1.5, the performance of THz photoconductive dipole antenna is interesting in terms of directivity in both the E- and H-planes. Further, the other physical parameter of photoconductive dipole antenna is the effective length ($l_e$) and its value has been computed considering following points.

- If the effective length of dipole is assumed to be same as the distance between coplanar strip lines i.e. $l_e = L$, then in this case $l_e = 30\mu\mathrm{m}$
- If the effective length of the dipole antenna is taken into the account: $l_e = 2\,L_2 + L$, and in this case $l_e = 50\ \mu\mathrm{m}$ with L2, the width of the strip-line which is 10 µm.

The choice of considering the effective length will affect the resonating frequency as $f_r = \mathrm{c}/(2l_e[(1 + \varepsilon_d)/2]^{1/2})$, where $f_r$ and $\in_d$ are the resonating frequency and the dielectric permittivity of GaAs substrate, respectively. If the effective length of dipole is assumed to be same as the distance between the coplanar strip-lines i.e. $l_e = L$, then by using $c = 3 \times 10^8\ \mathrm{m/s}$, $l_e = 30\ \mu\mathrm{m}$ and $\varepsilon_d = 12.9$ for GaAs, the resonance frequency $f_r = 1.89\ \mathrm{THz}$ is obtained. If the effective length of dipole antenna is chosen by considering the width of coplanar strip-lines i.e. $l_e = 2\,L_2 + L$, then the resonance frequency is $f_r = 1.14\ \mathrm{THz}$ . Now, by considering the values of physical parameters determined for the THz photoconductive dipole antenna of Ti-Au (lossy-metal) material with conductivity $\sigma = 1.6 \times 10^7$ S/m and thickness 0.35 µm, is designed on a photoconductive substrate GaAs (lossy) having dielectric permittivity $\varepsilon = 12.94$, magnetic permeability $\mu = 1$ and loss tangent $\delta = 0.006\ \mathrm{S/m}$. The antenna designed with this specifications is named as Design-A in the manuscript. However, we are interested to use this THz photoconductive dipole antenna for sensing and imaging application wherein high directivity is required, therefore for this purpose, two more designs are simulated. The Design-B is configured by using a superstrate which helps to enhance the radiation performance and efficiency of THz photoconductive dipole antenna [154]. A very thin superstrate of low-temperature grown GaAs (LT-GaAs) with thickness 1µm is placed in between the GaAs substrate and the antenna structure. In other antenna configuration that is Design-C, a silicon lens is used to enhance the directivity of the THz photoconductive dipole antenna. A small hemispherical Silicon lens is placed beneath the ground plane which is the direction of propagation of generated THz wave from the photoconductive dipole antenna.

The potential importance of using thin LT-GaAs superstrate and a silicon lens in the THz photoconductive dipole antenna is discussed as follows.

### 2.3.2.1 Use of thin LT-GaAs superstrate

With the illumination of the photoconductor by using a shot optical pulse from a femtosecond laser pulse, a current surge as shown in Figure 2.3 is noticed which results into the generation of the THz radiation. However, in case of long carrier lifetime of the photoconductive substrate the generated current keeps flowing even after the withdrawn of excitation short optical pulse. This results into broadening of the photocurrent pulse, which further broaden the output pulse and therefore, decrease the overall THz frequency bandwidth. Moreover, in case of arrival of next shot optical pulse before the current dies out (generated by previous short optical pulse) and excites the photoconductive dipole antenna, a new THz pulse is created, although at this time the presence of already existing background current due to previous short optical pulse may affect the generation of THz radiation. Therefore, to prevent this, photoconductors with sub-picosecond carrier lifetime such as low-temperature-grown gallium arsenide (LT-GaAs) having very small thickness in comparison to the GaAs substrate, may be used.

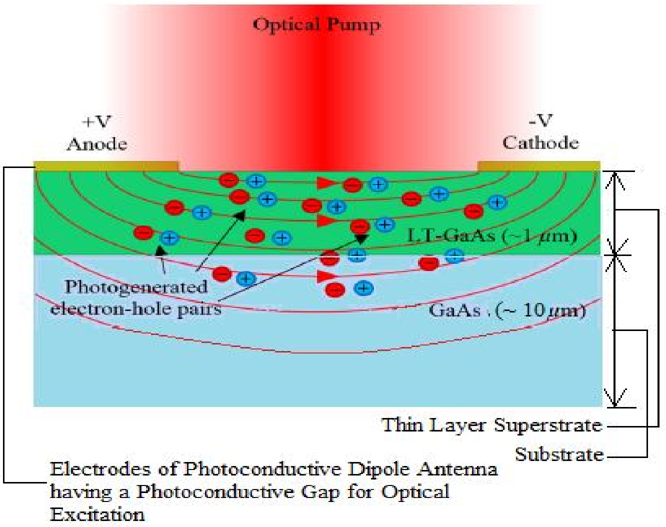

**Figure 2.3: Optical carrier generation at the photoconductive dipole gap of a LT-GaAs superstrate based THz photoconductive dipole antenna and the red arrows represent the flux lines of the electric field [116].**

Moreover, the THz photoconductive dipole antenna with a thin layer (nearly 1μm) of short carrier lifetime LT-GaAs as superstrate can avoid saturation at high frequency which helps to achieve peak power spectral density. The LT-GaAs has the relevant features such as very high electric breakdown field (~ 500KV/cm), short photo-carrier lifetime (0.1 ps) along with high mobility of charges (> 200 $cm^2$/Vs), therefore it is a good material for fabrication as a superstrate in the photoconductive antenna.

#### 2.3.2.2 Use of silicon hemispherical lens

For directivity enhancement of an antenna and because of the ease of built-up, an extended hemispherical dielectric lens (such as silicon lens) is beneficial in its use with photoconductive dipole antenna. Moreover, the silicon lens reduces loss due to the reflection and refraction of radiation at the substrate-air interface [155]. A silicon lens which is a hemisphere with radius R is generally located directly on the ground plane of THz photoconductive dipole antenna. The directivity (D) of a lens antenna in the direction of the main lobe of THz radiation can be found using the formula for the directivity of a circular aperture having radius R and uniform distribution of the electric field [156], as $D = 20\log((2\pi R)/\lambda 0)$, where $\lambda_0$ is the wavelength in free-space and $R$ is the lens radius. The width of the beam at -3dB of the directivity of the integrated lens antenna is estimated as $\Omega = 59^{\circ}(\lambda 0/2R)$. The use of a lens with THz photoconductive dipole antenna also provides the electronic beam-steering capability to the antenna by switching between two photoconductive dipole antenna elements with common bias lines and the ground plane. In such a case, the photoconductive dipole antennas need to be placed on a plane focal surface of the lens. The electronic beam steering allows antenna to automatically adjust the beam direction during initial alignment of transmitting and receiving antennas [157] and thus the photoconductive dipole antenna array with lens may be used for THz pulsed imaging with scanning.

## 2.4 SIMULATION MODEL

In the small gap photoconductive dipole antenna, the gap is of only few micrometers (µm) and thus, there is an insufficient acceleration of the charges which results in the inadequate field strength to generate THz radiations in comparison to that of the large aperture photoconductive antenna which results low antenna efficiency. Therefore, to increase the radiation efficiency of photoconductive dipole antenna, it is essential to consider the factors which affecting the total antenna efficiency. In the photoconductive dipole antenna, three types of efficiencies are considered to evaluate the total antenna efficiency ($\eta_t$), which are:

- Laser-to-electrical conversion efficiency ($\eta_{LE}$),
- Impedance matching efficiency ($\eta_m$) ,and
- Radiation efficiency ($\eta_r$).

The total efficiency of photoconductive dipole antenna (also known as optical-to-THz power conversion efficiency) represents the multiplication of these three efficiencies, is:

$$\eta_t = \eta_{LE} * \eta_m * \eta_r \tag{2.2}$$

### 2.4.1 Computation of laser-to-electrical conversion efficiency

When a short-duration optical pulse incidents onto the photoconductive gap of the proposed antenna, the induced photocurrent is expressed as [129]:

$$I = \frac{e\, E_{bias}\, \mu_e\, \tau \eta_L P_L}{h f_L G^2} \tag{2.3}$$

where $e$, $E_{bias}$, $\mu_e$, $\tau$, $h$, G, $f_L$, $P_L$, and $\eta_L$ are electron charge, the applied bias voltage, free-carrier mobility inside the photoconductor, photocurrent decay time, Planck's constant, gap length, laser frequency, laser power incident onto the photoconductive gap, and the illumination efficiency, respectively. Illumination efficiency takes into account of many issues such as a) the reflection of laser on the surface of the substrate, and b) the quantum efficiency. The optical-pump laser is focused onto the feeding gap wherein the photon energy of the laser is equal to or slightly greater than the band gap of the semiconductor substrate so as to ensure that free-electrons are efficiently created. Such electro–optical procedure converts the laser power $P_L$ to the electrical power $P_E$. To determine an expression for the electrical power, initially it is important to obtain the associated resistance, R such as:

$$R \approx \frac{h\, c\, f_R\, G^2}{\eta_L e\, \mu_e P_L \lambda_L} \tag{2.4}$$

where $f_R$ is the laser repletion frequency. From (2.3) and (2.4), the induced electric power on the photoconductor is:

$$P_E = I^2 R \approx \left(\frac{e\, E_{bias}\, \mu_e\, \tau \eta_L P_L}{h f_L G^2}\right)^2 \frac{h\, c\, f_R\, G^2}{\eta_L e\, \mu_e P_L \lambda_L} \tag{2.5}$$

Therefore, the laser-to-electrical power conversion efficiency is estimated as:

$$\eta_{LE} = \frac{P_E}{P_L} \approx \frac{e\, E_{bias}{}^2 \mu_e \tau^2 \eta_L f_R}{h f_L G^2} \tag{2.6}$$

From (2.6), it is clear that besides the laser source, the laser-to-electrical conversion efficiency factor also includes the bias voltage. Therefore, an electric power is not exclusively produced by the laser source.

### 2.4.2 Calculation of impedance matching efficiency

The impedance matching efficiency is:

$$\eta_m = 1 - \left(\frac{Z_a - Z_s}{Z_a + Z_s}\right)^2 \tag{2.7}$$

where $Z_a$and $Z_s$are the antenna impedance and source impedance, respectively. The value of source impedance is determined from the time-varying source conductance. The time-varying source conductance $G_S(t)$ in the THz photoconductive dipole antenna depends on the values of length (G) and width (W) of the gap. Moreover, the inverse of $G_S(t)$ of the photoconductive material is the time-variant resistance $R(t)$ which is used to determine the time or frequency variant impedance matching efficiency of the photoconductive dipole antenna.

### 2.4.3 Computation of radiation efficiency

The radiation efficiency of photoconductive dipole antenna is the ratio of gain and directivity of the antenna at the chosen frequency of operation, which is determined using an electromagnetic simulation tool CST Microwave Studio.

However, the low radiation efficiency is the major challenge to the present photoconductive dipole antenna and it occurs due to the excessive Ohmic losses at THz frequencies. Further, the impedance matching efficiency of antenna must be considered for proper impedance matching of laser source with photoconductive material of antenna. It is essential to mention here that the THz photoconductive dipole antenna is simulated using the CST Microwave Studio. It offers a simulation platform for all kind of electromagnetic field applications. We have used the Transient Solver which is based on the Finite Integration Technique (FIT) in which direct time-domain analysis is applied with broadband computation of S-parameters through one single calculation run on applying DFTs to the time signals. The simulation run for the proposed antenna is also supported by the adaptive-mesh refinement in 3D using S-parameters supported by the Transient solver of CST Microwave Studio. In our work, we have determined the length (and effective lengths) of the photoconductive dipole antenna for a specific terahertz frequency and the corresponding resonant frequencies have been computed numerically. The structure parameters considered for the proposed antenna is presented in Table 2.1. We have used the CST Microwave Studio to obtain the $S_{11}$ parameter from which, the resonant peaks can be determined and is compared with the values of resonant frequencies obtained mathematically. If we refer Figure 2.6 “The S-parameter (dB) for three proposed antenna design configurations” the three resonant peaks obtained for each antenna design are nearly same as that of the theoretical obtained values.

However, with the help of multi-physics finite-element solver (COMSOL) the response of the photoconductor of the designed dipole to the incident short-optical pulse can be estimated. In such case, the photo-generated carrier density is derived using the drift-diffusion model from the calculated optical intensity in the photo absorbing substrate along with the bias electric field data to compute the induced photocurrent [138]. Using Ti:Sapphire laser having characteristics of 800nm central wavelength, repetition rate of 76 MHz with pulse width of 100 fsec, an optical pump beam from the laser is allowed to get tightly focused onto the photoconductive antenna gap and is also positioned near the anode contact electrode to maximize the radiated power [158]. The generated terahertz power from photoconductive emitter can be measured using a pyroelectric detector.

**Table 2.1: The structure parameters for the proposed antenna.**

| Parameter | Value |
|---|---|
| **Dipole Antenna (Ti-Au) and Ground** | |
| Conductivity (S/m) | $1.6 \times 10^7$ |
| **Superstrate(LT-GaAs)** | |
| Carrier Lifetime, majority carriers (psec) | 0.1 |
| Mobility ($cm^2/Vs$) | Greater than 200 |
| Dielectric Permittivity | 13.26 [34] |
| Magnetic Permeability | 1 |
| Loss tangent (S/m) | 0.006 |
| Electric breakdown field (V/cm) | Greater than $5 \times 10^5$ |
| **Substrate (GaAs)** | |
| Carrier lifetime, majority carriers (psec) | 0.25 |
| Mobility ($cm^2/Vs$) | 200 |
| Dielectric permittivity | 12.9 |
| Magnetic permeability | 1 |
| Loss tangent(S/m) | 0.006 |
| Electric breakdown field (V/cm) | Nearly $4\times 10^5$ |
| **Silicon lens** | |
| Permittivity | 11.9 |
| Permeability | 1 |
| Loss tangent (S/m) | 0.00025 |
| **Voltage Source** | |
| DC voltage (V) | 30 |

Moreover, to determine the photoconductive dipole emitter characterization with the help of experimental setup in terms of device alignment, output power measurement and radiation spectral characterization, the stages which are required are mentioned in brief as follows on next page:

Stage 1: Device alignment

a) Initially, place the photoconductive THz emitter in the aluminium washer and using Ti: Sapphire mode-locked laser such as MIRA 900D V10 XW OPT 110V focus the optical laser pulse on the photoconductive gap of the antenna.
b) With the help of the parametric analyser provide the bias voltage to the co-planar striplines of photoconductive dipole antenna to measure the induced electric current.
c) To modulate the optical pump from the laser focused onto the gap of photoconductive dipole antenna an optical chopper such as Thorlabs MC2000 can be used.

Stage 2: Output power measurement

a) Using pyroelectric detector such as Spectrum Detector, Inc. SPI-A-65 THz, measure the output power of photoconductive dipole antenna.
b) To pull through terahertz power data at low noise levels, connect the output of pyroelectric detector with lock-in amplifier such as Stanford Research Systems SR830 along-with the reference frequency of optical chopper.

Stage 3: Radiation spectral characterization

a) Using a beam splitter, split the output optical beam of mode-locked Ti:Sapphire laser into pump beam and probe beam.
b) To generate the THz radiations focus the pump beam of laser on the photoconductive gap of photoconductive dipole antenna.
c) With the help of polyethylene spherical lens, collimate the THz beam generated from the photoconductive dipole antenna as emitter.
d) Merge the collimated THz beam coming from the polyethylene spherical lens with the probe beam using ITO coated glass filter.
e) At the combined focus of the optical and THz beam place a ZnTe crystal (of 1 mm thickness).
f) To vary the time delay occurring between the optical beam and the THz pulse which is interacting with ZnTe Crystal, place-in a controllable optical delay line in the path of optical probe beam with the help of a motorized linear stage such as Thorlabs NRT100.
g) With a Wollaston prism split the optical beam and using balance detectors linked to lock-in amplifier measure the optical beam power in each branch.
h) Join other end of motorized delay line as well as lock-in amplifier to the computer in which a Matlab script is encoded in such a way that iteration can be performed to move

the motorized delay line, pause and read the magnitude of the signal from lock-in amplifier.

i) By dividing the total optical delay length with speed of light convert the stage position to time-domain and further, using Matlab obtain the frequency domain data from discrete Fourier transform.

In the photoconductive antenna, the optical source is a femto-second laser pulse which has a Gaussian distribution at its output, therefore in the CST MSW simulation software, we have applied the Gaussian beam excitation into the substrate from the gap of photoconductive dipole antenna. The antenna configurations which are designed in CST Microwave studio are shown in Figure 2.4.

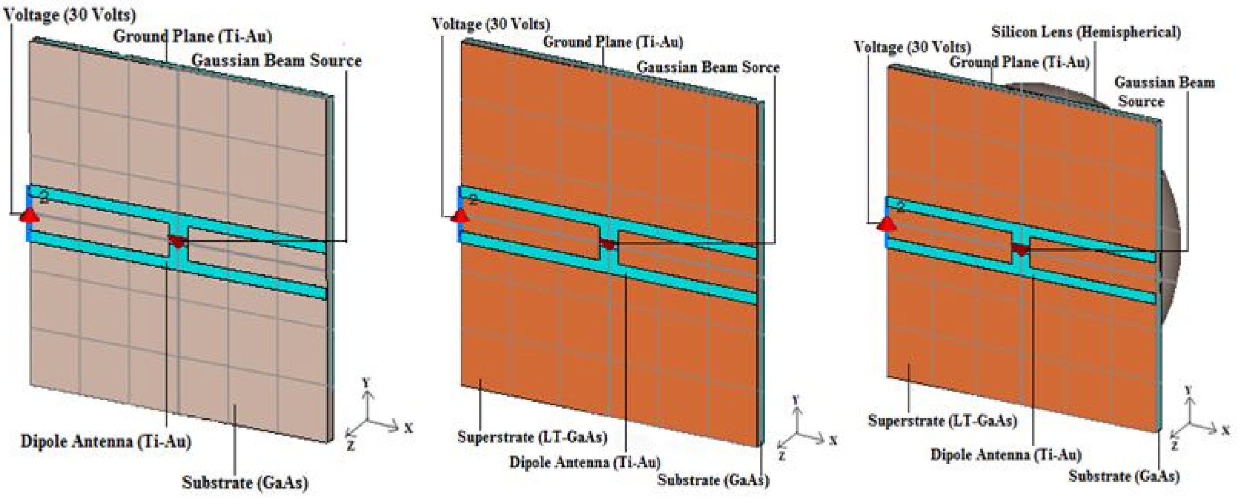

(i) Design-A (ii) Design-B (iii) Design-C

**Figure 2.4: Three configurations i) Design-A: Basic THz photoconductive dipole antenna, ii) Design-B: THz photoconductive dipole antenna with LT-GaAs superstrate, and iii) Design-C: THz photoconductive dipole antenna with LT-GaAs superstrate and silicon lens.**

## 2.5 SIMULATION RESULTS AND DISCUSSIONS

Initially, the comparison of THz photoconductive dipole antenna (Design-A) with different aspect ratio (*L/W*) is performed, choose and optimize the L/W for the proposed reference antenna (Basic THz photoconductive dipole antenna). The length and width of the co-planar strip lines is assumed constant 300µm and 10 µm, respectively. The thickness of substrate and ground plane is 10µm and 0.35µm, respectively with the antenna thickness 0.35µm. The distance between striplines (*L*) is kept constant 30µm and the width of the gap W is varied to observe the effect of aspect ratio on the performance of THz photoconductive dipole antenna. The values of *W* are chosen as 60, 30, 20, 15 (all in µm), respectively with fixed *L* as 30µm.

The comparison for several aspect ratios in terms of gain and directivity is presented in Table 2.2. The antenna efficiency is another important parameter which needs to be enhanced to use the antenna in the sensing and imaging applications. Therefore, the different aspect ratios, the radiation efficiency of the basic THz photoconductive dipole antenna is also presented in the Figure 2.5.

**Table 2.2: Comparison of values of gain (dB) and directivity (dBi) in both E and H plane of photoconductive dipole antenna for several aspect ratio at 1.5THz.**

| Aspect ratio (L/W) of THz photoconductive dipole antenna | Gain (dB) E-plane | Gain (dB) H-plane | Directivity (dBi) E-plane | Directivity (dBi) H-plane |
|---|---|---|---|---|
| 0.5 | 3.24 | 8 | 5.18 | 9.94 |
| 1.0 | 3.31 | 9.03 | 4.02 | 9.74 |
| 1.5 | 3.13 | 8.71 | 4.11 | 9.69 |
| 2.0 | 3.06 | 8.59 | 4.17 | 9.71 |

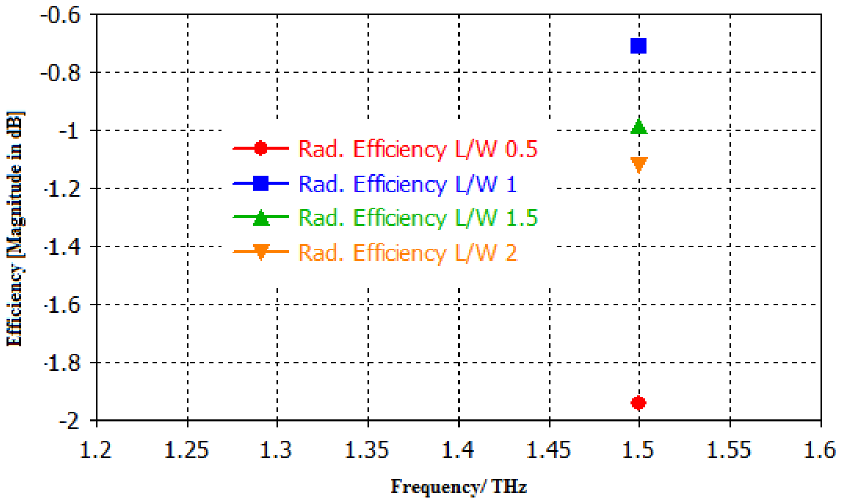

**Figure 2.5: Radiation efficiency at different values of aspect ratio of Design-A(THz photoconductive dipole antenna).**

From Table 2.2 and Figure 2.5 it is observed that the selection of aspect ratio is chosen either *L*/*W*=1 or *L*/*W* =1.5. If we choose the aspect ratio less than 1 then the gain and directivity of Design-A are interesting with respect to simple dipole design but the radiation efficiency is too small. On the other hand, if we choose the aspect ratio 2, the gain reduces. Furthermore, we have chosen the aspect ratio as 1.5 and for this *L* and *W* are 30µm and 20µm, respectively. Further the reason for this selection of aspect ratio is supported by the case wherein on providing adequate power from the laser beam onto the photoconductive gap the peak intensity get decreased considerably with an increase of the dipole width which results into constant total input current. Therefore, the width of dipole must be smaller than the length of the dipole. With the aspect ratio 1.5, the dipole length 30µm and width of dipole 20µm are considered for the design of basic photoconductive dipole antenna Design-*A*. The S-parameter (in dB) for: 1) Design-A, 2) Design-B and 3) Design-C are compared for the S-parameter (in dB) as shown in Figure 2.6. The resonant peaks observed in the results are in accordance with the expressions of resonance frequency discussed in section III with small deviations from their theoretical values. For all the three designed configurations, three bands are observed below -10dB as shown in Figure 2.6, and the comparison is performed corresponding to the highest resonant peak at $f$ = 1.587 THz.

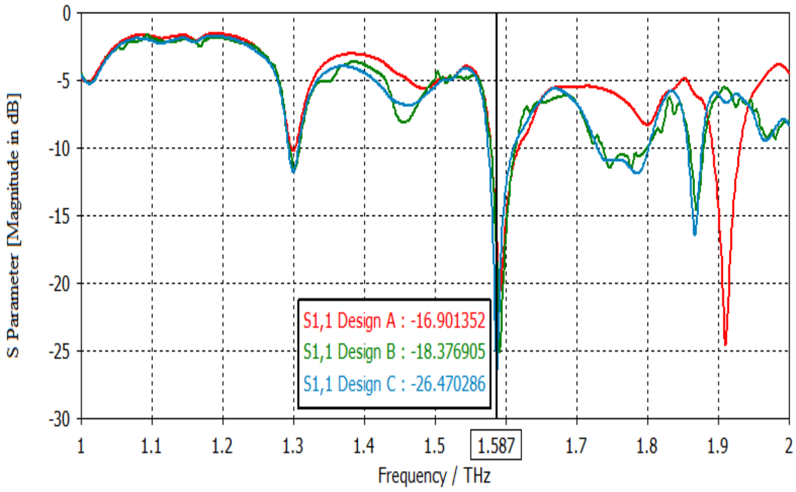

**Figure 2.6: The S-parameter (dB) for three proposed antenna design configurations, Design-A: Basic THz photoconductive dipole antenna, Design-B: THz photoconductive dipole antenna with LT-GaAs superstrate, and Design-C: THz photoconductive dipole antenna with LT-GaAs superstrate and silicon lens.**

In Design-A, the $S_{11}$ parameter at 1.3 THz, 1.593 THz and 1.9 THz are -10.22 dB, -20.32 dB and -24.568 dB, respectively. The 10dB impedance bandwidths obtained for each centre frequency are 50 GHz, 39 GHz and 39 GHz, respectively. For Design-B, the $S_{11}$ parameter at frequencies 1.301 THz, 1.587 THz and 1.868 THz are -11.65 dB, -18.37 dB and -16.30 dB, respectively. The 10dB impedance bandwidths obtained for each centre frequency are 14 GHz, 36 GHz and 20 GHz, respectively. Similarly, for the Design-C, the return loss values at frequencies 1.301 THz, 1.587 THz and 1.868 THz are 11.55 dB, 26.47 dB and 14.09 dB, respectively and the 10dB impedance bandwidths are 13 GHz, 35 GHz and 20 GHz, respectively. The potential reasons for small deviation in resonant peaks are:

- The resonance phenomena appear when the quality (Q) factor of the antenna is large enough. Moreover, the THz field does not propagate or reflect for a large distance along the antenna because of the significant losses associated with the antenna such as radiation loss and dielectric loss. Consequently, the Q-factor of the THz antenna is small (no standing wave) and therefore the resonance effect is not as effective as it is being observed in the microwave frequencies,

- Another reason is the slow decay time of the generated photocurrent and is approximately 0.5ps in case of GaAs photoconductive substrate which limits the generation of higher-frequency components of radiation, and
- Moreover, the absence of resonance peaks at the position of expected frequencies ought to be attributed to some other factors also, such as there is broadening of the resonance peak because of the large antenna width or damping of the switching response because of the dominance of the capacitance effect across the photoconductive gap at high frequency.

The performance of proposed antenna designs (Design-A, Design-B and Design-C) are also compared for Gain (dB) and Directivity (dBi), in the principal plane patterns. The simulated results are shown in Figure 2.7 and Figure 2.8, respectively.

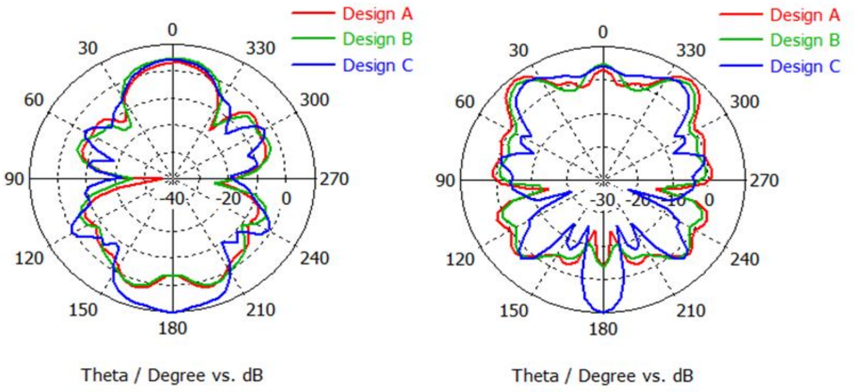

(a) (b)

**Figure 2.7: The antenna gain characteristics of all three configurations at 1.5 THz in (a) E-plane, (b) H-plane, Design-A: Basic THz photoconductive dipole antenna, Design-B: THz photoconductive dipole antenna with LT-GaAs superstrate, and Design-C: THz photoconductive dipole antenna with LT-GaAs superstrate and silicon lens.**

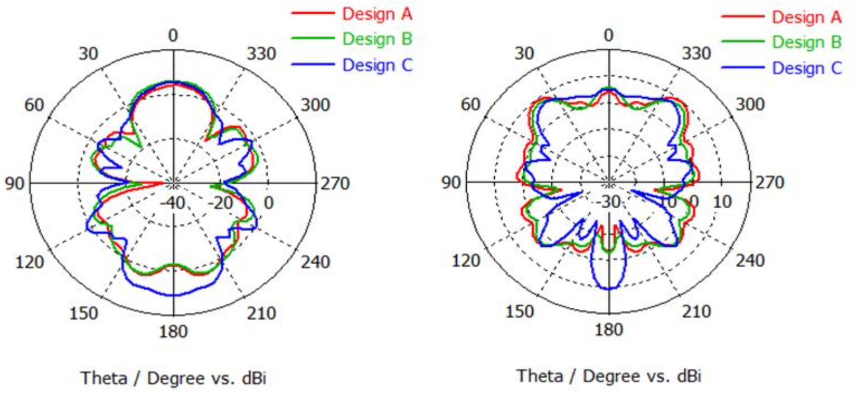

(a) (b)

**Figure 2.8: The antenna directivity of all three configurations at 1.5 THz in (a) E-plane, (b) H-plane, Design-A: Basic THz photoconductive dipole antenna, Design-B: THz photoconductive dipole antenna with LT-GaAs superstrate, and Design-C: THz photoconductive dipole antenna with LT-GaAs superstrate and silicon lens.**

For Design-A, the gain is 3.13 dB in E-plane with main lobe direction at $0^o$. The angular width (3-dB) is $34.2^o$ and the side lobe level is -0.8 dB and in H-plane, the gain is 8.71 dB with its main lobe direction is $40.0^o$. The angular width (3-dB) is $18.2^o$ having a side lobe level -5.6 dB. The directivity at E-plane is 4.11 dBi with main lobe direction at $0^o$. The angular width (3-dB) is $34.2^o$ and the side lobe level is -0.8 dB, and for H-plane, the directivity is 9.69 dBi with its main lobe direction $40^o$. The angular width (3-dB) is $18.2^o$ having a side lobe level -5.6 dB. The radiation efficiency obtained in E-plane and H-plane are 0.76 and 0.89 with power flow 5.12 × $10^{10}$ VA/$m^2$. As the radiation efficiency in E-plane is less than 80% and to increase the radiation efficiency of the THz photoconductive dipole antenna, a thin superstrate is used in this reference design. The simulated results for Design-B show the gain of 4.85 dB in E-plane with main lobe direction at $0^o$. The angular width (3-dB) is $39.6^o$ and the side lobe level is -3.0 dB. However, for H-plane, the gain is 7.3 dB with its main lobe direction $40^o$. The angular width (3-dB) is $18.5^o$ having a side lobe level -2.5 dB. The directivity in E-plane is 5.78 dBi with main lobe direction at $0^o$. The angular width (3-dB) is $39.6^o$ and the side lobe level is -3.0 dB and for H-plane, the directivity is 8.24 dBi with its main lobe direction $40^o$. The angular width (3-dB) is $18.5^o$ having a side lobe level -2.5 dB. The radiation efficiency obtained in E-plane and H-plane are 0.84 and 0.89 with power flow 6.24 × $10^{10}$ VA/$m^2$. It is clearly observed from the simulated results that the radiation efficiency has been increased in the E-plane from 76% to 84% along with the increase in the directivity from the 3.13 dBi to 5.78 dBi for the same direction of main-lobe i.e. $0^o$. Moreover, other interesting point which has been observed is that with the use of thin superstrate (LT-GaAs) along with the substrate (GaAs), the power flow has also been increased.

For the purpose of THz sensing applications there is a need of high-directional scanning photoconductive antennas with inexpensive steerable integrated lens. As the proposed photoconductive dipole antenna is a simple configuration, thus, it allows us to use the focusing property of the dielectric lens to excite the directed radiation. Therefore, to increase the directivity of THz photoconductive dipole antenna, we have used a silicon lens placed beneath the ground plane that is Design-C from where the THz radiations are generated. The simulation results for Design-C show the value of gain 9.8 dB in E-plane with main lobe direction at 180.0 degree. The angular width (3-dB) is $42.8^o$ and the side lobe level is -5.5 dB. For the H-plane, the gain remains same which is 9.8 dB with its main lobe direction same as in E- plane i.e. $180^o$. The angular width (3-dB) is $13.4^o$ having a side lobe level -3.5 dB. The directivity in the E- and H-planes is also having same values 10.7 dBi with main lobe direction at 180° for both cases. The angular width (3-dB) is 42.8° in the E-plane and the side lobe level is -5.5 dB. However, for H-plane, the directivity has the angular width (3-dB) as 13.4 degree having a side lobe level -3.5 dB. The radiation efficiency obtained in E-and H-planes are 91.59% with power flow $5.93 \times 10^{10}$ VA/$m^2$. It is clearly observed from the results that the radiation efficiency has been increased and is uniform in both the E-and H-planes. Therefore, the use of Silicon lens helps to achieve enhanced gain and directivity values with uniformity in both the principle planes. Moreover, according to the dipole approximation, the radiated electric field from a point source is proportional to the time derivative of the point current in the far-field. Using this relation, the electric field due to the distributed current is computed by taking the volume integration of time-derivative of the current density, $J(r', t')$ [128]. Therefore, the THz electric field emitted from the photoconductive dipole antenna is expressed in terms of the current density, $J(r', t')$ defined at a point r′ and time t′, is expressed as:

$$E_{THz}(r, t) = -\frac{1}{4\pi\varepsilon c^2} \int_0^{l_e} \left[\frac{\partial J(r', t')}{\partial t'}\right] \frac{\sin \Theta}{|r - r'|} d^3x' \tag{2.8}$$

where$E_{THz}$(r, t) is the THz electric field at the observation point r, and the observation time t. ε is the dielectric constant of the medium, and Θ represents the angle between the direction of current and the direction of observation.

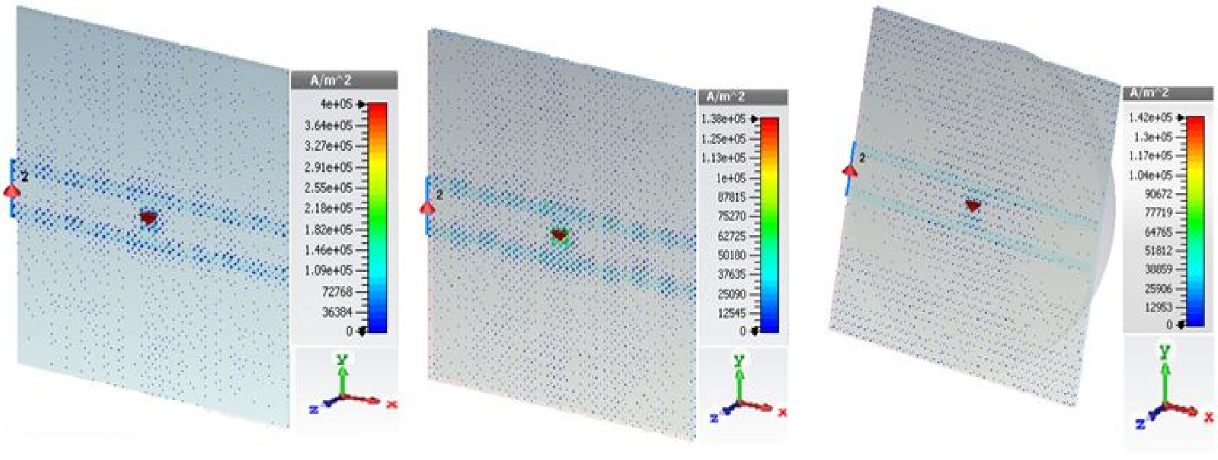

(i) Design A (ii) Design B (iii) Design C

**Figure 2.9: The current density distribution on the planar surface of three configurations at 1.5 THz presented using CST Microwave Studio, (i) Design-A: Basic THz photoconductive dipole antenna, (ii) Design-B: THz photoconductive dipole antenna with LT-GaAs superstrate, and (iii) Design-C: THz photoconductive dipole antenna with LT-GaAs superstrate and silicon lens.**

In photoconductive dipole antenna, when a biased field $E_{bias}$ is applied across the co-planar striplines then it acts as an initial driving force for the photo generated carriers to move towards the biased antenna electrodes. This results into the formation of time-varying photocurrent within the gap of the antenna and is given by:

$$J_{PC}(t) = \frac{\sigma(t)E_{bias}}{\left[\frac{\sigma(t)\,Z_0}{1+n}+1\right]} \tag{2.9}$$

where $\sigma(t)$is the conductivity of the photoconductive material, $Z_0$ represents characteristic impedance of the free-space and $n$ is the refractive index of the substrate. The numerator of (2.9) corresponds to the Ohm law and the denominator corresponds to the saturation effect which occurs due to the field screening by the charged carriers. Using simulation software, we have also illustrated the current density distribution of each of proposed antenna configurations (Design-A, Design-B and Design-C) as shown in Figure 2.9. In the Design-A, a very high current density $4 \times 10^5$ A/m is observed because the use of thick photoconductive substrate (GaAs) with thickness 10µm. For the Design-B and Design-C, the value of current density is $1.38 \times 10^5$ A/m and $1.42 \times 10^5$ A/m, respectively. The lower values of current density are due to the use of thin layer of superstrate LT-GaAs placed over the GaAs substrate. It is also observed from the Figure 2.9 that in the Design-C, the current density is more at the centre of the substrate near the photoconductive gap in comparison of the sides of substrate. This may be due to the use of Silicon lens which is making the THz field highly directive in both the principle planes patterns in the main lobe direction at $180^{o}$.

## 2.6 CONCLUSION

In this chapter, we have presented a simple synthesis technique to determine the physical parameters of photoconductive dipole antenna, which is used for THz sensing and imaging applications. For the Design-A, the choice of simple dipole antenna with small gap geometry has been proposed because of its simplicity in fabrication. However, the basic photoconductive dipole antenna illustrates low values of directivity and radiation efficiency. Therefore, by using thin superstrate (LT-GaAs) in the Design-B, the radiation efficiency increases in the E-plane from 76% to 84% along with the increase in directivity from 3.13 dBi to 5.78 dBi. Further, the proposed basic geometry of photoconductive dipole antenna with silicon lens is presented which enhances the antenna performance that is potentially useful for THz sensing and imaging application like the detection of hidden explosives (RDX, HMX, PETN, and TNT) along with some commonly used explosive related compounds. This proposed antenna (Design-C) shows significantly high directivity upto 10.7dBi and radiation efficiency of 91.59% in both E-plane and H-plane at 1.5 THz. A THz imaging system using THz photoconductive dipole antenna provides relatively good signal-to-noise ratio (SNR), large dynamic range with optimum bandwidth, however the optical-to-THz conversion efficiency of the system is very low. Therefore, it is necessary to analyse the practical constraints on choosing the antenna parameters using equivalent circuit approach which helps to improve the antenna total efficiency.

# CHAPTER 3

# ANALYTICAL FRAMEWORK OF SMALL-GAP PHOTOCONDUCTIVE DIPOLE ANTENNA USING EQUIVALENT CIRCUIT MODEL

## 3.1 INTRODUCTION

For the prospective demand to achieve large depth-of-field (DoF) so as to get a better image resolution in the THz imaging application there is a necessity to design a highly directive, compact, and planar THz antenna source with its capability of on-chip fabrication. The photoconductive dipole antenna has the significant use in THz imaging application because the antenna can be used at the emitter side as well as at the receiver side with same dimensions. However, the only difference is that at the receiver side no biased voltage is applied across the antenna electrodes. Further, the performance of the THz imaging system is mainly affected by photoconductive antenna as an emitter because the detected power level of the THz imaging system at the receiver side is mainly governed by the total radiated power of the emitter. Though, there are certain modalities for improving the photoconductive dipole antenna performance which are required to identify to achieve high THz average radiated power as well as improved total efficiency. Therefore, the unit-cell small-gap photoconductive dipole antenna radiation power enhancement techniques need to be optimized with respect to the antenna design parameters along with the selection of photoconductive material by means of theoretical simulation. Moreover, the potential improvement of coupling efficiency of THz wave with air in addition to femto-second laser incident efficiency are also important parameters to enhance the radiation power of small-gap photoconductive dipole antenna. Accordingly, it is crucial to have a detailed analytical analysis of the THz photoconductive dipole antenna as a radiating source.

When the semiconductor gap in the middle of the photoconductor contact electrodes is uniformly illuminated by the optical pump then the conjugate matching (for the maximum power transfer) of the photoconductor impedance to the antenna impedance maximizes the radiated power from the photoconductive dipole antenna [138]. However, concerning the extension of the gap size, the photoconductive antennas are classified as:

1) the narrow gap photoconductive antenna (also known as small-gap) in which the gap width is generally very much smaller than that of the radiation wavelength, (with gap-size order of $5\mu m - 50\mu m$) [159],

2) the large gap photoconductive antennas (also known as large aperture) in which the gap width is kept larger than that of the radiation wavelength, (with gap-size order of $0.5mm - 5mm$) [160], and
3) the semi-large photoconductive antennas in which the gap width lies in-between the two above mentioned types, (with gap-size order of $0.1mm - 2mm$) [161].

The large gap photoconductive antennas are popular configurations particularly as emitters since higher radiated powers can be attained. Moreover, in large gap photoconductive antennas the decrease in effective electric field across the antenna gap (phenomenon also known as screening effect) occurs at later in comparison to that of the small-gap antennas. Further, in large-aperture antennas with constant laser power the distance among the free carriers increases due to the large sized photoconductive area and as a result there is a significant decrease in the screening field. However, these large aperture antennas require a higher bias voltage which is generally in the kilovolt range [162]. On the other hand, the design of semi-large gap photoconductive dipole antenna helps to set down antenna electrodes of sufficient thickness which facilitates to accommodate the skin-depth and also reduce the heating effects. Conversely, the achievable bandwidth in case of semi-large gap photoconductive antenna is narrower than that of small-gap antennas. However, for the pulsed THz imaging system a broad frequency spectrum is desired for scanning purpose. Therefore, the small-gap photoconductive antenna has the superiority over the large-gap and semi-large gap photoconductive antenna in terms of radiation efficiency, broad bandwidth, and stability. Additionally, in small-gap photoconductive dipole antenna the geometry of the antenna electrodes have their significance on the spectral characteristics of the antenna [163]. Further, with the small-gap photoconductive dipole antenna the THz radiation over the broad frequency spectrum can be generated wherein the antenna electrode structure acts as a filter and establishes the radiated frequency spectrum. In photoconductive dipole antenna, the resonating frequency depends on the length of the electrodes $f_r = c/(2nL)$ where $c$, $n$, and $L$ are the speed of light in vacuum, refractive index of the material and total length of antenna electrodes, respectively. Moreover, in comparison with other types of THz emitting devices for example electro-optic (EO) crystals which needs the pump power of higher magnitude of 172.9mW, the photoconductive dipole antenna get triggered with the help of mode-locked Ti-sapphire laser providing 10mW average incident power on the photoconductive gap [164].

Furthermore, the technique of photo-detection using photoconductive antenna is comparatively stable against optical as well as thermal noise while the electro-optic (EO) sampling detection is especially sensitive to such noises. These noises occurs generally due to the fluctuation caused by the vibrations in the cavity length, shot noise on photon detection, and thermal-mechanical noise of the passive cavity components through the laser output on the EO crystal. Because of the increasing interest in THz systems in addition to the requirement for efficient imagers, interferometers, and broad bandwidth spectrometers for the imaging systems, various researchers are investigating the small size antenna concepts. In the small-gap photoconductive dipole antenna, the categorization of the multi-physical phenomenon which is taking place can be listed as:

1) light-matter interaction,
2) photo-excited carrier dynamics, and
3) full-wave propagation of the THz radiation.

To generate desired THz radiation from photoconductive dipole antenna, there is a requirement to have sufficient incoming laser power, a superior photoconductive material, an enough bias voltage along with a well designed antenna configuration. A biased voltage source in addition to the laser optical source drives the photoconductive gap acting as current source to produce THz radiations. However, the main issue with the photoconductive dipole antenna is the low THz output power as well as low antenna efficiency. To counter such issue, the optical illumination power and the applied bias voltage is increased in such a manner to yield higher output power. However, under such situations, the observable phenomenon such as saturation, field breakdown, velocity overshoot, and thermal breakdown happens within the system [165].

Moreover, in the material selection for photoconductive antenna there is a requirement of 1) maintenance of relatively high carrier mobility with suitable band gap, 2) control of zero bias photocurrent, 3) high breakdown voltage, and 4) low carrier lifetime with high resistivity. These parameters influence the performance of photoconductive antennas in terms of 1) output power, 2) bandwidth, 3) maximum optical pump power, and 4) signal-to-noise ratio (SNR), respectively [166]. For the pulse THz imaging application, to increase the SNR of spectroscopic system the THz radiation with high emission intensity is required which facilitates to perform fast scan of the object. The value of emission intensity of the THz radiation considerably increases with an enhancement in the dipole length [153]. Moreover, the emission efficiency of the THz radiation depends on the relative dimensions of the dipole. The efficiency increases appreciably by increasing the aspect ratio (the ratio of length and width of the antenna electrode, L/W). Similarly, another parameter which can be adjusted to reduce the screening effect and as a consequence to improve the radiation efficiency in small-gap photoconductive dipole antenna is through the excitation spot size which persuade the initial spatial distribution of the photo-excited carriers on the surface of the photoconductive substrate. On increasing bias voltage, higher THz output power can be achieved as under such situation the acceleration of the photo-excited carriers get increased. However, under such situation the breakdown voltage of device limits to give up maximum radiation power. To increase the level of breakdown voltage so that the antenna can withstand high biased voltages across the antenna electrodes, the properties of several photoconductive materials such as gallium arsenide (GaAs), low-temperature grown GaAs, alternating nanoscale multilayers of InGaAs, bulk indium gallium arsenide (InGaAs), indium aluminium arsenide (InAlAs), radiation damaged silicon on sapphire and amorphous silicon are investigated by numerous researchers for THz photoconductive antennas [167].

The small-gap photoconductive dipole antenna is simple in fabrication furthermore shows its potential use as THz source for pulsed broadband system of THz imaging application. However, there are certain prospective challenges to improve the conventional THz photoconductive dipole antenna as discussed above. Thus considering both the optical excitation effects as well as the antenna geometrical effects on the performance of a photoconductive antenna, a systematic analysis technique and a simulation procedure is necessary to design so as to have the better understanding of the phenomenon such as 1) static electric field creation, 2) photo-exited transient current generation in the near field, and 3) the THz radiation in both near and far field. Therefore, an analytical framework for modelling of pulsed THz small-gap photoconductive dipole antenna has been proposed to find out several factors contributing to the antenna performance parameters like THz average radiated power and the total efficiency. In this chapter, a systematic procedure employing precise mathematical expression leading to the physical behaviour of small-gap photoconductive dipole antenna is projected. Moreover, the effect of biased lines on the antenna performance parameters is also considered and is presented in the proposed equivalent circuit model. Further, the effect of gap-size of proposed photoconductive dipole antennas on the THz radiated power as well as on total radiation efficiency has been explored.

## 3.2 RELATED WORK AND PROBLEM FORMULATION

The main disparity in analyzing THz antennas in comparison to the microwave antennas is the optoelectronic characteristics that arise due the optical excitation and accordingly the response of the photoconductive material. Therefore, it demands the development of some novel simulation as well as an analysis procedure which incorporate the effects generated from both optical excitation and antenna geometry. In this respect, several researchers have explored different physical models so as to present the better understanding about the working of the photoconductive antenna. However, such physical models can be categorized under three different approaches as briefly mentioned below with each category having its own advantage as well as limitation.

- **Drude-Lorentz Model:** In this approach, the photo-excited carrier dynamics inside the semiconductor is described using Drude-Lorentz model [168]. It is a useful method to evaluate the dependence of THz radiation on the material's properties like doping density, carrier lifetime, carrier mobility, and laser source's intensity with its pulse width [169]. The use of this model can compute the photo-excited current inside the semiconductor in the near-field. However, the far-field radiation can only be realized in an approximate way. Therefore, one of the major limitations of this model is the different radiation properties such as radiated power, electric field strength, and efficiency of the antennas with various shapes cannot be distinguished. In addition, this model can hardly simulate the space-related phenomenon like the effect of asymmetrical illumination of the laser spot within the photoconductive gap.
- **Full-wave Finite-Difference Time-Domain (FDTD) Model:** The FDTD model couples the carrier's dynamics with the full-wave interaction along with propagation to simulate the phenomenon occurring in both near-field as well as far-field [170]. In this, the continuity equation is used to describe the carrier dynamics. Moreover, the drift-diffusion equation is used to depict the corresponding transient current wherein the photo-excited current is considered as the driving source of a photoconductive antenna [171]. However, the full-wave analysis is incapable to analyze the THz antenna with a large Silicon lens which is used to collimate the THz radiation in one particular direction. This is because the size of the lens is much larger than the wavelength [172]. Further, the analytical method such as diffraction theory also required to implement with FDTD for analyzing propagation behavior with large elements.
- **Equivalent Circuit Model (ECM):** In this approach, the photoconductive dipole antenna is considered as a special lumped element which comprises of a combination of voltage or current source with time-varying resistance and antenna impedance [173]. The laser induced resistance of the source is evaluated by means of carrier dynamics. This method is useful as it takes up the existing antenna theory for the analysis of photoconductive

antenna as well as all the antenna related aspects in its simulation. Moreover, with ECM it is simple to determine the impedance matching efficiency amid photo-excited source and radiating antenna [138]. Further, the ECM helps to study the antenna related properties to design photoconductive antenna with better performance. This approach provides a realistic description of the antenna by means of direct link among the parameters of the equivalent circuit model, the structure of the antenna, and the photoconductive material properties. In this respect, there are two types of equivalent circuit models which have been explored and discussed by the researchers in literature are as follows:

1) ECM obtained from electrical engineering perspective and based on large signal analysis: This method consider 1) the constant capacitance representing the gap-capacitance of the photoconductive antenna, 2) a time-dependent resistance of the photoconductive material, and 3) the antenna resistance [174]. In this model, the approach used is simple to implement because of the deployment of lumped element components. However, a major limitation of this model is to precisely envisage the local fields of photoconductive antenna.
2) ECM based on real physical performance of antenna using carrier dynamics: It is essential to consider the carrier dynamics in the generation of THz waves as it helps to find out the real physical behavior of the antenna. This method involves 1) the antenna resistance, 2) a time-varying field due to the space-charge screening effect, and 3) the time-varying source resistance [175]. The main benefit of this model in comparison to simplified lumped element model is improvement of the accuracy since more physical aspects are considered. However, there is a complexity in the derivation of equations. In addition, there are certain assumptions in its analysis which have been made and limit its applications. The photoconductive gap between the antenna electrodes is generally assumed to be fully and uniformly illuminated by the laser beam. Further, while calculating source resistance the exponential decay of the photocurrent caused due to the recombination of photo-excited carriers is ignored due to which the laser pulse information is lost. Moreover, it is also assumed that when there is no laser illumination (under the dark conditions), the photoconductive antenna is considered as a charged capacitor.

Several researchers have mentioned the use of these models in the literature for the photoconductive antennas [176, 177]. Such as in [178], the screening contribution because of the Coulomb and radiation screening effects of electromagnetic field in the photoconductive antenna is presented. The authors have used the Monte Carlo method to analyze the consequences of excitation spot-size as well as the excitation level onto the emitted THz radiations. Jepsen et al. [178] have anticipated a model based on the Drude-Lorentz theory of carrier transport to explain the details of the ultra-short carrier dynamics occurring in the small-gap photoconductive antenna. However, the authors have considered only the effect of space charge screening for carrier dynamics. Due to the statistical approach which has been used, the results obtained require high computational effort. Similarly, the use of semi-classical Monte Carlo model is presented in [179] to explain fast carrier dynamics occurring in the photoconductive antenna due to photo-excitation. In [180], the authors have shown the theoretical model based on Bloch-Floquet theorem using Maxwell’s equations to analyse the periodic dielectric structures along with the periodic low-temperature-grown GaAs strips within the gap between the antenna electrodes. They have proposed this model to increase the THz radiation power of photoconductive antenna. Khiabani et al. [181] have presented a theoretical modelling for the time variant conductance. In equivalent circuit model, they have used the lumped element approach to retain the simplicity of the model. However, the accuracy has been achieved in [181] by considering each lumped element component value based on complex physical mechanism. The only limitation of this model is that the non-uniformity of the applied bias field as well as the illuminated region has been ignored. In [182], saturation behaviour of the DC photocurrent in addition to velocity overshoot phenomenon has been observed. The authors discussed the hot-carriers effect using energy balance transport model. A characteristic equivalent electrical circuit of the plasma medium for photoconductive dipole antenna is shown in [183]. It includes a combination of circuits under dark as well as illuminated conditions of photoconductive gap with an assumption of no antenna losses (radiation efficiency of antenna equal to one).

However, the realization of plasma medium for small-gap photoconductive antenna is difficult in real-time application scenario. Therefore in our proposed antenna the LT-GaAs photoconductive superstrate of 1µm thickness is used which has high mobility and high breakdown field. Moreover, at THz range of electromagnetic spectrum, the ohmic losses increase therefore the antenna losses need to be considered. Further, in the basic geometry of small-gap photoconductive dipole antenna there is fixed bias line connecting the biased voltage source and the antenna electrodes. The length of these biased lines is generally half of the wavelength of operating frequency of the antenna. Therefore such biased line contributes to the emergence of constant physical parameters in the form of distributed elements on the line and need to be considered in the equivalent circuit model of small-gap photoconductive dipole antenna to achieve high matching efficiency. Moreover, at half of the wavelength of the biased lines, the phase delay as well as the interference of any reflections on the line becomes significant which can bring about unpredictable behaviour in the performance of the system. Further, the biased lines are also significant for their use to further extend beyond the antenna electrodes to facilitate the provision of antenna array implementation [106].

## 3.3 CIRCUIT MODELING USING NUMERICAL EQUATIONS

The working principle of a THz small-gap photoconductive antenna is generally based on 1) the laser excitation, 2) the antenna structure over photoconductive material, and 3) a fixed bias voltage. Initially, when the antenna electrodes are externally biased using the biased lines then a static field gets built up inside the bulk semiconductor. The electrons and holes start flowing in a certain direction under the influence of a fixed DC bias voltage which results into the formation of the current. The generation of electron-hole pairs occurs when the input energy inside the photoconductive substrate becomes larger than that of its bandgap energy. Moreover, this input energy varies rapidly on applying a short period optical pulse on the photoconductive gap. It results into the variation of the carrier density across the photoconductive gap and due to different current intensity there is emergence of the time-varying electric field which leads to the generation of electromagnetic waves [184]. The DC field presents an initial force to drive the photo-excited carriers towards the antenna electrodes. However, the carrier dynamics which develops initially is evaluated using the Poisson's Equation as:

$$\nabla^2 V = \frac{q}{\varepsilon}\,(n - p - N_D + N_A)$$

where $V$, $q$, $\varepsilon, n$, $p, N_D$, and $N_A$ are voltage distribution, electric charge, permittivity of semiconductor, density of electrons, density of holes, impurity concentration due to donor ions and impurity concentration due to acceptor ions, respectively. With the photo-illumination of small-gap photoconductive dipole antenna there is a generation of the time-dependent carrier density $n(t)$ which is determined using the Equation of continuity as:

$$\frac{d\,n(t)}{dt} = \frac{\eta_l\,\alpha}{hf_l w_G\,w_e}\,P_{av} - \frac{n(t)}{\tau_c}$$

where $\eta_l$, $f_l$, $h$, $\alpha$, ($w_G \times w_e$), $P_{av}$, and $\tau_c$ are the photoconductor external quantum efficiency, laser frequency, Planck's constant, optical absorption coefficient, effective optically illuminated area with $w_G$ width of the gap between the electrodes and $w_e$ is the width of the photoconductor contact electrodes, average optical power, and carrier lifetime, respectively. The above Equation can further be simplified and can be expressed in terms of laser beam intensity $I_l\,(r, t)$ which depends on the radial distance from the centre axis of the beam, $r$ and time instant, $t$ as:

$$\frac{d\,n(t)}{dt} = -\frac{n(t)}{\tau_c} + \frac{\alpha}{hf_l} I_l\,(r, t) \tag{3.1}$$

where $I_l\,(r, t) = \frac{\eta_l}{w_g\, w_e}\, P_{av}$. The general expression of the laser intensity having electric field distribution of Gaussian laser pulses along the axis of propagation is:

$$I_l\,(r, t) = I_l(1 - R)e^{\left(\frac{-2r^2}{w_0^2}\right)} e^{\left(\frac{-2t^2}{\tau_l^2}\right)} \tag{3.2}$$

where $I_l$, $R$, $\mathrm{w}_0$, and $\tau_l$ are the peak laser intensity, power reflection coefficient, optical beam waist radius at which the field amplitude and intensity drop to (1/e ) of the axial value, and laser pulse duration, respectively. Moreover, it is implicit that at $z = 0$, the beam waist of laser pulse is onto the photoconductive gap (G) of the THz antenna. On putting the value of $I_l\,(r, t)$ from (3.2) in (3.1), an expression for time-dependent carrier density $n(t)$ becomes:

$$\frac{d\,n(t)}{dt} = -\frac{n(t)}{\tau_c} + \frac{\alpha}{hf_l}\left(I_l(1 - R)e^{\left(\frac{-2r^2}{w_0^2}\right)} e^{\left(\frac{-2t^2}{\tau_l^2}\right)}\right)$$

This differential Equation for $n(t)$ is solved using the following integral identity.

$\int_{-\infty}^{a} e^{-u^2/T^2}\, du = \frac{\sqrt{\pi}}{2} T\,(1 + \mathrm{erf}(a))$ and $\mathrm{erf}(x) = \frac{2}{\sqrt{\pi}} \int_0^x e^{-t^2}\, dt$

Hence, the final expression for the time-dependent carrier density for $r = w_0$ is:

$$n(\mathrm{t}) = \left[\sqrt{2\pi}\ \tau_l\, \alpha I_l / 4\mathrm{h} f_l\right] (1 - \mathrm{R})\, \mathrm{e}^{(-2)} \mathrm{e}^{\left[(\tau_l^2/8\tau_c^2) - (\mathrm{t}/\tau_c)\right]} \left\{erf\left[\left(\sqrt{2}\, t/\tau_l\right) - \left(\sqrt{2}\, \tau_l/4\, \tau_c\right)\right] + 1\right\} \tag{3.3}$$

The separation of electron-hole pairs as well as their accumulation near the antenna electrodes contribute in the generation of THz radiation. The residual space-charge pairs lying in the vicinity of the metal contacts which are not capable to find the opposite sign pair for the recombination, remain as such near the dipole antenna electrodes. This results into the formation of time-dependent capacitance $C(t)$ and gets influenced by the generated carrier density $n(t)$ in addition to the recombination time of photoconductive semiconductor material.

$$\mathrm{C(t)} = (\tau_r/\mathrm{Z_a})\left[1 + \left(\mathrm{e}\, \mu_e \mathrm{Z_a S\, n(t)}\right)/\mathrm{G}\right] \tag{3.4}$$

where $\tau_r$, $Z_a$, e, and $\mu_e$ are the recombination lifetime, antenna impedance, electron charge and electron mobility in thin-layer photoconductive LT-GaAs superstrate, respectively. This time-varying capacitance $C(t)$ and time-dependent voltage controlled source $\beta(t)V_C(t)$ which is controlled by the voltage across capacitance $V_C(t)$ considers the screening effect across the photoconductive gap of dipole antenna. However, it is essential to consider this parameter in the equivalent circuit model as the screening effect limits the radiated THz power from the photoconductive antenna. An expression of $\beta(t)$ (described as the reverse voltage coefficient concerning the external bias voltage on the carrier density as well as the recombination lifetime) is expressed as:

$$\beta(t) = \left(e\,\mu_e n(t)\tau_r/\epsilon\xi\right) \tag{3.5}$$

where $\epsilon$ and $\xi$ are the permittivity of LT-GaAs superstrate and geometrical factor of the substrate which signify the screening effect, respectively. Moreover, the expressions for time-varying capacitance, $C(t)$ and reverse voltage coefficient, $\beta(t)$ are computed by: 1) comparing the first order differential equation of voltage across the antenna gap $V_C(t)$ as presented in [114] using the circuit analysis, and 2) the expression of electric field in the photoconductive gap considering the screening effect formulated in [185]. In the photoconductive antenna, the input signal for the antenna is generated with the illumination of femtosecond laser pulses and its interaction with the photoconductive material. Therefore, the photoconductive gap act as a current source for the antenna with its resistance operate as the source resistance $R_S\,(t)$ of the antenna. The time-dependent source conductance $G_S(t)$ can be determined using the expression for time-dependent source resistance of the active volume as mentioned.

$$R_S\,(t) = G_S(t)^{-1} = \rho(t)\frac{G}{S} = \frac{G}{\sigma(t)\,S}$$

where $G$, $\sigma(t)$, and $S$ are the gap length between the antenna electrodes, time-dependent bulk conductivity of photoconductive substrate material and cross-sectional area of the active volume that is normal to the DC bias electric field, respectively. In view of the laser penetration depth into the photoconductive material, the time-dependent conductance $G_S(t)$ of the active volume is expressed as:

$$G_S(t) = \int_0^{T_{LT-GaAs}} \frac{\sigma(t)\,e^{-\alpha z} W\,dz}{G}$$

where W and $T_{LT-GaAs}$ are the width of dipole antenna electrodes and laser skin depth at the excitation region, respectively. When the integral for $G_S(t)$ is further solved, then the time-dependent conductance of the active volume becomes:

$$G_S(t) = \frac{W}{\alpha G}\, \sigma(t)\left[1 - e^{(-\alpha\, T_{LT-GaAs})}\right]$$

However, the time-dependent bulk conductivity $\sigma(t)$ of photoconductive substrate material is expressed in terms of carrier density $n(t)$ across the active volume as $\sigma(t) = e\, \mu_e n(t)$. On considering the expression of $\sigma(t)$ and $n(t)$, the expression for the source conductance becomes:

$$\mathrm{G_S(t)} = \left(\frac{\mathrm{W}}{\mathrm{G}}\right) \left[1 - e^{(-\alpha\, T_{LT-GaAs})}\right] \mathrm{e}\, \mu_{\mathrm{e}}\ (1 - \mathrm{R})\, \mathrm{e}^{(-2)} \mathrm{e}^{[(\tau_l^2/8\tau_c^2) - (t/\tau_c)]} \left\{erf\left[\left(\sqrt{2}\, t/\tau_l\right) - \left(\sqrt{2}\, \tau_l/4\, \tau_c\right)\right] + 1\right\} \tag{3.6}$$

It is significant to identify the exact source conductance $\mathrm{G_S(t)}$ at the photoconductive gap because it provides a time-varying THz photo-current to the antenna electrodes. Moreover, the time-dependent voltage across the capacitance of the antenna electrodes also depends on the source conductance and is determined from the equation as shown in (3.7).

$$\frac{dV_C\,(t)}{dt} + \left[\left(\frac{1+\beta(t)}{\mathrm{Z_a} \times \mathrm{C(t)}}\right) + \frac{\mathrm{G_S(t)}}{\mathrm{C(t)}} + \frac{1}{\mathrm{C(t)}}\frac{dC(t)}{dt}\right] V_C\,(t) = \frac{E_{bias}}{\mathrm{Z_a} \times \mathrm{C(t)}} \tag{3.7}$$

where $E_{bias}$ is the constant biased voltage applied across the biased lines of photoconductive dipole antenna. The value of $V_C\,(t)$ is computed from (3.7) which is a first order differential equation and is solved for $V_C\,(t)$ using Runge-Kutta numerical analysis method. To perform a consistency and stability analysis to the ordinary differential equations, the fourth-order Runge-Kutta method is most commonly used method. However, one of the benefit of this method is that the operational analysis is identical for both types of differential equation either linear or non-linear. Moreover, the THz photocurrent which is induced at the photoconductive gap (G) is calculated using (3.8) where in the rise time of photocurrent is resolute by laser pulse duration and its decay time is influenced by the carrier lifetime of the photoconductive semiconductor material.

$$i_{PC}(t) = e\mu_e n(t) V_C(t) \frac{S}{G} \tag{3.8}$$

Besides these time-dependent lumped elements which are playing a considerable role in the antenna performance, the importance of biased lines which provides the initial biased potential from the fixed biased voltage ($E_{bias}$) cannot be ignored. Therefore, considering the equivalent circuit model based on the detailed numerical analysis [181], the contribution of constant valued half-wavelength biased lines parameters in the equivalent circuit model of small-gap photoconductive dipole antenna has been proposed. By considering the biased line distributed parameters along the length of line helps to improve the impedance matching efficiency of photoconductive dipole antenna. Moreover, the extension of these biased lines beyond the antenna electrodes also facilitates the implementation of linear array of photoconductive dipole antennas with half-wavelength spacing between the antenna elements on the common biased lines.

For THz imaging applications, there is a prospective demand of highly directive THz source so as to attain high depth-of-field to image the object under detection in addition to the high spatial resolution of imaging system. This can be realized by arranging the array configuration of photoconductive dipole antenna since a unit-cell photoconductive dipole antenna has a low directivity (5-7 dBi). However, for the array implementation of small-gap photoconductive dipole antenna, there is a necessity to optimize the unit-cell of small-gap photoconductive dipole antenna while realizing the physical phenomenon using an appropriate equivalent circuit model occurring across it. In Figure 3.1, a proposed unit-cell small-gap photoconductive dipole antenna is shown with its equivalent circuit. The physical parameters of the antenna configuration shown in Figure 3.1(a) are: 1) W is the width of antenna electrode, 2) G is photoconductive gap size, 3) L1 is width of the biased line, 4) L2 is length of antenna electrodes, 5) L is the separation between the biased lines, and 6) $l_e$ is effective length of dipole antenna. In fabrication of photoconductive dipole antenna using biased lines, it is customary and convenient to describe the fixed length biased lines in terms of its line parameters such as its 1) resistance per unit length $R$, 2) inductance per unit length $L_{ext}$, 3) conductance per unit length $G_{con}$, and 4) capacitance per unit length $C$. For each one biased line, the conductors are characterized by $\sigma_c$, $\mu_c$ and $\varepsilon_c = \varepsilon_0$ and the homogeneous dielectric separating the conductors is characterized by $\sigma$, $\mu$, and $\varepsilon$, where these are the conductivity, permeability and permittivity of the material, respectively. Moreover, to determine the values of the distributed parameters of half-wavelength biased lines, the following expressions are utilized.

$C = \varepsilon' \frac{L_2}{L} = \varepsilon_r \varepsilon_0 \frac{L_2}{L}$ ; $G_{con} = \sigma \frac{L_2}{L}$ ; $L_{ext} = \mu \frac{L}{L_2} = \mu_r \mu_0 \frac{L}{L_2}$; and $R = \frac{2}{\sigma_c \, \delta L_2}$, where $\delta = \frac{1}{\sqrt{\pi \, f \, \mu \, \sigma_c}}$ and $f$ is the skin depth and operating frequency of the antenna, respectively. The resultant equivalent circuit is designed and simulated in ORCAD PSPICE software and is illustrated in Figure 3.1(b).

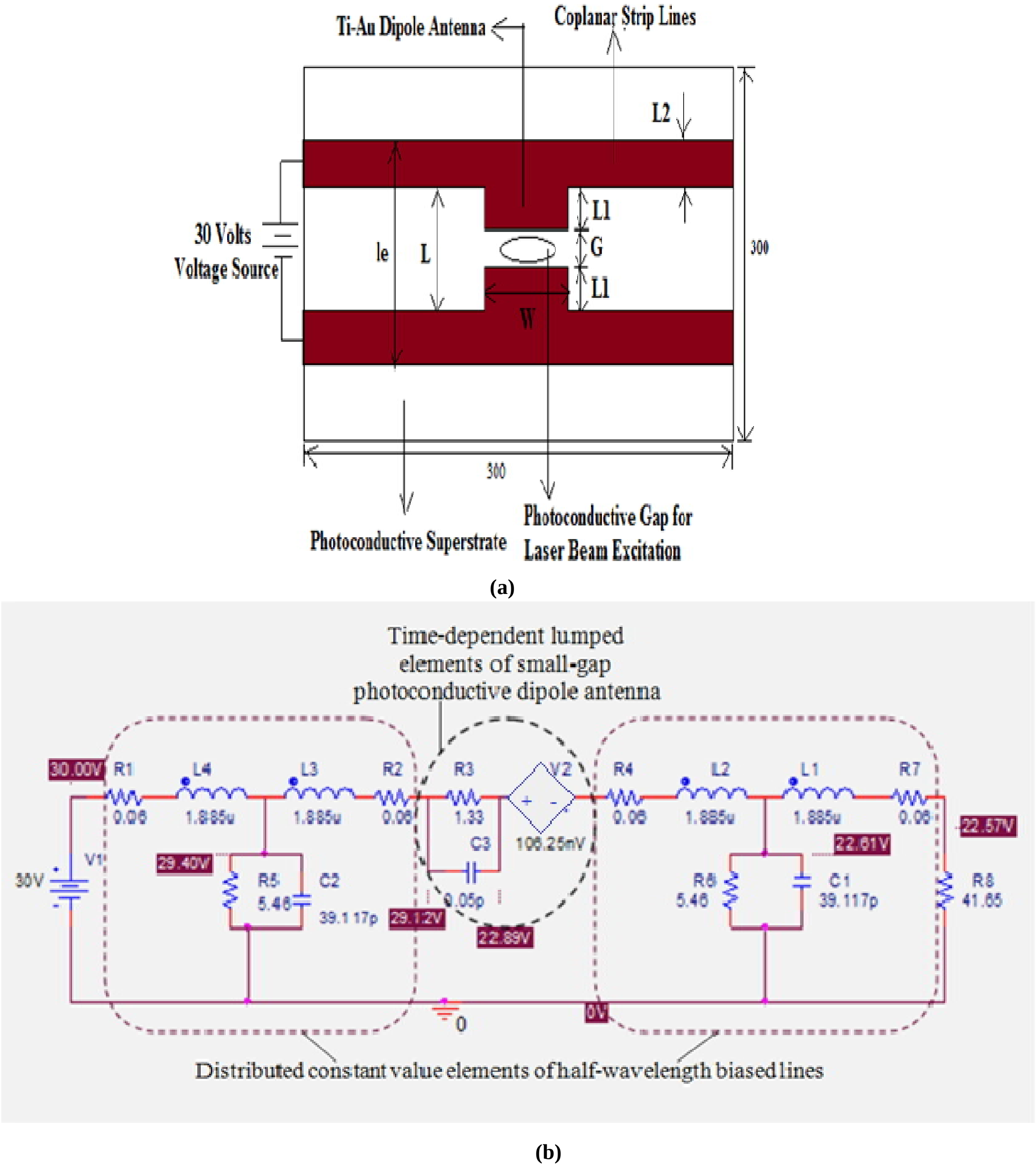

**Figure 3.1: The small-gap photoconductive dipole antenna (a) basic structure [115] and (b) the equivalent circuit model with half-wavelength biased line designed in ORCAD PSPICE software where $R3$, $C3$, and $V2$ are the source resistance determined from the time-dependent source conductance $G_S(t)$, time-dependent capacitance $C(t)$, and product of reverse voltage coefficient $\beta(t)$ and the voltage across the antenna gap $V_C(t)$,respectively. To determine the maximum power radiated from an antenna, the peak values of the time-dependent lumped elements of the small-gap photoconductive dipole antenna are taken [186].**

The radiated voltage across the antenna impedance R7 (taken as $Z_a = 41.65\,\Omega$, and the value is obtained from the simulation run of the antenna geometry in CST Microwave Studio) is attained through the PSPICE software. The voltage values at each node are also shown in

Figure 3.1(b). However, for the circuit analysis the peak conductance value in the photoconductive gap is considered for the reason that it corresponds to the maximum power generation in the antenna gap for maximum transformation of optical power to THz power. Mathematically, the time-dependent radiated voltage $V_{rad\,(t)}$ can be determined from (3.9) and the value depends on 1) antenna impedance, 2) carrier density, and 3) voltage across time-dependent capacitor developed across the antenna electrodes.

$$V_{rad\,(t)} = z_a e \mu_e n(t) V_c(t) \frac{S}{G} \tag{3.9}$$

Therefore, by selecting an appropriate material and using the above discussed structural framework based on the mathematical expressions to design THz small-gap photoconductive dipole antenna results into maximun radiated power from the antenna. Moreover, this analysis also helps to tune the THz imaging system with significantly improved effeciency.

## 3.4 RADIATED POWER AND TOTAL EFFECIENCY ANALYSIS OF SMALL-GAP PHOTOCONDUCTIVE DIPOLE ANTENNA

The THz photoconductive dipole antenna efficiency is defined as the ratio of radiated THz power to the laser power illuminated onto the photoconductive gap of antenna. In general, such efficiency is also identified as optical-to-THz power conversion efficiency. One of the major constraints of photoconductive antenna is the low efficiency of the antenna which obstructs its deployment in commercial applications of THz imaging system. Therefore, in this section the parameters which influence the antenna efficiency are determined. From (3.10) and (3.11), it is observed that the antenna radiated power $P_{THz}(t)$ and the total efficiency of antenna $\eta_t$ shows their dependence on the radiated voltage $V_{rad\,(t)}$ and optical laser source parameters.

$$P_{THz}(t) = \frac{{V_{rad\,(t)}}^2}{Z_a} \tag{3.10}$$

and

$$\eta_t = \frac{P_{THz}(t)_{Peak} \times \tau_l \times f_{rep}}{P_{av}} \tag{3.11}$$

where $P_{THz}(t)_{Peak}$ and $f_{rep}$ are the peak THz radiated power and repetition frequency of laser pulse, respectively. The Algorithm 1 describes the procedure to compute the radiated power and total efficiency for different values of average optical power of laser pulse across the gap of photoconductive dipole antenna. Moreover, the total antenna efficiency $\eta_t$ of the THz photoconductive antenna is determined from the multiplication of three different efficiencies: 1) the optical-to-electrical conversion efficiency ($\eta_{LE}$), 2) the impedance matching efficiency ($\eta_m$), and 3) the radiation efficiency ( $\eta_r$).

**Algorithm 1: Computation of time-varying components of equivalent circuit of photoconductive dipole antenna**

```
Input ($\varepsilon, \varepsilon_0, \mu_0, \sigma_c, h, c, e, \mu_{e,}\tau_l, f_l, f_{rep}, \alpha, R, w_0, \tau_c, \tau_r, \xi, E_{bias,}W, G, S, T_{LT-GaAs}, Z_a, n, A(t), P_{av}, t, D$)
Output (I(t), n(t), $G_S(t)$, C(t), $\beta(t), V_C(t), V_{rad}(t)$, $P_{opt-peak}$, $\eta_t$ )
BEGIN
{
Step 1: Variable declaration
$\varepsilon$ = permittivity of thin − layer superstrate;
$\varepsilon_0$ = permittivity of free space;
$\mu_0$ = permeability of free space;
$\sigma_c$ = conductivity of metal;
$h$ = Planck's constant;
c = speed of light in free space;
$e$ = electron charge;
$\mu_e$ = electron mobility in thin − layer superstrate;
$\tau_l$ = laser pulse duration;
$f_l$ = light frequency;
$f_{rep}$ = optical pulse repetition frequency;
$\alpha$ = optical absorption coefficient;
$R$ = power reflection coefficient;
$w_0$ = beam waist;
$\tau_c$ = carrier lifetime;
$\tau_r$ = recombination lifetime;
$\xi$ = geometrical factor of the substrate which denotes the screening factor;
$E_{bias}$ = biased voltage;
$W$ = width of antenna electrodes;
$G$ = photoconductive gap;
$S$ = photoconductive gap area;
$T_{LT-GaAs}$ = laser skin depth at the excitation region;
$Z_a$ = antenna impedance;
$n$ = refractive index of air;
$A(t)$ = temporal amplitude of Gaussian pulse laser;
$P_{av}$ = average optical power;
I(t) = temporal intensity function;
n(t) = time-varying carrier density;
$G_S(t)$ = time − varying source conductance;
C(t) = time-varying capacitance;
$\beta(t)$ = reverse voltage coefficient;
$V_C(t)$ = voltage at the antenna gap;
$V_{rad}(t)$ = voltage across the antenna gap or votage across the time − varying capacitor;
$P_{opt-peak}$ = peak laser poer;
$\eta_t$ = optical − to − THz conversion effeciency;
t = varying time;
D = diameter of the laser beam falling on the lens;
```

**Step 2: Computation of I(t) and then n(t)**

$$\mathrm{I(t)} = (\boldsymbol{\varepsilon_0} \times \boldsymbol{c/2})\left[\boldsymbol{e}^{(-2\,log_e 2\,(t/\tau_l)^2)}\right]^2$$

Peak of I(t) = $I_l$;

Compute the expression of n(t) in terms of t, by considering the peak value of I(t) for fixed value of $P_{av}$

$$\mathrm{n(t)} = \mathrm{I_l(1-R)exp}\,(-2\mathrm{r_0/w_0})\left[\sqrt{2\pi}\;\tau_l\;\alpha/4\mathrm{hf_l}\right]\mathrm{exp}[(\tau_l^2/8\tau_c^2) - (t/\tau_c)]\{erf\,[(\sqrt{2}\,t/\tau_l) - (\sqrt{2}\,\tau_l/4\,\tau_c)] + 1\}$$

**Step 3: Computation of C(t) and $\boldsymbol{\beta(t)}$**

Using the expression of n(t), C(t) and $\beta(t)$ are determined using the following expressions,

$$\mathrm{C(t)} = (\tau_r/\mathrm{Z_a})\left[1 + \left(\mathrm{e}\,\mu_e \mathrm{Z_a S\,n(t)}\right)/\mathrm{G}\right]\text{, and}$$

$$\beta(\mathrm{t}) = \left(\mathrm{e}\,\mu_e \mathrm{n(t)}\tau_r/\epsilon\xi\right)$$

**Step 4: Calculation of source conductance $\boldsymbol{G_S(t)}$**

$$\mathrm{G_S(t)} = \mathrm{(W/G)I_l e}\,\mu_e(1 - \mathrm{R})\mathrm{exp}\,(-2\mathrm{r_0}/\mathrm{w_0})\left[\sqrt{2\pi}\;\tau_l\;/4\mathrm{hf_l}\right][1-\mathrm{exp}(-\alpha \mathrm{T_{LT-GaAs}})]\mathrm{exp}[(\tau_l^2/8\tau_c^2) - (t/\tau_c)]\{erf\,[(\sqrt{2}\,t/\tau_l) - (\sqrt{2}\,\tau_l/4\,\tau_c)] + 1\}$$

**Step 5: Computation of voltage across the antenna gap or voltage across capacitor $\boldsymbol{V_c(t)}$**

Using Runga-kutta numerical analysis method for fourth order, the first order differential equation of $V_c(t)$ is computed to determine the value of $V_c(t)$.

$$\frac{dV_C\,(t)}{dt} + \left\{\left(\frac{1+\beta(t)}{\mathrm{Z_a}\times \mathrm{C(t)}}\right) + \frac{\mathrm{G_S(t)}}{\mathrm{C(t)}} + \frac{1}{\mathrm{C(t)}}\frac{dC(t)}{dt}\right\}V_C\,(t) = \frac{E_{bias}}{\mathrm{Z_a}\times \mathrm{C(t)}}$$

**Step 6: $\boldsymbol{V_{rad}(t)}$ *calculations for time varying expressions of* n(t) *and* $\boldsymbol{V_c(t)}$**

$$\mathrm{V_{rad\,(t)}} = \mathrm{z_a e\mu_e n(t)V_c(t)S/G}$$

**Step 7: Computation of radiated power $\boldsymbol{P_{THz}(t)}$**

$$\mathrm{P_{THz}} = \mathrm{V_{rad}^2(t)/Z_a}$$

**Step 8: For different values of average optical power compute peak laser power**

For defined optically illuminated area, Area= $\pi r^2$,

Where r = $\frac{4}{2\pi} \times$ (laser wavelength) $\times \left(\frac{\text{lens focal length}}{\text{D}}\right)$

$$P_{av} = I(t) \times Area$$

$$P_{opt-peak} = \frac{P_{av}}{f_{rep} \times \tau_l}$$

**Step 9: Computation of optical-to-THz conversion efficiency, $\eta_t$**

$$\eta_t = \frac{\mathrm{P_{THz}}}{P_{opt-peak}}$$

}

**END**

---

The laser-to-electrical power conversion efficiency [129] is determined as:

$$\eta_{LE} = \frac{P_E}{P_L} \approx \frac{eE_{bias}{}^2\mu_e\tau^2\eta_l f_{rep}}{hf_l G^2} \tag{3.12}$$

where $\tau$ is the photocurrent decay time and from (3.12) it is apparent that besides the laser source $(\tau, \eta_l, f_{rep}, f_l)$ this efficiency factor has also included another source which is the bias voltage $(E_{bias})$. Therefore, the electric power to the photoconductive dipole antenna is not exclusively provided by the laser source. However, the illumination efficiency $\eta_l$ takes into account the reflection of laser on surface of substrate and the quantum efficiency. When the laser beam is focused onto the feeding gap (photoconductive gap) with the photon energy of laser equal to or slightly greater than that of the band gap of the semiconductor substrate then the free-electrons are efficiently created. This electro–optical operation converts the laser power $P_L$ to the electrical power $P_E$. Next, the impedance matching efficiency $\eta_m$ is determined from the antenna impedance $Z_a$ and the source impedance $Z_s$ using the expression as shown in (3.13).

$$\eta_m = 1 - \left(\frac{Z_a - Z_s}{Z_a + Z_s}\right)^2 \tag{3.13}$$

The source impedance is realized using the equivalent circuit as shown in Figure 3.1(b), wherein the computation of constant valued biased line components is performed by considering the Algorithm 2. The radiation efficiency $\eta_r$ of photoconductive dipole antenna is defined as the ratio of gain and directivity of antenna at the frequency of operation which is obtained using an electromagnetic simulation tool CST Microwave Studio. The low radiation efficiency is the key challenge to the present photoconductive dipole antenna. It happens because of the occurrence of the excessive Ohmic losses at THz frequencies. On the other hand, the impedance matching efficiency of antenna must be taken in account for proper impedance matching of laser source with photoconductive material of antenna.

**Algorithm 2: Computation of constant valued biased line parameters of equivalent circuit of photoconductive dipole antenna**

---

```
Input ($\varepsilon_r, \varepsilon_0, \mu_0, \mu_r, \sigma_c, \sigma, f, \delta, L_2, L$)
Output (C, G, $L_{ext}, R$)
BEGIN
{
Step 1: Variable declaration
$\varepsilon_r$ = relative permittivity of photoconductive substrate
$\varepsilon_0$ = permittivity of free space
$\mu_0$ = permeability of free space
$\mu_r$ = relative permeability
$\sigma_c$ = conductivity of antenna
$\sigma$ = conductivity of photoconductive material
$f$ = operating frequency of antenna
$\delta$ = skin depth or depth of penetration
$L_2$ = width of biased line
$L$ = separation between biase lines
$C$ = line capacitance
$G_{con}$ = line conductance
$L_{ext}$ = line inductance
$R$ = line resistance
```

```
Step 2: Computation of C
$C = \varepsilon_r \varepsilon_0 \frac{L_2}{L}$
Step 3: Computation of $G_{con}$
$G_{con} = \sigma \frac{L_2}{L}$
Step 4: Computation of $L_{ext}$
$L_{ext} = \mu_r \mu_0 \frac{L}{L_2};$
Step 5: Computation of R
For $\delta = \frac{1}{\sqrt{\pi f \mu \sigma_c}};$
$R = \frac{2}{\sigma_c \delta L_2}$
}
END
```

## 3.5 SIMULATION RESULTS AND DISCUSSIONS

In the equivalent circuit model, the photoconductive gap source components are having time-dependent features. Therefore, by considering the parameters for (3.3) and (3.4) from Table 3.1, the numerically computed dynamics of $n(t)$ and $C(t)$ are shown in Figure 3.2(a) and Figure 3.2(b), respectively. The capacitance between the antenna electrodes which has the time-dependent behaviour depends on the recombination lifetime of the carriers and the carrier density of the generated carriers. Therefore, the nature of two graphs is analogous and is illustrated in Figure 3.2.

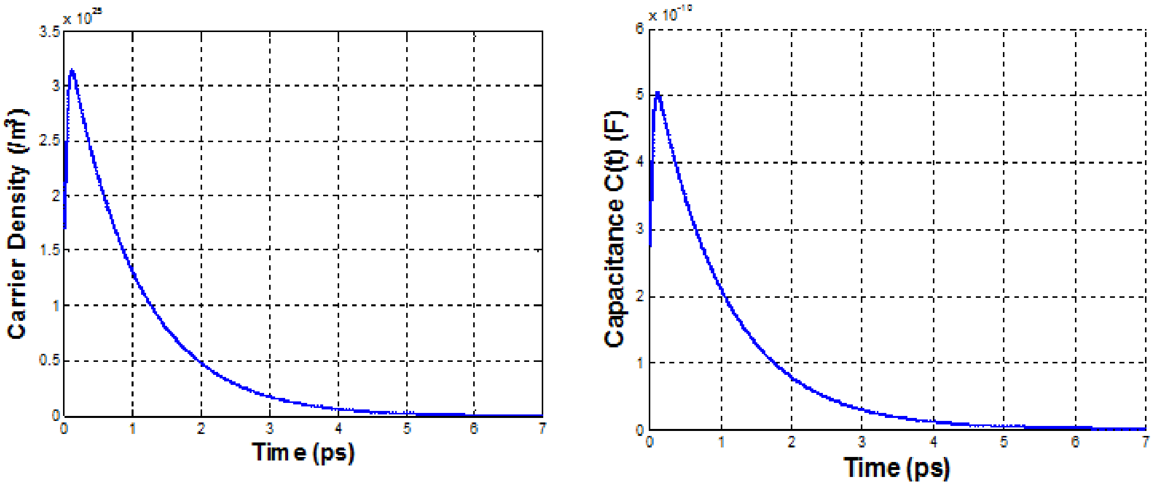

(a) (b)

**Figure 3.2: The response of time (ps) of optical illumination on photoconductive gap with single pulse of femto-second laser beam over the photoconductive dipole antenna on the (a) carrier density and (b) capacitance across the antenna electrodes.**

Moreover, the influence of antenna gap size on the capacitance is investigated with fixed value of average optical power $P_{av} = 1W$. Figure 3.3 demonstrates that for small gap size the capacitance is very large since it is inversely proportional to the gap size as shown in (3.4).

On the other hand, it also means that the opposing effect of the field screening is smaller in large gap antennas.

**Table 3.1: Physical parameters used in the proposed photoconductive dipole antenna simulation.**

| Parameter | Value |
|---|---|
| Light frequency $f_l$, (THz) | 375 |
| Laser pulse duration $\tau_l$, (fs) | 100 |
| Power Reflection coefficient, R | 0.318 |
| Optical absorption coefficient, $\alpha$ (/m) | $6\times 10^6$ |
| Electron mobility in LT-GaAs, $\mu_e$ $(m^2/V.\text{sec})$ | 0.1 |
| Laser skin depth at the excitation region, $T_{LT-GaAs}$ (m) | $10^{-6}$ |
| Recombination lifetime, $\tau_r$ (ps) | 100 |
| Geometrical factor of the substrate, $\xi$ | 900 |
| Photoconductive area for laser illumination, S $(\mu m^2)$ | $50\times 10^{-12}$ |
| Laser repetition frequency, $f_{rep}$ (MHz) | 80 |

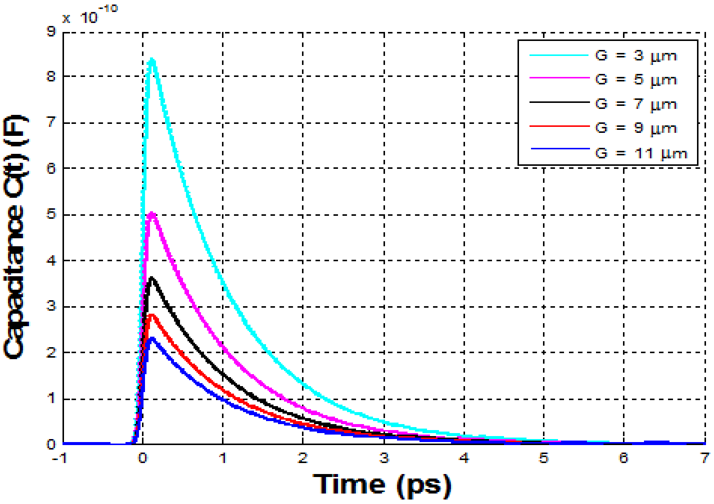

**Figure 3.3: The effect of change in photoconductive gap-size (G) on the time-dependent capacitance $C(t)$.**

Now, the subsequent step is the calculation of gap conductance $G_S(t)$ through the behaviour of generated carrier density $n(t)$. The $G_S(t)$ depends on parameters of 1) the optical source such as its power, pulse duration, and frequency, 2) the photoconductive material such as carrier lifetime, mobility, and 3) the antenna configuration which includes gap length and width of antenna electrodes. Therefore, under the peak laser power illumination the source resistance $R_S(t)$ corresponds to the maximum source conductivity $G_S(t)$ of the photoconductive semiconductor material is calculated as 1.33 Ω from Figure 3.4(a) for G= 5μm. Moreover, the change in source conductance with photoconductive gap size and width of antenna electrodes is illustrated in Figure 3.4. It is observed from the graphs that with the increase of photoconductive gap, the peak value of source conductance $G_S(t)$ decreases. This occurs for the reason that at constant optical power, an increase in the gap size results into an increase in the distance between the generated photo-carriers which further results into decrease in the carrier density in the photoconductive antenna gap. The decrease in carrier density marks significant decrease in source conductance due to decrease in time-dependent bulk conductivity $\sigma(t)$. Likewise on increasing the width of the antenna electrodes, the source conductance increases in view of the fact that time-dependent conductivity $\sigma(t)$ increases at the electrodes.

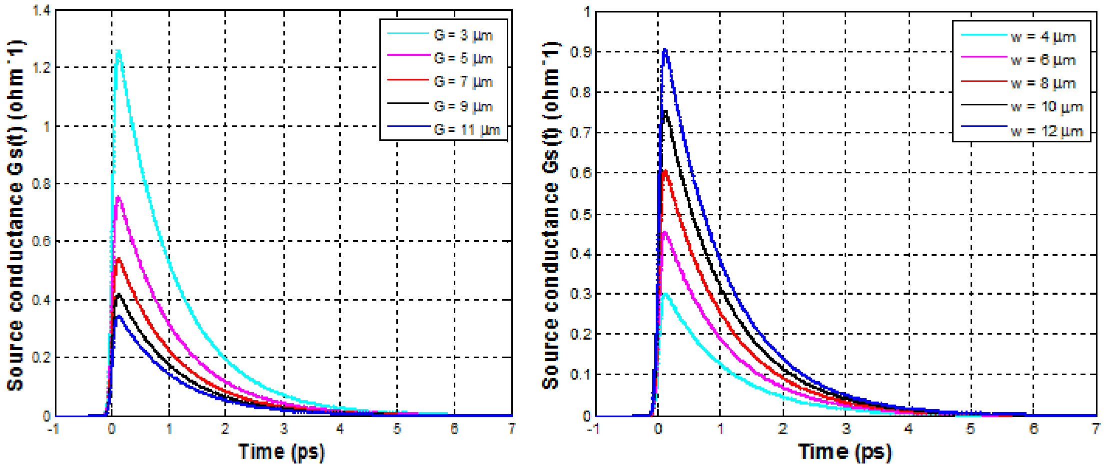

**(a)** **(b)**

**Figure 3.4: Variation in time-dependent source conductance $G_S(t)$ with change in (a) photoconductive gap-size (G), and (b) width of antenna electrodes (W), for constant average optical power $P_{av} = 1W$.**

In Figure 3.5, the variation in time-dependent radiated voltage $V_{rad}(t)$ with change in photoconductive gap size is shown. Moreover, it is observed that with an increase in gap size there is a decrease in source conductance as well as carrier density and it results into the decrease in the voltage across the time-dependent capacitor. Consequently, the values of the radiated voltage decrease.

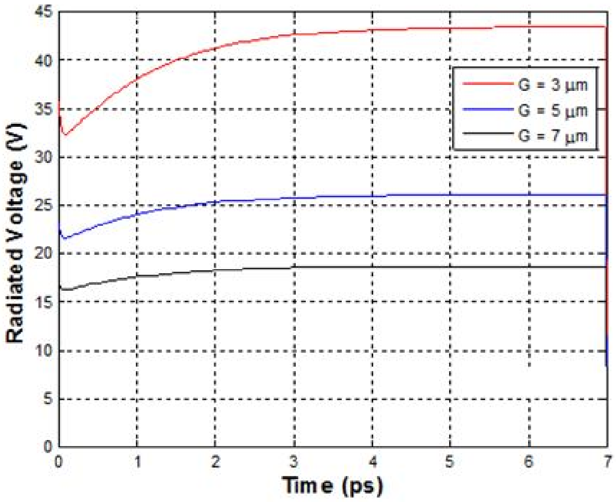

**Figure 3.5: Variation in radiated voltage of photoconductive antenna with gap size (G).**

To support the proposed analytical analysis, it is worth to emphasize here that the value of the radiated voltage shown in Figure 3.5 for gap size 5 $\mu m$ is almost same as the voltage value obtained across antenna load resistance R7 = $Z_a = 41.65\ \Omega$ from the equivalent circuit model realization using ORCAD PSPICE software as shown in Figure 3.1(b). Further, Figure 3.6 represents the variation in the values of the radiated power and the total efficiency with respect to an increase in the average optical power. For small values of average optical power $P_{av}$, the radiated power as well as the total efficiency increases with an approximately linear dependence. However, for higher intensities of the laser pulse more photo-generated carriers are generated in the photoconductive gap due to which a screening effect emerges near the electrodes because of the accumulation of the majority carriers. As a outcome there is an inner field which opposes the incident field resulting into the saturation of the radiated power for high values of average optical power. Moreover, the effect of gap size on these antenna parameters is also shown in Figure 3.6. It is observed that smaller the gap size of small-gap photoconductive dipole antenna such as for $G = 3\mu m$ higher is the radiated power as well as the total antenna efficiency. This happens because the generated electron-holes are nearly situated due to the smaller illuminated area. Further, the tight focusing of optical pump power across the small photoconductive gap can enhance the radiated power at low average optical power levels by reducing the carrier transport path to anode electrode. However, in such case at high average optical power the carrier screening effect as well as the thermal breakdown severely limits the optical-to-terahertz conversion efficiency. For this reason, the photoconductive antennas with large values of gap size can withstand large optical power as well as bias voltage with smaller likelihood of saturation effect and device breakdown.

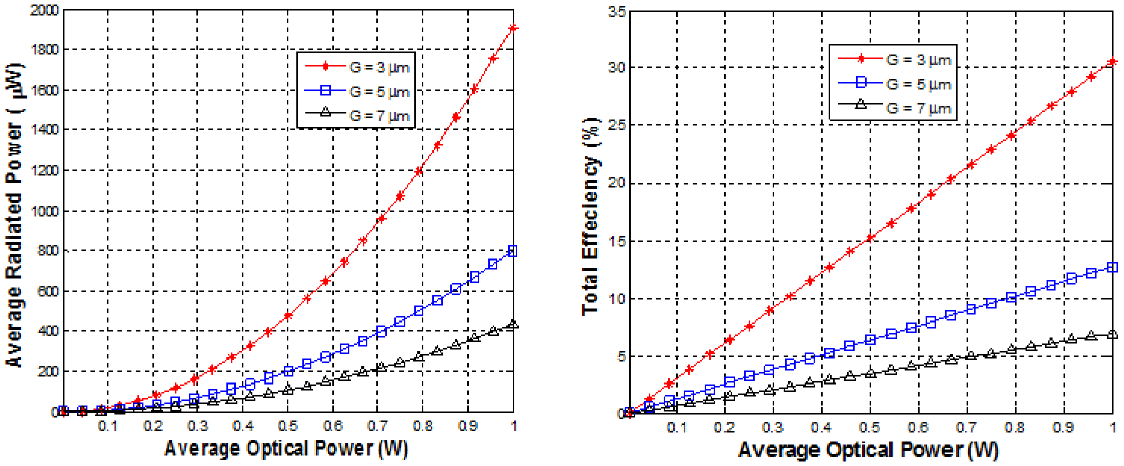

**(a)** **(b)**

**Figure 3.6: Variation in (a) average radiated power, and (b) total antenna efficiency, w.r.t. average optical power for different values of photoconductive gap-size (G).**

In real-time imaging system, the selection of THz photoconductive emitter also depends on the available optical source. When the laser sources with low optical powers are accessible for imaging system then the use of a small gap antenna marks significantly greater radiated power and optical-to-THz conversion efficiency in comparison to that of the large gap antennas. Therefore, the optimum photoconductive gap size of $5\,\mu m$ for small-gap photoconductive dipole antenna is useful as further increase in gap size results into 1) small source conductance, 2) low down radiated voltage, 3) small average radiated power, and 4) low total efficiency of the antenna. Moreover, the investigations on gap size of the small-gap photoconductive antenna reveals that for the large transmitted THz signal, the antenna gap size as well as the antenna electrode width should be kept small and optimized. Further, by calculating the total efficiency based on gap size of $5\mu m$ and the antenna parameters mentioned in Table 3.1 and 3.2, the maximum achievable total efficiency is 0.135. The consideration of biased line distributed elements with time-dependent antenna elements in the equivalent circuit model improves the matching efficiency and so the total efficiency of antenna increases for the antenna impedance of 41.65Ω.

Moreover, in free-space, from a small dipole antenna, the radiation field $E_{rad}(t)$ at a distance $r$ (which is much greater than the wavelength of the radiation), and time $t$ is defined as:

$$E_{rad}(t) = e\mu_e \frac{(1-R)}{hf_l}\frac{\tau_l E_{bias}}{G^2} P_{av} \tag{3.14}$$

From (3.14), it is also clear that the size of the photoconductive gap has its influence on the radiated field for constant average optical power. As the simulation technique provides a powerful tool to study the detailed features of THz electric transients on the antenna and in the space, from near-to far-field, thus enabling one to optimize the antenna geometries such as the design, dimension and dielectric constant of substrate. The Transient solver of CST Microwave Studio is used which is based on the Finite Integration Technique (FIT), and applies direct time-domain analysis and broadband computation of S-parameters from one single calculation run by applying DFTs to time signals. Therefore, the simulation software is used to determine the effect of gap size on the radiation characteristics of the proposed antenna by considering Table 3.2 in which the structure parameters for the proposed small-gap photoconductive dipole antenna are mentioned. The effect of gap size (G) of the photoconductive dipole antenna on the gain and directivity values observed from the simulation results are listed in Table 3.3 for quick comparison.

**Table 3.2: The structure parameters for proposed small-gap photoconductive dipole antenna considered for equivalent circuit realization.**

| Parameter | Value |
|---|---|
| **Biased Lines (Ti-Au)** | |
| Conductivity (S/m) | $1.6 \times 10^7$ |
| Width of line, $L_2$ $(\mu m)$ | 10 |
| Length of line, $(\mu m)$ | 200 |
| Separation between the lines, $L$ $(\mu m)$ | 30 |
| **Dipole Antenna (Ti-Au) and Ground** | |
| Conductivity (S/m) | $1.6 \times 10^7$ |
| Width of antenna, $W$ $(\mu m)$ | 10 |
| Photoconductive gap , $G$ $(\mu m)$ | 5 |
| Length of antenna electrodes, $L_1$ $(\mu m)$ | 12.5 |
| Ground Thickness, $(\mu m)$ | 0.35 |
| **Superstrate(LT-GaAs)** | |
| Carrier Lifetime, majority carriers (psec) | 0.1 |
| Mobility $(cm^2/Vs)$ | Greater than 200 |
| Dielectric Permittivity | 13.26 |
| Magnetic Permeability | 1 |
| Loss tangent (S/m) | 0.006 |
| Electric breakdown field (V/cm) | Greater than $5 \times 10^5$ |
| Conductivity, $\sigma$ (W/cm°C) | 0.55 |
| Thickness $(\mu m)$ | 1 |
| **Substrate (GaAs)** | |
| Carrier lifetime, majority carriers (psec) | 0.25 |
| Mobility $(cm^2/Vs)$ | 200 |
| Dielectric permittivity | 12.9 |
| Magnetic permeability | 1 |
| Loss tangent(S/m) | 0.006 |
| Electric breakdown field (V/cm) | Nearly $4\times 10^5$ |
| Thickness $(\mu m)$ | 10 |
| **Voltage Source** | |
| DC voltage , $E_{bias}$ (V) | 30 |

From Table 3.3, it is concluded that with photoconductive gap size 5µm an improved radiation characteristics in terms of gain and directivity are achievable in comparison to 3µm and 7µm gap size. Moreover, using the simulation software the computed radiation efficiency of photoconductive dipole antenna with photoconductive gap size 3µm, 5µm and 7µm is 76%, 81.2% and 80% along with power flow of 0.0566 $VA/\mu m^2$, 0.0624 $VA/\mu m^2$, and 0.0651 $VA/\mu m^2$, respectively. In Figure 3.7, the radiation characteristics of the photoconductive dipole antenna at 1.5THz with optimized photoconductive gap size (5μm) are shown.

**Table 3.3: The gain (dB) and directivity (dBi) for different values of gap size (G) of photoconductive dipole antenna at 1.5THz.**

| **Principle plane** | **Photoconductive gap size ($\mu m$)** | **Gain (dB)** | | | | **Directivity (dBi)** | | | |
|---|---|---|---|---|---|---|---|---|---|
| | | Main lobe magnitude (dB) | Main lobe direction (Degree) | 3-dB angular width (Degree) | Side lobe level (dB) | Main lobe magnitude (dB) | Main lobe direction (Degree) | 3-dB angular width (Degree) | Side lobe level (dB) |
| E (Phi = 0˚) | 3 | 4.71 | 0 | 39.6 | -2.9 | 5.75 | 0 | 39.6 | -2.9 |
| | 5 | 4.85 | 0 | 39.6 | -3.0 | 5.78 | 0 | 39.6 | -3.0 |
| | 7 | 4.78 | 0 | 40.3 | -2.7 | 5.65 | 0 | 40.3 | -2.7 |
| H (Phi =90˚) | 3 | 7.16 | 320 | 18.5 | -2.4 | 8.20 | 320 | 18.5 | -2.4 |
| | 5 | 7.40 | 40 | 18.5 | -2.5 | 8.27 | 40 | 18.5 | -2.5 |
| | 7 | 7.30 | 40 | 18.6 | -2.6 | 8.24 | 40 | 18.6 | -2.6 |

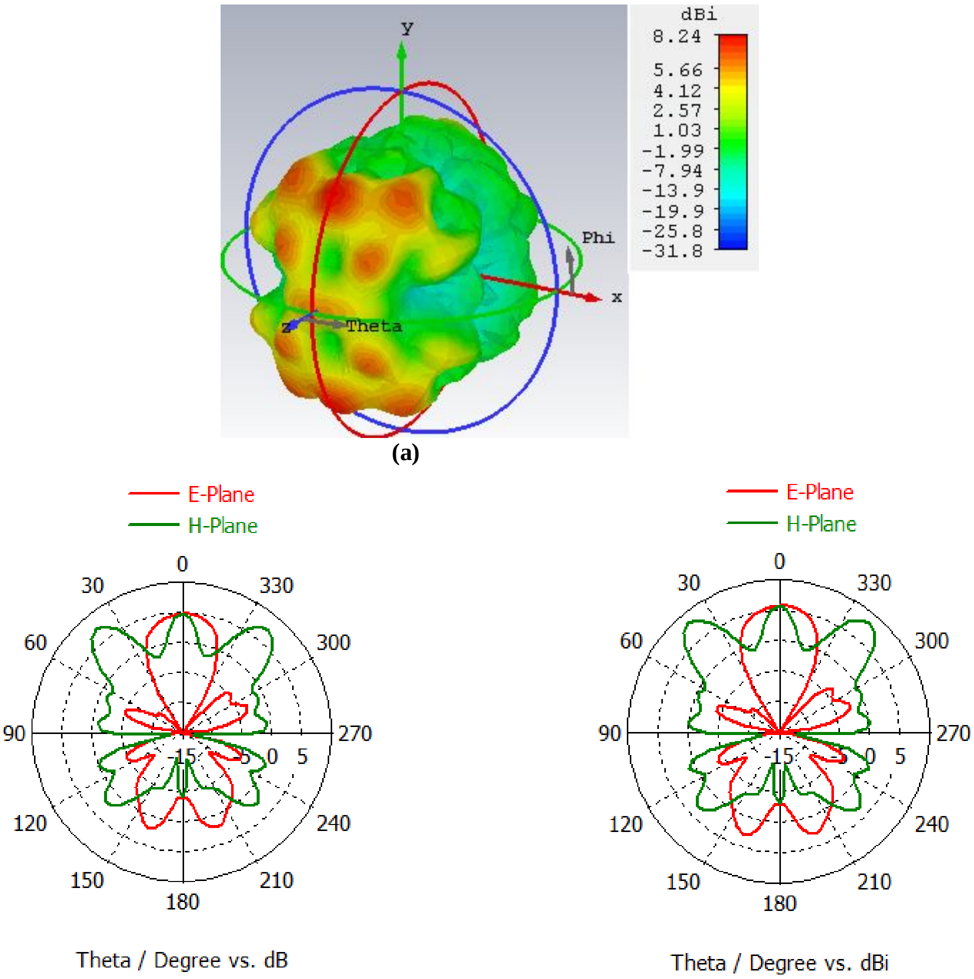

(a)

(b)

(c)

**Figure 3.7: (a) A far-field radiation pattern (3-D view) at 1.5THz, (b) the gain characteristics of the photoconductive dipole antenna with gap size 5$\mu m$ in both principle planes E and H at 1.5THz, and (c) the directivity characteristics of the photoconductive dipole antenna with gap size 5$\mu m$ in both principle planes E and H at 1.5THz.**

## 3.6 CONCLUSION

A pragmatic description of the small-gap photoconductive dipole antenna which includes the relationship among the parameters of equivalent circuit model, photoconductive material properties and the dimensions of the photoconductive dipole antenna electrodes is presented. For this, using equivalent circuit model an analytical approach is used employing both optoelectronic and biased-line properties of the THz photoconductive dipole antenna. The consequence of photoconductive gap-size on physical phenomenon such as time-dependent capacitance, radiated voltage, THz radiated power and total antenna efficiency across the antenna electrode are investigated. Moreover, the realization of distributed components for half-wavelength planar biased-lines assists to improve the impedance matching efficiency of the antenna resulting into an increase in the total antenna efficiency. The total antenna efficiency 0.135 is achieved for the analyzed photoconductive dipole antenna gap-size of 5μm which is supported by the simulation results obtained for the antenna geometry designed using CST Microwave Studio. Therefore, the THz antenna performance and effect of different parameters can be accurately examined by considering the proposed analytical approach of equivalent circuit model before its fabrication. Further, this analytical approach also provides a more precise efficiency assessment of a small-gap photoconductive dipole antenna.

# CHAPTER 4

# DIRECTIVITY ENHANCEMENT OF TERAHERTZ PHOTOCONDUCTIVE DIPOLE ANTENNA USING FREQUENCY SELECTIVE SURFACE FOR IMAGING APPLICATION

## 4.1 INTRODUCTION

For a photoconductive antenna emitter-detector configuration of THz pulsed imaging system, the main demerit to antenna is its low directivity along with low gain values. This indicates that the directivity enhancement methods of THz photoconducting dipole antenna needs the fair dealing, therefore, in this chapter efforts are made for a high efficiency antenna design and subsequently, expecting for an increased directivity of the THz photoconductive dipole antenna for imaging applications keeping the antenna configuration planar and compact. In the photoconductive dipole antenna, the radiation efficiency is also an imperative concern because of the reduced conductivity of the metal at the THz frequencies and particularly, the resonance effects of photoconductive antenna structure [187]. However, an array configuration [106] can be used to increase the gain or the radiation efficiency of the antenna as presented in next chapter of the thesis. The large size array configuration necessitates a higher illumination power from several separate femto-second lasers. Moreover, the use of lens substrate to increase the directivity limits the number of antenna elements in a specified area which is required in an imaging array.

Various researchers have accounted different directivity and gain enhancement techniques which are based on Fabry-perot cavity (FPC) resonator, in general, which operates as a partially reflecting surface (PRS) [187, 189]. Similarly, artificial electromagnetic materials like electromagnetic band gap (EBG), left-handed metamaterial (LHM), and frequency selective surface (FSS) are also explored to design high gain microwave antennas [190, 191]. Moreover, these materials have attracted significant research interest because of their special electromagnetic possessions which are applicable to a wide range of electromagnetic devices [192, 193]. Using Jerusalem Cross FSS structure, the radiation efficiency as well as the bandwidth of the microstrip patch antenna is enhanced and also results into considerable improvement in the microstrip patch antenna performance parameters [194]. Likewise, an EBG resonator antenna with strip dipole FSS array as a superstrate and tapered AMC ground substrate is presented in [195]. This results into an increase of gain with 2-3dB in addition to

2.5 times more bandwidth in comparison to an EBG resonator antenna with AMC ground substrate. The bandwidth improvement of the FPC resonator antenna using FSS which behaves as PRS is examined in [196] by changing the distance amid the FSS elements in PRS. Moreover, a considerable advancement in the transmission characteristics of cascaded configuration of two layered FSSs is revealed in [197] by introducing the resonators on one side of the each substrate layer which is positioned in a way that the resonators face each other with an air gap separating them. Such technique of using FSS with resonating antenna results into an improvement of the transmission response by bringing in an extra transmission zero at a frequency location that is lower than the resonant frequency. This helps to attain high roll-off rate for lower side of the stop band. Further, it also helps to suppress the unwanted resonances and so increasing the rejection/transmission bandwidth of the FSS filter. In [198], on applying metamaterials such as LHM, EBG and FSS the directivity enhancement of the patch antenna operating in the microwave frequency regime of electromagnetic spectrum is presented.

Moreover, the use of FSS structures at THz frequencies offers numerous interesting applications such as in imaging systems, laser cavities, Fabry-Perot interferometer, filter components, sensing systems, spectroscopy and non-destructive testing and inspection. Furthermore, because of the simple geometry along with planar structure and compact size, the utilization of FSS with photoconductive dipole antenna offers an ease of deployment of the THz source with superior performance parameters for sensing and imaging application. Such antenna configuration (PCA with FSS) also provides flexibility in portability due to small volumetric scale. In the THz regime of electromagnetic spectrum, there are two types of frequency selective practices which are utilized in the design of the FSS structure, such as: 1) The interference of electromagnetic waves reflected from the cascaded partially transmitting boundaries, and 2) The resonant interaction of electromagnetic waves with the segments of conductor (generally periodic arrays of the conducting elements in the dielectric) or the slots in the conducting screens for reflection / transmission of electromagnetic wave, respectively. In this paper, we have explored the process of resonant interaction of wave with array of bandpass FSS for the gain and directivity enhancement of photoconductive dipole antenna in the THz frequency regime of the electromagnetic spectrum for the detection of hidden explosives and explosive related compounds. In the next section, more discussion on the related work and our problem formulation has been compiled.

## 4.2 RELATED WORK AND PROBLEM FORMULATION

In imaging applications, researchers are working to develop different techniques to detect the hidden explosives and illicit drugs using THz radiations [121]. Appleby et al. [199] have examined different THz techniques in conjunction with atmospheric, material and component issues associated with the model design that provides potential applications in detection of weapons and contraband concealed on persons beneath clothing. Likewise, the detection of RDX by means of THz spectroscopic imaging using specular reflection has been established by Shen et al. [200]. In the real-world state of affairs, the targets generally have uneven surfaces moreover the surfaces are not aligned normal to the THz beam therefore the direction of the specular reflection is difficult to resolve. Therefore, it is more practical to detect and identify explosives using diffusely reflected THz waves [201]. In contrast, the transmission of THz wave through the object having flat spectra or the object which shows invariable background power spectrum helps to detect the type of object. In such THz spectroscopic system, the amplitude reduction in the THz wave due to the absorption of wave by the object facilitates to conclude the type of material. Moreover, the time shift of THz pulse also assists to discriminate the objects made of different explosives in powder form [118]. The angular frequency is an important parameter for designing a THz radiation source. If the source is capable of transmitting a THz pulse at the spectral fingerprint frequency of the material to be detected only then it would be absorbed by the material under detection, therefore the presence of such material is detected at the detector side using THz pulsed imaging system. The photoconductive antenna is a THz source which absorbs power of incident laser and creates a number of carriers and the applied bias voltage across the electrodes (acting as radiating source) accelerates the carriers and as a result a photocurrent flows through the radiation element. The antenna electrodes convert generated photocurrent to THz wave radiation. However, low efficiency in optical-to-THz conversion is an important drawback of photoconductive antenna. To enhance the performance parameters of photoconductive antenna, several methods have been adopted by researchers such as modifying the antenna layout [202, 203], the antenna contacts [204] or its structure and materials [180, 205, 206]. Singh et al. [202] have investigated the role of strip-line photoconductive THz antenna in a regime wherein both the direct emission of accelerated carriers in the semiconductor as well as the antenna-mediated emission from the strip-line is considerable. They have observed the effect of varying the widths of two electrodes on the THz emission efficiency because an enhanced efficiency of THz emission will progress the data quality for many applications such as chemical identification, material characterization and imaging. For enhancing the THz pulse emission, Park et al. [203] have presented a nano-plasmonic photoconductive antenna with metal nano-islands. These metal nano-islands serve up as plasmonic nano-antennas to locally increase the electric field of an ultrafast pulsed pump beam for the generation of large photocarriers. Their reported results show higher enhancement for THz pulse emission power by two times in comparison to the conventional photoconductive antenna. However, the use of plasmonic nano-structures within the photoconductive gap of photoconductive antenna is constrained by the factor of high cost involved in the nano-fabrication of metal nano-structures using the technique such as e-beam lithography. Optimization of the device contacts further enhances the performance of photoconductive antenna. Vieweg et al. [204] have shown the higher output power using a lower contact resistance of the AuGe ohmic metal for making contacts for photoconductive THz antenna with low temperature grown GaAs photoconductive substrate, which leads to increased current flow. They have also reported that Ti/Au ohmic metal contacts are also useful for systems with high stability requirement due to higher thermal stability shown by Ti/Au contacts with low temperature grown GaAs. The use of plasmonic structures does not carry out well in the case of laser pulse with short duration time and hence, its operation is limited to only transverse magnetic-polarized incident laser. Khorshidi et al. [180] have proposed the use of periodic dielectric structure inside the gap between the electrodes of photoconductive antenna to enhance the THz radiation power. In photoconductive dipole antenna the material inhomogeneities arise during the growth leads to varying the emission strength. Abdulmunem et al. [205] have shown the relationship between THz emission strength and the surface properties of low temperature grown photoconductive antenna. Such correlation also helps to establish the factors to enhance the antenna performance parameters. Yardimci et al. [206] have analyzed that the choice of the substrate composition in addition to its growth process having short carrier lifetimes for photoconductive antenna (which are essential in determining substrate resistivity, carrier drift velocity and carrier lifetime) have a direct impact on 1) optical-to-terahertz conversion efficiency, 2) radiation power, 3) radiation bandwidth, and 4) reliability of photoconductive emitters. Apart from above mentioned performance parameters of photoconductive antenna, for THz imaging application there is a need of highly directive THz source with optimum radiation efficiency. A highly directive photoconductive antenna is constructive to enhance the imaging capabilities of the THz imaging system to address the considerations such as limited depth-of-field (DoF) which is determined as the distance over which an object is considered in focus. When the THz source is deployed for short-range imaging then a THz imaging system needs a narrow DoF so as to make the ability of the system to identify the hidden explosive carried by an individual moving towards the imaging system only for the concise moment. Moreover, such scanning over an extended volume possibly will provide security such as in a public-place where the security is an essential concern however the visible display is not so much significant. Further, the size-weight-and-power (SWaP) of THz source for imaging application is another vital consideration. The use of compact and planar geometry of THz photoconductive dipole antenna with feasibility to have above-chip implementation supports the small SWaP values of THz source for imaging application. Moreover, high front-to-back ratio of THz antenna is advantageous in such applications so as to have interference free detection of hidden explosives.

Although the high directivity as required in THz imaging systems may be achieved by using THz photomixer as reported in [207] by using FSS, the photoconductive antenna [115, 116] in pulsed THz imaging system is reasonably attractive because of the system-on-chip compatibility, its ability to work at room temperature, relatively small size, low power consumption, low manufacturing cost, and availability of compact lasers. Further, to preserve the purity of incoming wave on the receiving antenna side where the electromagnetic interference (EMI) is the major obstruction [208], the use of FSS structure with antenna geometry in THz region is beneficial to enhance the antenna performance parameters. To increase the directivity of the elementary dipole as well as the planar antennas in the microwave frequency regime of the spectrum, highly reflective surfaces as superstrate is extensively used and it signifies that such type of arrangement is equally appropriate at the THz frequency [209]. In general, the directivity of antenna using FSS is envisaged by either using the transverse-equivalent-network model or the resonance-estimation ray tracing technique [191]. Although these techniques can only predict the peak directivity of antenna at resonance frequency in case of FSS array size and the ground plane size are adequately large or semi-infinite. When the FSS array or ground plane is curtailed, the directivity of cavity resonant antenna gets reduced and so in such conditions these techniques are not capable to predict the directivity of antenna accurately [210]. In such situations, the directivity of antenna array can be predicted using a comparison method at the THz frequency using FSS structure. In this chapter, a straightforward technique to improve the gain and directivity of the photoconductive dipole antenna using bandpass FSS as a superstrate at terahertz frequency for imaging and sensing applications is considered. Moreover, the THz absorption spectra has been well thought-out to design the THz photoconductive dipole antenna for commonly used explosives such as RDX, HMX, PETN, TNT and other explosive related compounds (ERCs) which illustrates their significant spectral absorption peaks in the range of 1-2 THz as accounted in [119, 121]. In this frequency regime of the spectrum (1-2THz), the RDX shows spectral fingerprints with absorption at 1.05THz, 1.30THz, 1.5THz, and 1.9THz. However, the HMX shows absorption at 1.58THz, 1.84THz, and 1.91THz. Further, the PETN and TNT also have one absorption fingerprint nearly at 2.0THz and 1.66THz, respectively.

## 4.3 THEORY OF OPERATION

The frequency selective surfaces (FSSs) are described as the resonant periodic arrangement of conducting materials in one- or two-dimensions which exhibit selectivity in the frequency and polarization [211, 212]. Several researchers have used different FSS structures such as dipole, tripod, cross dipole, Jerusalem cross, ring shaped, and square loop. From the literature, this has also been distinguished that the square loop shape of FSS presents superior performance in terms of bandwidth, band separation, and angular stability [213].

### 4.3.1 Analysis procedure of frequency selective surface

Various numerical techniques have been developed to analyze the frequency selective surface (FSS), where each one is connected with its own merits and demerits [214]. Moreover, the FSS structure can be designed as bandpass and bandstop spatial filter which are complementary to each other [215]. Among the analytical procedures to analyze the FSS, the equivalent circuit model is very well accepted. This is due to its simplicity in which the equivalent lumped parameters of a FSS are acquired from the inductive and capacitive behaviour of the conductive sheet placed over a dielectric. As in the proposed antenna design, the FSS structure along with photoconductive dipole antenna has been used to increase the gain and directivity therefore, the FSS as bandpass spatial filter is utilized. The unit-cell design of FSS bandpass and s-parameter response of unit cell FSS are shown in Figure 4.1. The metallic elements symbolize inductive screens which provide rise to total reflection, while apertures in a metallic sheet correspond to capacitive screens and offer rise to total transmission [216, 217]. The analysis and design of bandpass FSS depends on the physical parameters such as the periodicity ($P$) of the unit-cell FSS, length of the slot ($d$), slot width ($s$) in addition to gap between two slots ($g$). The synthesis process of unit-cell FSS is explained in [215] to determine the parameters of the square shape bandpass FSS. Therefore, using the same synthesis technique with some more specific use of that technique in designing bandpass square shape FSS has been presented.

Further, in the proposed antenna design, the dielectric loaded FSS bandpass is used instead of using free standing since the use of dielectric substrate with FSS provides physical integrity with the FSS structure. Moreover, it also offers stable reflection and transmission characteristics and can also change the fundamental resonance frequency [218]. The unit-cell configuration of bandpass FSS is shown in Figure 4.1(a), which is created using aluminium for metallic patch with conductivity $\sigma = 3.5 \times 10^7$ S/m and is placed over the dielectric substrate which is selected as thermocol having relative dielectric permittivity $\varepsilon_r = 1.05$. Moreover, the use of dielectric material transforms the performance of the FSS structure [218, 219]. It happens because the characteristic impedance above as well as below the FSS structure gets changed due to the presence of dielectric material.

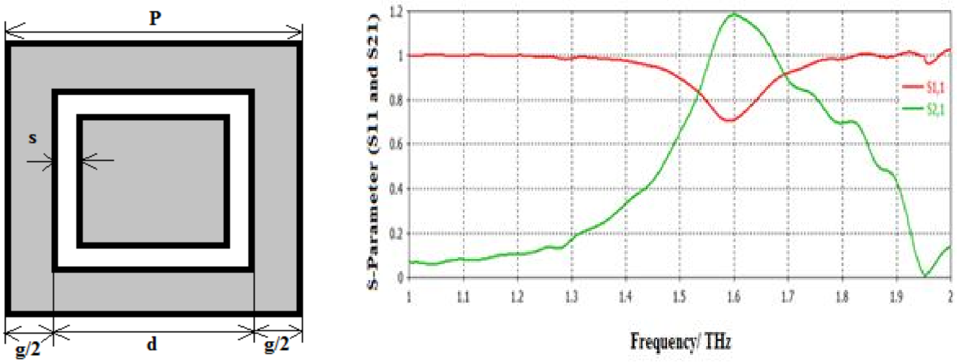

(a) (b)

**Figure 4.1: The single square loop FSS (a) the unit-cell configuration with bandpass characteristics and (b) S-parameter of unit-cell with $P = 75\ \mu m, d = 74.83\ \mu m, g = 0.17\ \mu m$ and $s = 8\ \mu m$.**

Moreover, in order to avoid the evanescent waves to propagate all the way through the FSS periodic structure, the thickness of the dielectric substrate must follow the relation, $h < \lambda_0/20$, where $h$ is the thickness of dielectric substrate of FSS and $\lambda_0$ is the wavelength in free-space, as in thicker dielectric substrates, the evanescent waves become stronger and affect the performance of the periodic structure [212]. Therefore, the thickness of substrate taken for bandpass FSS is 5μm. The equivalent circuit elements are determined for the transverse electric (TE) polarized wave, using [217] as:

$$\frac{\omega_r L}{Z_0} = \frac{d}{P}\cos\theta \times F(P, s, \lambda, \theta) \tag{4.1}$$

Where $F(P, s, \lambda, \theta) = \frac{P}{\lambda}\left[\ln csc\left(\frac{\pi s}{2P}\right) + G(P, s, \lambda, \theta\ )\right]$ (4.2)

And $$\frac{\omega_r C}{Y_0} = 4\frac{d}{\lambda}\sec\theta \times F(P, g, \lambda, \theta) \times \varepsilon_{eff} \tag{4.3}$$

Where $F(P, g, \lambda, \theta) = \frac{P}{\lambda}\left[\ln csc\left(\frac{\pi g}{2P}\right) + G(P, g, \lambda, \theta\ )\right]$ (4.4)

In (4.1) to (4.4), $\varepsilon_{eff}$, $G(P, s, \lambda, \theta)$, $G(P, g, \lambda, \theta)$, P, d, s, g, $Z_0$, and $Y_0$ are the effective dielectric permittivity of the media, the correction factors for the associated inductance and capacitance, periodicity of FSS unit-cell, length of the slot, slot width, gap between two FSS slots, characteristic impedance, and characteristic admittance, respectively.

In case, the correction factors are neglected at the cost of a minor deviation in the results, (4.1) and (4.3) can be re-written as:

$$\frac{\omega_r L}{Z_0} = \frac{d}{P}\cos\theta \times \frac{P}{\lambda}\ln\left[\csc\left(\frac{\pi s}{2P}\right)\right] \tag{4.5}$$

$$\frac{\omega_r C}{Y_0} = 4\frac{d}{\lambda}\sec\theta \times \frac{P}{\lambda}\ln\left[\csc\left(\frac{\pi g}{2P}\right)\right] \times \varepsilon_{eff} \tag{4.6}$$

With thermocol as the substrate ($\varepsilon_{eff} = 1.05$), the multiplication of (4.5) and (4.6) gives,

$$\omega_r{}^2 LC = 4.2\left(\frac{d}{P}\right)^2\left(\frac{P}{\lambda}\right)^2 \times \ln\left[\csc\left(\frac{\pi s}{2P}\right) + \csc\left(\frac{\pi g}{2P}\right)\right] \tag{4.7}$$

In (4.7), the left-hand side of the equation indicates the condition for resonance or anti-resonance. Therefore, for the resonance condition of the FSS, the value of left-hand side quantities must be 1 because $\omega_r{}^2 = \frac{1}{LC}$. Therefore, (4.7) can be re-written as:

$$1 = 4\left(\frac{d}{P}\right)^2\left(\frac{P}{\lambda}\right)^2 \times \ln\left[\csc\left(\frac{\pi s}{2P}\right) + \csc\left(\frac{\pi g}{2P}\right)\right] \tag{4.8}$$

Further (4.8) is made simpler as,

$$1 = 4\left(\frac{d}{P}\right)^2\left(\frac{P}{\lambda}\right)^2 \times \ln\left[\frac{1}{\sin\left(\frac{\pi s}{2P}\right)} + \frac{1}{\sin\left(\frac{\pi g}{2P}\right)}\right] \tag{4.9}$$

For $s \ll 2P$ and $g \ll 2P$, (4.9) is inscribed as,

$$1 = 4\left(\frac{d}{P}\right)^2\left(\frac{P}{\lambda}\right)^2 \times \ln\left[\frac{2P}{\pi s} + \frac{2P}{\pi g}\right] \tag{4.10}$$

For the bandpass FSS, from the geometry it is clear that the value of g is greater than $s$, therefore the ratio $\frac{2P}{\pi s}$ dominates over the ratio of $\frac{2P}{\pi g}$, so (4.10) is then simplified as shown in (4.11).

$$1 = 4\left(\frac{d}{P}\right)^2\left(\frac{P}{\lambda}\right)^2 \times \ln\left[\frac{2P}{\pi s}\right] \tag{4.11}$$

Moreover, it is also recognized that for a specified FSS structure, the response changes with the variation in the angle of incidence of the electromagnetic wave $\theta$ as well as with the period P of the FSS. Further, to circumvent the grating lobes, the wavelength $\lambda$ is related to P and $\theta$ by the following relation from [216] as mentioned in (4.12).

$$P(1 + \sin\theta) < \lambda \tag{4.12}$$

From (4.12), it is clear that for maximum incident angle ($\theta$), a mathematical relationship between P and $\lambda$ gets established on condition that the inequality is satisfied such as if a case is considered such that the structure must function satisfactorily over the angle $\theta_1$. Then choose the value of $\theta = \theta_2$ in (4.12) where $\theta_2 > \theta_1$. Therefore, the inequality of (4.12) is contented and the value of P is fixed as

$$P = M\lambda \tag{4.13}$$

In (4.13), $M$ is a constant and its value lies in-between 0 to 1. On substituting (4.13) in (4.11) the expression of (4.11) becomes

$$1 = 4\left(\frac{d}{P}\right)^2\left(\frac{P}{\lambda}\right)^2 \times \ln\left[\frac{2M\lambda}{\pi s}\right] \tag{4.14}$$

From (4.12) and (4.14), it is concluded that the length of the FSS loop can be determined and can further be optimized using 1) the known operating frequency, 2) the desired slot size as the fraction of wavelength $\left(\frac{s}{\lambda}\right)$, and 3) the maximum accepted angle of the incident wave. From Figure 4.1(b), the S-parameters of unit-cell of bandpass FSS with physical parameters $P = 75\,\mu m, d = 74.83\,\mu m, g = 0.17\,\mu m\ and\ s = 8\,\mu m,$ the magnitude of reflection coefficient, $|S_{11}| = 0.895$ and $|S_{21}| = 0.65$ are obtained at 1.5THz using CST Microwave Studio and ideally at this operating frequency of designed photoconductive dipole antenna the value of $|S_{11}|$ should be equal to 1.0 for the lossless condition. The slight difference of the value of $|S_{11}|$ from the ideal value is due to the losses and the potential challenges which are experienced while operating the FSS structures at THz regime of electromagnetic spectrum. Moreover, in the lossless condition, ideally $|S_{21}|^2 + |S_{11}|^2 = 1$ and this means that where $S_{11}$ is minimum the value of $S_{21}$ reaches to maximum. Moreover, the flatness of the transmission property of FSS gets enlarged. The reason for having the value greater than 1 is due to the presence of voltage source across the biased lines of the photoconductive dipole antenna. In the THz regime of the electromagnetic spectrum, the performance of the FSSs is largely influenced by the ohmic losses [220], surface roughness [221], and dispersion effect [222]. The ohmic loss gets considerably increased at THz regime because of the compact size of FSS and in such situation the metal no longer can be approximated as the perfect electric conductor (PEC) [223]. Moreover, owing to the resonant characteristics, the FSSs exhibit more losses than that of a metallic sheet. Therefore, the ohmic losses which occur from the finite conductivity of the metallic elements boost extensively and dominate the cause of heat dissipation in the FSSs. The surface roughness or deformities of FSS are also accountable for scattering in the THz region which together with the surface plasmons gives rise to a supplementary drop in the power reflectance [220]. Moreover, the effect of dispersion loss in FSS at THz frequency is because of the relative dielectric permittivity of the dielectric substrate which is generally a complex frequency dependent quantity. The real part of the relative dielectric permittivity corresponds to the energy stored and the imaginary part is associated to the dissipation. Therefore, for the dispersion less dielectric, the resonant frequency decreases as square root of the relative dielectric permittivity. Moreover, the dispersion becomes major concern at higher frequencies which results into modified reflection characteristics through contraction / expansion of bandwidth. In the THz regime of electromagnetic spectrum, the skin depth is much smaller than the conductor cross-section due to which the current flows mainly at the surface of the conductor and such occurrence further add to the dispersion loss and results into a substantial decrease in the performance of the FSSs [224]. In general, the aforementioned analysis procedure is equally-suitable for the TM polarized wave to determine the physical parameters of square shaped bandpass FSS. Since the square loop FSS is the polarization independent therefore, the formulae described for the TE mode are also applicable to TM mode of operation.

### 4.3.2 Modelling of FSS Bandpass Structure

The choice of dielectric in addition to conducting material is an imperative aspect to design the FSS, which also depends on the application in particular, still there are vital concerns related to the material selection and are required to be contemplate [225]. The material to be employed as a dielectric substrate must be transparent enough to demonstrate adequate absorption along with significant thickness so as to reduce the dielectric losses, dispersion and also evade the onset of the grating lobes over the frequency band of interest [221, 226]. On the other hand, the selection of conducting material is influenced by the value of conductivity of the material as well as the width of the material that considerably influenced the performance of FSS. Mainly metals such as aluminium or copper are utilized for the construction of FSS because of low conductor losses associated with such materials due to the high conductivity. Moreover, these metals are easily available with fiscal in use. However, aluminium is preferred above copper since the micro-fabrication processes are employed to fabricate the FSSs in terahertz region, consequently from the fabrication perspective, the dielectric substrate must endure the chemical reactions involved in common micro-fabrication processes and then again, aluminium is easy to use and provides ease in fabrication [227].

To analyze the theory discussed in the previous sub-section about the FSS bandpass unit-cell, the physical parameters of FSS unit-cell at 1.5THz have been computed. The physical parameters of FSS bandpass unit-cell as shown in Figure 4.1 are calculated for the normal incident wave (where $\Theta = 0^\circ$) because the Transient solver of CST Microwave Studio supports normal incident of the electromagnetic wave on to the structure and it is also presumed that THz radiations generated from PCA strikes the lower FSSs array with normal incidence only. Using (4.12), the relation between periodicity ($P$) and length of the slot ($d$) of the unit-cell of FSS at normal incidence i.e. $\Theta = 0^\circ$ of the plane wave, can be determined as $[P(1+\sin 0^\circ)] < \lambda$ and $P < \lambda$. The operating frequency of designed PCA is 1.5THz and the wavelength in free-space becomes 200μm. The periodicity of FSS unit-cell is kept below 200 μm. The substrate size of designed PCA is 300×300 $\mu m^2$ and for using FSS bandpass unit-cell array with the designed antenna with overall compact configuration, the size of the substrate for FSSs is also taken as 300×300 $\mu m^2$. With this, the periodicity $P$ for different size of arrays are taken as $P$ = 150μm for 2×2 FSSs, $P$ = 100μm for 3×3 FSSs and P = 75μm for 4×4 FSSs. In order to satisfy (4.13), for different values of $P$ (150μm, 100μm, and 75 μm), the value of $M$ is computed as 0.75, 0.5 and 0.375, respectively. When the value of $M$ is set then for different value of s/λ, the value for the length of slot is computed using (4.14) and are presented in Tables 4.1, 4.2 and 4.3, for three types of array setups with photoconductive dipole antenna corresponding to (2×2) FSSs, (3×3) FSSs and (4×4) FSSs, respectively. The numerical value for gap between two slots is also computed with the help of geometry of the FSS bandpass unit-cell shown in Figure 4.1.

**Table 4.1: FSS bandpass unit cell physical parameters for 2×2 FSS array.**

| s/λ | s (μm) for λ=200μm | P(μm) | d (μm) | g= P-d (μm) | g/2 (μm) |
|---|---|---|---|---|---|
| 0.01 | 2 | 150 | 49.64 | 100.36 | 50.18 |
| 0.02 | 4 | 150 | 54.77 | 95.23 | 47.62 |
| 0.03 | 6 | 150 | 58.69 | 91.31 | 45.66 |
| 0.04 | 8 | 150 | 61.97 | 88.03 | 44.015 |

**Table 4.2: FSS bandpass unit cell physical parameters for 3×3 FSS array.**

| s/λ | s (μm) for λ=200μm | P(μm) | d (μm) | g= P-d (μm) | g/2 (μm) |
|---|---|---|---|---|---|
| 0.01 | 2 | 100 | 53.76 | 46.24 | 23.12 |
| 0.02 | 4 | 100 | 60.12 | 39.88 | 19.94 |
| 0.03 | 6 | 100 | 65.07 | 34.93 | 17.47 |
| 0.04 | 8 | 100 | 69.44 | 30.56 | 15.28 |

**Table 4.3: FSS bandpass unit cell physical parameters for 4×4 FSS array.**

| s/λ | s (μm) for λ=200μm | P(μm) | d (μm) | g= P-d (μm) | g/2 (μm) |
|---|---|---|---|---|---|
| 0.01 | 2 | 75 | 56.14 | 18.86 | 9.43 |
| 0.02 | 4 | 75 | 63.5 | 11.5 | 5.75 |
| 0.03 | 6 | 75 | 69.57 | 5.43 | 2.715 |
| 0.04 | 8 | 75 | 74.83 | 0.17 | 0.085 |

However, it is observed from the simulation results presented in the section of numerical analysis and simulation results that for the fixed value of $P$ and an increase in the value of s/λ, there is an increase in the deviation of the resonant frequency from the intended frequency. It is also being observed from the simulation results, that with an increase in value of the slot size, the capacitive effect of FSS array gets increased which causes the bandwidth enhancement.

## 4.4 DESIGN OF FSS-PCA

Three geometrical configurations of a photoconductive dipole antenna are presented in Figure 4.2. The front-view and top-view of basic structure of photoconductive dipole antenna are shown in Figure 4.2(a) and Figure 4.2(b), respectively. It consists of an antenna structure, a thin layer of photoconductive superstrate (1µm thick) followed by a photoconductive substrate (10µm thick) and a ground plane (0.35µm thick) is placed under the substrate. The antenna has a photoconductive gap of 5 µm at the centre of the dipole antenna with distance between the coplanar striplines of 30 µm. The length, width and thickness of the antenna coplanar striplines are 150µm, 10µm and 0.35µm. The coplanar striplines are biased with a voltage source of 30 volts. In the photoconductive dipole antenna, the optical source is a femto-second laser pulse which has a Gaussian beam distribution at its output, therefore in the CST simulation software we have applied the Gaussian beam excitation with pulse duration less than 100fs on to the superstrate from the gap of the photoconductive dipole antenna. The antenna length ($L$) is computed at operating frequency 1.5 THz, $f = c/2nL$, where $c$ is the speed of light in vacuum, $L$ is the separation distance between the two coplanar striplines (length of the dipoles) and $n$ is the refractive index of the material. This value of frequency has been chosen so that the designed antenna must show high gain and directivity at this frequency to sense the RDX explosive which shows its spectral fingerprint by absorbing the frequency at 1.5THz. For the resonance condition, $L = m \times \lambda_n/2$ where, m = 1, 2, 3…., and the wavelength $\lambda_n$ in the material depends on the refractive index $n$ which is given by $\lambda_n = \lambda/n$. If we take m = 1, then $L = \lambda/2n$. The refractive index ($n$) of semiconductor antenna material for low temperature Gallium Arsenide (LT-GaAs) at THz frequencies is 3.4 and for frequency 1.5 THz, the value of $L$ (length of dipole) is obtained as, $L = c/(2nf_r) = 30\mu m$ and $n = [(1 + \varepsilon_d)/2]^{1/2}$, where $\varepsilon_d = 12.9$ is the dielectric permittivity of GaAs substrate used for photoconductive dipole antenna.

An increase of the effective refractive index of the substrate (GaAs) results into the shift of resonant frequency towards the lower value. Moreover, an accurate assessment of the refractive index with change of the substrate in the present case is not straight forward since its local value depends on the local THz electric field in a nonlinear manner. Further, the use of material with high dielectric permittivity results into the emergence of shock wave at the air-substrate interface in the THz regime of the electromagnetic spectrum [131]. In addition, the application of thick substrate leads to surface wave loss because of the trapping of energy within the substrate [228], and reduction in the substrate thickness reduces the performance as well as mechanical strength of the antenna. In order to reduce the surface wave loss either the effective dielectric permittivity or thickness of material has to be trim down. However, the effective dielectric permittivity can be reduced by artificially transformed the property of material by using the periodic air-defects in the homogeneous host material which generally acts as photonic bandgap material. In the proposed antenna model, the thickness of photoconductive substrate GaAs is taken as 10µm which is small enough to minimize the surface wave loss while providing sufficient strength to the THz antenna structure. Figure 4.2 (c) shows the surface current distribution on the planar surface of photoconductive dipole antenna when an optical beam of short duration (approximately 100fs duration) is allowed to excite the photoconductive gap of the antenna. From the Maxwell's equations, the THz electric field in the far-field region is proportional to the time derivative of the transient current [161] and is expressed as: $E(t) \propto$ dJ/dt$\propto$ $E_b$(dn(t)/dt) where $J$, $E_b$, and $n$ are the current density, applied bias field and current density, respectively. In Figure 4.2(d), the FSS bandpass array is placed below the PCA with air gap distance of 8.65µm from the ground plane of PCA. This value is computed using parameter sweep of Transient solver of CST Microwave Studio to optimize the height of PCA from FSS bandpass array for desired increase in the performance parameters of PCA. In Figure 4.2(e), an additional FSS bandpass array is used as superstrate (placed at 8.65µm above the structure of PCA with air gap in between) to PCA so as to observe its effect on the complete antenna configuration performance in terms of resonance frequency, bandwidth, gain, directivity, radiation efficiency and front-to-back ratio.

All THz-PCA antenna configurations are designed using the CST Microwave Studio which is one of the simulation modules of CST Studio Suite. It provides a simulation platform for all types of electromagnetic field applications. Moreover, in CST Microwave Studio multiplicities of different solvers operating in time and frequency domains are included. The Transient Solver of CST Microwave Studio is used to obtain the simulation results. It works on Finite Integration Technique (FIT) in which DFTs to time signals are applied for the direct time-domain analysis and broadband calculation of S-parameters using single calculation run. The adaptive mesh refinement in 3D using S-Parameters is also used in the simulation run which is supported by the Transient solver of CST Microwave Studio.

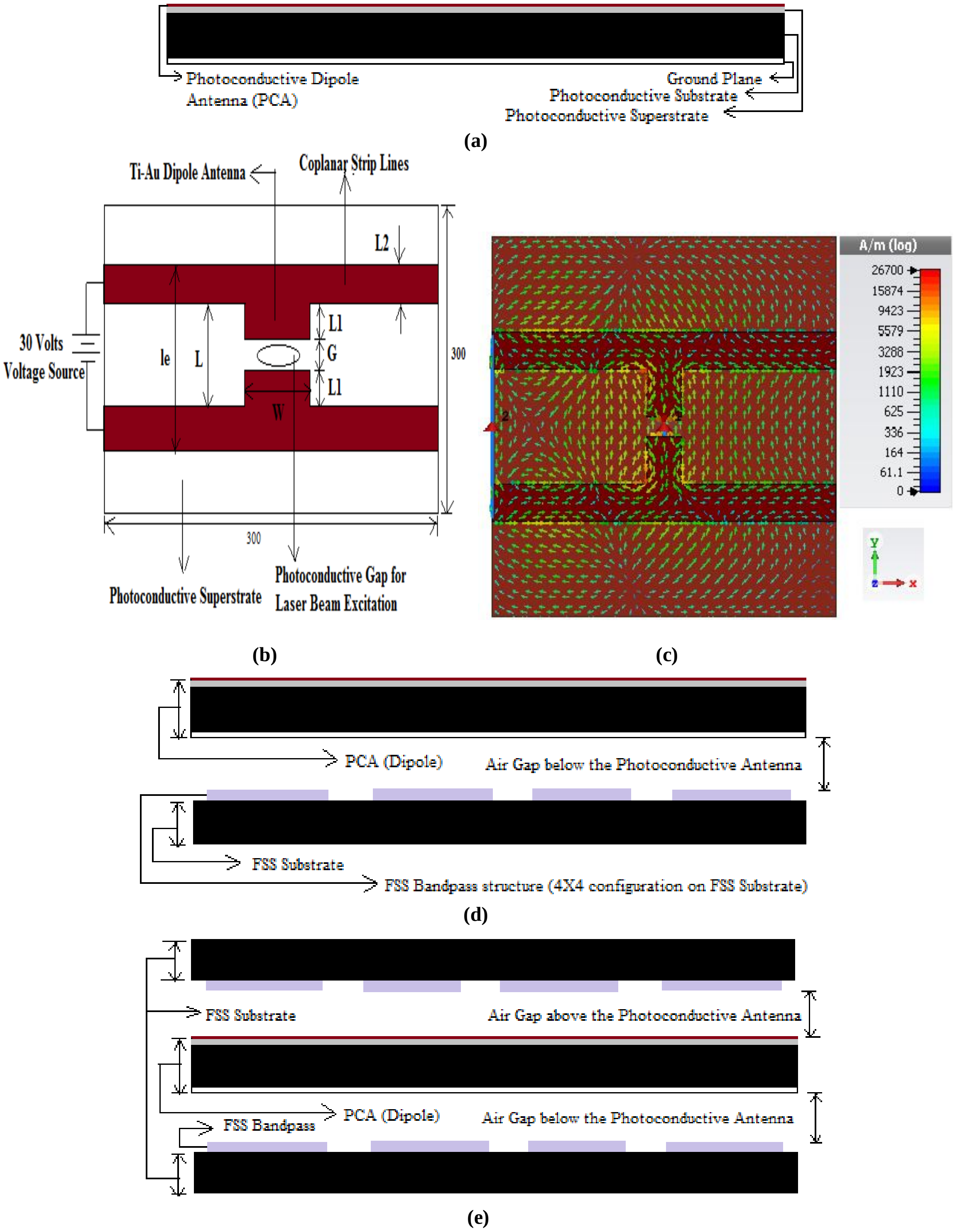

**Figure 4.2: The photoconductive dipole antenna (a) front-view, (b) top-view, (c) the surface current distribution on the planar surface using CST Microwave Studio (d) with 4×4 FSS bandpass substrate placed below the ground plane of photoconductive dipole antenna (PCA) at 8.65µm with air gap, and (e) with two 4×4 FSS bandpass substrate placed above and below of the photoconductive dipole antenna (PCA) at 8.65µm with air gap distance on both sides of antenna.**

Table 4.4 presents the parameters in terms of material conductivity, dielectric permittivity, magnetic permeability and loss tangent considered in CST Microwave Studio for designing the three geometrical configurations of photoconductive dipole antenna as shown in Figure 4.2.

**Table 4.4: The parameters used in simulation performed in transient solver of CST Microwave Studio.**

| Parameter | Value |
|---|---|
| **Dipole Antenna (Ti-Au) and Ground** | |
| Conductivity (S/m) | $1.6 \times 10^7$ |
| **Superstrate (LT-GaAs)** | |
| Carrier Lifetime, majority carriers (psec) | 1 |
| Mobility $(cm^2/Vs)$ | Greater than 200 |
| Permittivity | 13.26 |
| Permeability | 1 |
| Loss tangent (S/m) | 0.006 |
| Electric breakdown field (V/cm) | Greater than $5 \times 10^5$ |
| Surface recombination velocity(m/s) | 5000 |
| **Substrate (GaAs)** | |
| Carrier Lifetime, majority carriers (psec) | 20 |
| Mobility $(cm^2/Vs)$ | 200 |
| Permittivity | 12.9 |
| Permeability | 1 |
| Loss tangent(S/m) | 0.006 |
| Electric breakdown field (V/cm) | Nearly $4 \times 10^5$ |
| **FSS Bandpass Unit Cell (Aluminium)** | |
| Conductivity (S/m) | $3.5\times10^7$ S/m |
| **FSS Substrate** | |
| Permittivity | 1.05 |
| Permeability | 1 |

## 4.5 NUMERICAL ANALYSIS AND SIMULATION RESULTS

The designed photoconductive dipole antenna at 1.5THz frequency is simulated using CST Microwave Studio, and then three resonance frequencies have been observed as shown in Figure 4.3, at 1.3THz, 1.58THz and 1.87THz. Mathematically, these frequencies are computed using the expression $f_r = c/(2l_e[(1+\varepsilon_d)/2]^{1/2})$, where $f_r$ is the resonance frequency, $c$ is the speed of light in vacuum, $l_e$ is the effective length of dipole antenna and $\varepsilon_d$ is the dielectric permittivity of LT-GaAs superstrate of photoconductive dipole antenna. With the computation of effective length of dipole antenna, the width of the coplanar stripline is also considered as shown in Figure 4.2(a) top-view of photoconductive dipole antenna, then $l_e$ = $L_2$ +L+ $L_2$ = 50μm and for $\varepsilon_d$ = 13.26 with LT-GaAs superstrate of photoconductive dipole antenna, the resonating frequency $f_r$ = 1.124 THz. However, if the effective length, is considered equal to the separation between the coplanar striplines, $l_e$ = L = 30μm the resonating frequency $f_r$ = 1.87 THz. However, there is a small deviation seen from the simulated results of return loss in the lower resonant frequency values which may be caused by the effect of relative dielectric permittivity of the GaAs substrate of thickness 10μm placed below the LT-GaAs superstrate. The return loss values at 1.3 THz, 1.58 THz and 1.87 THz are -11.54dB, -22.26dB, and -15dB with 10dB impedance bandwidth of 13.9GHz, 35.8GHz and 20.1GHz, respectively. Further, in order to achieve an antenna configuration with improved antenna performance, it is important to study the effect of the slot size of FSS unit-cell and the effect of using variable size bandpass FSS array on the performance parameters of photoconductive dipole antenna.

### 4.5.1 Effect of slot size on antenna performance parameters

When a bandpass FSS is placed below the photoconductive dipole antenna, firstly, the effect of varying the slot size and s/λ ratio of FSS bandpass unit-cell with different array sizes in the values of S-parameters of antenna configurations are observed as mentioned in Table 4.1, Table 4.2 and Table 4.3, respectively. For the comparison, the simulated results for the smallest value of s/λ= 0.01 with 2μm slot size and for largest value of s/λ= 0.04 with 8μm slot size corresponding to 300×300$\mu m^2$ FSS substrate area are shown in Figure 4.3.

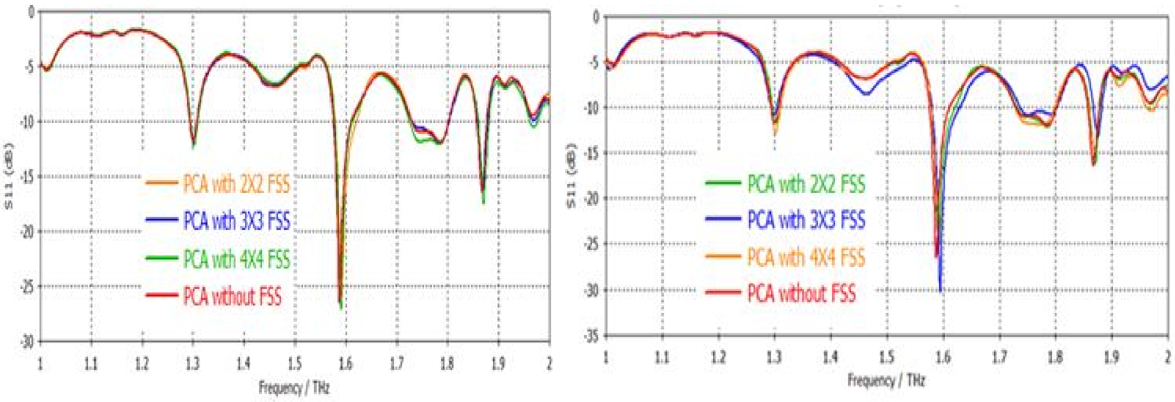

**(a)** **(b)**

**Figure 4.3: The frequency response of S-parameter of the proposed antenna with different FSS configurations at (a) s/λ = 0.01 and s = 2μm and (b) s/λ = 0.04 and s = 8μm.**

For the small slot size, s = 2μm, at 1.3 THz, the return loss of the proposed antenna with 2×2 FSSs, 3×3 FSSs and 4×4 FSSs confuguration are -11.76dB, -11.97dB, and -12.23dB, respectively and the corresponding 10dB impedance bandwidth are 13.8GHz, 14.2GHz and

14.6GHz. However, at 1.58 THz, the return loss of the proposed antenna with 2×2 FSSs, 3×3 FSSs and 4×4 FSSs confuguration are -25.40dB, -24.34dB and -27.08dB with 10dB impedance bandwidth of 42.2GHz, 36.4GHz and 35.7GHz, respectively. Similarly, at 1.87 THz, the values are -16.07dB, -16.13dB and -17.51dB with 10dB impedance bandwidth of 19.4GHz, 20GHz and 21GHz, respectively. Here, it can be concluded from the observed results that for all the three resonant frequency values, the return loss for photoconductive dipole antenna with FSS below the antenna is showing significant increase in its respective values in comparison to that of the photoconductive dipole antenna without FSS. With incresed slot size, s = 8µm, at 1.3 THz, the return loss values are -11.38dB, -10.79dB, and -12.68dB for 2×2 FSSs, 3×3 FSSs and 4×4 FSSs, respectively and the corresponding 10dB impedance bandwidth are 13.7GHz, 10.9GHz and 16.5GHz. However, at 1.58 THz, with these FSS configurations, the corresponding S-parameters are -21.02 dB, -17.44dB and -19.58dB with 10dB impedance bandwidth of 42.5GHz, 49.5GHz and 33.3GHz, respectively. Similarly, at 1.87THz, the values are -16.24dB, -11.65dB and -14.93dB with 10dB impedance bandwidth of 18.8GHz, 15GHz and 18.4GHz, respectively. For quick comparison of the values of return loss and 10dB bandwidth is presented in Table 4.5. It is observed from the obtained results that for all the three resonant frequency values, the return loss for photoconductive dipole antenna having 4×4 FSSs structure below the antenna is illustrating significantly improved values. Moreover, at 1.58THz 3×3 FSSs with slot size 8µm, a bandwidth with almost 50GHz is obtained.

**Table 4.5: The return loss (dB) and 10-dB impedance bandwidth (GHz) comparison of various FSS array structure used below the PCA.**

| Frequency (THz) | Parameter | PCA without FSS | FSS placed below the ground plane of PCA with 8.65µm air gap distance and slot size $s = 2\ \mu m$ | | | FSS placed below the ground plane of PCA with 8.65µm air gap distance and slot size $s = 8\ \mu m$ | | |
|---|---|---|---|---|---|---|---|---|
| | | | *PCA with* $(2 \times 2)$ *FSS* | *PCA with* $(3 \times 3)$ *FSS* | *PCA with* $(4 \times 4)$ *FSS* | *PCA with* $(2 \times 2)$ *FSS* | *PCA with* $(3 \times 3)$ *FSS* | *PCA with* $(4 \times 4)$ *FSS* |
| 1.3 | Return Loss (dB) | -11.54 | -11.76 | -11.97 | -12.23 | -11.38 | -10.79 | -12.68 |
| | 10dB Bandwidth (GHz) | 13.9 | 13.8 | 14.2 | 14.6 | 13.7 | 10.9 | 16.5 |
| 1.58 | Return Loss (dB) | -22.26 | -25.40 | -24.34 | -27.08 | -21.02 | -17.44 | -19.58 |
| | 10dB Bandwidth (GHz) | 35.8 | 42.2 | 36.4 | 35.7 | 42.5 | 49.5 | 33.3 |
| 1.87 | Return Loss (dB) | -15 | -16.07 | -16.13 | -17.51 | -16.24 | -11.65 | -14.93 |
| | 10dB Bandwidth (GHz) | 20.1 | 19.4 | 20 | 21 | 18.8 | 15 | 18.4 |

Furthermore, with an increase in the value of slot size, the capacitive effect of FSS array gets increased and this causes the increase in the width of the scattering parameter at resonating frequency 1.58 THz. However, the simulation results for directivity and gain values remain almost same at the resonant frequencies when these three types of FSS bandpass array structure (2×2, 3×3 and 4×4) is individually placed below the photoconductive dipole antenna, as shown in Figure 4.4 and Figure 4.5.

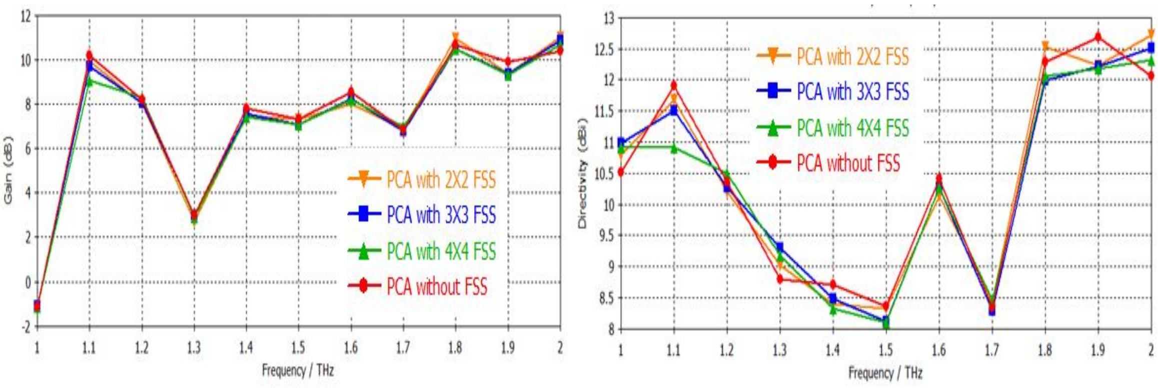

(a) (b)

**Figure 4.4: The frequency response with different FSS configuration of the proposed antenna over the (a) gain and (b) directivity for the chosen values of s/λ = 0.01 and s = 2μm.**

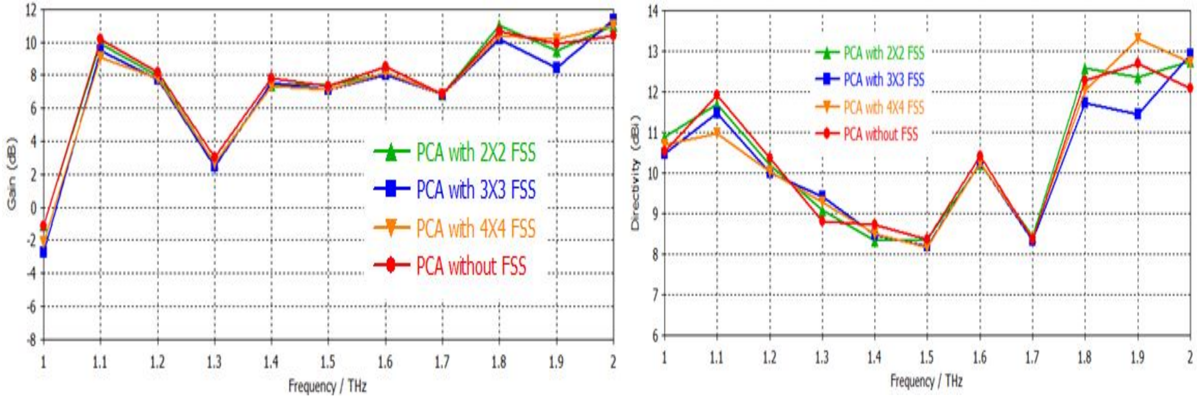

(a) (b)

**Figure 4.5: The frequency response with different FSS configuration of the proposed antenna over the (a) gain and (b) directivity for chosen values of s/λ = 0.04 and s = 8μm.**

The values of gain and directivity at operating frequency of our designed photoconductive dipole antenna are shown in Table 4.6.

**Table 4.6: The gain (dB) and directivity (dBi) comparison of various FSS array structure used below the Photoconductive dipole antenna (PCA).**

| Antenna Performance Parameter | PCA without FSS | PCA with 2×2 FSS | PCA with 3×3 FSS | PCA with 4×4 FSS |
|---|---|---|---|---|
| Gain (dB) at 1.5THz with s = 2μm | 7.29 | 7.34 | 7.08 | 7.07 |
| Gain (dB) at 1.5THz with s= 8μm | 7.29 | 7.38 | 7.09 | 7.11 |
| Directivity (dBi) at 1.5THz with s = 2μm | 8.36 | 8.32 | 8.12 | 8.09 |
| Directivity (dBi) at 1.5THz with s= 8μm | 8.24 | 8.36 | 8.18 | 8.15 |

As duscussed in preceeding sections, for THz sensing and imaging application there is a requirement of highly directive photoconductive dipole antenna at THz frequencies to obtain a high resolution image of detected hidden explosive material. Therefore, to enhance the gain and directivity of photoconductive dipole antenna, an array of FSS bandpass structure is placed above the photoconductive dipole antenna at the air gap distance of 8.65μm from the Ti-Au dipole antenna structure of photoconductive dipole antenna and the observed effect on the antenna performance parameters is discussed below.

### 4.5.2 Effect of FSS as Superstrate

With the use of bandpass FSS above and below the photoconductive dipole antenna, the resonance peaks shifts to higher frequencies and their number has also been increased as shown in Figure 4.6. It has been observed from the simulated results that the FSS has the ability to enhance the performance of photoconductive dipole antenna at 1.5THz because of the electromagnetic wave collimation effect of the effectively low refractive indexed metamaterial and is prominent while using FSSs as superstrate.

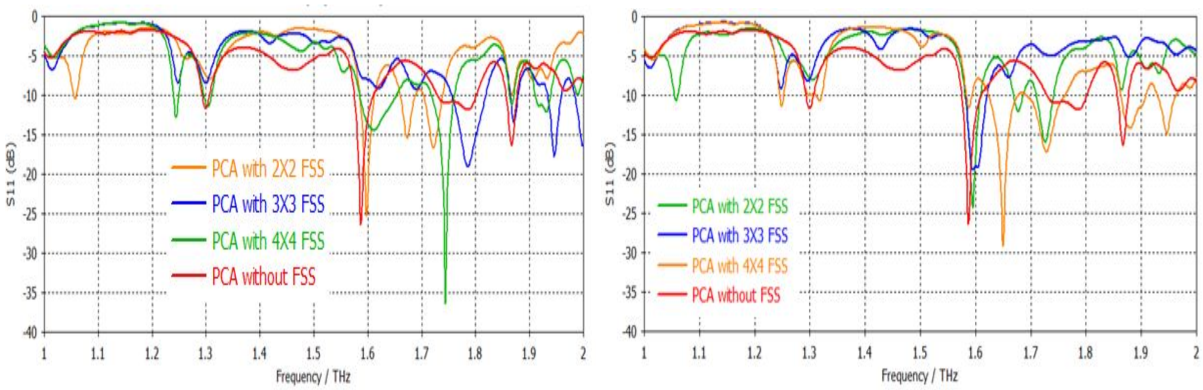

**(a)** **(b)**

**Figure 4.6: The S-parameters for different configuration of FSS over (a) s/λ = 0.01 and s = 2μm and (b) s/λ = 0.04 and s = 8μm.**

For the small slot size, s = 2μm, at 1.3 THz, only 4×4 FSSs bandpass structure shows the resonant peak with return loss -11.66dB with 10-dB impedance bandwidth of 14.5GHz. At 1.59 THz, 2×2 FSSs bandpass structure shows the resonant peak of -25dB with 27.3GHz impedance bandwidth alongwith two more shifted resonant peaks at 1.673 THz and 1.722 THz having return loss values -15.41dB and -16.74dB, respectively. The 10-dB impedance bandwidth at these resonant peaks are 27.7GHz and 35.4GHz, respectively. Similarly, for 3×3 FSSs bandpass structure, the resonance peak is at 1.744 THz with return loss -36.45dB and 42.7GHz 10 dB impedance bandwidth. The 3×3 FSSs bandpass structure is also showing the a resonant peaks at 1.87 THz and 1.94 THz with return loss -17.73dB and -17.76dB with 10dB impedance bandwidth 26GHz and 25GHz, respectively. In case of 4×4 FSSs bandpass structure, the resonant peaks are observed at 1.24 THz, 1.3 THz, 1.61 THz and 1.785 THz with -12.81dB, -11.66dB, -14.46dB and -19.04dB & 9 GHz, 14.5GHz, 68 GHz and 62.8GHz 10dB impedance bandwidth, respectiely. Moreover, at 1.87 THz, only 4×4 FSSs bandpass structure is resonating with return loss -10.57dB and 8GHz 10dB impedance bandwidth. At 1.93 THz, there is one more resonant peak being obsered for 4×4 FSSs bandpass structure with return loss -12.15dB and 28GHz 10dB impedance bandwidth From these results, it is easy to say that the use of 4×4 FSSs structure as superstrate as well as same structure below the photoconductive dipole antenna, not only shows the resonant peaks at same frequency as shown by the photoconductive dipole antenna without FSS structure but also, more resonant peaks with significantly increased 10dB impedance bandwidth are observed.

Further, to check the performance of 4×4 FSSs bandpass structure with photoconductive dipole antenna, the antenna design with FSS unit-cell slot size of 8µm has also been simulated. With incresed slot size, *s* = 8µm, at 1.3 THz, again only 4×4 FSSs bandpass structure shows the resonant peak with return loss -10.72dB and 11GHz 10-dB impedance bandwidth. Along with this, it also shows one more resonant peak at 1.249 THz with return loss -11.36dB and 7.5GHz 10-dB impedance bandwidth. The 2×2 FSSs bandpass structure shows two shifted resonant peaks at 1.6 THz and 1.72 THz having return loss values -12.05dB and -15.99dB, respectively. The 10-dB impedance bandwidth corresponding to these frequencies are 17.6GHz and 31.2GHz, respectively. For 3×3 FSSs bandpass structure the resonance peak is at 1.58 THz with return loss -19.49dB and 38.4GHz 10-dB impedance bandwidth. Moreover, in case of 4×4 FSSs bandpass structure, the resonant peak is observed at 1.65 THz with -25.6dB and 54.2GHz 10-dB impedance bandwidth. These result can be used for the detection of RDX explosive which shows its absoption spectral fingerprint at this frequency [119]. The other resonant band shown by 4×4 FSSs is at 1.728 THz with return loss -17.19dB and 71GHz 10-dB impedance bandwidth which can be used to detect the HMX explosive whose spectral fingerprint of absoption is at 1.78 THz for the range 1-2 THz [119]. At 1.87 THz, again only 4×4 FSSs bandpass structure is resonating with return loss -14.16dB and 45.5GHz 10-dB impedance bandwidth. One more resonating band is shown by 4×4 FSSs, and it is located at 1.946 THz with return loss -14.85dB and 33.8GHz 10-dB impedance bandwidth. This result is again useful to detect the RDX explosive which has one more spectral fingerprint of absorption at 1.9 THz [119]. Further with this analysis, it is depicted that by varying the value of s/λ, the desired band of the transmission of signal is attainable.

Moreover, from the simulated results it is observed that when the length of slot (d) is reduced and the slot width (s) is increased, the transmission bandwidth of FSS also gets increased and with the enhancement in the length of the slot (d), the bandwidth decreased in case of bandpass FSS at frequency of operation 1.5THz. This means the bandwidth is inversely related to the length of slot and therefore, with the periodicity of FSS. In this paper, we have chosen two values of slot size $s = 2\mu m$ and $s = 8\mu m$ for comparison of each case for $(2 \times 2)$, $(3 \times 3)$ and $(4 \times 4)$ FSS of Tables 4.1-4.3. From the simulation results, it is observed that with an increase in the value of length of the slot, the resonance frequency shifts downwards. This happens because of the reduction in the quality factor which gets reduced due to change in the capacitive value (where the capacitance is related to the slot width of FSS). For quick comparison of the values of return loss and 10dB bandwidth is presented in Table 4.7.

**Table 4.7: The return loss (dB) and 10-dB bandwidth (GHz) comparison of various FSS array structure used as superstrates above and below the PCA.**

| **Frequency (THz)** | **Parameter** | **PCA without FSS** | **FSS placed above and below the PCA with 8.65μm air gap distance on both sides and slot size $s = 2\ \mu m$** | | | **FSS placed above and below the PCA with 8.65μm air gap distance on both sides and slot size $s = 8\ \mu m$** | | |
|---|---|---|---|---|---|---|---|---|
| | | | *PCA with* $(2 \times 2)$ *FSS* | *PCA with* $(3 \times 3)$ *FSS* | *PCA with* $(4 \times 4)$ *FSS* | *PCA with* $(2 \times 2)$ *FSS* | *PCA with* $(3 \times 3)$ *FSS* | *PCA with* $(4 \times 4)$ *FSS* |
| 1.3 | Return Loss (dB) | -11.54 | No resonant peak at 1.3THz | No resonant peak at 1.3THz | -11.66 | No resonant peak at 1.3THz | No resonant peak at 1.3THz | -10.72 |
| | 10dB Bandwidth (GHz) | 13.9 | | | 14.5 | | | 11 |
| 1.58 | Return Loss (dB) | -22.26 | -25 | Shifted to 1.744THz with -36.45 dB return loss and 42.7 GHz 10dB bandwidth | Shows multiple resonances at 1.61THz and 1.785THz with -14.46dB and -19.04 dB return loss & 68 GHz and 62.8 GHz 10dB bandwidth | Shifted to 1.6THz with -12.05 dB return loss and 17.6 GHz 10dB bandwidth | -19.49 | Shows multiple resonance at 1.65THz and 1.728THz with -25.6 dB, -17.19 dB return loss and 54.2 GHz, 71 GHz 10dB bandwidth, respectively |
| | 10dB Bandwidth (GHz) | 35.8 | 27.3 | | | | 38.4 | |
| 1.87 | Return Loss (dB) | -15 | Resonates at 1.673THz and 1.722THz with -15.41 dB and -16.74 dB return loss& 27.7 GHz and 35.4 GHz 10dB bandwidth, respectively | -17.73 | -10.57 | Shifted to 1.72THz with -15.99 dB return loss and 31.2 GHz 10dB bandwidth | No resonant peak at 1.87THz | -14.16 |
| | 10dB Bandwidth (GHz) | 20.1 | | 26 | 8.0 | | | 45.5 |
| | | | | Also resonates at 1.94 THz with -17.76 dB return loss and 25 GHz 10dB bandwidth | Also resonates at 1.93 THz with -12.15dB return loss and 28 GHz 10dB bandwidth | | | Also resonates at 1.946 THz with -14.85 dB return loss and 33.8 GHz 10dB bandwidth |

In addition to bandwidth and return loss, the other performance parameters like gain and directivity are also important. Therefore, we have illustrated the effect of size of FSS array on the gain and directivity of the photoconductive dipole antenna. Figure 4.7 and Figure 4.8 show the values of gain and directivity for different values of slot size of FSS unit-cell in the frequency range 1-2 THz. Further, with this simulation results, it is observed that there is a significant change in the values of gain as well as directivity of an antenna with the use of FSS superstrate with the photoconductive dipole antenna. By using FSS as superstrate along with the FSS structure of same size below the photoconductive dipole antenna, with equal air gaps from the antenna, results the formation of cavity-resonator-type antenna at 1.5 THz. The enhancement in gain and directivity at the frequency of operation of the resulting antenna configuration occurs because of the electromagnetic wave collimation effect of the effectively low refractive indexed metamaterial inside the cavity. Moreover, with the reduction in periodicity of FSS, the transmission bandwidth gets increased and the directivity gets decreased. This is the reason due to which at some values of frequency in the range 1-2 THz, $(2 \times 2)$ FSS shows better gain and directivity in comparison to that of $(4 \times 4)$ FSS.

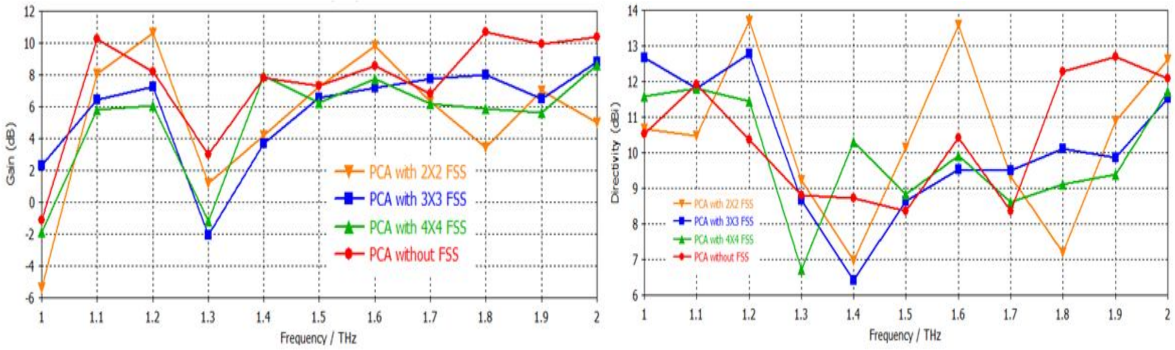

**(a)** **(b)**

**Figure 4.7: The frequency response of the proposed antenna for different FSS configuration over (a) gain and (b) directivity for chosen value of s/λ =0.01 and s = 2µm.**

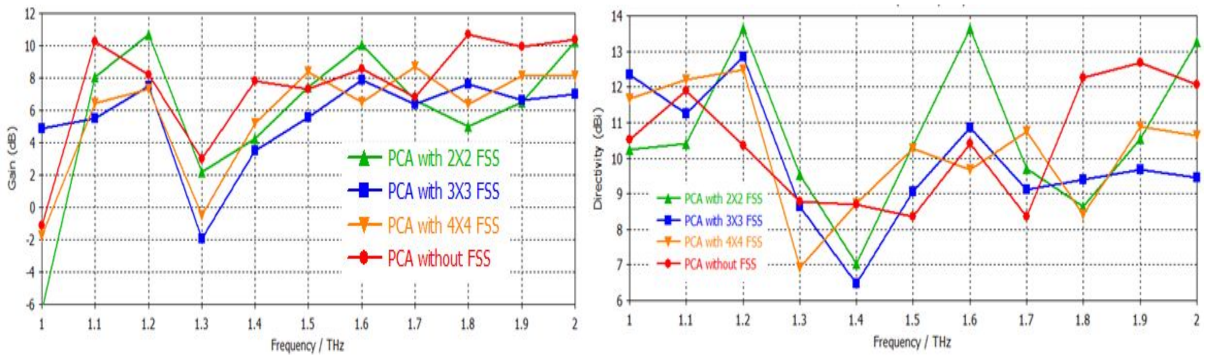

**(a)** **(b)**

**Figure 4.8: The frequency response for different configuration of FSS over the (a) gain and (b) directivity for chosen values of s/λ =0.04 and s = 8µm.**

As the proposed antenna configuration has been designed to use for detection of explosive particular for which has its spectral fingerprint at 1.5 THz, therefore the values of gain and directivity are tabulated in Table 4.8. It is clearly observed that by using 4×4 FSSs bandpass structure with slot size 8µm, the value of gain and directivity has been increased.

**Table 4.8: The gain (dB) and directivity (dBi) comparison of various FSS array structure used as superstrates with Photoconductive dipole antenna (PCA).**

| Antenna Performance Parameter | PCA with 2×2 FSS | PCA with 3×3 FSS | PCA with 4×4 FSS |
|---|---|---|---|
| Gain (dB) at 1.5THz with s = 2µm | 7.26 | 6.55 | 6.26 |
| Gain (dB)at 1.5THz with s=8µm | 7.41 | 5.56 | 8.38 |
| Directivity (dBi) at 1.5THz with s = 2µm | 10.12 | 8.63 | 8.81 |
| Directivity (dBi)at 1.5THz with s=8µm | 10.36 | 9.07 | 10.27 |

The other important antenna performance parameter has been considered for highly directive antenna is the front-to-back ratio (FBR). Therefore, a comparison of FBR for all configurations of photoconductive dipole antenna with different sized FSS array is shown in Figure 4.9. It is illustrated that at 1.5 THz the FBR ratio has also been improved significantly with the use of 4×4 FSSs bandpass structure with photoconductive dipole antenna.

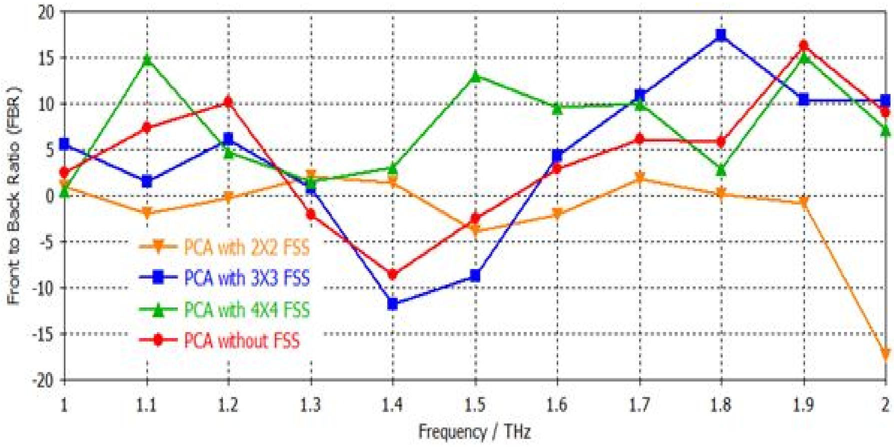

**Figure 4.9: The frequency response over front-to-Back Ratio (FBR) for chosen values of s/λ =0.04 and s = 8µm.**

In general, with various array configurations of FSS used with photoconductive dipole antenna and simulated using CST Microwave Studio reveals that when the periodicity, *P* is close to the wavelength ($\lambda$ = 200µm, as in proposed antenna design), multiple resonances are acheived. Therefore, the analysis procedure perhaps be used in the design of multi-resonance FSS structure [229]. It is also observed from the simulation results that for wideband selection smaller slot size is required. However, for the high directivity and less return loss, the periodicity of FSS structure has to be very small in comparison to that of the wavelength and the slot size must be large enough to transmit the selected frequency. Therefore, the band of operation of FSS bandpass array is mainly influenced by the slot length (*d*) and slot size (*s*). When the slot length is reduced and slot size is increased, the transmission bandwidth of FSS gets increased. However, with an increase in the slot length, the bandwidth reduces with fixed value of periodicity (*P*) of FSS unit-cell. Therefore, with the use of different sized FSS bandpass unit-cell for array configuration, the resonance condition of the structure can be used to detect other explosives which shows their spectral fingerprints in the range of 1-2 THz.

## 4.6 PROPOSED PHOTOCONDUCTIVE DIPOLE ANTENNA WITH 4×4 FSS BANDPASS SUPERSTRATE

On the basis of proposed simulated results as discussed in preceeding sections on S-parametrs, gain and directivity are related to three types of array configurations of FSS bandpass structure with photoconductive dipole antenna. For the detection of explosive corresponding to its prominent spectral fingerprint absorption peaks, it is useful to design photoconductive antenna with 4×4 FSSs bandpass structure placed above as well as below the antenna. The electric field pattern in the principle planes obtained from the simulation result is shown in Figure 4.10. For both the principle planes, the maximum electric field is obtained in main lobe direction at 180°with main lobe magnitude of 20.8 dBV/m. The 3-dB angular width of 47.8°and 11.5° is obtained in E- and H-plane, respectively.

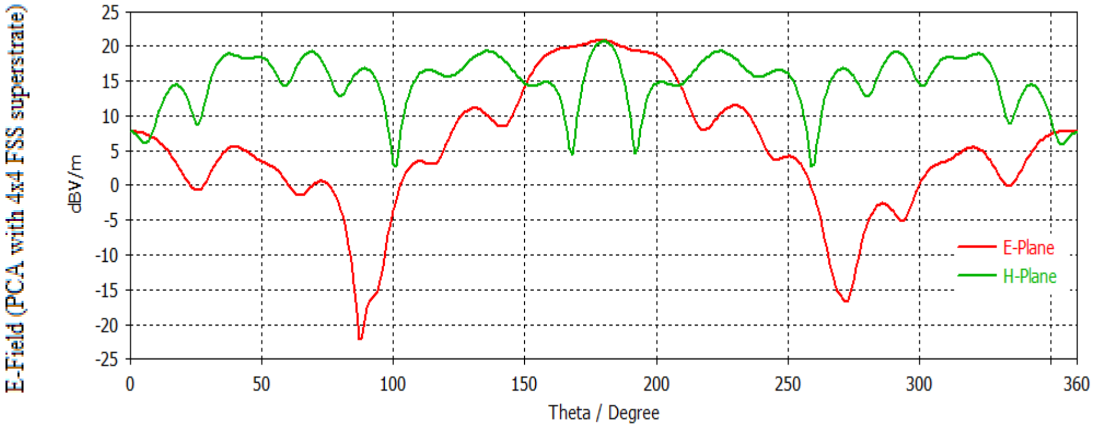

**Figure 4.10: The electric field of PCA at 1.5THz in both principle planes with 4×4 FSS in E-plane and H-plane.**

The directivity of an antenna depends on the electric field as:

$$D(\theta,\varphi) = \frac{4\pi}{\Omega_A}|E_{norm}(\theta,\varphi)|^2 \tag{4.15}$$

where $D(\theta,\varphi)$ is the directivity of the antenna configuration. $\Omega_A = \iint |E_{norm}(\theta,\varphi)|^2 \sin\theta \, d\theta d\varphi$ is the beam solid angle and $|E_{norm}(\theta,\varphi)|$ is the normalized magnitude of the electric field pattern. The gain (G) of the antenna configuration is related to the directivity (D) of the antenna as $G = \eta D$ where η is the radiation effeciency of the antenna. The radiation patterns for gain (dB) and directivity (dBi) obtained in the principle planes for PCA without FSS structure and with 4×4 FSSs structure are illustrated in Figure 4.11 and Figure 4.12. By means of 4×4 FSSs bandpass structure above as well as below the photoconductive dipole antenna, significantly high gain and directivity is achieved which is required for the use of this antenna configuration for THz sensing and imaging of explosives in powder form.

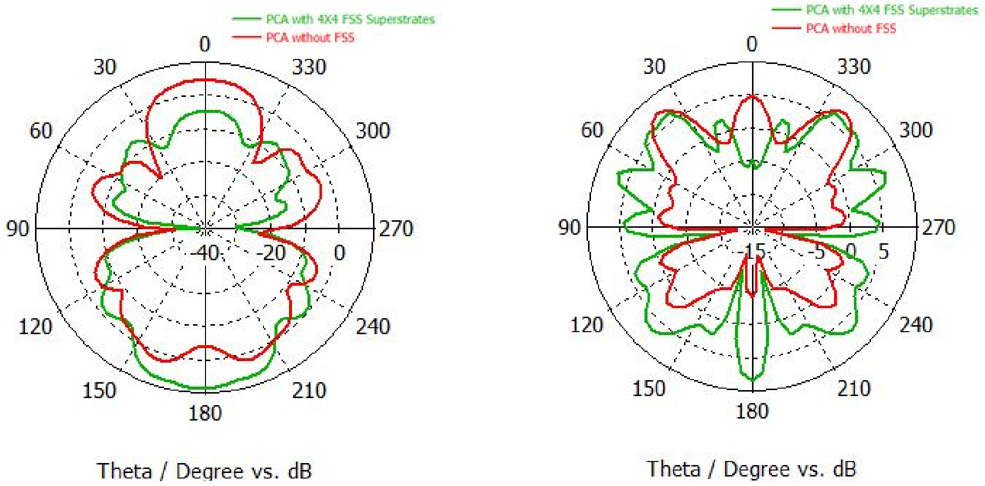

**(a)** **(b)**

**Figure 4.11: The radiation characteristics such as gain (dB) for photoconductive dipole antenna without FSS and with FSS at 1.5THz in (a) E-Plane and (b) H-Plane.**

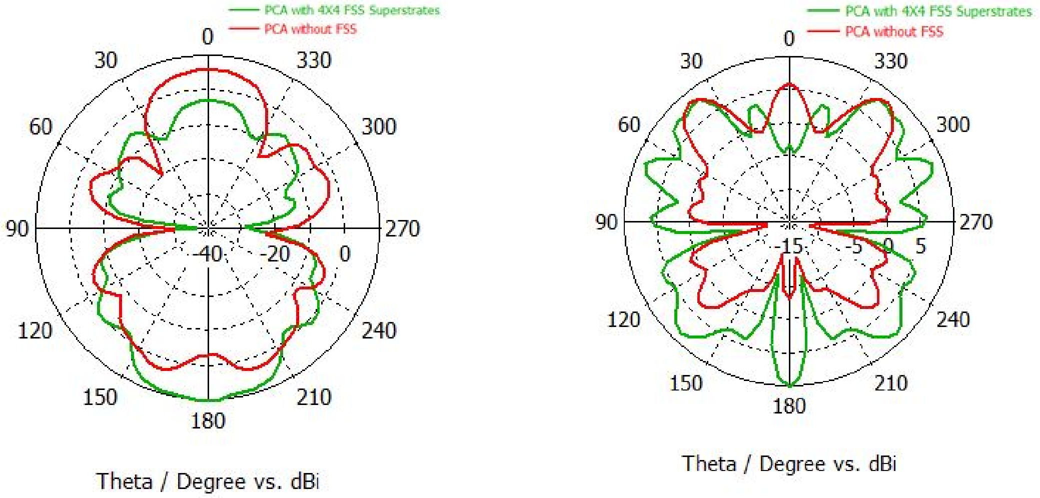

**(a)** **(b)**

**Figure 4.12: The radiation characteristics such as directivity (dBi) for photoconductive dipole antenna without FSS and with FSS at 1.5THz in (a) E-Plane and (b) H-Plane.**

For the antenna configuration without FSS, the gain of antenna is 4.85dB and 7.3dB in E-plane and H-plane, respectively. However, the gain is increased upto 8.38dB in both E-plane and H-plane with the use of 4×4 FSSs bandpass structure (having slot size of unit cell 8μm and $s/\lambda = 0.04$) with photoconductive dipole antenna. Similarly, the directivity of photoconductive dipole antenna without FSS is 5.78dBi and 8.24dBi in E-plane and H-plane, respectively. With the use of 4×4 FSSs bandpass structure (having slot size of unit cell 8μm and $s/\lambda = 0.04$), the directivity of photoconductive dipole antenna has been increased to 10.27dBi in both the principle planes at 1.5THz. The radiation effeciency of the proposed antenna configuration at 1.5THz is 81.6%.

## 4.7 CONCLUSION

In this chapter, the significant improvement of gain and directivity of the photoconductive dipole antenna using bandpass FSSs as a superstrate at terahertz frequency for sensing and imaging is presented. Further, the effect of unit-cell periodicity of FSS on the resonance condition of antenna structure is studied. From the proposed analysis, it is illustrated that by varying the value of $s/\lambda$, the required band of transmission of the THz signal is acheived using FSS superstrate with photoconductive dipole antenna. The proposed photoconductive dipole antenna with 4×4 FSS bandpass structure is used above as well as below the antenna, which demonstrate significant improvement in the performance values of the return loss, gain, directivity and front-to-back ratio. Therefore, the proposed antenna can be used to enhance the imaging capabilities of THz radiating source to address the considerations such as limited depth-of-field (DoF) which is the distance over which an object is considered in focus. However, the performance of the FSS is widely affected by the ohmic losses and various other factors such as surface roughness, dispersion through the conductor and the skin depth, which become prominent in the THz regime of the electromagnetic spectrum. Further, the implementation of array structure of photoconductive dipole antenna with FSS bandpass superstrate is a challenging isuue, which is discussed in detail in the next chapter.

# CHAPTER 5

# DESIGN OF HIGHLY DIRECTIVE LENS-LESS PHOTOCONDUCTIVE DIPOLE ANTENNA ARRAY WITH FREQUENCY SELECTIVE SURFACE FOR TERAHERTZ IMAGING APPLICATIONS

## 5.1 INTRODUCTION

Among the concepts for THz imaging, several non-coherent techniques like micro-bolometer arrays are presented [230] whereas to increase the measurement speeds, such approach provides only limited information owing to lack of information about the phase. However, the pulsed THz systems using coherent techniques offer potential advantage of broad spectral information with a single scan. However, the most basic coherent imaging can be attained by raster scanning a sample through the THz wave focus and creating complete spectroscopic information at each pixel corresponding to the antenna structure. On the other hand, based on the delay line concept, the required lock-in time constants to record a high-quality THz pulse takes a long time to trace out the full image [231] with single antenna. Therefore, to speed up the measurements, there is a requirement of making a THz system for parallel or accelerated measurements. One potential approach to such parallelization is the implementation of multi-antenna setup which reduces the measurement time through deployment of number of THz emitter and detector pairs. On the other hand, the compact size arrays need to be used to counter the increase of system cost [232].

In broadband pulsed THz systems, the optical gating of photoconductive dipole antennas is one of the most accepted THz generation and detection techniques [179, 233-234]. Using the photoconductive dipole antenna sources and detectors in the imaging system, the setup measures a first pulse with no sample in the THz beam path and a second pulse after passing through the sample to be detected which allows the concurrent extraction of the refractive index, the absorption coefficient in addition to the thickness of sample and therefore, provides the detailed information about sample under investigation [235]. The visualization techniques for coherent THz image information comprises of 1) peak-to-peak measurement, 2) time-of-flight measurement, 4) amplitude measurement with single frequency, 5) integrated signal amplitude over a specified frequency range, and 6) evaluation of the dielectric material properties such as the refractive index and absorption coefficient. Therefore, several images revealing different kinds of information can be produced from a single data set corresponding to the phase and amplitude of the detected THz pulses. Likewise, the information such as variation in thickness, humidity, material composition, density, and inclusions of air or other impurities in the sample [236] are obtained.

For the THz imaging applications, the planar THz antennas such as photoconductive antennas have convinced advantages such as: a) low profile, b) easy integration to other planar devices, and c) easy fabrication [52]. Moreover, the fabrication of planar transmission–line [237] at THz frequencies also proves a potential means of the fabrication of array of planar THz antennas. Therefore, a sub-millimeter wave highly directive photoconductive dipole array antenna is presented in this chapter for terahertz (THz) imaging system operating in 1.4-2.2 THz frequency range. The array antenna is formed on a single photoconductive substrate to make it compact and suitable for THz imaging applications. The photoconductive dipole array antenna improves the gain and directivity and therefore, is useful to enhance the imaging capabilities to address the considerations such as limited depth-of-field (DoF) that is the distance over which an object is well thought-out in focus and size-weight-and-power (SWaP) of THz source for imaging applications. These are important considerations for applications like stand-off imaging and surveillance of moving targets where the high angular resolution as well as extended depth-of-field is the key for successful detection of hidden explosives and illicit drugs. A technique of using frequency selective surface with photoconductive array antenna is also presented to further enhance the directivity from the radiating structure to yield high image resolution. Moreover, by means of this technique, radiation energy gets confined to the desired frequency band rather than spreading over a broad spectrum range.

## 5.2 RELATED WORK AND PROBLEM FORMULATION

For imaging application, both the photoconductive antenna and photomixer techniques are considered as a THz sources by THz community. The THz antennas based upon the photoconduction method have several advantages as compared to that of the other THz pulsed sources such as THz antennas work in the room temperature environment and compact which can be used both at the emitter as well as detector of pulsed imaging system. Moreover, the THz generation and detection using photoconductive antenna is useful for coherent THz imaging since this technique has the ability to record THz waves in the time-domain together with both the intensity and phase information which can further be utilized to acquire more details of the target for example spectral and depth information. For photoconductive antenna emitter-detector configuration of THz pulsed imaging system, the potential efforts are made for a high efficiency antenna design and consequently expecting for an increased directivity of a THz photoconductive dipole antenna for sensing and imaging applications. There are several ways to increase the directivity like the use of array configuration [238] or a lens substrate [239]. Earlier, to achieve high image resolution, a lens-based system is generally used with photoconductive dipole antenna for diffraction limited image extraction. Pradarutti et al. [117] have presented THz line detection with sixteen channels using micro-lens array coupled photoconductive antenna array. However, using a large apertures and lens-based systems results into volumetric scale to the THz source and also presents challenges from a portability perspective. On the other hand, the array configuration requires a higher illumination power from multiple femto-second lasers, however, the use of lens substrate limits the number of antenna elements in a specified area which is required in an imaging array. Moreover, with the advent of $Er^+$-doped femto-second fibre lasers have replaced high system cost of using titanium: sapphire lasers for pulsed THz systems based on photoconductive array antenna. In addition, the phenomenon of scanning through array implementation over an extended volume could offer security such as in a public marketplace where the security is essential but a visible display is not so much important. Therefore for this specific application of imaging, a compact array structure of photoconductive dipole antenna with pulsed optical beam from femto-second laser pulse can be used with highly directive ability of the radiating THz source. Even though in THz imaging, multi-pixel approaches provides an acceleration of THz measurements and therefore leads to attractive system architectures in future however stern problems in the alignment process are still major shortcomings which needs to improve.

## 5.3 UNIT-CELL ANTENNA MODELLING

The designed photoconductive dipole antenna as shown in Figure 5.1 consists of a dipole structure of Ti-Au metal with coplanar transmission line of length $\lambda/2$ on both sides of the dipole antenna. The complete metal structure is placed on a thin layer of LT-GaAs superstrate which is stacked on GaAs photoconductive substrate. A ground plane with same material as of antenna is used below the substrate. The antenna has a photoconductive gap length ($G$) and width ($W$) at the centre of dipole antenna of effective length ($L = l_e$) also considered as the distance between the transmission lines, which is biased with a voltage source and is illuminated at the centre by means of femto-second laser pulse. The distance between the transmission-lines or the effective length is determined from the relation $L = c/2nf$, where $c$ is the speed of light in free-space and $n$ is the refractive index of material.

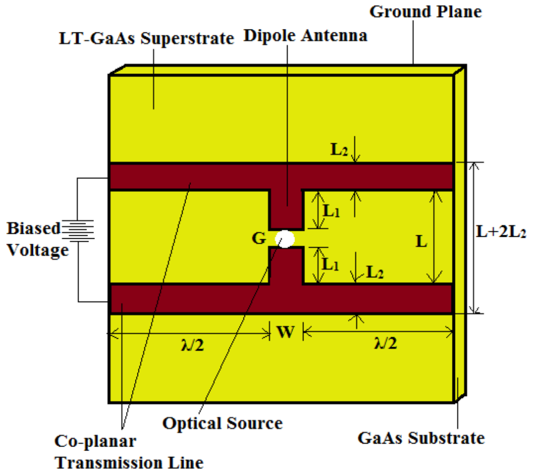

**Figure 5.1: The basic structure of THz photoconductive dipole antenna designed in CST Microwave Studio.**

At 1.5THz, using the value of refractive index $(n = 3.4)$, for GaAs photoconductive material the effective length of dipole antenna $l_e$ is 30µm. The resonant frequency of the photoconductive dipole antenna is determined using the relation $f_r = c/(2l_e[(1 + \varepsilon_d)/2]^{1/2})$, where $f_r$ is the resonating frequency, $\varepsilon_d$ is the dielectric permittivity of GaAs substrate and is taken as 12.9. By putting the values of $c$, $\varepsilon_d$ and $l_e$ , the resonant frequency of the designed photoconductive dipole antenna is 1.95 THz. The length of coplanar transmission line is generally set to be long enough to evade the reflection at the line end. In the designed photoconductive dipole antenna the length of transmission lines is taken as 110 µm with width and thickness 10µm and 0.35µm, respectively. As the emission efficiency is inversely proportional to the photoconductive dipole antenna gap while the bias field and pump-power are considered to be constant. For that reason, it is important to exploit a photoconductive gap as small as possible by focusing the laser beam (optical excitation) very closely to the gap. Therefore, the photoconductive gap is taken as 5µm for small gap photoconductive dipole antenna in all antenna designed configurations in this paper. Moreover, the dimensions of the superstrate, substrate and ground are taken as $(110 \times 110)\ \mu m^2$, with thickness 1µm, 10µm and 0.35µm, respectively.

## 5.4 DESIGN OF PCA ARRAY

In THz imaging applications there is a requirement of efficient THz antennas in terms of losses and cost both at transmitter and receiver side. Moreover, in case of active imaging systems the image acquisition time is required to be small. Therefore, several types of illumination of the object with THz radiation under investigation are selected such as single frequency, multi-frequency or ultra-wide band signals [240]. For such arrangement, highly directive and optimum radiation efficiency from the radiating source is essential. In THz imaging applications to yield enhanced depth-of-field (DoF) for imaging purpose by using THz source the high directivity of the radiating source is required. Various other antenna configurations such as spiral type, bow-tie shape are used however the photoconductive dipole antenna is comparatively attractive as small gap dipole antenna because of its ease of fabrication and are also useful for system-on-chip compatibility in spite of its poor directivity. One straightforward solution to overcome this problem is to design an array of photoconductive dipole antenna [241]. Moreover, the noise equivalent power (NEP) of an imaging array depends on the antenna efficiency. Therefore, it is essential to facilitate high-efficiency on-chip antennas for low system NEP. Such on-chip antennas can be put into practice with different radiation phenomena like above-chip radiation, above-chip with focusing techniques, below-chip radiation, and below-chip with a dielectric lens as discussed in [242]. Here, Uzunkol et al. [242] have recommended the use of above-chip radiation from the THz array source due to low-cost and most robust system as it work with low-cost carrier substrate. Moreover, use of THz system with above-chip also supports the small size-weight-and-power (SWaP) values of THz source for imaging applications. Therefore, the above-chip radiation phenomena and above-chip with focusing technique such as use of frequency selective surface (FSS) to further increase the directivity of the THz array antenna are presented in this chapter. The array designs are shown in Figure 5.2(a) and Figure 5.2(b), respectively.

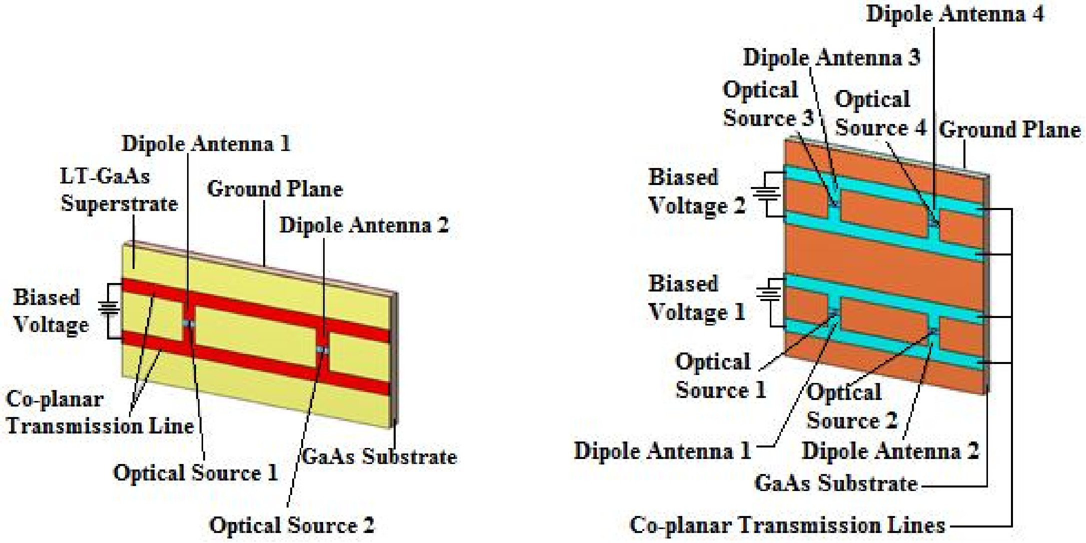

**(a)** **(b)**

**Figure 5.2: Photoconductive dipole antenna array (a) $(1 \times 2)$ photoconductive dipoles, (b) $(2 \times 2)$ photoconductive dipoles.**

Firstly, a $(1 \times 2)$ photoconductive dipole linear array antenna has been designed to determine the radiation parameters. Then, $(2 \times 2)$ photoconductive dipole array antenna is designed to evaluate the radiation parameters such as gain, directivity and radiation efficiency. The spacing between photoconductive dipole antennas in an array arrangement is taken as $\lambda/2$ and for $(2 \times 2)$ photoconductive dipole array the spacing between two sets of transmission line is also considered as $\lambda/2$. Both types of arrays designed are further considered for directivity enhancement using FSS used as superstrate and is placed above the antenna array with air gap separation between the antenna structure and FSS structure. The detailed discussion on making a choice of using FSS is presented in next section.

## 5.5 FREQUENCY SELECTIVE SURFACE FOR PCA ARRAY

To increase the directivity of the elementary dipole and planar antennas in the microwave frequency regime of the spectrum, extremely reflective surfaces as superstrate is extensively used [243-245] and it signify that such type of structure is equally appropriate at the terahertz frequency [209, 246]. In general, the directivity of antenna using FSS is calculated by either using the transverse-equivalent-network model or the resonance-estimation ray tracing technique. However, these techniques can only predict the peak directivity of the antenna at the resonance frequency while the FSS array and the ground plane size are suitably large or semi-infinite. When the FSS array or ground plane is truncated, the directivity of the cavity resonant antenna is reduced, and then these techniques are unable to predict the directivity of the antenna correctly [210]. In such case, using a comparison method the directivity of antenna array can be predicted at the THz frequency using FSS structure.

### 5.5.1 Analysis of unit-cell frequency selective surface

In the photoconductive dipole array antenna design, the FSS structure is used along with $(1 \times 2)$ and $(2 \times 2)$ antenna array configurations to enhance the gain and directivity, therefore, the FSS as bandpass spatial filter is used. The unit-cell design of FSS bandpass is shown in Figure 5.3. The FSS structure made of copper with thickness 0.35μm is followed by the polytetrafluoroethylene substrate. Moreover, in order to keep away from evanescent waves to propagate through the periodic structure, the thickness of dielectric substrate must follow the relation, $h < \lambda_0/20$, where $h$ is the thickness of dielectric substrate of FSS and $\lambda_0$ is the wavelength in free-space. Therefore, the thickness of substrate taken for bandpass FSS is 5μm. The metallic elements signify inductive screens and give rise to total reflection, while apertures in a metallic sheet symbolize capacitive screens and give rise to total transmission.

The performance of bandpass FSS depends on the physical parameters such as the periodicity (*P*) of the unit-cell, length of the slot (*d*), slot width (*s*) and gap between two slots (*g*).

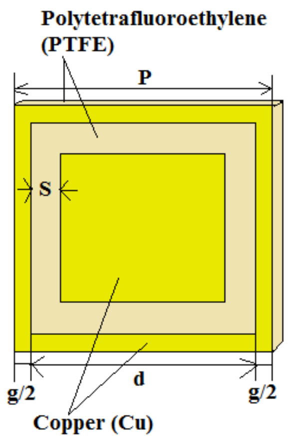

**Figure 5.3: The unit-cell configuration of bandpass FSS with FSS structure made of copper.**

The values of the physical parameters of the FSS unit cell are determined using the synthesis technique of single square loop bandpass FSS at resonance frequency as mentioned in [247]. The relation between the physical parameters of unit cell FSS is described as $4\ (d/\lambda)^2\ ln(2M\lambda/\pi s)\varepsilon_{eff} = w_r{}^2LC$, where $M$ is a constant of equality which is related as $P = M\lambda$ where $\lambda$ is the operating wavelength, $\varepsilon_{eff}$ is the effective dielectric permittivity of the FSS substrate. From the geometry of the unit-cell in Figure 5.3, it is clear that $P - d = g$ and for fixed value of $P$, the value $d$ can be evaluated for the resonance condition $w_r{}^2LC = 1$, using $4\ (d/\lambda)^2\ ln(2M\lambda/\pi s)\varepsilon_{eff} = 1$.

### 5.5.2 Estimation of resonance condition using ray tracing

The ray tracing technique [192] is used to calculate the height $(h)$ of the superstrate above the ground plane of the photoconductive dipole array antenna. When the unit-cell FSS surface as in Figure 5.3, is excited with a normal incident wave, whose electric field is aligned along the length of the surface, then bandpass unit-cell FSS shows the high-transmission property. Such surface property is achieved through simulating the unit-cell FSS in the transient solver of the CST microwave studio. The amplitude as well as the phase of the s-parameter at resonance frequency obtained are: $mag(S_{11}) = 0.845$ and $\emptyset_{FSS} = 16.46^{\circ}$ at resonance frequency. The value of the ground plane phase is determined using the relation $\emptyset_g = \pi - 2tan^{-1}(Z_d tan\,(\beta d)/Z_0)$, where $Z_d$ and $Z_0$ are the characteristic impedance of the dielectric substrate and air, respectively. The value obtained is $\emptyset_g = 49.66^{\circ}$. $\beta$ represents the dielectric phase constant and $d$ is the dielectric substrate thickness. The resonant air-gap length $(l)$ of value 118.37µm is obtained using the relation: $l = (N\lambda/2) + [(\emptyset_{FSS} + \emptyset_g)/\pi](\lambda/4)$ ,where $N$ is an integer number. The schematic view of the designed photoconductive dipole array antennas with $(2 \times 2)$ FSS unit cell structure across each dipole of the photoconductive array antenna is shown in Figure 5.4.

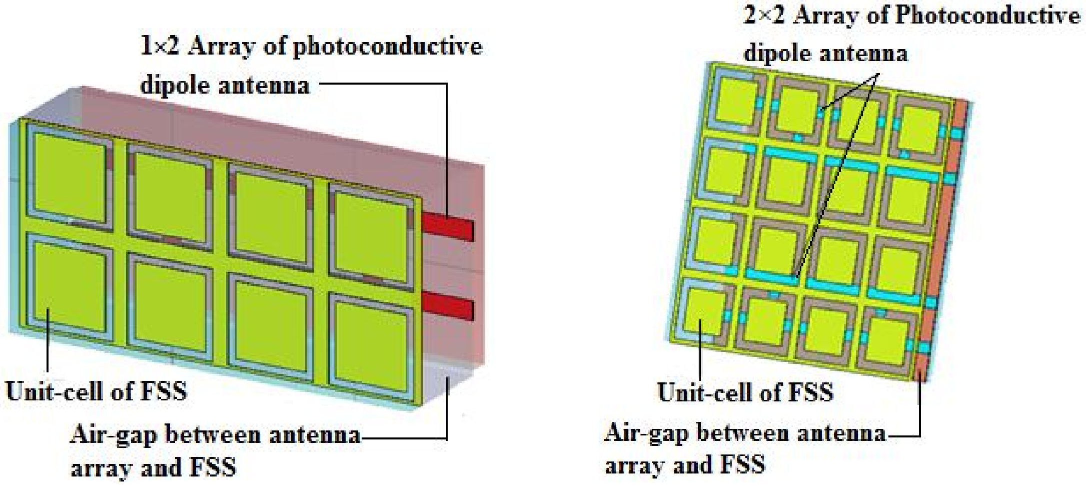

**(a)** **(b)**

**Figure 5.4: Schematic of photoconductive dipole array antenna with $(2 \times 2)$ array of FSS structure across each dipole antenna with periodicity $P = 62.4\mu m$ of unit-cell FSS across (a) $(1 \times 2)$ photoconductive dipole linear array antenna and (b) $(2 \times 2)$ photoconductive dipole array antenna.**

**Table 5.1: The parameters used in simulation performed using the transient solver of CST Microwave Studio.**

| **Parameter** | **Value** |
|---|---|
| **Photoconductive Dipole Antenna (Ti-Au), transmission lines and Ground** | |
| Conductivity (S/m) | $1.6 \times 10^7$ |
| **Superstrate (LT-GaAs)** | |
| Carrier Lifetime, majority carriers (psec) | 0.25 |
| Mobility $(cm^2/Vs)$ | Greater than 200 |
| Permittivity | 13.26 |
| Permeability | 1 |
| Loss tangent (S/m) | 0.006 |
| Electric breakdown field (V/cm) | Greater than $5 \times 10^5$ |
| **Substrate (GaAs)** | |
| Carrier Lifetime, majority carriers (psec) | 0.1 |
| Mobility $(cm^2/Vs)$ | 200 |
| Permittivity | 12.9 |
| Permeability | 1 |
| Loss tangent(S/m) | 0.006 |
| Electric breakdown field (V/cm) | Nearly $4 \times 10^5$ |
| **FSS Bandpass Unit Cell (Copper)** | |
| Conductivity (S/m) | $5.8\times10^7$ S/m |
| **FSS Substrate (Polytetrafluoroethylene)** | |
| Permittivity | 2.08 |
| Loss tangent(S/m) | 0.0004 |

However, the Table 5.1 presents the parameters in terms of material conductivity, dielectric permittivity, magnetic permeability and loss-tangent considered in CST Microwave Studio for simulating the antenna configurations. The results of single unit, array antenna implementation of (1 × 2) and (2 × 2) modeling, design and simulation for photoconductive dipole antenna and implementation of highly-reflective bandpass FSS superstrate are presented in next section.

## 5.6 NUMERICAL ANALYSIS AND SIMULATION RESULTS

The designed single unit of photoconductive dipole antenna at 1.95THz frequency is simulated using transient solver of CST Microwave Studio, and the 10-dB impedance bandwidth of 317.1GHz is obtained as shown in Figure 5.5, with S-parameter magnitude of -21.88dB.

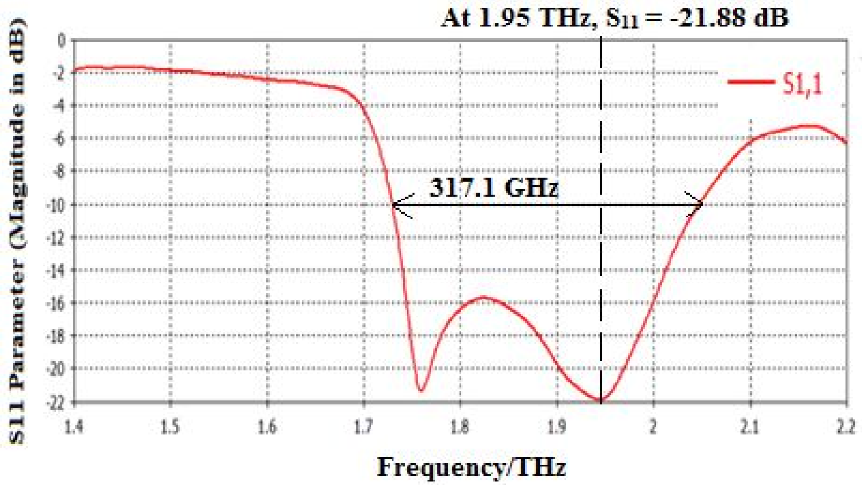

**Figure 5.5: The frequency response of S-parameter for simple photoconductive dipole antenna for 1.4-2.2 THz.**

The radiation patterns for gain (dB) and directivity (dBi) obtained in the principle planes for photoconductive dipole antenna is illustrated in Figure 5.6.

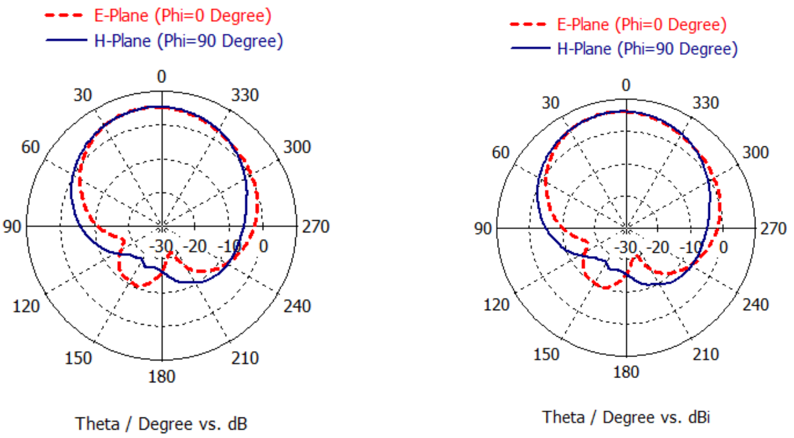

(a) (b)

**Figure 5.6: The radiation characteristics of single photoconductive dipole antenna at 1.95THz (a) gain (dB) in E- and H-plane, (b) directivity (dBi) in E- and H-plane.**

The simulated results in Figure 5.6(a) shows the value of gain 5.47 dB in E-plane with main lobe direction at 8.0 degree. The angular width (3-dB) is 72.3 degree with the side lobe level -16.4 dB. However, in H-plane, the gain is 5.35 dB with its main lobe direction 5.0 degree. The angular width (3-dB) is 82.2 degree having a side lobe level -22.3 dB. In Figure 5.6(b), the directivity in E-plane is 6.25 dBi with main lobe direction 8.0 degree. The angular width (3-dB) is 72.3 degree and the side lobe level is -16.4 dB and in H-plane, the directivity is 6.14 dBi with its main lobe direction 5.0 degree. The angular width (3-dB) is 82.2 degree having a side lobe level -22.3 dB. The radiation efficiency and total efficiency obtained are 0.84 and 0.83, respectively, with current density of $1.06 \times 10^{7} A/m^{2}$. It is clearly observed from simulated results as shown in Figure 5.6 and the theory of operation discussed in previous section for a single photoconductive dipole antenna, the gain and directivity values are very small inspite of its wide band of operation. Therefore, there is a requirement to use the array technique to increase the values of gain and directivity so that the simple THz photoconductive dipole antenna can be used in imaging applications. Initially, a linear array implementation of photoconductive dipole antenna is proposed. In this, the photoconductive dipoles are constructed with common bias and ground plane and are placed at $\lambda/2$ spacing, which makes the fabrication easy. The antenna geometry is placed on a $220 \times 110 \mu m^{2}$ area of photoconductive substrate. The simulation results obtained in terms of radiation patterns for gain and directivity is shown in Figure 5.7. The simulated results in Figure 5.7(a) shows the radiation pattern of gain 5.86 dB in E-plane with main lobe direction at 1.0 degree. The angular width (3-dB) is 27.6 degree and the side lobe level is -3.3 dB. However, in H-plane, the gain is 5.83 dB with its main lobe direction 359.0 degree. The angular width (3-dB) is 82.2 degree having a side lobe level -17 dB.

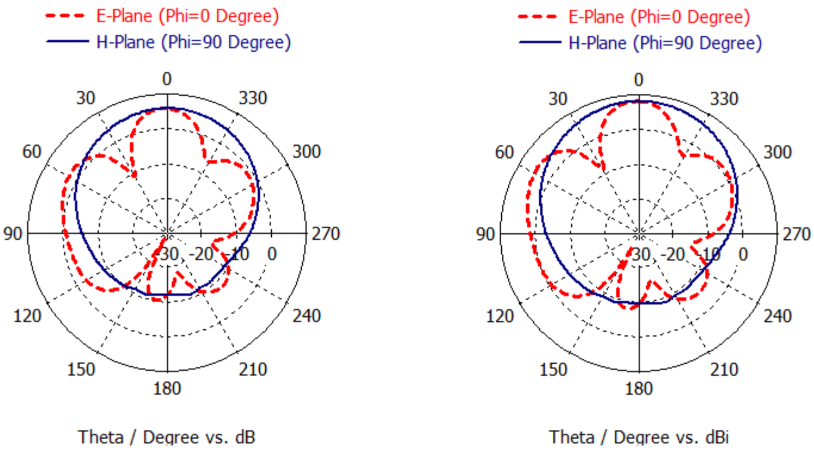

**(a)** **(b)**

**Figure 5.7: The radiation characteristics of $(1 \times 2)$ photoconductive dipole array antenna at 1.95THz (a) gain (dB) in E- and H-plane, (b) directivity (dBi) in E- and H-plane.**

Likewise, the simulated results as in Figure 5.7 (b) show the directivity in E-plane of 8.14 dBi with main lobe direction at 1.0 degree. The angular width (3-dB) is 27.6 degree and the side lobe level is -3.3 dB and for H-plane, the directivity is 8.11 dBi with its main lobe direction 359.0 degree. The angular width (3-dB) is 82.2 degree having a side lobe level -17 dB. The radiation efficiency and total efficiency obtained are 0.72 and 0.59, respectively, with current density of $2.37 \times 10^7 A/m^2$. It is observed that with the increase in dipole antenna elements in linear form, the directivity gets increased by 2dBi but there is not much increase in the gain value. Moreover, the radiation efficiency of the $(1 \times 2)$ photoconductive linear dipole array antenna decreases and it affects the total efficiency of the array antenna. The main reason for the enhancement in the directivity is the increase in the current density across the two dipoles of linear array arrangement.

However, for imaging application, an optimum gain and radiation efficiency values are also required. Therefore, the FSS structure is used as superstrate with $(1 \times 2)$ array antenna which is placed at a height of 118.37µm from the ground plane of the photoconductive dipole array antenna. The radiation patterns obtained from the simulation result are shown in Figure 5.8. Figure 5.8(a) shows the simulated results for gain with value 7.74 dB in E-plane and main lobe direction at 1.0 degree. The angular width (3-dB) is 31.1 degree and the side lobe level is -10.2 dB. However, in H-plane, the gain is 7.73 dB with its main lobe direction 359.0 degree. The angular width (3-dB) is 65.7 degree having a side lobe level -10.3 dB. The directivity in E-plane is 10.8 dBi with main lobe direction at 1.0 degree as shown in Figure 5.8(b). The angular width (3-dB) is 31.1 degree and the side lobe level is -10.2 dB and in H-plane, the directivity is 10.8 dBi with its main lobe direction 359.0 degree.

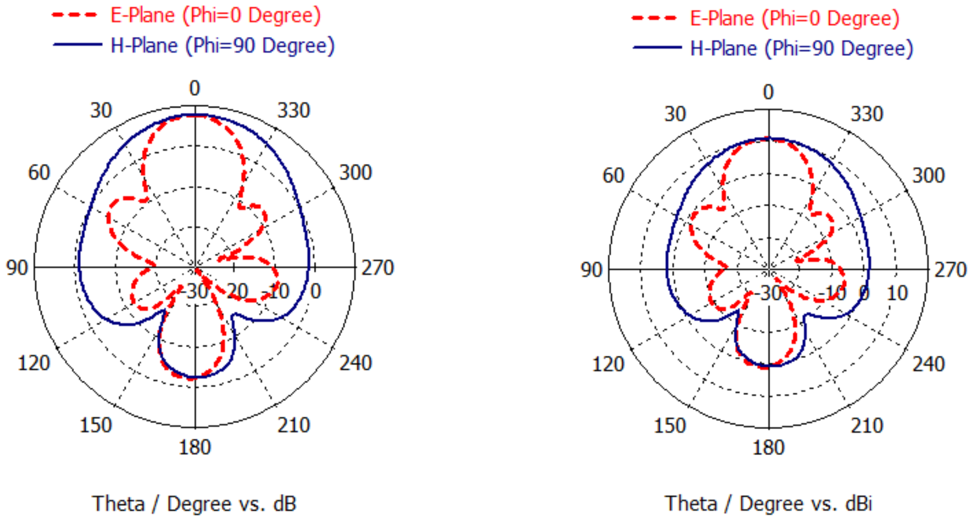

**(a)** **(b)**

**Figure 5.8: The radiation characteristics of $(1 \times 2)$ photoconductive dipole array antenna with FSS superstrate at 1.95THz (a) gain (dB) in E- and H-plane, (b) directivity (dBi) in E- and H-plane.**

The angular width (3-dB) is 65.7 degree having a side lobe level -10.3 dB. The radiation efficiency and total efficiency obtained are 0.72 and 0.59, respectively, with current density of $2.6 \times 10^7 A/m^2$. The use of FSS as superstrate with photoconductive dipole array antenna results into a further increase in the value of directivity by 2.66 dBi and gain by 2 dB. Furthermore, an array of four dipole antennas is designed by using two separate set of transmission lines separated by λ/2 distance. The complete $(2 \times 2)$ photoconductive dipole array antenna is placed on $(220\times\ 220)\mu m^2$ area of photoconductive substrate. The radiation parameters obtained from the simulation results are shown in Figure 5.9.

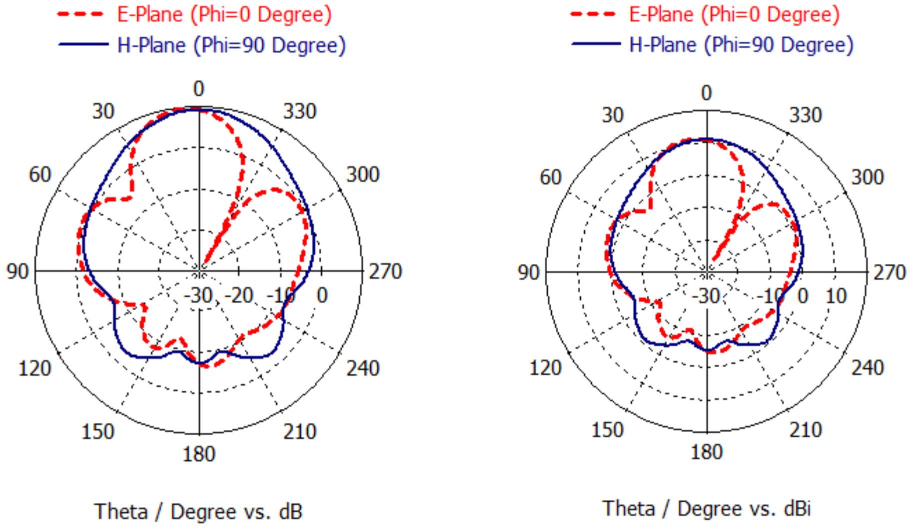

**(a)** **(b)**

**Figure 5.9: The radiation characteristics of $(2 \times 2)$ photoconductive dipole array antenna at 1.95THz (a) gain (dB) in E- and H-plane, (b) directivity (dBi) in E- and H-plane.**

The simulated results, Figure 5.9(a) show the value of gain 9.58 dB in E-plane with main lobe direction at 6.0 degree. The angular width (3-dB) is 32.2 degree with the side lobe level -8.7 dB. However, in H-plane, the gain is 9.15 dB with its main lobe direction 0.0 degree. The angular width (3-dB) is 50.7 degree having a side lobe level -12.5 dB. In Figure 5.9(b), the directivity in E-plane is 11.4 dBi with main lobe direction at 6.0 degree. The angular width (3-dB) is 32.2 degree and the side lobe level is -8.7 dB and in H-plane, the directivity 10.9 dBi with its main lobe direction 0.0 degree is obtained. The angular width (3-dB) is 50.7 degree having a side lobe level -12.5 dB. The radiation efficiency and total efficiency are 0.84 and 0.67, respectively, with current density of $2.7 \times 10^5 A/m^2$. In comparison to $(1 \times 2)$ photoconductive dipole array antenna, the $(2 \times 2)$ photoconductive dipole array antenna shows high gain and directivity values in both principle planes. Moreover, the radiation efficiency and the total efficiency of the array configuration are also increased. To further enhance the radiation parameters of array antenna, the FSS structure is placed above the array configuration. The radiation patterns obtained from the simulation are shown in Figure 5.10. The gain with value 10.4 dB in E-plane and main lobe direction at 3.0 degree having angular width (3-dB) 26.5 degree and the side lobe level -6.4 dB is shown in Figure 5.10(a). However, in H-plane, the gain is 10.3 dB with its main lobe direction 0.0 degree. The angular width (3-dB) is 27.0 degree having a side lobe level -9.2 dB. In Figure 5.10(b), the directivity obtained in E-plane is 13.2 dBi with main lobe direction at 3.0 degree. The angular width (3-dB) is 26.5 degree and the side lobe level is -6.4 dB and in H-plane, the directivity is 13.1 dBi with its main lobe direction 0.0 degree. The angular width (3-dB) is 27.0 degree having a side lobe level -9.2 dB. The radiation efficiency and total efficiency obtained are 0.79 and 0.52, respectively, with current density of $2.74 \times 10^5 A/m^2$. Therefore, the use of FSS as superstrate with photoconductive dipole array antenna results into further increase in the value of directivity by 3dBi.

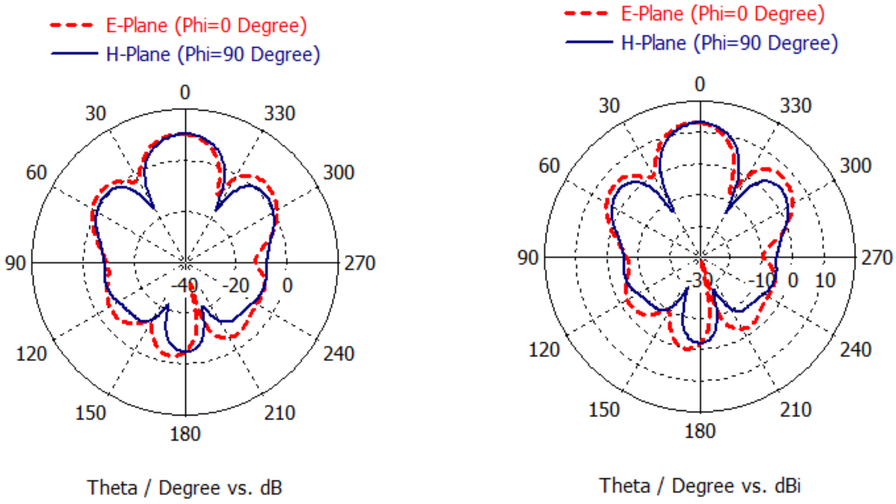

(a) (b)

**Figure 5.10: The radiation characteristics of $(2 \times 2)$ photoconductive dipole array antenna with FSS superstrate at 1.95THz (a) gain (dB) in E- and H-plane, (b) directivity (dBi) in E- and H-plane.**

## 5.7 CONCLUSION

Because of the limitation of small gain and directivity values of single photoconductive dipole antenna, we have explored linear and planar array implementation of photoconductive dipole antennas for THz imaging application. However, for imaging applications there is a requirement of planar and compact THz antenna sources which provide high directivity so as to achieve large DoF for improved image resolution. In this paper, a technique of using frequency selective surface to further enhance the radiation parameters of array configuration of photoconductive dipole antenna is discussed. The resulting array antenna configuration produced a radiation efficiency of 72% for $(1 \times 2)$ and 84% for $(2 \times 2)$ PCA array, respectively. The directivity of 10.8dBi and 13.2dBi is obtained using FSS superstrate with $(1 \times 2)$ and $(2 \times 2)$ photoconductive dipole array antenna in comparison with 6.25dBi directivity of single photoconductive dipole antenna at the resonance frequency 1.95THz. The proposed array antenna with FSS results into planar configuration of highly directive radiating THz source for the imaging applications.

# CHAPTER 6

# BEAM STEERING CHARACTERISTICS OF HIGHLY DIRECTIVE PHOTOCONDUCTIVE DIPOLE PHASED ARRAY ANTENNA

## 6.1 INTRODUCTION

An antenna array permits us to attain high gain with multiple radiating elements and a phased array additionally put forward the possibility to shape as well as steer the beam without varying the array geometry. Conventionally, phased arrays have been used in defence applications, mainly for radar, but their deployment is changing with an increase in demand for the commercial use, especially with the arrival of on-the-move access to high bandwidth data. However, the challenge lies in realizing the radiating characteristics using phased array antenna while keeping the undesired effects such as the mutual coupling between the elements because of their proximity to each other. The design of large phased arrays is characteristically accomplished in two steps where firstly, the element design is obtained by optimizing the active element impedance and active element pattern over all frequencies along with scan angles. Secondly, the array design is authenticated by inspecting the real scanning behaviour besides including the non-periodic structure effects. Each of aforementioned stages/steps entitles for an appropriate array design functionality which makes the design of phased arrays, at both the cell and full array level substantially more efficient and powerful.

For commercial imaging applications, fast measurements are required when the THz imaging technique is applied especially to the scrutiny of large number of targets [248]. Conventionally, the THz images are obtained by moving the samples in the course of the focused beam or else by scanning the emitter and detector in the case of immobile samples. However, efficient methods of steering the THz beam are essential for practical applications as the measurement speed is primarily limited by the speed of the mechanical devices used in conventional imagers. Moreover, due to the lack of active system components required to dynamically manage free-space THz wave propagation still obstruct the broad scale accomplishment of THz imaging systems. The potential of dynamically controlling the propagation of free-space THz waves such as by steering or focusing the THz beams is the solution to a multiplicity of THz imaging applications [249]. For example, in THz sensing and imaging application, beam steering devices can be used to substitute the mechanical scanning stages and therefore can results into a significant increase in the measurement speed as well as the level of system integration [250, 251]. Further, a high speed beam steering technique also provides new avenues to several THz measurement methodologies, for instance, single pixel THz imaging depending on compressed sensing [252], imaging of moving objects through tracking the targets by means of THz beams, etc. Primarily, to achieve THz beam steering, the simple technique is to either use mechanical scanning device or deployment of spatial phase modulator which generally operates as phased arrays and are extensively used in microwave regime of electromagnetic spectrum. In Figure 6.1, by combining the THz antenna with graphene THz phase shifters, a reconfigurable transmitter [253] with functionalities such as beam forming and beam steering is illustrated.

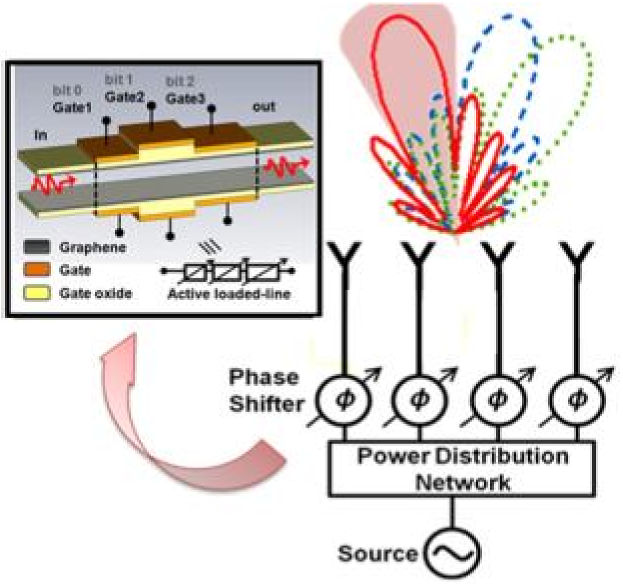

**Figure 6.1: THz phased array antenna based on graphene phase shifters [253].**

Initially, the functioning of THz phase shifters has been realized on free carrier excitation in semiconductors [254-256]. In this, the dielectric characteristics of the semiconductor material gets modulated through the externally excited free charge carriers which results into phase shift in the THz wave while passing through the medium. However, according to the Kramers-Kronig relation, the real part as well as the imaginary part of the dielectric of the semiconductor material is dependent on each other, therefore the phase modulation as a consequence generate insertion losses which are inseparable from the amplitude modulation [257-259]. Similarly, structures based on resonant metamaterial phase shifters are designed and reported in [260-262] in addition to the phase shifters using liquid crystals [263-265] which operate at high voltages and low speed. Another simple approach of beam steering which has been explored in our proposed antenna configuration is the phase controlled optical excitation of arrays of small-gap photoconductive dipole antenna. Since this approach necessitates ultrashort optical laser pulse excitation, therefore the number of potential applications is limited. However, as reported in [266-268] by using the spatial dispersion of ultrafast laser pulse the phenomena of beam steering from THz antenna array has been achieved. Moreover, in THz active imaging systems, the deployment of THz antenna array with beam steering capability reduces the image acquisition time [269].

For millimetre-wave imaging systems, several measurement setups are anticipated which are either based on a rotary scanner with variable radius [270], or mechanically rotating mirrors with linear movement of the probe [271]. A THz imaging setup based on THz frequency scanning antenna array is shown in Figure 6.2 wherein a Vector Network Analyzer (VNA) is used with auxiliary circuitry [272]. The object under inspection (placed on an azimuthal positioned) is illuminated with the help of frequency scanning antenna array whose main radiating lobe is steered in the vertical plane [273]. The beam is progressively rotated to evaluate the response for multiple incidence angles. To receive the reflected power from the object under inspection which is illuminated from different vertical segments, a directive horn antenna is used. For the implementation of power divider as well as the phase shifting network, a rectangular waveguide structure is used and open ended waveguides are used as radiating elements.

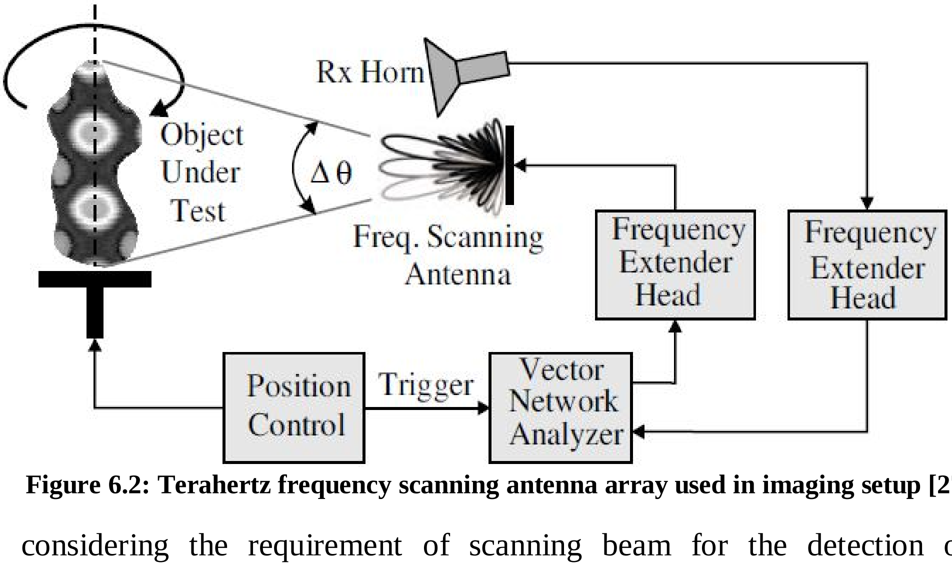

**Figure 6.2: Terahertz frequency scanning antenna array used in imaging setup [273].**

Therefore, considering the requirement of scanning beam for the detection of hidden explosives carried by some moving object, there is a need for exploring the beam steering characteristics of highly directive THz antenna array with features of compact size and planar profile.

## 6.2 RELATED WORK AND PROBLEM FORMULATION

A phased array antenna comprises of a number of radiating elements (antennas) each with a phase shifter. Beams are produced by shifting the phase of the signal emitted from each radiating element resulting into constructive or destructive interference in order to steer the beams in the desired direction. Therefore, the phenomenon of beam steering is about varying the direction of the main lobe of a radiation pattern created from the phased array antenna. However, in case of radio systems the beam steering is achieved by either switching the antenna elements or by altering the relative phases of the RF signals which derives the antenna elements. A THz beam steering technique has been exemplify from strip-line photoconductive phased array antenna using difference in frequency generation obtained from two spatially dispersed beams produced from an ultrafast laser [248]. Similarly, THz beam steering has been achieved by means of varying the angle of incidence of an ultrafast laser beam on to the photoconductive wide-gap area. However, such technique offers difficulty in quick steering of the THz beam over a wide angle [274]. By applying periodic bias voltages across the photoconductive antenna array, the THz beam generated from the antenna configuration also gets steered as reported in [275]. The only limitation to such technique is to control the period of the bias in addition to the period of the optical pulses in the train at each tuning frequency. Beam steering using micro-mechanical method [276] has also been reported. Using optical phase shifters [277], the microwave beam is steered through the control of phase of each element with high speed and wide angle.

With electronic 2-D steering capability (i.e. covering azimuth plane and elevation plane), a fixed frequency Fabry-Perot antenna configuration is demonstrated in [278]. The authors of [278] have presented the beam steering capability of antenna by controlling the leaky-wave propagation constant across the antenna configuration. For THz stand-off imaging, a programmable THz diffraction grating is achieved using array of metallic cantilevers for a wide frequency band 0.15 THz to 0.9 THz [249]. The authors of [249] have used the switching technique between different grating patterns so as to facilitate the tailoring of spatio-temporal profiles of the THz wave which results into steering the THz beam. The beam-steering and beam-forming phenomenon have been presented using array of ultra-wideband antenna elements [279] wherein a mode-locked laser is deployed to synchronize the jitter-free pulses radiated from each antenna element to create a radiated field pattern which gets steerable with the help of optical time delay technique. A scalable transmitter architecture based on distributed active radiation from the distributed active radiator (DAR) is designed at

THz frequency with integrated beam scanning capabilities using silicon [280]. For the desired electromagnetic field profiles, the DAR with self-oscillating active electromagnetic structure contains two loops which carry on out-of-phase currents at the fundamental frequency in addition to the in-phase currents at the second harmonic. The fundamental signal gets spatially filtered, at the same time as the second harmonic is radiated selectively. The simulation results presented in [280] shows that at 0.28 THz, the beam steers in 2-D over 80 degrees in both azimuth and elevation planes.

In this chapter, a novel and simple approach to realize terahertz (THz) dynamic two-dimensional (2D) beam steering antenna configuration based on $(2 \times 2)$ photoconductive dipole phased array antenna with FSS is presented with its operation in the range 1.4 THz - 2.2THz for sensing and imaging the hidden explosives carried by some moving object.

## 6.3 DESIGN OF $(2 \times 2)$ PHOTOCONDUCTIVE DIPOLE PHASED ARRAY ANTENNA WITH FSS

The resonant frequency of the photoconductive dipole antenna is determined using the relation $f_r = \mathrm{c}/(2l_\mathrm{e}[(1+\varepsilon_\mathrm{d})/2]^{1/2})$, where $f_r$ is the resonating frequency, $\varepsilon_d$ is the dielectric permittivity of GaAs substrate and is taken as 12.9. By putting the values of $c$, $\varepsilon_d$ and $l_\mathrm{e}$ , the resonant frequency of the designed photoconductive dipole antenna is 1.95 THz. Figure 6.3 shows the schematic of the four elements of photoconductive dipole antennas forming an array with FSS for improved directivity. Moreover, the dimensions of the superstrate, substrate and ground are taken as $(110 \times 110)\ \mu m^2$, with thickness 1µm, 10µm and 0.35µm, respectively. The spacing between photoconductive dipole antennas in an array arrangement is taken as λ/2 and for $(2 \times 2)$ photoconductive dipole array the spacing between two sets of transmission line is also considered as λ/2. In the designed photoconductive dipole antenna the length of transmission lines is taken as 110 µm with width and thickness 10µm and 0.35µm, respectively. The FSS structure made of copper with thickness 0.35µm is followed by the polytetrafluoroethylene substrate.

Initially, the progressive phase shift is performed in single direction (i.e. along x-axis only), the beam steering occurs in E-plane, whereas only the change in magnitude is observed in H-plane. Similarly, on performing the progressive phase shift along y-axis, the beam steering occurs in H-plane along with slight change in magnitude of the main lobe of radiation characteristics in E-plane. However, when the progressive phase shift is applied in both the directions (x-axis and y-axis) then the beam steering phenomenon occurs in both the principle planes (E-plane and H-plane). The progressive phase shift is applied to the optical sources and the biased voltage sources are kept constant with 30 Volts.

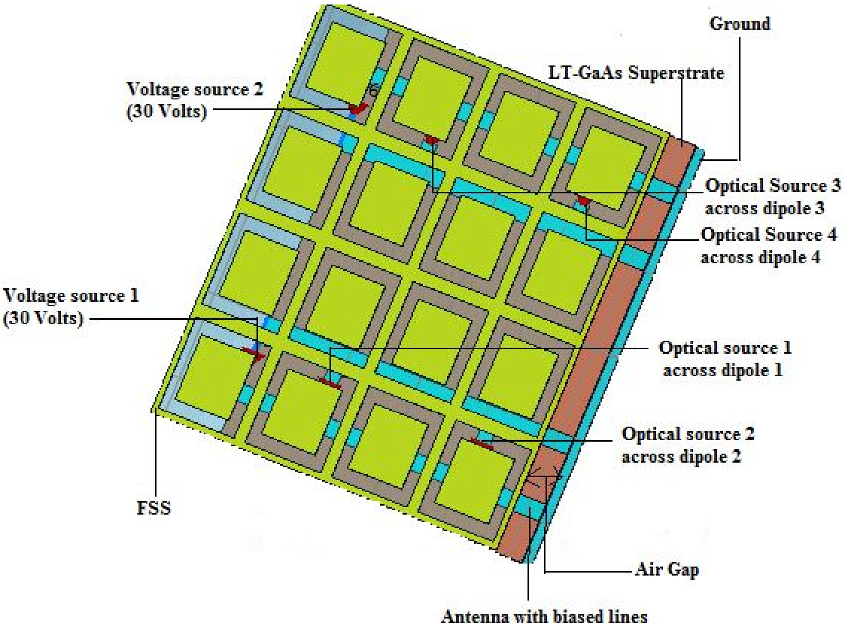

**Figure 6.3: Schematic of $(2 \times 2)$photoconductive dipole array antenna used for phased array implementation for the beam steering phenomenon operating at 1.95 THz.**

The uniform current distribution is applied individual array element and the results are investigated for the scan angle $(0° \leq \theta \leq 40°)$ where $\varphi = 0°$. The enhancement in the directivity of small-gap photoconductive dipole antenna is achieved by using frequency selective surface (FSS).

## 6.4 NUMERICAL ANALYSIS AND SIMULATION RESULTS

Initially, $(2 \times 2)$ small-gap photoconductive dipole antenna array with operating frequency 1.95THz is simulated using transient solver of CST Microwave Studio. The radiation patterns 3-D as well as 2-D view for directivity (dBi) are obtained in the principle planes for the array configuration and is illustrated in Figure 6.4. The simulated results in Figure 6.4(b) show the value of directivity 14.2dBi in E-plane with main lobe direction at 354.0 degree. The angular width (3-dB) is 29.8 degree with the side lobe level – 9.6 dB. However, in H-plane, the directivity is 13.7 dBi with its main lobe direction 0 degree. The angular width (3-dB) is 26.6 degree having a side lobe level -11.7 dB. Here, the amplitude and the phase of all the four optical sources are kept uniform with 1W power input and 0 Degree phase shift. However, for the design of phased array antenna and its simulation in CST Microwave Studio, the Transient solver supports several excitation patterns such as uniform distribution, cosine distribution, Taylor distribution, Binomial distribution, Chebyshev distribution and Gaussian distribution.

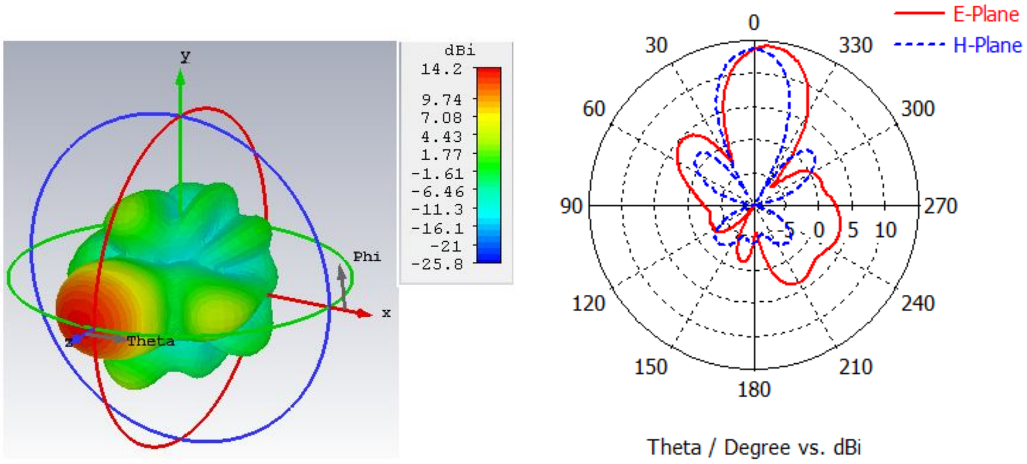

(a) (b)

**Figure 6.4: A far-field radiation pattern (directivity) (a) 3-D view, (b) 2-D view, in both principle planes E and H.**

To determine the beam steering characteristics of the $(2 \times 2)$ small-gap photoconductive dipole antenna array configuration for THz imaging application, we kept the input power from the optical source constant for the simplicity and ease of feasibility of the antenna configuration for the desired application. Moreover, a uniform distribution of amplitude excitation is provided to each unit of photoconductive dipole array antenna. First of all, the progressive phase shift of 10 Degree is performed along x-axis of the optical sources across the respective antenna elements. Figure 6.5 shows the simulation results wherein the beam steering occurs in E-Plane and in H-Plane only the magnitude changes.

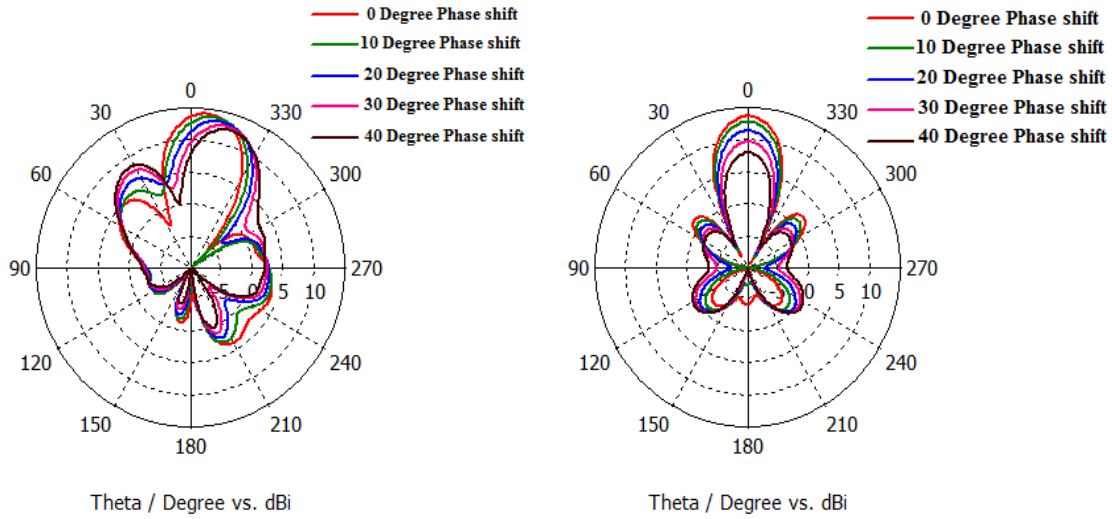

(a) (b)

**Figure 6.5: The radiation characteristics (directivity, dBi) with beam steering at angle 0° (red), 10° (green), 20° (blue), 30° (pink), and 40° (brown) progressive phase shift along x-axis of $(2 \times 2)$ small-gap photoconductive dipole array antenna in (a) E-Plane, and (b) H-Plane.**

Moreover, it is observed that the proposed phased array antenna configuration successfully scans for $(0^\circ \le \theta \le 40^\circ)$ where $\varphi = 0^\circ$. The values obtained from the progressive 10 Degree phase shift along the x-axis for both the principle planes are listed in Table 6.1.

**Table 6.1: The beam steering of $(2 \times 2)$ small-gap photoconductive dipole array antenna for $(0^\circ \le \theta \le 40^\circ)$ with $10^\circ$ progressive phase shift along x-axis of the array antenna configuration.**

| Progressive Phase Shift (Degree) | | Main lobe directivity (dBi) | Main lobe direction (Degree) | Angular width (dB) | Side-lobe level (dB) |
|---|---|---|---|---|---|
| 0 | E-Plane | 14.2 | 354 | 29.8 | -9.6 |
| 10 | | 13.8 | 351 | 30.9 | -8.7 |
| 20 | | 13.3 | 348 | 31.1 | -6.8 |
| 30 | | 12.9 | 345 | 31.2 | -5.1 |
| 40 | | 12.4 | 342 | 31.4 | -3.9 |
| 0 | H-Plane | 13.7 | 0 | 26.6 | -11.7 |
| 10 | | 12.7 | 0 | 26.7 | -11.7 |
| 20 | | 11.4 | 0 | 26.8 | -11.4 |
| 30 | | 9.71 | 0 | 26.9 | -9.4 |
| 40 | | 7.93 | 0 | 27.0 | -7.3 |

While scanning at every 10 Degree, the main beam shifts by 3 Degrees in E-Plane, however, only the magnitude of the main lobe reduces in the H-Plane. However, the decrease in the magnitude of the main lobe of the radiation characteristics is contributed by the occurrence of the mismatch between the antenna and the feed network with an increase in the phase shift. To determine the beam steering phenomenon in H-Plane, the progressive phase shift is applied along the y-axis of the $(2 \times 2)$ small-gap photoconductive dipole antenna array configuration.

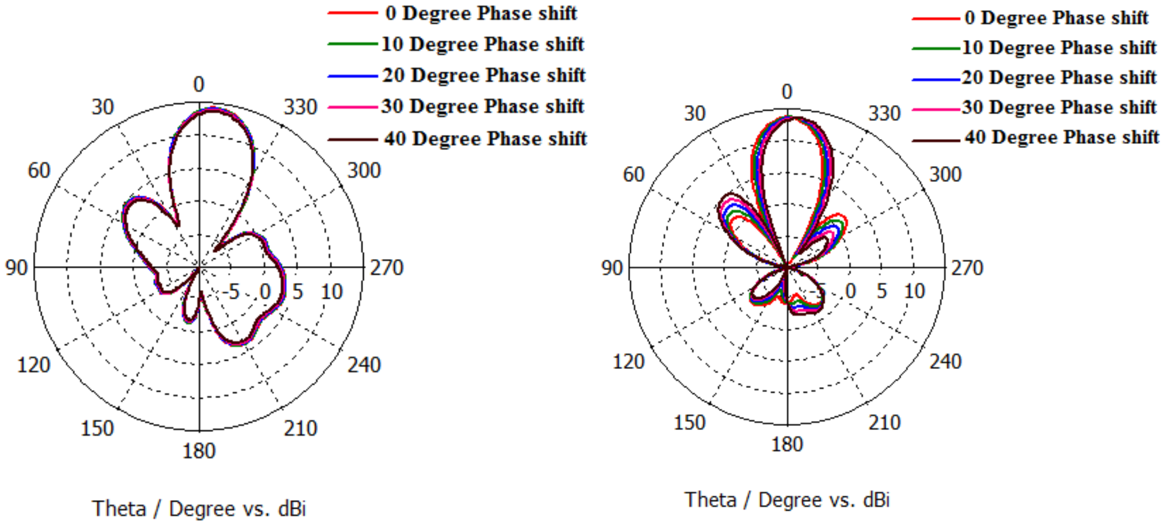

(a) (b)

**Figure 6.6: The radiation characteristics (directivity, dBi) with beam steering at angle $0^\circ$ (red), $10^\circ$ (green), $20^\circ$ (blue), $30^\circ$ (pink), and $40^\circ$ (brown) progressive phase shift along y-axis of $(2 \times 2)$ small-gap photoconductive dipole array antenna in (a) E-Plane, and (b) H-Plane.**

For the scanning range $(0^\circ \leq \theta \leq 40^\circ)$ with $\varphi = 0^\circ$ and $10$ Degree progressive phase shift along y-axis of the array configuration, it is observed that the beam steering occurs in H-Plane with very small change in the magnitude of main lobe of the radiation characteristics in E-Plane. The simulation results are shown in Figure 6.6 and are listed in Table 6.2, respectively. On providing the $10$ Degree progressive phase shift along y-axis of the array antenna elements, the main beam shifts by 1 Degrees in H-Plane, however, only the slight change in the magnitude of the main lobe is observed in the E-Plane.

**Table 6.2: The beam steering of $(2 \times 2)$ small-gap photoconductive dipole array antenna for $(0^\circ \leq \theta \leq 40^\circ)$ with $10^\circ$ progressive phase shift along x-axis of the array antenna configuration.**

| Progressive Phase Shift (Degree) | | Main lobe directivity (dBi) | Main lobe direction (Degree) | Angular width (dB) | Side-lobe level (dB) |
|---|---|---|---|---|---|
| 0 | E-Plane | 14.2 | 354 | 29.8 | -9.6 |
| 10 | | 14.2 | 354 | 29.8 | -9.6 |
| 20 | | 14.1 | 354 | 29.9 | -9.5 |
| 30 | | 13.9 | 354 | 30.0 | -9.4 |
| 40 | | 13.7 | 354 | 30.1 | -9.2 |
| 0 | H-Plane | 13.7 | 0 | 26.6 | -11.7 |
| 10 | | 13.6 | 359 | 26.7 | -11.3 |
| 20 | | 13.5 | 358 | 26.8 | -10.3 |
| 30 | | 13.4 | 357 | 26.8 | -9.4 |
| 40 | | 13.3 | 356 | 26.9 | -8.6 |

For the THz imaging application to detect the hidden explosives there is a need of scanning the suspicious object in both the principle planes. Therefore, it is essential to make the ability of the highly directive small-gap photoconductive dipole array antenna to scan or to steer the main lobe of the radiation characteristics in both the principle planes. To achieve this, the progressive phase shift is applied in both directions i.e. in the X-Y-directions of the $(2 \times 2)$ small-gap photoconductive dipole antenna array antenna configuration.

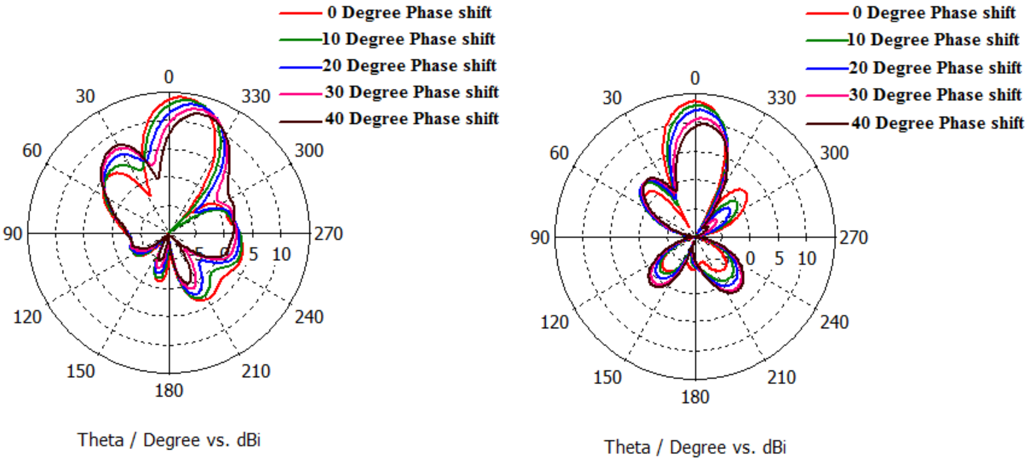

(a) (b)

**Figure 6.7: The radiation characteristics (directivity, dBi) with beam steering at angle $0^\circ$ (red), $10^\circ$ (green), $20^\circ$ (blue), $30^\circ$ (pink), and $40^\circ$ (brown) progressive phase shift along x-y-axis of $(2 \times 2)$ small-gap photoconductive dipole array antenna in (a) E-Plane, and (b) H-Plane.**

Figure 6.7 shows the simulation results wherein the beam steering occurs in both E-Plane and H-Plane, respectively. The values obtained from the progressive 10 Degree phase shift along the X-Y-axis for both the principle planes are listed in Table 6.3.

**Table 6.3: The beam steering of $(2 \times 2)$ small-gap photoconductive dipole array antenna for $(0° \leq \theta \leq 40°)$ with $10°$ progressive phase shift along x-y-axis of the array antenna configuration.**

| Progressive Phase Shift (Degree) | | Main lobe directivity (dBi) | Main lobe direction (Degree) | Angular width (dB) | Side-lobe level (dB) |
|---|---|---|---|---|---|
| 0 | E-Plane | 14.2 | 354 | 29.8 | -9.6 |
| 10 | | 13.8 | 351 | 30.9 | -8.7 |
| 20 | | 13.2 | 348 | 31.1 | -6.7 |
| 30 | | 12.6 | 345 | 31.0 | -5.1 |
| 40 | | 11.9 | 342 | 31.5 | -3.8 |
| 0 | H-Plane | 13.7 | 0 | 26.6 | -11.7 |
| 10 | | 12.9 | 359 | 26.7 | -10.1 |
| 20 | | 12.2 | 358 | 26.9 | -9.1 |
| 30 | | 10.7 | 357 | 27.3 | -7.6 |
| 40 | | 9.7 | 356 | 27.7 | -6.7 |

It is observed from the simulation results that the proposed phased array antenna configuration successfully scans for $(0° \leq \theta \leq 40°)$ with $\varphi = 0°$ and progressive phase shift of 10 Degree in both principle planes provides the beam steering by 3 Degrees and 1 Degree in E-Plane and H-Plane, respectively. Therefore, the obtained beam steering capabilities of highly directive $(2 \times 2)$ small-gap photoconductive dipole array antenna using progressive phase shift at 1.95 THz operating frequency is useful to detect the hidden explosive such as RDX and HMX concealed in some baggage or carried by some object because such explosives show their absorption spectras at this frequency

## 6.5 CONCLUSION

In this chapter, highly directive $(2 \times 2)$ small-gap photoconductive dipole phased array antenna at 1.95 THz is presented which can be used in the detection of hidden explosives in THz imaging application. The scanning of the beam is primarily performed in single direction (x-axis), hence the beam gets steered in one plane, i.e. in E-Plane. With every 10 Degree shift of the scan angle, the highly directive beam gets steered by 3 Degree. However, when the progressive phase shift is applied in y-axis, then scanning of the beam occurs in H-Plane only. In this case, with every 10 Degree shift of the scan angle, the highly directive beam gets steered by 1 Degree in H-Plane with small reduction in the magnitude of beam in the same direction for E-Plane. Moreover, for the full electronic beam steering, there is a requirement to shift the beam in both the principle planes. Therefore, the progressive phase shift is applied along both the x-axis and y-axis. For the scanning range $(0° \leq \theta \leq 40°)$ with $\varphi = 0°$, for every 10 Degree progressive phase shift, the main beam gets steered by 3 Degree in E-Plane and by 1 Degree in H-Plane, respectively.

# CHAPTER 7

## CONCLUSION AND FUTURE SCOPE

Recently, due to unique properties of terahertz wave which are favourable to various applications such as non-ionizing radiation, better resolution than a microwave, unique spectral absorption, and an ability to propagate through many types of materials, is attracting a lot of attention of the researchers and scientists. Further, with significant progress in the generation of pulsed terahertz radiation with its importance to THz spectroscopy for the diagnostics of different materials and media in medicine, biology, security and technology, the powerful research is taking place in the field of terahertz spectroscopy. The most relevant and specific features are a very wide frequency spectrum, the real possibility of generation of extremely short pulses, and direct detection of radiation electric-field strength within the framework of the pulsed THz spectroscopy.

In this thesis, the main aim is to investigate the pulsed terahertz source particularly, the terahertz photoconductive antenna which is employed in pulsed terahertz spectroscopy for imaging applications. The choice of simple dipole antenna with small-gap geometry has been investigated because of its simplicity in fabrication as well as compatible with device integration. The performance limitation of conventional small-gap THz photoconductive dipole antenna with low gain and directivity in addition to the small optical-to-THz conversion efficiency are the major concerns for its use in security application. Therefore, the key modalities of improving small-gap photoconductive dipole antennas performance are identified for imaging applications and variants to improve the directivity of photoconductive dipole antenna are also investigated.

However, the conventional photoconductive dipole antenna shows the low directivity and for the THz imaging applications a highly directive antenna is required. With the use of a simple dipole antenna with thin superstrate and silicon lens, we are able to achieve the directivity of 10.7dBi and radiation efficiency of 91.59% in both E- and H-plane. Further, by employing the proposed equivalent circuit model, the performance of antenna is examined. The effect due to the variation in the photoconductive gap size has been observed for the time-dependent physical phenomenon such as time-dependent source capacitance, source conductance and radiated voltage. Moreover, several techniques are used to increase the directivity of proposed photoconductive dipole antenna. With the use of thin superstrate of LT-GaAs, the directivity of photoconductive dipole antenna is increased by 1.67dBi and on further using a silicon lens with this antenna configuration the directivity is increased by 6.59dBi. For the planar configuration, the use of frequency selective surface (FSS) results an increase in directivity of antenna by 6.16dBi. With the use of silicon lens or frequency selective surface with photoconductive dipole antenna, a uniform value of directivity in two principle plane patterns is achieved. The use of FSS not only keeps the planar profile of antenna array configuration with enhanced directivity but also limits the fabrication complexity as compared to the silicon lens.

Furthermore, for parallelization of THz source in pulsed imaging system to enhance the image acquisition speed, there is a need of array assembly of antenna. For this purpose, the design of (1×2) and (2×2) photoconductive dipole antenna array is proposed. Using array configuration, the directivity is increased by 1.89dBi in E-plane and 2.07dBi in H-plane for (1×2) array assembly and 5.15dBi in E-plane and 4.76dBi in H-plane for (2×2) array assembly. Further, employing FSS as directivity enhancement technique for array assembly the results are also obtained. The directivity is increased by 4.55dBi in E-plane and 4.66dBi in H-plane for (1×2) array assembly with (2X2) FSS and 6.95dBi in E-plane and 6.96dBi in H-plane for (2×2) array assembly with (2X2) FSS. The proposed array antenna with FSS results into planar configuration of highly directive radiating THz source for the imaging applications. For THz imaging application for the detection of hidden explosives, there is a requirement of scanning beam in both the principle planes from the THz source. Therefore, the beam steering characteristics of highly directive (2 × 2) small-gap photoconductive dipole antenna with phased array configuration is explored. When a progressive phase shift of 10 Degree is provided in both x-y-axes, then the beam gets steered by 3 Degrees and 1 Degree in E-Plane and H-Plane, respectively. Such compact size, planar configuration of highly directive small-gap photoconductive dipole phased array antenna is useful in THz imaging application for the detection of hidden/ concealed explosives in baggage or carried by some moving object from the security point of view. With employing this kind of photoconductive antenna, a new imaging scheme can be explored to achieve high imaging resolution, fast imaging speed and low system cost which will be an effective and acceptable terahertz imager for standoff personal screening.

However, there are certain design techniques which can be incorporated in the basic structure of photoconductive dipole antenna to further improve its performance parameters such as the dielectric structure with periodic LT-GaAs strips within gap area and the use of anti-reflection coating materials. The use of plasmonic nano-islands in the gap area of photoconductive dipole antenna can enhance the field generated within the gap due to an increase in the generated photocarriers. A graphene based artificial magnetic conductor for directivity enhancement of photoconductive dipole antenna can be investigated for tuneable antenna applications in THz pulsed imaging system.

Moreover, the proposed THz antenna configurations have been designed for stand-off/ far-field application for the detection of explosives such as RDX, HMX, and PETN carried by people approaching a check-point. For close-range/near-field applications such as screening of mail, packages and baggage there is a need of using THz impulse scanning technique. In such technique, the time-delayed THz signals are generally utilized to stack an image. Therefore, the generation of time-delayed THz beam from the proposed antenna configuration to obtain a fine transverse resolution of an image can further be work upon.

# REFERENCES

[1] X. Zhang, “Terahertz wave imaging: horizons and hurdles,” *Physics in Medicine and Biology*, vol. 47, no. 21, pp. 3667-3677, 2002.

[2] M. Nnagai, K. Tanaka, H. Ohtake, T. Bessho, T. Sugiura, T. Hirosumi, and M. Yoshida, “Generation and detection of terahertz radiation by electro-optical process in GaAs using 1.56$\mu m$ fiber laser pulses,” *Applied Physics Letters*, vol. 85, no. 18, pp. 3974-3976, 2004.

[3] S. S. Dhillon, M. S. Vitiello, E. H. Linfield, A. G. Davies, M. C. Hoffmann, J. Booske, C. Paoloni, M. Gensch, P. Weightman, G. P. Williams, E. C. Camus, D. R. S. Cumming, F. Simoens, I. E. Carranza, J. Grant, S. Lucyszyn, M. K. Gonokami, K. Konishi, M. Koch, C. A. Schmuttenmaer, T. L. Cocker, R. Huber, A. G. Markelz, Z. D. Taylor, V. P. Wallace, J. A. Zeitler, J. Sibik, T. M. Korter, B. Ellison, S. Rea, P. Goldsmith, K. B. Cooper, R. Appleby, D. Pardo, P. G. Huggard, V. Krozer, H. Shams, M. Fice, C. Renaud, A. Seeds, A. Stohr, M. Naftaly, N. Ridler, R. Clarke, J. E. Cunningham, and M. B. Johnston, “The 2017 terahertz science and technology roadmap,” *Journal of Physics D: Applied Physics*, vol. 50, no. 4, pp. 043001/1-49, 2017.

[4] C. Yu, S. Fan, Y. Sun, and E. Pickwell-MacPherson, “The potential of terahertz imaging for cancer diagnosis: a review of investigations to date,” *Quantitative Imaging in Medicine and Surgery*, vol. 2, no. 1, pp. 33-45, 2012.

[5] I. Amenabar, F. Lopez, and A. Mendikute, “In introductory review to THz non-destructive testing of composite mater,” *Journal of Infrared, Millimeter, and Terahertz Waves*, vol. 34, no. 2, pp. 152-169, 2013.

[6] L. A. Skvortsov, “Standoff detection of hidden explosives and cold and fire arms by terahertz time-domain spectroscopy and active spectral imaging,” *Journal of Applied Spectroscopy*, vol. 81, no. 5, pp. 725-749, 2014.

[7] C. Zhang, C. Deng, Y. Zhao, and X. Zhang, “Passive terahertz imager with an opto-mechanical scanner,” *36th International Conference on Infrared, Millimeter and Terahertz Waves (IRMMW-THz)*, pp. 1-2, 2-7 October, 2011, Houston, TX, USA.

[8] E. V. Yakovlev, K. I. Zaytsev, I. N. Dolganova, and S. O. Yurchenko, “Non-destructive evaluation of polymer composite materials at the manufacturing stage using terahertz pulsed spectroscopy,” *IEEE Transactions on Terahertz Science and Technology*, vol. 5, no. 5, pp. 810-816, 2015.

[9] J. Federici and L. Moeller, “Review of terahertz and subterahertz wireless communications,” *Journal of Applied Physics*, vol. 107, no. 11, pp. 111101/ 1-23, 2010.

[10] S. Sy, S. Huang, Y.-X. J. Wang, J. Yu, A. T. Ahuja, Y.-t. Zhang, and E. Pickwell-MacPherson, “Terahertz spectroscopy of liver cirrhosis: investigating the origin of contrast,” *Physics in Medicine and Biology*, vol. 55, no. 24, pp. 7587-7596, 2010.

[11] K. B. Cooper, R. J. Dengler, N. Llombart, T. Bryllert, G. Chattopadhyay, E. Schlecht, J. Gill, C. Lee, A. Skalare, I. Mehdi, and P. H. Siegel, “Penetrating 3-D imaging at 4-and 25-m range using a submillimeter-wave radar,” *IEEE Transactions on Microwave Theory and Techniques*, vol. 56, no. 12, pp. 2771-2778, 2008.

[12] E. K. Rahani, T. Kundu, Z. Wu, and H. Xin, “Mechanical damage detection in polymer tiles by THz radiation,” *IEEE Sensors Journal*, vol. 11, no. 8, pp. 1720-1725, 2011.

[13] P. Mousavi, F. Haran, D. Jez, F. Santosa, and J. S. Dodge, “Simultaneous composition and thickness measurement of paper using terahertz time-domain spectroscopy,” *Applied Optics*, vol. 48, no. 33, pp. 6541-6546, 2009.

[14] T. Yasui, T. Yasuda, K.-i. Sawanaka, and T. Araki, "Terahertz paintmeter for noncontact monitoring of thickness and drying progress in paint film," *Applied Optics,* vol. 44, no. 32, pp. 6849-6856, 2005.

[15] S. Wietzke, C. Jördens, N. Krumbholz, B. Baudrit, M. Bastian, and M. Koch, "Terahertz imaging: a new non-destructive technique for the quality control of plastic weld joints," *Journal of the European Optical Society-Rapid Publications,* vol. 2, pp. 07013/1-5, 2007.

[16] E. Nguema, V. Vigneras, J.-L. Miane, and P. Mounaix, "Dielectric properties of conducting polyaniline films by THz time-domain spectroscopy," *European Polymer Journal,* vol. 44, vol. 1, pp. 124-129, 2008.

[17] D. Banerjee, W. Von Spiegel, M. Thomson, S. Schabel, and H. Roskos, "Diagnosing water content in paper by terahertz radiation," *Optics Express,* vol. 16, no. 12, pp. 9060-9066, 2008.

[18] J. -W. Park, K. -H. Im, D. K. Hsu, J. -A. Jung, and I.-Y. Yang, "Terahertz spectroscopy approach of the fiber orientation influence on CFRP composite solid laminates," *Journal of Mechanical Science and Technology,* vol. 26, no. 7, pp. 2051-2054, 2012.

[19] K. Kawase, T. Shibuya, S. i. Hayashi, and K. Suizu, "THz imaging techniques for nondestructive inspections," *Comptes Rendus Physique,* vol. 11, no. 7-8, pp. 510-518, 2010.

[20] S. -T. Han, W. K. Park, Y. -H. Ahn, W. -J. Lee, and H. S. Chun, "Development of a compact sub-terahertz gyrotron and its application to t-ray real-time imaging for food inspection," *37th International Conference on Infrared, Millimeter, and Terahertz Waves (IRMMW-THz),* pp. 1-2, 23-28 September, *2012*, Wollongong, NSW, Australia.

[21] C. Jördens and M. Koch, "Detection of foreign bodies in chocolate with pulsed terahertz spectroscopy," *Optical Engineering,* vol. 47, no. 3, pp. 037003/1-5, 2008.

[22] Y. L. Hor, J. F. Federici, and R. L. Wample, "Nondestructive evaluation of cork enclosures using terahertz/millimeter wave spectroscopy and imaging," *Applied Optics,* vol. 47, no. 1, pp. 72-78, 2008.

[23] H. Hoshina, Y. Sasaki, A. Hayashi, C. Otani, and K. Kawase, "Noninvasive mail inspection system with terahertz radiation," *Applied spectroscopy,* vol. 63, no. 1, pp. 81-86, 2009.

[24] M. C. Kemp, "Explosives detection by terahertz spectroscopy—a bridge too far?," *IEEE Transactions on Terahertz Science and Technology,* vol. 1, no. 1, pp. 282-292, 2011.

[25] H. Zhong, A. Redo-Sanchez, and X. -C. Zhang, "Standoff sensing and imaging of explosive related chemical and bio-chemical materials using THz-TDS," *International Journal of High Speed Electronics and Systems,* vol. 17, no. 02, pp. 239-249, 2007.

[26] Y. Kurmi and V. Chaurasia, "Hidden explosive detection systems for vehicle," *International Journal of Computer Applications,* vol. 130, no. 10, pp. 16-19, 2015.

[27] M. Lu, J. Shen, N. Li, Y. Zhang, C. Zhang, L. Liang, and X. Xu, "Detection and identification of illicit drugs using terahertz imaging," *Journal of Applied Physics,* vol. 100, no. 10, pp. 103104/1-6, 2006.

[28] J. F. Federici, B. Schulkin, F. Huang, D. Gary, R. Barat, F. Oliveira, D. Zimdars, "THz imaging and sensing for security applications—explosives, weapons and drugs," *Semiconductor Science and Technology,* vol. 20, no. 7, pp. S266-280, 2005.

[29] G. J. Wilmink and J. E. Grundt, "Invited review article: current state of research on biological effects of terahertz radiation," *Journal of Infrared, Millimeter, and Terahertz Waves,* vol. 32, no. 10, pp. 1074-1122, 2011.

[30] A. Amicelle, C. Aradau, J. Jeandesboz, G. Valkenburg, and I. van der Ploeg, "Materialities between security and privacy: A constructivist account of airport security scanners," *Security Dialogue,* vol. 46, no. 4, pp. 326-344, 2015.

[31] E. Heinz, T. May, D. Born, G. Zieger, S. Anders, G. Thorwirth, V. Zakosarenko, M. Schubert, T. Krause, M. Starkloff, and A. Kruger, "Passive submillimeter-wave stand-off video camera for security applications," *Journal of Infrared, Millimeter, and Terahertz Waves,* vol. 31, no. 11, pp. 1355-1369, 2010.

[32] P. U. Jepsen, U. Møller, and H. Merbold, "Investigation of aqueous alcohol and sugar solutions with reflection terahertz time-domain spectroscopy," *Optics Express,* vol. 15, no. 22, pp. 14717-14737, 2007.

[33] J. -H. Son, Terahertz Biomedical Science and Technology: *CRC Press*, 13 June, 2014.

[34] G. J. Wilmink, B. D. Rivest, C. C. Roth, B. L. Ibey, J. A. Payne, L. X. Cundin, J. E. Grundt, X. Peralta, D. G. Mixon, and W. P. Roach, "In vitro investigation of the biological effects associated with human dermal fibroblasts exposed to 2.52 THz radiation," *Lasers in Surgery and Medicine,* vol. 43, no. 2, pp. 152-163, 2011.

[35] J. -H. Son, "Terahertz electromagnetic interactions with biological matter and their applications," *Journal of Applied Physics,* vol. 105, no. 10, pp. 102033/1-11, 2009.

[36] T. C. Bowman, M. El-Shenawee, and L. K. Campbell, "Terahertz imaging of excised breast tumor tissue on paraffin sections," *IEEE Transactions on Antennas and Propagation,* vol. 63, no. 5, pp. 2088-2097, 2015.

[37] Z. D. Taylor, R. S. Singh, D. B. Bennett, P. Tewari, C. P. Kealey, N. Bajwa, M. O. Culjat, A. Stojadinovic, H. Lee, J. P. Hubschman, and E. R. Brown, "THz medical imaging: in vivo hydration sensing," *IEEE transactions on terahertz science and technology,* vol. 1, no. 1, pp. 201-219, 2011.

[38] R. Woodward, V. Wallace, D. Arnone, E. Linfield, and M. Pepper, "Terahertz pulsed imaging of skin cancer in the time and frequency domain," *Journal of Biological Physics,* vol. 29, no. 2-3, pp. 257-259, 2003.

[39] C. Zhang, G. Zhao, B. Jin, Y. Hou, H. Jia, J. Chen, and P. H. Wu, "Terahertz imaging on subcutaneous tissues and liver inflamed by liver cancer cells," *Terahertz Science Technology,* vol. 5, no. 3, pp. 114-123, 2012.

[40] S. J. Oh, Y.-M. Huh, J.-S. Suh, J. Choi, S. Haam, and J.-H. Son, "Cancer diagnosis by terahertz molecular imaging technique," *Journal of Infrared, Millimeter, and Terahertz Waves,* vol. 33, no. 1, pp. 74-81, 2012.

[41] E. Berry, A. J. Fitzgerald, N. N. Zinov'ev, G. C. Walker, S. Homer-Vanniasinkam, C. D. Sudworth, R. E. Miles, J. M. Chamberlain, and M. A. Smith, "Optical properties of tissue measured using terahertz-pulsed imaging," *Proceedings of SPIE: Medical Imaging 2003*: *Physics of Medical Imaging,* vol. 5030, pp. 459-470, 15-20 February, 2003, San Diego, California, United States.

[42] D. M. Charron, K. Ajito, J.-Y. Kim, and Y. Ueno, "Chemical mapping of pharmaceutical cocrystals using terahertz spectroscopic imaging," *Analytical Chemistry,* vol. 85, no. 4, pp. 1980-1984, 2013.

[43] Y. -C. Shen, "Terahertz pulsed spectroscopy and imaging for pharmaceutical applications: a review," *International Journal of Pharmaceutics,* vol. 417, no. 1, pp. 48-60, 2011.

[44] Y. -C. Shen and P. F. Taday, "Development and application of terahertz pulsed imaging for nondestructive inspection of pharmaceutical tablet," *IEEE Journal of Selected Topics in Quantum Electronics,* vol. 14, no. 2, pp. 407-415, 2008.

[45] L. Maurer and H. Leuenberger, “Terahertz pulsed imaging and near infrared imaging to monitor the coating process of pharmaceutical tablets,” *International Journal of Pharmaceutics,* vol. 370, no. 1, pp. 8-16, 2009.

[46] J. P. Guillet, B. Recur, L. Frederique, B. Bousquet, L. Canioni, I. Manek-Hönninger, P. Desbarats, and P. Mounaix, “Review of terahertz tomography techniques,” *Journal of Infrared, Millimeter, and Terahertz Waves,* vol. 35, no. 4, pp. 382-411, 2014.

[47] H. Zhong, J. Xu, X. Xie, T. Yuan, R. Reightler, E. Madaras, and X. C. Zhang, “Nondestructive defect identification with terahertz time-of-flight tomography,” *IEEE Sensors Journal,* vol. 5, no. 2, pp. 203-208, 2005.

[48] H. Zhong, N. Karpowicz, J. Xu, Y. Deng, W. Ussery, M. Shur, and X. C. Zhang, “Detection of space shuttle insulation foam defects by using a 0.2 THz Gunn diode oscillator and pyroelectric detector,” *In Frontiers in Optics, Optical Society of America,* p. FTuG28, 2004.

[49] E. K. Rahani, T. Kundu, Z. Wu, and H. Xin, “Heat induced damage detection by terahertz (THz) radiation,” *Journal of Infrared, Millimeter, and Terahertz Waves,* vol. 32, no. 6, pp. 848-856, 2011.

[50] P. D. Cunningham, N. N. Valdes, F. A. Vallejo, L. M. Hayden, B. Polishak, X.-H. Zhou, J. Luo, A. K-Y. Jen, J. C. Williams, and R. J. Twieg, “Broadband terahertz characterization of the refractive index and absorption of some important polymeric and organic electro-optic materials,” *Journal of Applied Physics,* vol. 109, no. 4, pp. 043505/1-5, 2011.

[51] T. Nagatsuma, G. Ducournau, and C. C. Renaud, “Advances in terahertz communications accelerated by photonics,” *Nature Photonics*, vol. 10, no. 6, pp. 371-379, 2016.

[52] K. R. Jha and G. Singh, “Terahertz planar antennas for future wireless communication: A technical review,” I*nfrared Physics & Technology*, vol. 60, pp. 71-80, 2013.

[53] T. Kürner and S. Priebe, “Towards THz communications-status in research, standardization and regulation,” *Journal of Infrared, Millimeter, and Terahertz Waves,* vol. 35, no. 1, pp. 53-62, 2014.

[54] Z. Chen, Z. Tan, Y. Han, R. Zhang, X. Guo, H. Li, J. Cao, and H. C. Liu, “Wireless communication demonstration at 4.1 THz using quantum cascade laser and quantum well photodetector,” *Electronics Letters,* vol. 47, no. 17, pp. 1002-1004, 2011.

[55] G. Ducournau, P. Szriftgiser, F. Pavanello, E. Peytavit, M. Zaknoune, D. Bacquet, A. Beck, T. Akalin, and J. –F. Lampin, “THz communications using photonics and electronic devices: the race to data-rate,” *Journal of Infrared, Millimeter, and Terahertz Waves,* vol. 36, no. 2, pp. 198-220, 2015.

[56] X. Li, Z. Dong, J. Yu, N. Chi, Y. Shao, and G. Chang, “Fiber-wireless transmission system of 108 Gb/sdata over 80 km fiber and 2× 2multiple-input multiple-output wireless links at 100 GHz W-band frequency,” *Optics Letters,* vol. 37, no. 24, pp. 5106-5108, 2012.

[57] H. -J. Song, J.-Y. Kim, K. Ajito, M. Yaita, and N. Kukutsu, “Fully integrated ASK receiver MMIC for terahertz communications at 300 GHz,” *IEEE Transactions on Terahertz Science and Technology,* vol. 3, no. 4, pp. 445-452, 2013.

[58] J. Antes, F. Boes, D. Meier, T. Messinger, U. Lewark, A. Tessmann, S. Wagner, and I. Kallfass, “Ultra-wideband single-balanced transmitter-MMIC for 300 GHz communication systems,” *IEEE International Microwave Symposium (IMS), IEEE MTT-S,* 2014, pp. 1-3, 1-6 June, 2014, Tampa, Florida, USA.

[59] C. Jansen, S. Priebe, C. Moller, M. Jacob, H. Dierke, M. Koch, and T. Kurner, "Diffuse scattering from rough surfaces in THz communication channels," *IEEE Transactions on Terahertz Science and Technology,* vol. 1, no. 2, pp. 462-472, 2011.

[60] I. Kallfass, F. Boes, T. Messinger, J. Antes, A. Inam, U. Lewark, A. Tessmann, and R. Henneberger, "64 gbit/s transmission over 850 m fixed wireless link at 240 ghz carrier frequency," *Journal of Infrared, Millimeter, and Terahertz Waves,* vol. 36, no. 2, pp. 221-233, 2015.

[61] A. Hirata, T. Kosugi, H. Takahashi, J. Takeuchi, K. Murata, N. Kukutsu, Y. Kado, S. Okabe, T. Ikeda, F. Suginosita, and K. Shogen, "5.8-km 10-Gbps data transmission over a 120-GHz-band wireless link," *IEEE International Conference on Wireless Information Technology and Systems (ICWITS)*, pp. 1-4, 28 August- 3 September, *2010,* Honolulu, HI, USA.

[62] J. Y. Suen, "Terabit-per-second satellite links: a path toward ubiquitous terahertz communication," *Journal of Infrared, Millimeter, and Terahertz Waves,* vol. 37, no. 7, pp. 615-639, 2016.

[63] G. Grüner, "Millimeter and submillimeter wave spectroscopy of solids," *Millimeter and Submillimeter Wave Spectroscopy of Solids,* vol. 1, 1998.

[64] D. L. Woolard, J. O. Jensen, and R. J. Hwu, "Terahertz science and technology for military and security applications," *World Scientific,* vol. 46, 2007.

[65] J. A. Zeitler and L. F. Gladden, "In-vitro tomography and non-destructive imaging at depth of pharmaceutical solid dosage forms," *European Journal of Pharmaceutics and Biopharmaceutics,* vol. 71, no. 1, pp. 2-22, 2009.

[66] T. Kleine-Ostmann, P. Knobloch, M. Koch, S. Hoffmann, M. Breede, M. Hofmann, G. Hein, K. Pierz, M. Sperling, and K. Donhuijsen, "Continuous-wave THz imaging," *Electronics Letters,* vol. 37, no. 24, pp. 1461-1463, 2001.

[67] N. T. Yardimci, S.-H. Yang, C. W. Berry, and M. Jarrahi, "High-power terahertz generation using large-area plasmonic photoconductive emitters," *IEEE Transactions on Terahertz Science and Technology,* vol. 5, no. 2, pp. 223-229, 2015.

[68] T. Satoh, Y. Toya, S. Yamamoto, T. Shimura, K. Kuroda, Y. Takahashi, M. Yoshimura, Y. Mori, T. Sasaki, and S. Ashihara, "Generation of mid-to far-infrared ultrashort pulses in 4-dimethylamino-N-methyl-4-stilbazolium tosylate crystal," *JOSA B,* vol. 27, no. 12, pp. 2507-2511, 2010.

[69] H. Hirori, A. Doi, F. Blanchard, and K. Tanaka, "Single-cycle terahertz pulses with amplitudes exceeding 1 MV/cm generated by optical rectification in LiNbO 3," *Applied Physics Letters,* vol. 98, no. 9, pp. 091106/1-4, 2011.

[70] M. Ghoranneviss, M. A. Kashani, A. Hogabri, A. Kohiyan, and A. Anvari, "Design and modification of the FIR HCN laser," *SPIE's International Symposium on Optical Science, Engineering, and Instrumentation*, pp. 85-87, 19-24 July, 1998, San Diego, CA, USA.

[71] M. Y. Frankel, J. F. Whitaker, and G. A. Mourou, "Optoelectronic transient characterization of ultrafast devices," *IEEE Journal of Quantum Electronics,* vol. 28, no. 10, pp. 2313-2324, 1992.

[72] S. Pavlov, H. -W. Hübers, J. N. Hovenier, T. O. Klaassen, D. A. Carder, P. J. Phillips, B. Redlich, H. Riemann, R. K. Zhukavin, and V. N. Shastin, "Stimulated terahertz stokes emission of silicon crystals doped with antimony donors," *Physical Review Letters,* vol. 96, no. 3, pp. 037404/1-4, 2006.

[73] J. Hebling, A. Stepanov, G. Almási, B. Bartal, and J. Kuhl, "Tunable THz pulse generation by optical rectification of ultrashort laser pulses with tilted pulse fronts," *Applied Physics B: Lasers and Optics,* vol. 78, no. 5, pp. 593-599, 2004.

[74] H. Eisele, A. Rydberg, and G. I. Haddad, “Recent advances in the performance of InP Gunn devices and GaAs TUNNETT diodes for the 100-300-GHz frequency range and above,” *IEEE Transactions on Microwave Theory and Techniques,* vol. 48, no. 4, pp. 626-631, 2000.

[75] M. Tani, O. Morikawa, S. Matsuura, and M. Hangyo, “Generation of terahertz radiation by photomixing with dual-and multiple-mode lasers,” *Semiconductor Science and Technology,* vol. 20, no. 7, pp. S151-S163, 2005.

[76] F. Capasso, C. Gmachl, R. Paiella, A. Tredicucci, A. L. Hutchinson, D. L. Sivco, J. N. Baillargeon, A. Y. Cho, and H. C. Liu, “New frontiers in quantum cascade lasers and applications,” *IEEE Journal of Selected Topics in Quantum Electronics,* vol. 6, no. 6, pp. 931-947, 2000.

[77] A. Leitenstorfer, S. Hunsche, J. Shah, M. Nuss, and W. Knox, “Detectors and sources for ultrabroadband electro-optic sampling: Experiment and theory,” *Applied Physics Letters,* vol. 74, no. 11, pp. 1516-1518, 1999.

[78] D. Fast, W. Hurlbut, and V. G. Kozlov, “Extending spectral coverage of BWOs combined with frequency multipliers to 2.6 THz,” *International Society for Optics and Photonics, SPIE OPTO,* pp. 82610L/1-11, 12-16 August, 2012, San Diego, California, USA.

[79] N. Large, M. Abb, J. Aizpurua, and O. L. Muskens, “Photoconductively loaded plasmonic nanoantenna as building block for ultracompact optical switches,” *Nano Letters,* vol. 10, no. 5, pp. 1741-1746, 2010.

[80] P. Piot, D. Douglas, and G. Krafft, “Longitudinal phase space manipulation in energy recovering linac-driven free-electron lasers,” *Physical Review Special Topics-Accelerators and Beams,* vol. 6, no. 3, pp. 030702/1-11, 2003.

[81] M. J. Rodwell, M. Kamegawa, R. Yu, M. Case, E. Carman, and K. S. Giboney, “GaAs nonlinear transmission lines for picosecond pulse generation and millimeter-wave sampling,” *IEEE Transactions on Microwave Theory and Techniques,* vol. 39, no. 7, pp. 1194-1204, 1991.

[82] T. S. Hartwick, “Far infrared imaging techniques for law enforcement applications,” *SPIE/SPSE Technical Symposium*, pp. 139-140, 18 April, 1977, East-Reston.

[83] K. J. Siebert, T. Löffler, H. Quast, M. Thomson, T. Bauer, R. Leonhardt, S. Czasch, and H. G. Roskos, “All-optoelectronic continuous wave THz imaging for biomedical applications,” *Physics in Medicine and Biology,* vol. 47, pp. 3743- 3748, 2002.

[84] N. Karpowicz, H. Zhong, J. Xu, K. -I. Lin, J. -S. Hwang, and X. Zhang, “Comparison between pulsed terahertz time-domain imaging and continuous wave terahertz imaging,” *Semiconductor Science and Technology,* vol. 20, no. 7, pp. S293-299, 2005.

[85] D. Auston and X. Zhang, “Large-aperture photoconducting antennas,” *Proceedings of Optical Society of America OSA,* vol. 9, pp. 2-8, 1991.

[86] Q. Wu and X. C. Zhang, “Free-space electro-optic sampling of terahertz beams,” *Applied Physics Letters,* vol. 67, no. 24, pp. 3523-3525, 1995.

[87] V. P. Wallace, E. MacPherson, J. A. Zeitler, and C. Reid, “Three-dimensional imaging of optically opaque materials using nonionizing terahertz radiation,” Journal of Optical Society of America A, vol. 25, no. 12, pp. 3120-3133, 2008.

[88] D. M. Sheen, T. E. Hall, R. H. Severtsen, D. L. McMakin, B. K. Hatchell, and P. L. Valdez, “Standoff concealed weapon detection using a 350-GHz radar imaging system,” *SPIE Defense, Security, and Sensing*, pp. 767008/1-12, 5-9 April, 2010, Orlando, Florida, United States.

[89] M. Kowalski and M. Kastek, “Comparative studies of passive imaging in terahertz and mid-wavelength infrared ranges for object detection,” *IEEE Transactions on Information Forensics and Security,* vol. 11, no. 9, pp. 2028-2035, 2016.

[90] E. Grossman, J. Gordon, D. Novotny, and R. Chamberlin, “Terahertz active and passive imaging,” *in Proceedings of 8th European Conference on Antennas and Propagation (EuCAP),* pp. 2221-2225, 6-11 April, 2014, Netherlands.

[91] W. Deal, X. Mei, K. M. Leong, V. Radisic, S. Sarkozy, and R. Lai, “THz monolithic integrated circuits using InP high electron mobility transistors,” *IEEE Transactions on Terahertz Science and Technology,* vol. 1, no. 1, pp. 25-32, 2011.

[92] V. Radisic, K. M. Leong, X. Mei, S. Sarkozy, W. Yoshida, and W. R. Deal, “Power amplification at 0.65 THz using INP HEMTs,” *IEEE Transactions on Microwave Theory and Techniques,* vol. 60, no. 3, pp. 724-729, 2012.

[93] F. Friederich, W. Von Spiegel, M. Bauer, F. Meng, M. D. Thomson, S. Boppel, A. Lisauskas, B. Hils, V.Krozer, A. Keil, and T. Loffler, “THz active imaging systems with real-time capabilities,” *IEEE Transactions on Terahertz Science and Technology,* vol. 1, no. 1, pp. 183-200, 2011.

[94] B. Hu and M. Nuss, “Imaging with terahertz waves,” *Optics Letters,* vol. 20, no. 16, pp. 1716-1718, 1995.

[95] Y. H. Lo and R. Leonhardt, “Aspheric lenses for terahertz imaging,” *Optics Express,* vol. 16, no. 20, pp. 15991-15998, 2008.

[96] A. J. Huber, F. Keilmann, J. Wittborn, J. Aizpurua, and R. Hillenbrand, “Terahertz near-field nanoscopy of mobile carriers in single semiconductor nanodevices,” *Nano Letters,* vol. 8, no. 11, pp. 3766-3770, 2008.

[97] M. A. Patrick, J. A. Holt, C. D. Joye, and F. C. De Lucia, “Elimination of speckle and target orientation requirements in millimeter-wave active imaging by modulated multimode mixing illumination,” *Journal of Optical Society of America A,* vol. 29, no. 12, pp. 2643-2656, 2012.

[98] G. C. Trichopoulos, H. L. Mosbacker, D. Burdette, and K. Sertel, “A broadband focal plane array camera for real-time THz imaging applications,” *IEEE Transactions on Antennas and Propagation,* vol. 61, no. 4, pp. 1733-1740, 2013.

[99] I. C. Mayorga, A. Schmitz, T. Klein, C. Leinz, and R. Gusten, “First in-field application of a full photonic local oscillator to terahertz astronomy,” *IEEE Transactions on Terahertz Science and Technology,* vol. 2, no. 4, pp. 393-399, 2012.

[100] K. Han, T. K. Nguyen, I. Park, and H. Han, “Terahertz Yagi-Uda antenna for high input resistance,” *Journal of Infrared, Millimeter, and Terahertz Waves,* vol. 31, no. 4, pp. 441-454, 2010.

[101] R. Singh, C. Rockstuhl, C. Menzel, T. P. Meyrath, M. He, H. Giessen, F. Lederer, and W. Zhang, “Spiral-type terahertz antennas and the manifestation of the Mushiake principle,” *Optics Express,* vol. 17, no. 12, pp. 9971-9980, 2009.

[102] K. Topalli, G. C. Trichopoulos, and K. Sertel, “An indirect impedance characterization method for monolithic THz antennas using coplanar probe measurements,” *IEEE Antennas and Wireless Propagation Letters,* vol. 11, pp. 3-5, 2012.

[103] M. Jarrahi, “Advanced photoconductive terahertz optoelectronics based on nano-antennas and nano-plasmonic light concentrators,” *IEEE Transactions on Terahertz Science and Technology,* vol. 5, no. 3, pp. 391-397, 2015.

[104] C. W. Berry, N. Wang, M. R. Hashemi, M. Unlu, and M. Jarrahi, “Significant performance enhancement in photoconductive terahertz optoelectronics by incorporating plasmonic contact electrodes,” *Nature Communications,* vol. 4, pp. 1622/1-10, 2013.

[105] S. -G. Park, K. H. Jin, M. Yi, J. C. Ye, J. Ahn, and K. -H. Jeong, "Enhancement of terahertz pulse emission by optical nanoantenna," *ACS Nano,* vol. 6, no. 3, pp. 2026-2031, 2012.

[106] N. Zhu and R. W. Ziolkowski, "Photoconductive THz antenna designs with high radiation efficiency, high directivity, and high aperture efficiency," *IEEE Transactions on Terahertz Science and Technology,* vol. 3, no. 6, pp. 721-730, 2013.

[107] T. K. Nguyen, H. Han, and I. Park, "Numerical study of a full-wavelength dipole antenna on a GaAs membrane structure at terahertz frequency," *Journal of Infrared, Millimeter, and Terahertz Waves,* vol. 32, no. 6, pp. 763-777, 2011.

[108] P. Maraghechi and A. Y. Elezzabi, "Experimental confirmation of design techniques for effective bow-tie antenna lengths at THz frequencies," *Journal of Infrared, Millimeter, and Terahertz Waves,* vol. 32, no. 7, pp. 897-901, 2011.

[109] D. Rutledge, D. Neikirk, and D. Kasilingam, "Integrated-circuit antennas," *Infrared and Millimeter Waves*, vol. 10, no. 2, pp. 1-90, 1983.

[110] M. Y. Frankel, S. Gupta, J. A. Valdmanis, and G. A. Mourou, "Terahertz attenuation and dispersion characteristics of coplanar transmission lines," *IEEE Transactions on Microwave Theory and Techniques,* vol. 39, no. 6, pp. 910-916, 1991.

[111] M. Beck, H. Schäfer, G. Klatt, J. Demsar, S. Winnerl, M. Helm, and T. Dekorsy, "Impulsive terahertz radiation with high electric fields from an amplifier-driven large-area photoconductive antenna," *Optics Express,* vol. 18, no. 9, pp. 9251-9257, 2010.

[112] M. Tani, Y. Hirota, C. T. Que, S. Tanaka, R. Hattori, M. Yamaguchi, S. Nishizawa, and M. Hangyo, "Novel terahertz photoconductive antennas," *International Journal of Infrared and Millimeter Waves,* vol. 27, no. 4, pp. 531-546, 2006.

[113] J. F. O'Hara, J. Zide, A. Gossard, A. Taylor, and R. Averitt, "Enhanced terahertz detection via ErAs: GaAs nanoisland superlattices," *Applied Physics Letters,* vol. 88, no. 25, pp. 251119/1-4, 2006.

[114] N. Khiabani, Y. Huang, Y. -C. Shen, and S. Boyes, "Theoretical modeling of a photoconductive antenna in a terahertz pulsed system," *IEEE Transactions on Antennas and Propagation,* vol. 61, no. 4, pp. 1538-1546, 2013.

[115] I. Malhotra, K. R. Jha, and G. Singh, "Analysis of highly directive photoconductive dipole antenna at terahertz frequency for sensing and imaging applications," *Optics Communications,* vol. 397, pp. 129-139, 2017.

[116] N. M. Burford and M. O. El-Shenawee, "Review of terahertz photoconductive antenna technology," *Optical Engineering,* vol. 56, no. 1, pp. 010901-010901, 2017.

[117] B. Pradarutti, R. Müller, W. Freese, G. Matthäus, S. Riehemann, G. Notni, S. Nolte, and A. Tunnermann, "Terahertz line detection by a microlens array coupled photoconductive antenna array," *Optics Express,* vol. 16, no. 22, pp. 18443-18450, 2008.

[118] M. Tani, M. Herrmann, and K. Sakai, "Generation and detection of terahertz pulsed radiation with photoconductive antennas and its application to imaging," *Measurement Science and Technology,* vol. 13, no. 11, pp. 1739-1745, 2002.

[119] H. -B. Liu, H. Zhong, N. Karpowicz, Y. Chen, and X. -C. Zhang, "Terahertz spectroscopy and imaging for defense and security applications," *Proceedings of the IEEE,* vol. 95, no. 8, pp. 1514-1527, 2007.

[120] J. Chen, Y. Chen, H. Zhao, G. J. Bastiaans, and X. -C. Zhang, "Absorption coefficients of selected explosives and related compounds in the range of 0.1–2.8 THz," *Optics Express,* vol. 15, no. 19, pp. 12060-12067, 2007.

[121] J. Liu, W. -H. Fan, X. Chen, and J. Xie, "Identification of high explosive RDX using terahertz imaging and spectral fingerprints," In *Journal of Physics: Conference Series,*

vol. 680, no. 1, pp. 012030/1-9, IOP Publishing, 28-31 October, 2016, Hangzhou, China.

[122] L. Ho, M. Pepper, and P. Taday, "Terahertz spectroscopy: Signatures and fingerprints," *Nature Photonics,* vol. 2, no. 9, pp. 541-543, 2008.

[123] Y. Huang, N. Khibani, Y. Shen, and D. Li, "Terahertz photoconductive antenna efficiency," *In Proceedings of International Workshop on Antenna Technology (iWAT),* pp. 152-156, 7-9 March, 2011, Hong Kong.

[124] S. –G. Park, A. M. Weiner, M. R. Melloch, C. W. Siders, J. L. W. Siders, and A. J. Taylor, "High-power narrow-band terahertz generation using large-aperture photoconductors," IEEE Journal of Quantum Electronics, vol. 35, no. 8, pp. 1257-1268, 1999.

[125] D. Jackson and N. Alexopoulos, "Microstrip dipoles on electrically thick substrates," *International Journal of Infrared and Millimeter Waves,* vol. 7, no. 1, pp. 1-26, 1986.

[126] T. K. Nguyen, W. T. Kim, B. J. Kang, H. S. Bark, K. Kim, J. Lee, I. Park, T. –I. Jeon, and F. Rotermund, "Photoconductive dipole antennas for efficient terahertz receiver," *Optics Communications,* vol. 383, pp. 50-56, 2017.

[127] G. Mourou, C. Stancampiano, A. Antonetti, and A. Orszag, "Picosecond microwave pulses generated with a subpicosecond laser-driven semiconductor switch," *Applied Physics Letters,* vol. 39, no. 4, pp. 295-296, 1981.

[128] D. Auston, K. Cheung, and P. Smith, "Picosecond photoconducting Hertzian dipoles," *Applied Physics Letters,* vol. 45, no. 3, pp. 284-286, 1984.

[129] P. R. Smith, D. H. Auston, and M. C. Nuss, "Subpicosecond photoconducting dipole antennas," *IEEE Journal of Quantum Electronics,* vol. 24, no. 2, pp. 255-260, 1988.

[130] C. Fattinger and D. Grischkowsky, "Terahertz beams," *Applied Physics Letters,* vol. 54, no. 6, pp. 490-492, 1989.

[131] D. Grischkowsky, I. Duling III, J. Chen, and C.-C. Chi, "Electromagnetic shock waves from transmission lines," *Physical Review Letters,* vol. 59, no. 15, pp. 1663- 1666, 1987.

[132] J. V. Rudd, M. W. Warmuth, S. L. Williamson, and D. A. Zimdars, "Compact fiber pigtailed terahertz modules," *Washington, DC, U.S. Patent 6,816,647,* issued November 9, 2004.

[133] C. Fumeaux, G. D. Boreman, W. Herrmann, F. K. Kneubühl, and H. Rothuizen, "Spatial impulse response of lithographic infrared antennas," *Applied Optics,* vol. 38, no. 1, pp. 37-46, 1999.

[134] G. M. Rebeiz and D. B. Rutledge, "Integrated horn antennas for millimeter-wave applications," *In Annales des télécommunications,* vol. 47, no. 1-2, pp. 38-48, Sspringer-Verlag, 1992.

[135] T. K. Nguyen, F. Rotermund, and I. Park, "A traveling-wave stripline dipole antenna on a substrate lens at terahertz frequency," *Current Applied Physics,* vol. 14, no. 8, pp. 998-1004, 2014.

[136] M. Tani, S. Matsuura, K. Sakai, and S.-I. Nakashima, "Emission characteristics of photoconductive antennas based on low-temperature-grown GaAs and semi-insulating GaAs," *Applied Optics,* vol. 36, no. 30, pp. 7853-7859, 1997.

[137] S. Hughes, M. Tani, and K. Sakai, "Vector analysis of terahertz transients generated by photoconductive antennas in near-and far-field regimes," *Journal of Applied Physics,* vol. 93, no. 8, pp. 4880-4884, 2003.

[138] C. W. Berry and M. Jarrahi, "Principles of impedance matching in photoconductive antennas," *Journal of Infrared, Millimeter,and Terahertz Waves,* vol. 33, no. 12, pp. 1182-1189, 2012.

[139] E. Moreno, M. Pantoja, F. Ruiz, J. Roldán, and S. García, “On the numerical modeling of terahertz photoconductive antennas,” *Journal of Infrared, Millimeter, and Terahertz Waves,* vol. 35, no. 5, pp. 432-444, 2014.

[140] J. Yang, W. Fan, and B. Xue, “Biased electric field analysis of a photoconductive antenna for terahertz generation,” *Nuclear Instruments and Methods in Physics Research Section A: Accelerators, Spectrometers, Detectors and Associated Equipment,* vol. 637, no. 1, pp. S165-S167, 2011.

[141] K. R. Jha and G. Singh, “Analysis and design of ring-resonator integrated hemi-elliptical lens antenna at terahertz frequency,” *Optics Communications,* vol. 285, no. 16, pp. 3445-3452, 2012.

[142] N. Khiabani, Y. Huang, and Y.-C. Shen, “Discussions on the main parameters of THz photoconductive antennas as emitters,” *Proceedings of the 5th European Conference on Antennas and Propagation (EUCAP),* pp. 462-466, 11 April, 2011, Rome, Italy.

[143] K. Moon, J. Choi, J. -H. Shin, S.-P. Han, H. Ko, N. Kim, J. W. Park, Y. J. Yoon, K. Y. Kang, H. C. Ryu, and K. H. Park, “Generation and detection of terahertz waves using low-temperature-grown GaAs with an annealing process,” *ETRI Journal,* vol. 36, no. 1, pp. 159-162, 2014.

[144] T. -A. Liu, M. Tani, M. Nakajima, M. Hangyo, K. Sakai, S. -I. Nakashima, and C. –L. Pan, “Ultrabroadband terahertz field detection by proton-bombarded InP photoconductive antennas,” *Optics Express,* vol. 12, no. 13, pp. 2954-2959, 2004.

[145] L. Hou, W. Shi, and S. Chen, “Noise Analysis and Optimization of Terahertz Photoconductive Emitters,” *IEEE Journal of Selected Topics in Quantum Electronics,* vol. 19, no. 1, pp. 8401305/1-5, 2013.

[146] M. Venkatesh, K. Rao, T. Abhilash, S. Tewari, and A. Chaudhary, “Optical characterization of GaAs photoconductive antennas for efficient generation and detection of Terahertz radiation,” *Optical Materials,* vol. 36, no. 3, pp. 596-601, 2014.

[147] S. L. Chuang, “Physics of Photonic Device,” Second Edition, *John Wiley & Sons*, 2008.

[148] H. Skulason, H. Nguyen, A. Guermoune, V. Sridharan, M. Siaj, C. Caloz, and T. Szkopek, “110 GHz measurement of large-area graphene integrated in low-loss microwave structures,” *Applied Physics Letters,* vol. 99, no. 15, pp. 153504/1-4, 2011.

[149] P. -Y. Chen, C. Argyropoulos, and A. Alu, “Terahertz antenna phase shifters using integrally-gated graphene transmission-lines,” *IEEE Transactions on Antennas and Propagation,* vol. 61, no. 4, pp. 1528-1537, 2013.

[150] M. Dragoman, A. Muller, D. Dragoman, F. Coccetti, and R. Plana, “Terahertz antenna based on graphene,” *Journal of Applied Physics,* vol. 107, no. 10, pp. 104313/1-3, 2010.

[151] I. Llatser, C. Kremers, D. N. Chigrin, J. M. Jornet, M. C. Lemme, A. Cabellos-Aparicio, and E. Alarcon, “Characterization of graphene-based nano-antennas in the terahertz band,” *6th European Conference on Antennas and Propagation (EUCAP),* pp. 194-198, 26-30 March, 2012, Prague, Czech Republic.

[152] M. Tamagnone, J. Gomez-Diaz, J. Mosig, and J. Perruisseau-Carrier, “Analysis and design of terahertz antennas based on plasmonic resonant graphene sheets,” *Journal of Applied Physics,* vol. 112, no. 11, pp. 114915/1-4, 2012.

[153] F. Miyamaru, Y. Saito, K. Yamamoto, T. Furuya, S. Nishizawa, and M. Tani, “Dependence of emission of terahertz radiation on geometrical parameters of dipole photoconductive antennas,” *Applied Physics Letters,* vol. 96, no. 21, pp. 211104/1-3, 2010.

[154] B. Choudhury, A. R. Sonde, and R. M. Jha, “Terahertz antenna technology for space applications,” *Terahertz Antenna Technology for Space Applications,* pp. 1-33, Springer, Singapore, 2016.

[155] W. Dou and Z. Sun, “Ray tracing on extended hemispherical and elliptical silicon dielectric lenses,” *International Journal of Infrared and Millimeter Waves,* vol. 16, no. 11, pp. 1993-2002, 1995.

[156] A. Artemenko, A. Mal'tsev, R. Maslennikov, A. Sevastyanov, and V. Sorin, “Studying integrated silicon-lens antennas for radio communication systems operated in the 60 GHz frequency band,” *Radiophysics & Quantum Electronics,* vol. 55, no. 8, pp. 511-519, 2013.

[157] A. A. Artemenko, V. N. Sorin, R. O. Maslennikov, and A. V. Mozharovskiy, “Lens antenna with electronic beam steering capabilities,” U. S. Patent Application 14/593,552, filed January 9, 2015.

[158] P. C. Upadhya, W. Fan, A. Burnett, J. Cunningham, A. G. Davies, E. H. Linfield, J. Lloyd-Hughes, E. Castro-Camus, M. B. Johnston, and H. Beere, “Excitation-density-dependent generation of broadband terahertz radiation in an asymmetrically excited photoconductive antenna,” *Optics Letters,* vol. 32, no. 16, pp. 2297-2299, 2007.

[159] J. Diao, F. Yang, L. Du, J. Ou Yang, and P. Yang, “Enhancing terahertz radiation from dipole photoconductive antenna by blending tips,” *Progress In Electromagnetics Research Letters,* vol. 25, pp. 127-134, 2011.

[160] H. Jafari, H. Heidarzadeh, G. Rostami, M. Dolatyari, and A. Rostami, “Continuous terahertz wave generation based on photomixers coupled to Fibonacci fractal tree antennas,” *Optical and Quantum Electronics,* vol. 48, no. 12, pp. 534/1-14, 2016.

[161] M. R. Stone, M. Naftaly, R. E. Miles, J. R. Fletcher, and D. P. Steenson, “Electrical and radiation characteristics of semilarge photoconductive terahertz emitters,” *IEEE Transactions on Microwave Theory and Techniques,* vol. 52, no. 10, pp. 2420-2429, 2004.

[162] M. Awad, M. Nagel, H. Kurz, J. Herfort, and K. Ploog, “Characterization of low temperature GaAs antenna array terahertz emitters,” *Applied Physics Letters,* vol. 91, no. 18, pp. 181124/1-4, 2007.

[163] E. Moreno, M. Pantoja, A. R. Bretones, M. Ruiz-Cabello, and S. G. Garcia, “A comparison of the performance of THz photoconductive antennas,” *IEEE Antennas and Wireless Propagation Letters*, vol. 13, pp. 682-685, 2014.

[164] Y. Zhang, X. Zhang, S. Li, J. Gu, Y. Li, Z. Tian, C. Ouyang, M. He, J. Han, and W. Zhang, “A broadband THz-TDS system based on DSTMS emitter and LTG InGaAs/InAlAs photoconductive antenna detector,” *Scientific Reports,* vol. 6, pp. 26949/1-6, 2016.

[165] S. B. Qadri, D. H. Wu, B. D. Graber, N. A. Mahadik, and A. Garzarella, “Failure mechanism of THz GaAs photoconductive antenna,” *Applied Physics Letters,* vol. 101, no. 1, pp. 011910/1-4, 2012.

[166] R. Emadi, N. Barani, R. Safian, and A. Z. Nezhad, “Hybrid computational simulation and study of terahertz pulsed photoconductive antennas,” *Journal of Infrared, Millimeter, and Terahertz Waves,* vol. 37, no. 11, pp. 1069-1085, 2016.

[167] M. M. Seyedsharbaty and R. A. Sadeghzadeh, “Antenna gain enhancement by using metamaterial radome at THz band with reconfigurable characteristics based on graphene load,” *Optical and Quantum Electronics,* vol. 49, no. 6, pp. 221/1-13, 2017.

[168] Z. Piao, M. Tani, and K. Sakai, “Carrier dynamics and terahertz radiation in photoconductive antennas,” *Japanese Journal of Applied Physics,* vol. 39, no. 1R, pp. 96-100, 2000.

[169] K. Ezdi, B. Heinen, C. Jördens, N. Vieweg, N. Krumbholz, R. Wilk, M. Mikulics, and M. Koch, “A hybrid time-domain model for pulsed terahertz dipole antennas,” *Journal of the European Optical Society-Rapid publications*, vol. 4, pp. 09001/1-7, 2009.

[170] J. Zhang, “Characterization of the terahertz photoconductive antenna by three-dimensional finite-difference time-domain method,” *Physics Optics*, arXiv preprint arXiv:1406.3872, pp. 1- 21, 2014.

[171] E. Moreno, M. F. Pantoja, S. G. Garcia, A. R. Bretones, and R. G. Martin, “Time-domain numerical modeling of THz photoconductive antennas,” *IEEE Transactions on Terahertz Science and Technology*, vol. 4, no. 4, pp. 490-500, 2014.

[172] Y. -S. Chung, C. Cheon, J. -H. Son, and S. -Y. Hahn, “FDTD analysis of propagation characteristics of terahertz electromagnetic pulses,” *IEEE Transactions on Magnetics,* vol. 36, no. 4, pp. 951-955, 2000.

[173] K. Moon, H. Han, and I. Park, “Terahertz folded half-wavelength dipole antenna for high output power,” *International Topical Meeting on Microwave Photonics, MWP 2005,* pp. 301-304, 12-14 October, 2005, Seoul, South Korea.

[174] J. Suen, W. Li, Z. Taylor, and E. Brown, “Characterization and modeling of a terahertz photoconductive switch,” *Applied Physics Letters*, vol. 96, no. 14, pp. 141103 1-4, 2010.

[175] G. C. Loata, M. D. Thomson, T. Löffler, and H. G. Roskos, “Radiation field screening in photoconductive antennae studied via pulsed terahertz emission spectroscopy,” *Applied Physics Letters,* vol. 91, no. 23, pp. 232506 1-4, 2007.

[176] M. Teich, “Field- theoretical treatment of photomixing,” *Applied Physics Letters,* vol. 14, no. 6, pp. 201-203, 1969.

[177] D. Saeedkia and S. Safavi-Naeini, “A comprehensive model for photomixing in ultrafast photoconductors,” *IEEE Photonics Technology Letters,* vol. 18, no. 13, pp. 1457-1459, 2006.

[178] J. H. Kim, A. Polley, and S. E. Ralph, “Efficient photoconductive terahertz source using line excitation,” *Optics Letters,* vol. 30, no. 18, pp. 2490-2492, 2005.

[179] E. Castro-Camus, J. Lloyd-Hughes, and M. Johnston, “Three-dimensional carrier-dynamics simulation of terahertz emission from photoconductive switches,” *Physical Review B,* vol. 71, no. 19, pp. 195301 1-7, 2005.

[180] M. Khorshidi and G. Dadashzadeh, “Dielectric Structure with Periodic Strips for Increasing Radiation Power of Photoconductive Antennas: Theoretical Analysis,” *Journal of Infrared, Millimeter, and Terahertz Waves,* vol. 38, no. 5, pp. 609-629, 2017.

[181] N. Khiabani, Y. Huang, Y. -C. Shen, and S. Boyes, “Time varying conductance in THz photoconductive antennas,” *Terahertz Science and Technology,* vol. 4, no. 3, pp. 116-122, 2011.

[182] R. Emadi, R. Safian, and A. Z. Nezhad, “Theoretical modeling of terahertz pulsed photoconductive antennas based on hot-carriers effect,” *IEEE Journal of Selected Topics in Quantum Electronics,* vol. 23, no. 4, pp. 1-9, 2017.

[183] J. Prajapati, M. Bharadwaj, A. Chatterjee, and R. Bhattacharjee, “Circuit modeling and performance analysis of photoconductive antenna,” *Optics Communications*, vol. 394, pp. 69-79, 2017.

[184] D. Li, Y. Huang, Y. -C. Shen, and N. Khiabani, “Effects of substrate on the performance of photoconductive thz antennas,” *International Workshop on Antenna Technology (iWAT), 2010,* pp. 1-4, 1-3 March, 2010, Lisbon, Portugal.

[185] G. C. Loata, “Investigation of low-temperature-grown GaAs photoconductive antennae for continuous-wave and pulsed terahertz generation,” *Ph.D. Thesis*, Goethe Universitat, Frankfurt, 2007.

[186] I. Malhotra, P. Thakur, S. Pandit, K. R. Jha, and G. Singh, “Analytical framework of small-gap photoconductive dipole antenna using equivalent circuit model,” *Optical and Quantum Electronics*, vol. 49, pp. 334/1-23, 2017.

[187] A. Raisanen, “Challenges of terahertz,” *The Second European Conference on Antennas and Propagation, EuCAP 2007,* pp. 1-4, 11-16 November, 2007, EICC, Edinburgh, UK.

[188] F. Costa and A. Monorchio, “Design of subwavelength tunable and steerable Fabry-Perot/leaky wave antennas,” *Progress In Electromagnetics Research*, vol. 111, pp. 467-481, 2011.

[189] G. V. Trentini, “Partially reflecting sheet arrays,” *IRE Transactions on Antennas and Propagation*, vol. 4, no. 4, pp. 666-671, 1956.

[190] A. Pirhadi, F. Keshmiri, M. Hakkak, and M. Tayarani, “Analysis and design of dual band high directive EBG resonator antenna using square loop FSS as superstrate layer,” *Progress In Electromagnetics Research*, vol. 70, pp. 1-20, 2007.

[191] D. H. Lee, Y. J. Lee, J. Yeo, R. Mittra, and W. S. Park, “ "Directivity enhancement of circular polarized patch antenna using ring-shaped frequency selective surface superstrate,” *Microwave and Optical Technology Letters, vol.* 49, no. 1, pp. 199-201, 2007.

[192] A. Foroozesh and L. Shafai, “Investigation into the effects of the patch-type FSS superstrate on the high-gain cavity resonance antenna design,” *IEEE Transactions on Antennas and Propagation*, vol. 58, no. 2, pp. 258-270, 2010.

[193] H. Yang and N. Alexopoulos, “Gain enhancement methods for printed circuit antennas through multiple superstrates,” *IEEE Transactions on Antennas and Propagation*, vol. 35, no. 7, pp. 860-863, 1987.

[194] H. Gharbaninejad-Foumani and M. Khalaj-Amirhosseini, “Compact spatial band-pass filters using FSS”, *Progress in Electromagnetic Research C*, vol. 21, pp. 59-73, 2011.

[195] J. Yeo and D. Kim, “Novel design of a high-gain and wideband Fabry-Perot cavity antenna using a tapered AMC substrate”, *Journal of Infrared, Millimetre and Terahertz Waves*, vol. 30, no. 3, pp. 217-224, 2009.

[196] H. Boutayeb, T. A. Denidni, and M. Nedil, “Bandwidth widening technique for directive antenna based on partially reflecting surfaces,” *Progress in Electromagnetic Research*, vol. 74, pp. 407-419, 2007.

[197] S. Vegesna, Z. Yanhan, A. Bernussi, and M. Saed, “Terahertz two-layer FSSs with improved transmission characteristics,” *IEEE Transactions on Terahertz Science and Technology*, vol. 2, no. 4, pp. 441-448, 2012.

[198] H. Liu, S. Lei, X. Shi, and L. Li, “Study of antenna superstrates using metamaterials for directivity enhancement based on fabry-perot resonant cavity”, *International Journal of Antennas and Propagation*, vol. 13, pp. 1-10, 2013.

[199] R. Appleby and H. B. Wallace, “Standoff detection of weapons and contraband in the 100 GHz to 1 THz region,” *IEEE Transactions on Antennas and Propagation,* vol. 55, no. 11, pp. 2944-2956, 2007.

[200] Y. Shen, A. T. Lo, P. Taday, B. Cole, W. Tribe, and M. Kemp, “Detection and identification of explosives using terahertz pulsed spectroscopic imaging,” *Applied Physics Letters,* vol. 86, no. 24, pp. 241116 1-4, 2005.

[201] H. -B. Liu, Y. Chen, G. J. Bastiaans, and X.-C. Zhang, “Detection and identification of explosive RDX by THz diffuse reflection spectroscopy,” *Optics Express,* vol. 14, no. 1, pp. 415-423, 2006.

[202] A. Singh, S. Winnerl, J. C. König-Otto, D. R. Stephan, M. Helm, and H. Schneider, “Plasmonic efficiency enhancement at the anode of strip line photoconductive terahertz emitters,” *Optics Express,* vol. 24, no. 20, pp. 22628-22634, 2016.

[203] S. -G. Park, Y. Choi, Y. -J. Oh, and K. -H. Jeong, “Terahertz photoconductive antenna with metal nanoislands,” *Optics Express,* vol. 20, no. 23, pp. 25530-25535, 2012.

[204] N. Vieweg, M. Mikulics, M. Scheller, K. Ezdi, R. Wilk, H.-W. Hübers, and M. Koch, "Impact of the contact metallization on the performance of photoconductive THz antennas," *Optics Express,* vol. 16, no. 24, pp. 19695-19705, 2008.

[205] O. Abdulmunem, K. Hassoon, J. Völkner, M. Mikulics, K. Gries, and J. Balzer, "Photoconductive LT-GaAs terahertz antennas: correlation between surface quality and emission strength," *Journal of Infrared, Millimeter, and Terahertz Waves,* vol. 38, no. 5, pp. 574-582, 2017.

[206] N. T. Yardimci, R. Salas, E. M. Krivoy, H. P. Nair, S. R. Bank, and M. Jarrahi, "Impact of substrate characteristics on performance of large area plasmonic photoconductive emitters," *Optics Express,* vol. 23, no. 25, pp. 32035-32043, 2015.

[207] T. K. Nguyen, H. Han, and I. Park, "Frequency selective surface for directivity enhancement of a terahertz photomixer antenna," *International Workshop on Antenna Technology (iWAT),* pp. 100-103, 4-6 March, 2013, Karlsruhe, Germany.

[208] S. Monni, A. Neto, G. Gerini, F. Nennie, and A. Tijhuis, "Frequency-selective surface to prevent interference between radar and SATCOM antennas," *IEEE Antennas and Wireless Propagation Letters,* vol. 8, pp. 220-223, 2009.

[209] P. Carelli, F. Chiarello, S. Cibella, A. D. Gaspare, R. Leoni, M. Ortolani, and G. Torrioli, "A fast terahertz spectrometer based on frequency selective surface filters," *Journal of Infrared, Millimeter, and Terahertz Waves*, vol. 33, no. 5, pp. 505-512, 2012.

[210] K. R. Jha, and G. Singh, "Prediction of highly directive probe-fed microstrip antenna at terahertz frequency," *International Journal of Numerical Modelling: Electronic Networks, Devices and Fields,* vol. 25, no. 2, pp. 175-191, 2012.

[211]T. -K. Wu, "Frequency Selective Surface and Grid Array," First Edition, Wiley-Interscience, 1995.

[212] B. A. Munk , "Frequency Selective Surfaces: Theory and Design," Wiley Online Library, 2000.

[213] F. Bayatpur, "Metamaterial-Inspired Frequency-Selective Surfaces," Ph.D. Thesis, *Uniersity of Michigan*, 2009.

[214] R. Mittra, C. H. Chan, and T. Cwik, "Techniques for analyzing frequency selective surfaces-a review," *Proceedings of the IEEE,* vol. 76, no. 12, pp. 1593-1615, 1988.

[215] K. R. Jha, G. Singh, and R. Jyoti, "A simple synthesis technique of single-square-loop frequency selective surface," *Progress In Electromagnetics Research B,* vol. 45, pp. 165-185, 2012.

[216] J. A. Reed, "Dissertation Proposal: Frequency selective surfaces with multiple periodic elements," Ph.D. Thesis, *University of Texas at Dallas*, 1997.

[217] A. E. Yilmaz and M. Kuzuoglu, "Design of the Square Loop Frequency Selective Surfaces with Particle Swarm Optimization via the Equivalent Circuit Model," *Radioengineering,* vol. 18, no. 2, pp. 95-102, 2009.

[218] P. Callaghan, E. A. Parker, and R. J. Langley, "Influence of supporting dielectric layers on the transmission properties of frequency selective surfaces," *In IEEE Proceedings on Microwaves, Antennas and Propagation*, vol. 138, no. 5, pp. 448-454, IET Digital Library, 29-30 April, 1991.

[219] N. Behdad, M. Al-Joumayly, and M. Salehi, "A low-profile third-order bandpass frequency selective surface," *IEEE Transactions on Antenna and Propagation*, vol. 57, no. 2, pp. 460-466, 2009.

[220] J. E. Raynolds, B. A. Mank, J. B. Pryor, and R. J. Marhefka, "Ohmic loss in frequency-selective surfaces," *Journal of Applied Physics*, vol. 93, no. 9, pp. 5346-5358, 2003.

[221] E. D. Palik, "Handbook of Optical Constants of Solids," American Press: London, 1985.

[222] P. W. Gilberd, “The anomalous skin effect and the optical properties of metals,” *Journal of Physics F: Metal Physics*, vol. 12, no. 8, pp. 1845-1860, 1982.

[223] J. S. Fernandez, G. Goussetis, and R. Cheung, “Tunable 2D electromagnetic bandgap (EBG) structures based on micro-electro-mechanical systems (MEMS) for THz frequencies,” *Proceedings of IEEE International Symposium on Antennas and Propagation Society (APSURSI)*, July 11-17, Toronto, 2010, pp. 1-4.

[224] T. K. Ostmann, K. Pierz, G. Hein, P. Dawson, and M. Koch, “Audio signal transmission over THz communication channel using semiconductor modulator,” *Electronics Letter*, vol. 40, no. 2, pp. 124-126, 2004.

[225] G. Bharti, K. R. Jha, and G. Singh, “Terahertz frequency selective surface for future wireless communication systems,” *Optik-International Journal for Light and Electron Optics*, vol. 126, no. 24, pp. 5909-5917, 2015.

[226] M. E. MacDonald, A. Alexanian, R. A. York, Z. Popovic, and E. N. Grossman, “Spectral transmittance of lossy printed resonant-grid terahertz bandpass filters,” *IEEE Transactions on Microwave Theory and Techniques*, vol. 48, no. 4, pp. 712-718, 2000.

[227] N. Engheta and R. W. Ziolkowski (Eds.), “Metamaterials: Physics and Engineering Explorations,” *John Wiley & Sons*, 2006.

[228] A. K. Bhattacharya, “Characteristics of space and surface waves in a multilayered structure,” *IEEE Transactions on Antennas and Propagation*, vol. 38, no. 8, pp. 1231-1238, 1990.

[229] A. Pirahadi, F. Keshmiri, M. Hakkak, and M. Tayarani, “Analysis and design of dual band high directivity EBG resonator antenna using square loop FSS as superstrate layer,” *Progress In Electromagnetic Research*, vol. 70, pp. 1-20, 2007.

[230] A. W. Lee and Q. Hu, “Real-time, continuous-wave terahertz imaging by use of a microbolometer focal-plane array,” *Optics Letters*, vol. 30, no. 19, pp. 2563-2565, 2005.

[231] C. Jansen, S. Wietzke, O. Peters, M. Scheller, N. Vieweg, M. Salhi, N. Krumbholz, C. Jordens, T. Hochrein, and M. Koch, “Terahertz imaging: applications and perspectives,” *Applied Optics*, vol. 49, no. 19, pp. E48-E57, 2010.

[232] B. Pradarutti, R. Müller, G. Matthäus, C. Brückner, S. Riehemann, G. Notni, S. Nolte, and A. Tunnermann, “Multichannel balanced electro-optic detection for terahertz imaging,” *Optics Express*, vol. 15, no. 26, pp. 17652-17660, 2007.

[233] X. -C. Zhang and D. Auston, “Optically induced THz electromagnetic radiation from planar photoconducting structures,” *Journal of Electromagnetic Waves and Applications*, vol. 6, no. 1-4, pp. 85-106, 1992.

[234] S. E. Ralph and D. Grischkowsky, “Trap-enhanced electric fields in semi-insulators: The role of electrical and optical carrier injection,” *Applied Physics Letters*, vol. 59, no. 16, pp. 1972-1974, 1991.

[235] M. Scheller, C. Jansen, and M. Koch, “Analyzing sub-100-μm samples with transmission terahertz time domain spectroscopy,” *Optics Communications*, vol. 282, no. 7, pp. 1304-1306, 2009.

[236] M. Herrmann, M. Tani, and K. Sakai, “Display modes in time-resolved terahertz imaging,” *Japanese Journal of Applied Physics*, vol. 39, no. 11R, p. 6254, 2000.

[237]Y. Kadoya, “THz wave propagation on strip lines: Devices, properties, and applications,” *In 19th International Conference on Applied Electromagnetics and Communications, ICECom*, pp. 1-4, 24-26 September, 2007, Dubrovnik, Croatia .

[238] A. Rivera-Lavado, L.-E. García-Muñoz, A. Generalov, D. Lioubtchenko, K.-A. Abdalmalak, S. Llorente-Romano, A. Garcia-Lamperez, D. Segovia-Vargas, and A. V. Raisanen, “Design of a dielectric rod waveguide antenna array for millimeter waves,” *Journal of Infrared, Millimeter, and Terahertz Waves*, vol. 38, no. 1, pp. 33-46, 2017.

[239] G. C. Trichopoulos, G. Mumcu, K. Sertel, H. L. Mosbacker, and P. Smith, “A novel approach for improving off-axis pixel performance of terahertz focal plane arrays," *IEEE Transactions on Microwave Theory and Techniques,* vol. 58, no. 7, pp. 2014-2021, 2010.

[240] R. Camblor-Diaz, S. Ver-Hoeye, C. Vazquez-Antuna, G. R. Hotopan, M. Fernandez-Garcia, and F. Las Heras Andres, “Sub-millimeter wave frequency scanning 8 x 1 antenna array,” *Progress In Electromagnetics Research,* vol. 132, pp. 215-232, 2012.

[241] G. H. Döhler, L. E. Garcia-Muñoz, S. Preu, S. Malzer, S. Bauerschmidt, J. Montero-de-Paz, E. Ugarte-Munoz, A. Rivera-Lavado, V. Gonzalez-Posadas, and D. Segovia-argas, “From arrays of THz antennas to large-area emitters,” *IEEE Transactions on Terahertz Science and Technology,* vol. 3, no. 5, pp. 532-544, 2013.

[242] M. Uzunkol, O. D. Gurbuz, F. Golcuk, and G. M. Rebeiz, “A 0.32 THz SiGe 4x4 imaging array using high-efficiency on-chip antennas,” *IEEE Journal of Solid-State Circuits,* vol. 48, no. 9, pp. 2056-2066, 2013.

[243] G. Bharti, K. R. Jha, G. Singh, and R. Jyoti, “Azimuthally periodic wedge-shaped metal vane loaded circular ring frequency selective surface,” *International Journal of Microwave and Wireless Technologies,* vol. 7, no. 1, pp. 95-106, 2015.

[244] G. Bharti, K. R. Jha, G. Singh, and R. Jyoti, “Design of dual-polarized and angular stable new bandpass frequency selective surface in X-band,” *Telecommunication Systems,* vol. 61, no. 3, pp. 559-567, 2016.

[245] T. K. Nguyen and I. Park, “Broadband single-feed microstrip antenna in a fabry-perot resonator,” *In International Workshop on Antenna Technology (iWAT),* pp. 333-334, 4-6 March, 2015, Seoul, Korea.

[246] S. Vegesna, Y. Zhu, A. Bernussi, and M. Saed, “Terahertz two-layer frequency selective surfaces with improved transmission characteristics,” *IEEE Transactions on Terahertz science and Technology,* vol. 2, no. 4, pp. 441-448, 2012.

[247] G. Bharti, K. R. Jha, and G. Singh, “A synthesis technique of single square loop frequency selective surface at terahertz frequency,” *Optik-International Journal for Light and Electron Optics,* vol. 125, no. 21, pp. 6428-6435, 2014.

[248] K. Maki, and C. Otani, “Terahertz beam steering and frequency tuning by using the spatial dispersion of ultrafast laser pulses,” *Optics Express,* vol. 16, no. 14, pp. 10158-10169, 2008.

[249] Y. Monnai, K. Altmann, C. Jansen, H. Hillmer, M. Koch, and H. Shinoda, “Terahertz beam steering and variable focusing using programmable diffraction gratings,” *Optics Express,* vol. 21, no. 2, pp. 2347-2354, 2013.

[250] P. U. Jepsen, D. G. Cooke, and M. Koch, “Terahertz spectroscopy and imaging – modern techniques and applications,” *Laser and Photonics Reviews,* vol. 5, no. 1, pp. 124–166, 2011.

[251] K. Kawase, Y. Ogawa, Y. Watanabe, and H. Inoue, “Non-destructive terahertz imaging of illicit drugs using spectral fingerprints,” *Optics Express,* vol.11, no. 20, pp. 2549–2554, 2003.

[252] W. L. Chan, K. Charan, D. Takhar, K. F. Kelly, R. G. Baraniuk, and D. M. Mittleman, “A single-pixel terahertz imaging system based on compressed sensing,” *Applied Physics Letters,* vol. 93, no. 12, pp. 121105/1-3, 2008.

[253] P. Y. Chen, M. Farhat, A. N. Askarpour, M. Tymchenko, and A. Alu, “Infrared beam-steering using acoustically modulated surface plasmons over a graphene monolayer,” Journal of Optics, vol. 16, no. 9, pp. 094008/ 1-9, 2014.

[254] I. H. Libon, S. Baumgärtner, M. Hempel, N. E. Hecker, J. Feldmann, M. Koch, and P. Dawson, “An optically controllable terahertz filter,” *Applied Physics Letters*, vol. 76, no. 20, pp. 2821-2823, 2000.

[255] R. Kersting, G. Strasser, and K. Unterrainer, “Terahertz phase modulator,” *Electronics Letters*, vol. 36, no. 13, pp. 1156-1158, 2000.

[256] S. Busch, B. Scherger, M. Scheller, and M. Koch, “Optically controlled terahertz beam steering and imaging,” Optics Letters, vol. 37, no. 8, pp. 1391-1393, 2012.

[257] I. H. Libon, S. Baumgärtner, M. Hempel, N. E. Hecker, J. Feldmann, M. Koch, and P. Dawson, “An optically controllable terahertz filter,” *Applied Physics Letters*, vol. 76, no. 20, pp. 2821-2823, 2000.

[258] R. Kersting, G. Strasser, and K. Unterrainer, “Terahertz phase modulator,” *Electronics Letters*, vol. 36, no. 13, pp. 1156-1158, 2000.

[259] S. Busch, B. Scherger, M. Scheller, and M. Koch, “Optically controlled terahertz beam steering and imaging,” *Optics Letters*, vol. 37, no. 8, pp. 1391-1393, 2012.

[260] H. T. Chen, W. J. Padilla, M. J. Cich, A. K. Azad, R. D. Averitt, and A. J. Taylor, “A metamaterial solid-state terahertz phase modulator,” *Nature Photonics*, vol. 3, no. 3, pp. 148-151, 2009.

[261] H. T. Chen, J. F. O’Hara, A. K. Azad, A. J. Taylor, R. D. Averitt, D. B. Shrekenhamer, and W. J. Padilla, “Experimental demonstration of frequency-agile terahertz metamaterials,” *Nature Photonics*, vol. 2, no. 5, pp. 295-298, 2008.

[262] H. T. Chen, W. J. Padilla, J. M. O. Zide, A. C. Gossard, A. J. Taylor, and R. D. Averitt, “Active terahertz metamaterial devices,” *Nature*, vol. 444, no. 7119, pp. 597-600, 2006.

[263] C. F. Hsieh, R. P. Pan, T. T. Tang, H. L. Chen, and C. L. Pan, “Voltage-controlled liquid-crystal terahertz phase shifter and quarter-wave plate,” *Optics Letters*, vol. 31, no. 8, pp. 1112-1114, 2006.

[264] H. Y. Wu, C. F. Hsieh, T. T. Tang, R. P. Pan, and C. L. Pan, “Electrically tunable room-temperature 2π liquid crystal terahertz phase shifter,” IEEE Photonics Technology Letters, vol. 18, no. 14, pp. 1488-1490, 2006.

[265] B. Scherger, M. Reuter, M. Scheller, K. Altmann, N. Vieweg, R. Dabrowski, J. A. Deibel, and M. Koch, “Discrete terahertz beam steering with an electrically controlled liquid crystal device,” *Journal of Infrared, Millimetre and Terahertz Waves*, vol. 33, no. 11, pp. 1117-1122, 2012.

[266] N. M. Froberg, B. B. Hu, X. C. Zhang, and D. H. Auston, “Terahertz radiation from a photoconducting antenna array,” *IEEE Journal of Quantum Electronics*, vol. 28, no. 10, pp. 2291-2301, 1992.

[267] K. Uematsu, K. Maki, and C. Otani, “Terahertz beam steering using interference of femtosecond optical pulses,” *Optics Express*, vol. 20, no. 20, pp. 22914-22921, 2012.

[268] K. Maki and C. Otani, “Terahertz beam steering and frequency tuning by using the spatial dispersion of ultrafast laser pulses,” *Optics Express*, vol. 16, no. 14, pp. 10158-10169, 2008.

[269] D. M. Sheen, D. L. McMakin, and T. E. Hall, “Three-dimensional millimeter-wave imaging for concealed weapon detection,” *IEEE Transactions on Microwave Theory and Techniques*, vol. 49, no. 9, pp. 1581–1592, 2001.

[270] M. T. Ghasr, D. Pommerenke, J. T. Case, A. McClanahan, A. Aflaki-Bbeni, M. Abou-Khousa, S. Kharkovsky, K. Guinn, F. D. Paulis, and R. Zoughi, “Rapid rotary scanner and portable coherent wideband Q-band transceiver for high-resolution millimeter-wave imaging applications,” *IEEE Transactions on Instrumentation and Measurement*, vol. 60, no. 1, pp. 186–197, 2008.

[271] H. P. Tran, F. Gumbmann, J. Weinzierl, and L. P. Schmidt, “A fast scanning w-band system for advanced millimetre-wave short range imaging applications,” *3rd European Radar Conference, EURAD 2006*, pp. 146–149, 13-15 September, Manchester, UK, 2006.

[272] C. H. Tseng, and T. H. Chu, “An effective usage of vector network analyzer for microwave imaging,” *IEEE Transactions on Microwave Theory and Techniques*, vol. 53, no. 9, pp. 2884–2891, 2005.

[273] R. Camblor Diaz, S. Ver Hoeye, C. V´azquez, G. Hotopan, M. Fern´andez, and F. Las Heras, “ Sub-millimeter wave frequency scanning 8X1 antenna array,” *Progress in Electromagnetic Research*, vol. 132, pp. 215-232, 2012.

[274] B. B. Hu, J. T. Darrow, X. C. Zhang, and D. H. Auston, “Optically steerable photoconducting antennas,” *Applied Physics Letters*, vol. 56, no.10, pp. 886-888, 1990.

[275] N. M. Froberg, B. B. Nu, X. –C. Zhang, and D. H. Auston, “Terahertz radiation from a photoconducting antenna array,” *IEEE Journal of Quantum Electronics*, vol. 28, no. 10, pp. 2291-2301, 1992.

[276] T. D. Drysdale, E. D. Walsby, and D. R. S. Cumming, “Measured and simulated performance of a ceramic micromechanical beam steering device at 94 GHz,” *Applied Optics*, vol. 47, no. 13, pp. 2382-2385, 2008.

[277] Y. Kamiya, Y. Murakami, W. Chojo, and M. Fujise, “An electro-optic BFN for array antenna beam forming,” *IEICE Transactions on Electronics*, vol. 78, no. 8, pp.1090-1094, 1995.

[278] R. Guzmán-Quirós, A. R. Weily, J. L. Gómez-Tornero, and Y. J. Guo, “A fabry-perot antenna with two-dimensional electronic beam scanning,” *IEEE Transactions on Antenna and Propagation*, vol. 64, no. 4, pp. 1536-1541, 2016.

[279] E. E. Funk, and C. H. Lee, “ Free-space power combining and beam steering of ultra-wideband radiation using an array of laser-triggered antennas,” *IEEE Transactions on Microwave Theory and Techniques*, vol. 44, no. 11, pp. 2039-2044, 1996.

[280] K. Sengupta, and A. Hajimiri, “A 0.28 THz power-generation and beam-steering array in CMOS based on distributed active radiators,” *IEEE Journal of Solid-State Circuits*, vol. 47, no. 12, pp. 3013-3031, 2012.